THE CHARACTERISTICS AND FEASIBILITY OF AN IN-LINE DEBRIS CONTROL TECHNIQUE FOR KrF EXCIMER LASER ABLATIVE MICROMACHINING

A thesis submitted in accordance with the requirements of
LOUGHBOROUGH UNIVERSITY
for the degree of Doctor of Philosophy

by

Colin Frank Dowding (BEng)

August 2009

Wolfson School of Mechanical and Manufacturing Engineering
Loughborough University

LIST OF PUBLICATIONS

Journal Papers

1. Dowding, C. F., Lawrence, J. "Use of thin laminar liquid flows above ablation area for control of ejected material during excimer machining", *Proceedings of the Institution of Mechanical Engineers Part B: Journal of Engineering Manufacture*, 2009, **223** (7), pp.759-775.
2. Dowding, C. F., Lawrence, J. "Impact of open de-ionized water thin film laminar immersion on the liquid immersed ablation threshold and ablation rate of features machined by KrF excimer laser ablation of bisphenol A polycarbonate", *Optics and Lasers in engineering*, 2009, **47** (11), pp.1169-1176.
3. Dowding, C. F., and Lawrence, J. "Ablation debris control by means of closed thick film filtered water immersion", *Proceedings of the Institution of Mechanical Engineers Part B: Journal of Engineering Manufacture*.

   Accepted 24 September 2009.

4. Dowding, C. F., Lawrence, J., Holmes, A. S. "Effects of closed immersion filtered water flow velocity on the ablation threshold of bisphenol A polycarbonate during excimer laser machining", *Applied Surface Science*.

   Submitted for review 6 July 2009

5. Dowding, C. F., Lawrence, J., Holmes, A. S. "Excimer laser machining of bisphenol A polycarbonate under closed immersion filtered water with varying flow velocities and the effects thereof on etch rate", *Journal of Physics, part D: Applied Physics*.

   Submitted for review 16 July 2009

6. Dowding, C. F., Lawrence, J., Holmes, A. S. "The impact of medium chemistry to flowing liquid closed immersion ablation of bisphenol A polycarbonate", *Proceedings of the Royal Society A: Mathematical, Physical and Engineering Sciences*.

   Submitted for review 16 July 2009

7. Dowding, C. F., Lawrence, J. "Impact of open thin film flowing de-ionized water immersion on the topography and geometry of features machined by KrF excimer laser ablation of bisphenol A polycarbonate.", *Journal of Laser Applications*.

   Submitted for review 22 July 2009

8. Dowding, C. F., Lawrence, J. "Topography of features machined into bisphenol A polycarbonate using closed thick film flowing filtered water immersed KrF excimer laser ablation.", *Proceedings of the Royal Society A: Mathematical, Physical and Engineering Sciences*.

   Submitted for review 27 July 2009

9. Dowding, C. F., Lawrence, J. "Analysis of beam modification caused by the closed thick film immersed KrF excimer laser ablation technique", *International Journal of Machine Tools & Manufacture*.

   Submitted for review 30 July 2009

Conference Papers

1. Dowding, C. F. and Lawrence, J. "Use of thin laminar liquid flows above ablation area for control of ejected material during excimer machining", *The proceedings of The 27th International Congress on Application of Lasers and Electro-Optics: Laser Materials Processing Section*, 2008, pp.872-880.

2. Dowding, C. F., and Lawrence, J. Analysis of the excimer laser ablation characteristics of bisphenol A polycarbonate in ambient air and under thin film laminar flow water immersion. *The proceedings of The 27th International Congress on Application of Lasers and Electro-Optics: Laser Materials Processing Section*, 2008, pp.202-211.

3. Dowding, C. F., and Lawrence, J. "Impact Of Closed Thick Film Flowing Filtered Water Immersion On KrF Excimer Laser Ablation Characteristics", *The proceedings of The 28th International Congress on Application of Lasers and Electro-Optics: Laser Materials Processing Section*, 2009. **ACCEPTED.**

4. Dowding, C. F., and Lawrence, J. "Use Of Enclosed Thin Laminar Liquid Flows Above Ablation Area For Control Of Ejected Material During Excimer Machining", *The proceedings of The 28th International Congress on Application of Lasers and Electro-Optics: Laser Materials Processing Section*, 2009. **ACCEPTED.**

ABSTRACT

To observe KrF excimer laser ablation through thin liquid film of de-ionized (DI) water and the effects thereof on debris control, equipment was designed to contain a small control volume that could be supplied with a fixed flow velocity thin film of DI water to immerse a bisphenol A polycarbonate workpiece. Using the same equipment comparison with ablation in ambient air was possible.

The positional debris deposition of samples machined in ambient air was found to show modal tendency reliant on the feature shape machined and according to species size. This is proposed to be due to the interaction of multiple shockwaves at the extent of ablation plumes generated at geometry specific locations in the feature. Debris was deposited where the shockwaves collide. Ablating under a flowing thin film of DI water showed potential to modify the end position and typical size of the debris produced, as well as increased homogeneity of deposition density. Compared with a sample machined in ambient air, the use of immersion has reduced the range of debris deposition by 17% and the deposition within the boundary of the ablation plume has a comparatively even population density. Unlike samples machined in ambient air, outside the ablation plume extents positional control of deposited debris by thin film flowing DI water immersion was evidenced by rippled flow line patterns, indicating the action of transport by fluid flow. A typical increase in debris size by an order of magnitude when using DI water as an immersing liquid was measured, a result that is in line with a colloidal interaction response.

Using KrF excimer laser ablation of bisphenol A polycarbonate under open thin film flowing DI water immersion 26% more surface waviness and 17% more surface roughness was measured over features ablated in ambient air. A 20% reduction in ablation rate was observed under open thin film flowing DI water immersion conditions. Since attenuation of the KrF excimer laser beam in the DI water was negligible, this decrease resulted from confinement of the vapour plume by the liquid medium which caused plume shielding and splashing events - critical mechanisms that modified the primary ablation characteristics. Indeed, whereas in ambient air the threshold fluence was measured as 37 mJ/cm^2, in the open thin film regime threshold fluences of 83.9 and 58.6 mJ/cm^2 were observed with and without splashing respectively. This also contributed to the loss of total etching efficiency. Flow ripple in the immersing fluid caused uneven amplification of photomechanical ablation, resulting in uneven surface waviness.

Because the performance of laser ablation generated debris control by means of open immersion techniques were limited by flow surface ripple effects and plume pressure losses, a closed technique has been developed to eradicate these issues by ensuring a controlled geometry for both the optical interfaces of the flowing liquid film. This had the action of preventing splashing, ensuring repeatable machining conditions and allowed for control of liquid flow velocity.

A 93% decrease in debris deposition was observed when KrF excimer laser ablation machining under closed thick film flowing filtered water immersion compared with ablation in ambient air. In addition the mean debris particle size became larger when KrF excimer laser

machining under closed thick film regime liquid immersion, with an equal proportion of small and medium sized debris being produced. This is due to colloidal interactions motivated by micro-bubbles generated in the immersing fluid. At any flow velocity, large debris was displaced more than smaller debris, indicating that the action of flow turbulence in the duct had more impact on smaller debris. What is more, this suggests that closed thick film regime flowing liquid immersion techniques would facilitate finer pitch for arrays of laser machined features.

KrF excimer laser ablation immersed using a turbulent regime flow velocity demonstrated similar ablation threshold and ablation rate magnitudes to KrF excimer laser ablation in ambient air. This was a marked improvement open thin film DI water immersion.

Laminar regime flow velocities yielded negligible ablation threshold modification and caused a 26.6% reduction in the ablation rate over ablation in ambient air and were found to be less effective at controlling the positional trend of deposition than turbulent flow velocities. This indicates that low flow velocity did not significantly distort the ablation plume resulting in maximum plume shielding of the laser beam, also un-removed suspended debris interfered with the laser beam, further reducing the fluence upon arrival at the image. Increases in flow velocity beyond the laminar regime to the turbulent regime resulted in decreases in the ablation threshold and increases in the ablation rate. Between 2.78 and 3.24 m/s the minimum ablation threshold of 112 mJ/cm^2 and the maximum ablation rate of 160 nm/pulse were achieved. This increase in flow velocity was capable of removing debris from the feature before the arrival of the following laser pulse. Simultaneously, the compressed ablation plume causing plume shielding of the beam was moderately distorted. This in turn reduced the distance traversed by the laser beam through the dense laser ablation plume; consequently increasing fluence at the image. Flow velocities above 3.24 m/s resulted in debris deposition that was dominated by turbulence. Also the distortion of the laser ablation plume by these relatively high flow velocities was significant, effecting reduced etching efficiency.

Ablating using closed thick film flowing filtered water immersion brings about modification to the contributors that combine to produce laser ablation: laser etching, acoustic type mechanical etching and thermal effects, by increased plume confinement. It is clear that the proportional contributions were further modified by variations to the flow velocity of the plume confining medium. Laminar flow velocities confined the plume without distortion which promoted beam attenuation whilst increasing mechanical etching and thermal effects. As flow velocity increased to 2.78 to 3.24 m/s ablation was augmented by reduced beam attenuation caused by flow induced distortion, but without removal, of the plume which still amplified mechanical etching. Further increases in flow velocity result in the destruction of the plume, thereby allowing minimal attenuation of the laser beam, but at the expense of simultaneous removal of the plume etching contribution. Feature topography was also dependant upon flow velocity, caused by flow induced modification of the ablation mechanism rather than variation of the fluence used.

Use of DI water resulted in close ablation rate and threshold agreement with results gained using filtered water, displaying a marginal loss in ablation threshold and ablation rate of 4.3% and 11.7% respectively. This loss is proposed to be caused by electrostatic insulation of DI water supporting the action of colloidal grouping of small debris particles to form medium sized items that more completely attenuate the laser beam.

ACKNOWLEDGEMENTS

My mum, **Janet** and dad, **Michael**: you supplied the house, advice and support. Without it I would not have been able to live in Loughborough and do this. It was a huge undertaking and a big risk in 2006, hopefully it has been worth it. Also, for the odd bailout when the university chose not to pay me at regular intervals. Thanks to my dad for all the work, time and money that he has spent on the house with me to make it the building it is now; I wish we had more photos to track its development, but there are plenty of images left in my mind. Thanks for all of them.

My supervisor, **Jonathan Lawrence**. I don't have very much room here to say thanks for a lot of things. I think our 14 hour session to finish this on 9-10 August sums it up. I never dreamed I'd be a doctor until I met you. It was a rollercoaster like you predicted; but, it was the best I've ever been on.

My Brother, **Robert**, for chats about cars, games, engines, computers, planes, stand up comedy and where to go to university. You'll have a good time anywhere. Just make sure you cherish it.

My Girlfriend, **Sarai**, for her support and presence during the many times of stress.

Andrew Holmes for letting me use his brand new excimer laser micromachining centre – this would have taken another year without you. I am indebted to you.
James Pedder for introducing me to Andrew Holmes and putting a good word in for me.
Exitech, Ltd. (as it was) for inspiring me to work with lasers and to attempt a solution for the problem outlined in this thesis.

David Waugh – for answering all of my stupid questions, being organized for me when I didn't organize myself and generally putting up with the undesirable prospect of sharing a broom cupboard with me (and my mess) for 2 long years.
Matthew Gibson for help, a spare hand and a wall for idea bouncing.
Simon (Andy) Wormald for anything to do with MATLAB, optics or computing.
Michael O'Tool for a sage understanding and quiet contemplation of my rants, quirks and ponderings about this universe we live in, over a beer, a coffee or an orange, pear and banana.

Peter Wileman and **Dave Britton** for maintenance of equipment.

The brave **Members of Badgers Den**, and my **School Friends** that now lie spread across our wide and glorious land. Here's to the beers, the tears and the laughter (not to mention the coffee and the hangovers afterwards). *Long may it continue* - wherever we reside.

Lastly, my trusty **Toshiba Satellite Pro U200**. It really wasn't meant to build something like this, but it never skipped a beat! I'm going to put it in a display case full of formaldehyde for prosperity once this is printed.

CONTENTS

CHAPTER 1

CHAPTER 2

CHAPTER 6

CHAPTER 7

CHAPTER 8

LIST OF FIGURES

CHAPTER 1

CHAPTER 2

CHAPTER 3

CHAPTER 4

CHAPTER 5

CHAPTER 6

CHAPTER 7

CHAPTER 8

CHAPTER 9

CHAPTER 10

CHAPTER 11

CHAPTER 12

CHAPTER 13

CHAPTER 14

CHAPTER 15

LIST OF TABLES

CHAPTER 1

CHAPTER 2

CHAPTER 3

CHAPTER 10

NOMENCLATURE

A	Hamaker Constant	J	a	Radial Area	m^2
A'	Absorptance Coefficient	--	a_1	Cross-sectional Area of a Particle	m^2
C_d	Drag Coefficient	--			
F_{ad}	Total Force of Adhesion	N			
F_{CAP}	Capillary Adhesion Force	N			
F_{Der}	Derjaguin Predicted Force	N			
F_{drag}	Flow Drag Force	N			
F_{el}	Long Range Electrostatic Force	N			
F_i	Electrostatic Image Force	N			
$F_{\Delta P}$	Force Due to Atmospheric Pressure Differential	N			
F_T	Tensile Force	N			
F_{vdW}	van der Waals Force	N			
F'	Separation Load	N			
G	Energy Release Rate	J/s			
			h	Lifshitz - van der Waals Constant	--
			h_{asp}	Asperity Height	m
I	Irradiance	W/m^2	i	Directional Component	--
I_a	Ray with Maximum Angle of Incidence in an Imaging System	--			
I_b	Ray Passing from Edge of Objective and Through Centre of Lens in an Imaging System	--			
I_i	Incident Beam	--			
I_t	Transmitted Beam	--			
			j	Directional Component	--
K	Geometric Deformation Ratio	--	k	Extinction Coefficient	--
K_p	Geometric Deformation Ratio of Particle	--	k_p	Surface Packing Density	--
L_{asp}	Peak - to - Peak Distance Between Surface Asperities	m			
L_c	Distance Between Charge Centres	m			
L_s	Separation Distance between Surfaces	m			
			m	Mass	Kg
			n	Real Refractive Index	--
			$\tilde{n}$	Complex Refractive Index	--
			n_1	Refractive Index of Medium Being Passed From	--

			n_2	Refractive Index of Medium Being Passed To	--
P	Normal Load	N	p_H	Hertz Pressure	Pa
P_l	Apparent Normal Load	N	p_{max}	Maximum Pressure	Pa
P_a	Adhesion Tension	N			
P_i	Incident Power Intensity	J/sm^2			
P_t	Power Transmission	J/s			
Q_A	Kinetic Energy Resultant of Long-range Attraction Forces	J	q	Charge	C
Q_A'	Kinetic Energy Resultant of Short-range Attraction Forces	J			
Q_E	Deformation Energy	J			
Q_e	Partial Elastic Region Deformation Energy	J			
Q_{el}	Simple Elastic Deformation Energy	J			
Q_{elE}	Total Elastic Energy in a Plastic - Elastic Material	J			
Q_{elP}	Total Plastic Energy in a Plastic - Elastic Material	J			
Q_I	Kinetic Energy	J			
Q_L	Dissipated Energy	J			
Q_P	Pure Plastic Region Deformation Energy	J			
Q_p	Partial Plastic Region Deformation Energy	J			
Q_W	Energy Loss due to Elastic Wave Propagation.	J			
R_a	Mean Surface Roughness Constant	m	r_1	Macroscopic Orthogonal Radius of the Particle	m
R_{ku}	Surface Kurtosis Constant	m	r_2	Parallel Planar Radius of the Particle	m
R_q	Route Mean Square Surface Roughness Constant	m	r_a	Contact Radius After Deformation	m
R_{sk}	Constant of Roughness Data Skew	m	r_b	Contact Radius when Normal Load is Negligible	m
R_t	Peak - Trough Height	m	r_c	Dynamic Contact Radius	m
R_{var}	Modal Surface Roughness Constant	m	r_e	Effective Radius	m
R_z	Ten Point Height	m	r_p	Particle Radius	m
R'	Reflectance Coefficient	--	r_{MAX}	Contact Radius at Maximum Tensile Stress Before Particle-surface Separation	m
S	Illuminated Surface Area	m^2			
T	Surface Tension	N			
T_c	Critical Temperature	K			
T_g	Glass Transition Temperature	K			
T'	Transmissivity Coefficient	--			
U	Contact Potential Difference	mV			
			v_C	Critical Rebound Velocity	m/s

			v_{CP}	Critical Rebound Velocity Considering Plastic Deformation	m/s
			v_{el}	Threshold Velocity Before Exceeding Elastic Rebound Limit	m/s
			v_{impact}	Particle Impact Velocity	m/s
W_A	Work of Adhesion	J			
W_q	Constant Route Mean Square Waviness	m			
Y	Young's Modulus	Pa			
Y_S	Young's Modulus of The Surface	Pa			
Z	Shock Impedance	Ns/m^3	z	Local Surface Height	m
Z_{air}	Shock Impedance of Air	Ns/m^3	z_0	Lennard-Jones Separation Distance	m
Z_{target}	Shock Impedance of the Ablated Material	Ns/m^3	$z(i, j)$	Height Data in Matrix Format	m
Z_{water}	Shock Impedance of Water	Ns/m^3			
			α'	Absorption Coefficient	--
			γ	Surface Energy	eV
			γ_{12}	Interfacial Energy	eV
			γ^d	Dispersion Forces	eV
			γ^p	Polar Forces	eV
Δl	Focal Length	m	δ	One-dimensional Deformation	m
			ε_0	Permittivity of Free Space	$A^2s^4kg^{-1}m^{-3}$
			ε_M	Dielectric Constant of Medium	$A^2s^4kg^{-1}m^{-3}$
			θ	Angle	°
			θi	Angle of Incidence	°
			θ_{ia}	Angle of Incidence of Ray 'a'	°
			θ_{ib}	Angle of Incidence of Ray 'b'	°
			θ_{ii}	Angle of Incidence At 2nd Medium Interface	°
			θ_r	Angle of Refraction	°
			θ_{ra}	Angle of Refraction of Ray 'a'	°
			θ_{rr}	Angle of Refraction At 2nd Medium Interface	°
			θ_{rra}	2nd Angle of Refraction of Ray 'a'	°
			θ_{rrb}	2nd Angle of Refraction of Ray 'b'	°
			λ	Maugis - Dugdale Dimensionless Parameter	--
			ν'	Dynamic Viscosity of Fluid	Pa/s
			ξ	Maugis - Dugdale Fitting Parameter	--
			π	Pi	--
			ρ	Density	kg/m^3
			ρ_M	Medium Density	kg/m^3

		ρ_p	Particle Density	kg/m^3
		ρ_S	Surface Density	kg/m^3
		σ_0	Theoretical Separation Stress	Pa
	Fraction of Internal Energy			
Ω	Released as Thermal Energy	--		

GLOSSARY OF TERMS

AFM	Atomic Force Microscope
CCD	Charge Coupled Device
CFC's	Chlorofluorocarbons
CFD	Computation Fluid Dynamics
COS	Carpick Ogletree Salmeron
DI	De-ionized
DLVO	Derjaguin, Landau, Verwey and Overbeek
DMT	Derjaguin, Muller and Toperov
DoF	Depth of Focus
FNPT	Female National Pipe Threads
HAZ	Heat Affected Zone
HEPA	High Efficiency Particulate Air
IPA	Isopropanol
JKR	Johnson, Kendal and Roberts
LCP	Liquid Crystal Polymer
LCU	Laser Control Unit
LIBWE	Laser Induced Backside Wet Etching
MD	Maugis - Dugdale
MNPT	Male National Pipe Threads
NPT	National Pipe Threads
PC	Polycarbonate
PET	Polyethylenetelephthalate
PI	Polyimide
PLA	Pulsed Laser Ablation
PMMA	Polymethylmethacrylate
RGB	Red, Green and Blue
RH	Relative Humidity
RMS	Route Mean Square
SPRI	Surface Plasmon Resonance Imaging
ToF-MS	Time-of-flight Mass Spectrometry
TRIC	Trichloroethane
UHV	Ultra High Vacuum
UV	Ultraviolet
VUV	Vacuum Ultraviolet
WLI	White Light Interferometer
XPS	X-ray Photoelectron Spectroscopy

INTRODUCTION

Research Rationale

The need for micromachining technology and current status

Modern manufacturing methods are key to ensuring the economy of the UK can be competitive on the world stage. Micromachining is at the vanguard of modern manufacturing and it is vital that this industry's demands for the means for producing complex micron-scale features are met. Laser micromachining has established itself as the most effective and efficient means of machining complex micro- and nano-scale features, but like any other machining operation laser micromachining produces debris and the effect of this micron-scale particulate debris is considerable [1, 2, 3].

In recent times the capability of some laser manufacturing techniques has increased to a level where tooling performance is limited not by the repeatability and resolution of the machining method, but the effect of the debris created during the process [2]. Quality is of utmost importance to mass production industries. In engineering quality has a different meaning to its traditional sense. Quality is a measure of process repeatability rather than a measure of perceived level of craftsmanship [4]. Quality is critical to micromachining industries if they are to continue to develop at the rapid rate, following Moore's law, that has been achieved thus far [5].

Laser ablation used in micromachining

In the last four decades the proliferation of the transistor circuit and the event of new techniques in manufacturing; particularly those using laser radiation as a machining method have presented a new, urgent need to fully understand and more importantly control micron scale particles around the machining area [1]. Laser machining is now used in a wide range of applications: removing layers of grease and dust from valuable works of art [6, 7], scribing resist coated silicone wafers to provide electrical insulation between cells [1] right through to the main interest of this thesis: the production of micron scale, complex 2.5D features [1 - 3, 6,].

Debris is of particular interest to this new machining discipline due to the nature of the process itself. Like most commercial manufacturing techniques, laser processing is a subtractive process; however, laser machining differs from traditional machining processes by the scale of the debris it produces along with its requirement for a relatively inert, transparent medium to work in [8]. Laser machining is most efficient when all of the energy generated at the source is delivered to the point of ablation. This is not possible in practice due to losses in optics and any medium the radiation passes through on its way to the target [9]. When the radiation hits the target it removes a layer of material from the surface of an object by thermal, chemical and mechanical processes, known collectively as ablation. The thickness of this layer can be controlled by the energy density of the shot and the length of the pulse [9]. In practice this is not a perfect process, some of the energy is wasted as sound and heat; consequently, this heat gives rise to the need for a relatively inert machining

medium [10]. In contrast, the coolant used for traditional machining methods is oil based; opaque in visible light, full of impurities and flammable. The debris it removes can be easily seen by the human eye. The debris produced during typical micromachining is of molecular scale [11].

The machining method

The basic premise of all experiments conducted in this body of work is the ablation of a sample in a confined environment; this is to contain escaping debris and fume in a localized area and ensure controllable conditions for the experiment to be conducted in. The method used to do this will be outlined in this Section; any elaboration on the techniques covered here will be discussed in detail in the description of the specific experiment later in this thesis. Initially an open thin film of flowing liquid will be applied to the surface of the material to be laser machined. This is a technique novel to that attempted and patented by Scaggs [12]. This flowing film technique is intended to overcome the likely optical disruption to the laser beam afforded by a fine mist of liquid obstructing its path. Further more, employment of a flow, to removed gathered debris is believed to be more effective than use of a fine spray, as attempted by Scaggs, as a fine spray will have a tendency to gather floating debris material, before settling onto the substrate surface to allow capillary adhesion to take hold. A flowing film is intended to flow from the material surface whilst still suspending the debris from contact with the surface.

Issues arising from debris in laser micromachining

The effect of micron-scale particulate debris in industry is considerable; affecting a wide range of industries [13].The display industry offers a useful example: machining generated debris can be produced ejected and deposited on the surface of the micro-lens array used for even diffusion of coloured light towards the viewer during or after the machining process. This can impact optical quality *via* disruption of typical machining interactions or by residual attenuation and refraction of light after machining has ended during use [9]. Screens with sufficient debris motivated machining error would be classed as a quality failure and hence the manufacturing yield rate for manufactured items can be badly affected by debris issues. The existence of debris after the machining process has ended requires all screens deemed to exhibit sufficient geometric quality require post process cleaning to prevent debris attenuation of light during use [2].

Another technological area where reliance on reliability, and therefore quality, is paramount are the patterning processes for the semiconductor industry. Semiconductors are digital items, hence they have a quality threshold, If this is exceeded the item will malfunction, since there is a statistical likelihood that one of its many millions of transistors will not be correctly electrically isolated [14], and must be discarded as faulty. Again the displays industry offers a good example of this. Debris left on the surface of an electrode array etched into photoresist coated glass of polymer after machining can cause shorting, or debris formed during machining can impact further machining to have similar detrimental effect. This can result in dead pixels, stuck pixels or worse still, catastrophic malfunction of the entire product [1]. Electrical isolation is simple to achieve using light etching through techniques such as immersion lithography and this is currently the manufacturing method of choice

for most semiconductor microprocessors [14]; however, immersion lithography is rapidly reaching its technical boundaries. A competing method is to etch the resist with a shaped excimer beam, but this technique is blighted with debris issues. Debris can compromise the electrical isolation of the circuit paths, hence rendering the semiconductor faulty [15].

Debris can also effect the further machining of products directly by settling back onto a surface to be machined, or in the case of laser machining by floating above the wafer and partially absorbing the beam before it arrives at the desired surface [8]. Indirectly, debris can build up in the supply tubes or become a friction inducing aggregate in lubricants and bearings; thus lowering tool linearity and in turn accuracy. There are many applications other than the micro manufacturing industries that research in this area could be of benefit [16, 17].

Not only can debris on a machined surface cause issues to the machining of the component itself, but also to its installation into a system: debris may cause a poor connection, or the whole item to be seated incorrectly [15]. Many micron scale devices are manufactured and assembled in clean environments where large amounts are spent maintaining a low particulate count in the working atmosphere through filtering, pressurisation, complex task routines and expensive clothing for workers [18]. All of this money is wasted when the machining process itself produces large amounts of particulate debris that can catastrophically contaminate other devices during machining or assembly. Consequently research towards containment and prevention of such floating debris is required. One of the factors that make debris such an issue to manufacturing is its relatively unpredictable nature. The forces involved with particles of a sub micron-scale are small, often measured in dynes, yet when compared to the effect of gravity or fluid drag forces on a particle of such small mass they are the predominate force [19].

Particles that are airborne pose many issues, both to the manufacturing process, facility running costs and to the worker's health [20, 21]. Much effort and cost is expended to maintain a clean environment for manufacturing micron scale products. Manufacturing facilities are specially built; with air tight seals for doors and all points of contact with the non-filtered surrounding atmosphere. High powered air conditioning systems supply accurately temperature moderated air through high efficiency particulate air (HEPA) filters. Workers must wear varying levels of protective clothing, not for their own safety; but to prevent their own bodily detritus such as moisture from breath, bacteria carried upon the person, flakes of skin and shed hairs from contaminating the expensively cleaned environment and the products they work upon [18]. All of this effort requires great capital cost, both to build the facility, buy in the HEPA filters and the clothing for the staff and to train the staff to work correctly, safely and sympathetically for the environment. Once a facility is ready for use; running costs are equally high. Large amounts of energy are expended by the large air conditioning systems, HEPA filters must be maintained and have a finite life time. Staff tend to demand an increased salary due to the training that has already been invested in them and the sometimes difficult working conditions they operate in: inhibited by the clothing forced upon them. It seems silly then that the machining process taking place in such a facility is a source of copious amounts of exactly the debris that was initially prevented from entering. For laser micromachining this is currently the case. Not only does the debris produced by the laser micromachining process cause limitations to laser micromachining, but it can soil otherwise acceptable assemblies or affect

other machining processes. Furthermore, there are significant health issues associated with particulate debris [22]. Fine particulate dust can be inhaled by workers or be absorbed into bodily fluids through the eyes and tear ducts, raising medical concerns: machining processes of this type have not been in existence long enough to have generated noted medical cases but workers from other powder based industries such as cement or asbestos are proof that fine debris can lead to cirrhosis of the lungs or lung cancer respectively, hence this is another critical reason for controlling debris in such applications.

Often components that require high levels of cleanliness for operation are cleaned after manufacture, creating yet another mandatory process that adds complexity, risk and eventually cost to every item produced. Wafer cleaning is recognized as the single most repeated process in the manufacturing process of semiconductors [23]. Clearly it would be more beneficial for both the quality of the product, for manufacturing cost and for user health to clean manufactured items as they are made, removing the debris before it has a chance to cause any of the potential problems described above.

This can be termed an 'in-line' methodology and is the specified target of this thesis so as to gain understanding of the causes of debris adhesion and therefore aide in the prediction of debris associated issues, allowing manufacturers to decide on the feasibility of a product from a yield perspective before a test run is conducted. Along with this product planning aide, methods of controlling debris in real time during the manufacturing process should result from this thesis.

This thesis will result in the recommendation of a tool to be attached to the machine head, along with a recipe for successful debris reduction for any specific machining regime, fluence level or material. The difficulty in achieving this result is in the detail: how to control rapidly generated small particle debris in a high energy environment without damage to the substrate or loss of machining quality or clarity. The literature review and experimental components of this thesis will be focused on answering this question.

Key Interactions Considered in this Work

Laser ablation

In gaseous or vacuum media, the expansion of the laser ablation shockwave has been studied in depth by use of fast photographic imaging [11, 24 - 27], with respect to laser fluence, wavelength, pulse duration and temporal shape. This work has identified the complex relationship that exists between many contributing mechanisms such as phase explosion and surface evaporation [28, 29], photothermal effects [30, 31] or photomechanical and acoustic interactions [32] act individually or in a combination thereof, as discussed in the review of Georgiou and Koubenakis [33]; moreover, Prasad *et al* have conducted extensive effort into modelling such interactions [34].

Adhesion science

Much work has been conducted to glean understanding of the mechanism of adhesion between particles and surfaces. In a dry system, there are three primary adhesion forces: van der Waals [35,

36]; electrostatic (of which there are two forms – long range (image forces) [37], and contact (double-layer) [38]); and capillary forces (where the surface tension of liquid meniscus between particles holds a particle to the surface [39]). Van der Waals and long range electrostatic forces act to attract a floating particle to a larger surface. Once lodged to the surface the action of van der Waals, electrostatic double layer and capillary forces combine to adhere the particle to the surface [16]. The action of capillary adhesion can increase the adhesion force by a factor of 5-7 and even prolonged baking in an attempt to evaporate the liquid forming the meniscus only acts to increase the adhesion force [40].

The size of a particle is of great significance to the effect of adhesion forces upon that particle in comparison to more commonly recognized forces such as gravity or fluid drag forces. Adhesion forces grow stronger with increasing size [16]; however the effect of gravity and drag forces increase much more rapidly; therefore large particles are easier to remove than small ones. For a particle at the micron scale, the adhesion forces can provide a combined effect many thousands of times greater than that of gravity [7, 19], meaning that smaller particles appear to adhere more tenaciously than large ones [23].

Modification of the medium surrounding an adhesion interaction has been shown to reduce the strength of all adhesion forces. Immersion in water has been shown to reduce the van der Waals attraction by as much as 50% [38] and will massively reduce or negate the action of capillary adhesion during emersion due to closer correlation of liquid viscosities between the adhesion meniscus and the immersing fluid [16]. The use of a conducting medium negates or even reverses the action of electrostatic forces by action of the Yukawa repulsion [41].

Impact of medium on laser ablation

Previously, the typical control solution for ablation generated debris is post process removal by the employment one of a number of cleaning techniques: ultrasonic bathing [42]; surfactant jetting [43]; contact scrubbing [44]; laser cleaning passes [16]; and chemical interactions [19] are all common. They are all limited in two ways: possible damage of a wafer that has already had significant manufacturing effort expended upon it [16] and post process cleaning can only remove debris left behind after machining has finished - it cannot prevent the effects of debris during machining. Because of this, an in-line technique is preferential. A number of in-line techniques have been detailed in literature that covers two main groups: positive pressure gas jetting (using a number of flow geometries, ranging from cross-flow to vortex [45, 46]) and vacuum gas removal [47].

A technique for delivering a long wavelength laser wavelength by use of a fine jet of water proves that use of such media do not pose unacceptable attenuation of the beam [48]. Others [49] have used a novel technique known as laser induced backside wet etching (LIBWE), to machine laser wavelength transparent materials by passing the beam through and focussing the beam just beyond the back surface of the material that is immersed in a liquid medium. The production of nano and micro particles has also caused immersion of the sample during lasing to be experimented with, proving to entirely capture all ablation generated debris [50 - 52], so use of a liquid medium to control ablation generated debris during machining appears achievable. Sattari *et al* [53] used ablation of ceramics

immersed in 4 to 6 mm of distilled water running at a constant flow rate of 116 ml/min to produce controlled collection of nanoparticles at the surface of the immersing liquid. Particle productivity has been shown to be proportional to liquid flow rate [53]. The dependence of particle size is less clear, Sattari *et al* state that laser fluence was inversely proportional to the size of nanoparticles produced (supporting the dominance of a photomechanical etching mechanism of a confined ablation plume as described by Berthe *et al* [54]). Katto *et al* [55] found that particle size is governed by the wavelength of the laser (a result common with traditional laser machining in gaseous media) and is proportional with the fluence of the beam.

When using liquid as a media for laser ablation, Zhu *et al* [56] demonstrated that a threshold film thickness for immersing liquids exists, lying at 1.1 mm. Using a closed flowing thick film filtered water immersion depth below this value significantly reduced the ablation rate compared to that of ablation in ambient air. Use of an immersing liquid depth greater than the 1.1 mm value and the opposite was true.

Research Objectives

In-line debris control

The primary objective of this thesis is to achieve understanding and a resultant level of user control of debris generated by ablation during KrF excimer laser machining of a surface. This control will allow features to be machined with reduced deposited debris populations both inside and around their geometry. Furthermore, since laser micromachining is often used for the production of large, regular arrays of features across a wide area, this thesis will aim to produce a technique that allows debris to be controlled without detrimental effect on features are to be or have already been machined.

Debris control technique impact on feature quality

It is perceived that the technique used to control debris that is ejected from a laser machined feature will also modify the laser ablation mechanisms involved. As a direct result, the uniformity and repeatability of etching may be modified; thus, offering a simple method for interpretation of ablation mechanism modification. The factor of primary importance to any manufacturing technique is the quality of the machined item; thus the definition and repeatability of features machined whilst applying a debris control technique must be evaluated.

Modification of laser ablation characteristic by debris control technique

If the debris control technique does modify the ablation mechanism in terms of proportional contribution levels of the constituent etching mechanisms outlined above, then it is expected that such a change will be identifiable and readily characterized by interpretation of the primary etching characteristics: ablation threshold fluence and ablation rate.

The ablation threshold describes the impact of a quantifiable volume of photon energy has on a specific materials atomic structure when coupling between the two occurs [9]. The depth of a machined feature is compared to laser fluence used to produce it and, therefore, the number of

photons supplied to the material for coupling. Plotting the depths of many features machined with respect to the natural logarithms (to allow linear comparison of equivalent spatial units) of vastly different laser fluence magnitudes used to machined them over large number of pulses for result averaging, given repeatable laser, material and machining environment variables [57] results in a linear relationship. The interpolated intersection depth of this relationship; that is, the fluence at which zero depth is machined, is classified as the threshold fluence. It must be noted that this value is only an estimation based upon empirical definition and the simplistic application of the Beer-Lambert law.

Ablation rate is useful to the observer as it is an easily measured technique means for quantifying the efficiency of coupling between a photon stream and a material once above the threshold fluence – an event well known to be a probabilistic [9]. The gradient of a linear relationship that exists between the depth of a laser machined feature and the number of pulses used to produce it describes this barometer of laser beam-molecular matrix coupling.

Both of these easily adopted and well understood methods of quantifying laser etching performance on a material surface will be employed for further understanding of the implications of using the technology developed in this thesis.

Modification of laser machined feature surface topography

Further to this extensive analysis of possible laser ablation mechanism modification, the surface topography of the feature machined using the laser ablation-generated debris control techniques will be compared to features machined using more traditional laser ablation machining in ambient air. This analysis will take into account the nuances of surface topography measurement.

This idea can be illustrated with use of a simple analogy: if a pilot was flying over a desert covering mountainous terrain at high altitude, his eyesight would resolve the large amplitude, long wavelength undulations of the mountains and the smaller amplitude and wavelength undulations of the desert sand dunes and waviness and roughness respectively; a man standing on the desert surface would see the dunes as large wavelength and amplitude undulations but recognise the smaller, short term wind generated ripples in the sand as relative surface roughness; an insect on the desert surface would recognise these short term wind generated ripples as large undulation waviness and classify the texture of the sand grains as surface roughness. The route mean square (RMS) amplitude value in μm is quoted in this thesis for waviness (W_q) and roughness (R_q) as a measure of the deviation from the planar average.

It has been shown [9] each constituent etching mechanism involved in the process termed ablation in combination, has a characteristic resultant surface topography. This fact will allow further identification of modifications to the proportional contributions of these etching mechanisms when applying a debris control technique.

Importance of medium to debris control and laser machining

The analysis outlined above will offer detailed insight into the current capability for laser generated debris control, given current understanding of the interactions involved. It will clearly demonstrate the impact, if any of changing the medium surrounding a laser ablation event on debris deposition, feature

geometry, surface topography and the primary laser ablation characteristics. However, it would be of interest to use a more subtle modification of medium to observe the implications to the same measurable parameters. This exercise will also be useful in a role of verification of the trends identified in the work outlined above.

Thesis Organization

This thesis addresses a number of technological and scientific aspects associated with the task and related interaction modifications of laser ablation generated debris. As such, this thesis is split into four distinct parts.

Part I: A Review of the Literature Relevant to this Thesis. Here understanding gathered by previous research that is important to the problem considered by this thesis is presented.

Part II: Open Thin Film Regime Flowing Liquid Immersed KrF Excimer Laser Ablation of Bisphenol A Polycarbonate. A technique is developed given the understanding demonstrated in Part I. Assessment of this solution based upon this solution, using the technique outline above is presented.

Part III: Closed Thick Film Regime Flowing Liquid Immersed KrF Excimer Laser Ablation of Bisphenol A Polycarbonate. Further evolution of the debris control technique that comes as a result of Part II is presented with evaluation of the performance of the evolved design.

Part IV: Verification of Closed Thick Film Flowing Liquid Immersion Ablation of Bisphenol A Polycarbonate by Modification of Liquid Chemistry. This part details the observations resultant from subtle modification to the medium surrounding the laser ablation event.

Part I

A Review of the Literature Relevant to this Thesis.

CHAPTER 1

BEAM INTERACTIONS

1.1 Beam Energy Loss Through a Medium

1.1.1 Contributors to beam energy loss

On route to the target any beam must pass through a medium of some sort unless the system is contained within a vacuum, a technique that will be covered in greater detail later in this review. When a beam passes through an interface between two differing media, e.g. from a gaseous medium to a silica lens, it will experience reflectance, R', defined as the ratio of reflected power to incident power, resulting in a loss of energy at the image [58]. Every medium has a transmittance, T', for each wavelength of electromagnetic radiation, defined as the ratio of the transmitted power to the incident power [59]. The transmittance of a medium is the amount of energy that enters the new medium rather than being reflected. The third possible means of energy loss as a beam passes a medium boundary is absorptance, A'' - a phenomena that occurs only in metals, it is coupled to a phase shift in the wave [60]. Thus there are two possible energy conservation equations to choose from, one for metallic substances and one for non metals. The absorptance will not be examined further in this review as its value will always be small, although non-zero, and it is not useful to the media required for use in this thesis.

As a governing rule to the following Section, it must always be remembered that there is the conservation of energy to be maintained; all energy supplied must be conserved, thus for metallic media the energy supplied can be split into the fractions

$$T'+R'+A''=1 \tag{1}$$

whereas for non-metals, including ceramics, polymers and organic materials the conservation model is correct:

$$T'+R'=1 \tag{2}$$

These are the only destinations for beam energy as it passes a medium boundary [58].

Once travelling through a medium it is the absorption, A', of that medium for a given wavelength, commonly termed attenuation, that is critical to the final output of the material. Absorption is defined as the amount of light extinguished from a beam traversing a medium [61]. This Section will explore the nature of each of these effects in a generalized form. Figure 1-1 schematically describes the relationship between these three factors and the way that they share the incident beam, I_i.

The pointing vector, $\boldsymbol{S}$, is a method of not only giving the magnitude of energy flux per unit time, but also its direction. The power per unit area across a surface in a vacuum with a normal parallel to the pointing vector can be found [58]. As the electric and magnetic fields of an

electromagnetic wave oscillate, the pointing vector also oscillates. The mean average of the pointing magnitude over one period of a wave is termed the radiant flux density or irradiance.

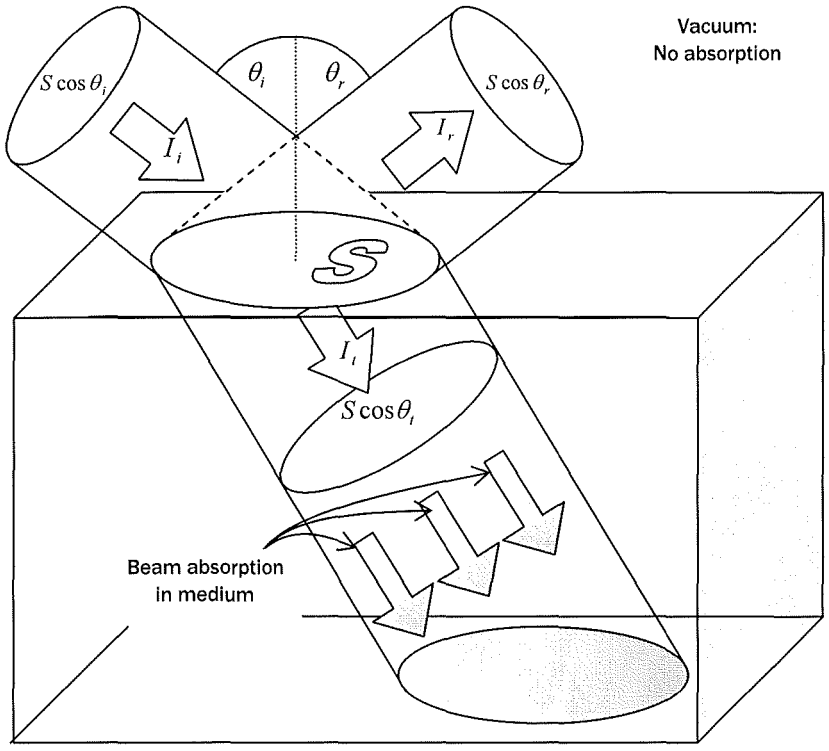

Figure 1-1: Schematic diagram describing the three fundamental routes an incident beam of light, I_i, can take in a medium.

1.1.2 Reflectance

Taking the situation described in Figure 1-1 as an example, the laser power supplied to a surface by a laser beam can be calculated by defining the mean irradiance, I, arriving at the material surface area, denoted as S, which can be modified by modifying the angle of incidence, θ, [60]. The reflectance is simply a measure of the proportion of the incident beam reflected from a surface. Since the angle of reflection will always equal the angle of incidence, the importance of area and angle of incidence becomes negligible, thus

$$R' = \frac{I_r}{I_i} \tag{3}$$

1.1.3 Transmittance

Using the same method as that for finding beam power, the power transmission, P_t, can be found by finding the irradiance of the transmitted beam, I_t, over the beam illuminated area. In the same fashion as reflectance, the transmittance is a proportional measurement of the energy transmitted into the new medium compared to the original energy that arrived at the medium boundary; hence, using the notation defined in Figure 1-1 as the area value for both properties is always identical [60]

$$T' = \frac{I_t \cos\theta_t}{I_i \cos\theta_i} \tag{4}$$

1.1.4 *Attenuation*

The attenuation of light in a medium is due to the scattering and absorption of electromagnetic waves by the atomic structure of the medium as the wave passes through [8]. Attenuation is depth dependant, and can be found using the extinction coefficient, k, which represents the resistance faced by an electromagnetic wave by the medium. The parameter used to describe the interaction of electromagnetic waves with matter is the complex index of refraction, $\tilde{n}$, which has a real part (the typically quoted refractive index, n) and imaginary part [60]. Care must be taken not to confuse the complex and standard versions of this parameter.

k simulates a drop in the size of the electric field of a wave as it travels further into a medium. It must be noted that the irradiance of the wave is merely the square of the magnitude of the electric field. For any electromagnetic wave travelling through an absorbing medium the decrease in I over a distance traversed is proportional to the instantaneous value of I [60]:

$$\frac{dI(z')}{dz'} = -\alpha' I(z') \tag{5}$$

This relationship is commonly known as the Beer-Lambert law [60], where α' is the absorption coefficient:

$$\alpha' = \frac{2\omega' k}{c} \tag{6}$$

where k and α' are related by the expression

$$k = \frac{\lambda}{4\pi}\alpha' \tag{7}$$

The only reliable method of gaining accurate values for the extinction coefficient is through experimental analysis. The absorption coefficient of KrF excimer laser beam, which will be used for the experimental section of this thesis, has been documented by previous authors in air [62], pure water [63, 64] and de-ionized (DI) water [65] as 0.0003, 0.0005 and 0.00075 respectively.

1.1.5 *Light absorption coefficient of air and pure water*

The wavelength of electromagnetic radiation propagating through a medium is critical to the resistance it faces from the molecules of the medium. The photon energy absorption of short wavelength laser radiation in ambient air is very high (1.19/m for 120 nm light); the photon energy absorption by air decreases to negligible levels at 190 nm and remains so for larger wavelengths [66]. This trend is plotted in Figure 1-2, and allows easy comparison to the low photon energy absorption offered to laser radiation across a broad spectrum of wavelengths in Figure 1-3 that has been collated for this thesis from a number of separate references [67-71]. In contrast to the absorption of photons by air, pure water has low absorption across a broad spectrum of light, bracketed by increased

absorption at the shortest and longest ends of the sampled spectrum that light in the deep UV and near IR wavelengths. This difference in photon absorption demonstrates the criticality of media in laser machining processes.

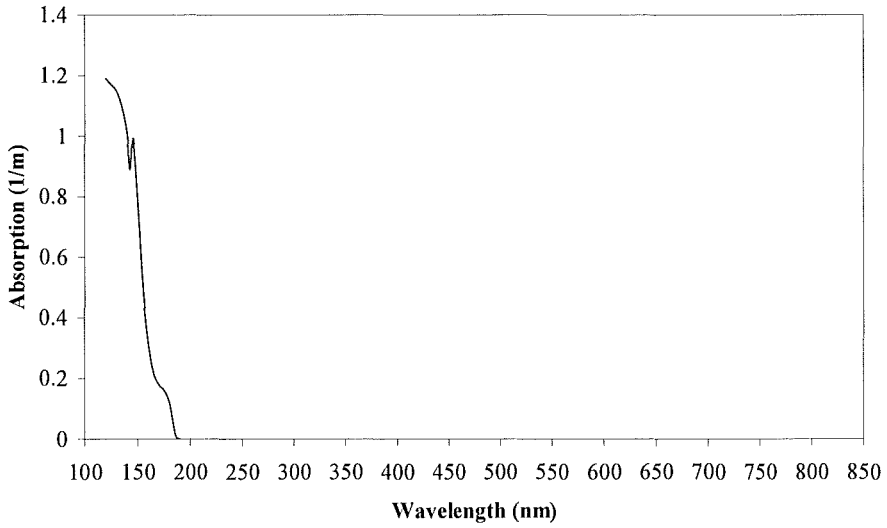

Figure 1-2: Graph plotting the optical absorption coefficient of cold air with respect to beam wavelength.

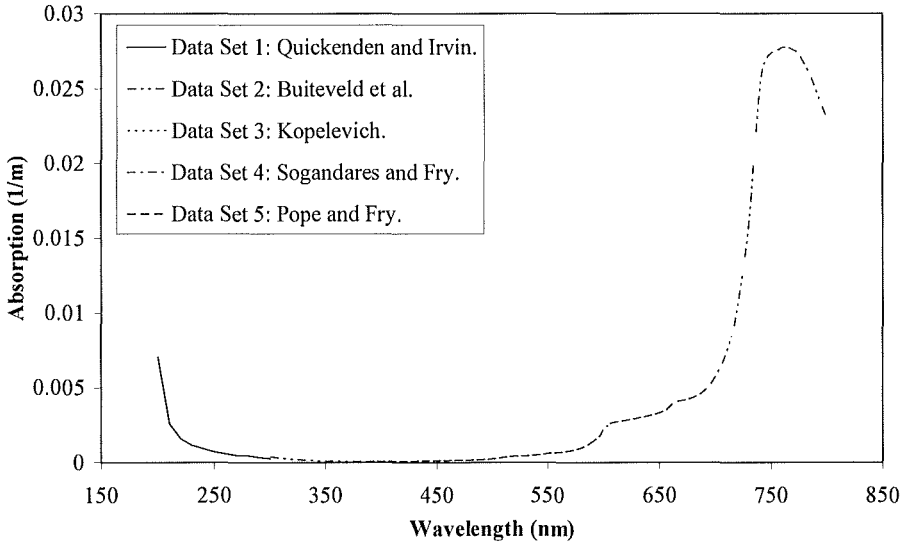

Figure 1-3: Graph plotting the optical absorption coefficient of pure water with respect to beam wavelength using data sets gained from various sources: Quickenden and Irvin [67] (1); Buiteveld *et al* [68] (2); Kopelevich [69] (3); Sogandares and Fry [70] (4); and, Pope and Fry [71] (5).

1.2 Ablation Kinetics

1.2.1 Ablation: A broad term

Ablation is the principle means of material removal when using pulsed lasers. Ablation is an obscure term; firstly it is sensible to note its definition in the Oxford dictionary: "1. n. the loss of solid material by melting, evaporation, or erosion. 2. n. the surgical removal of body tissue." [72]. "*Ablatio*" is Latin for "to remove" [73]. It is clear from these definitions that this is a blanket term to describe many

instances. Laser ablation was originally envisioned as a possible alternative or complimentary manufacturing technique to conventional photolithography, however traditional engineering polymers, such as polymethylmethacrylate (PMMA) polyimide (PI) or polycarbonate (PC) have severe limitations, including low sensitivity, carbonization during irradiation and ablation generated debris issues [74, 75]. For the progression of this research the precise nature of ablation for a specific material and process is necessary. This understanding will be gained both from literature and interpretation of the characteristic symptoms of laser ablation, the ablation threshold fluence, the ablation rate and the topography of the features machined using laser ablation during the experimental work conducted for this thesis. In this thesis the events that combine to produce ablation will be described as 'the mechanism of ablation', as this is descriptive of the phenomenon's complex nature.

The mechanism of ablation is highly dependent upon the material with which photons are interacting. The materials can be organized qualitatively into a small number of concise groups as described in Table 1-1:

Table 1-1: Table categorizing the nature of interaction and resultant ablation mechanism for material categories at UV wavelengths

Group	Atomic structure	Typical interaction between UV light and material	Typical action of UV light on structure	Mode of removal
Thermosetting polymers	Polycrystalline	High photon absorption	Photochemical	Photothermal & photochemical
Thermoplastic polymers	Fibrous	High photon absorption	Photochemical	Photothermal & photochemical
Crystalline Ceramic	Crystalline	High photon absorption	Photochemical	Solid state bond breaking
Non-crystalline Ceramic	Non-Newtonian Liquid			
Metals	Crystalline	High Reflectance	Photothermal	Melt pool & evaporation
Other Organic	Fibrous	High photon absorption	Photothermal Photochemical	Explosive evaporation

Interestingly, little comment has been found in the literature concerning the coupling interaction between a short wavelength laser beam and non-crystalline ceramics. This is a reflection of the complex chemistry and atomic structure of such materials.

1.2.2 *Ablation of metals: The proposal of explosive vaporization*

Historically it had been accepted that surface superheating was the main cause of particulate formation from the ablation of metals [76]: the subsurface region has a higher temperature during irradiation than that of the surface which is able to diffuse heat to the surrounding temperature. This temperature distribution causes an uneven pressure distribution, with higher pressures in the subsurface region than at the surface; thus an explosion takes place. However, Kelly and Miotello [30] realized that the maximum temperature difference between the subsurface region and the surface was negligible when appropriate boundary conditions were applied. Instead the explosive vaporization mechanism was postulated; when the laser fluence is sufficiently high and the pulse length short, the temperature of the specimen could be raised to well above its boiling temperature. At $0.9T_c$, where T_c is the thermodynamic critical temperature, homogenous

bubble nucleation occurs. The surface now rapidly changes from superheated liquid to a mixture of vapour and liquid droplets.

1.2.3 The ablation of polymers: Importance of polymer type

One aspect of laser machining that is known to be fact, and critical to the research presented in this thesis, is that ultraviolet (UV) radiation brings less thermal damage to an irradiated material than longer wavelength radiation [77]. This is due to the short penetration depths and short pulse lengths achievable with UV sources, resulting in low thermal propagation [78, 79]. During ablation new phases are formed, these are ejected from the ablation spot to the surrounding areas [80]; a number of plausible mechanisms have been proposed. Current discussions revolve around the true nature of the photon-atomic structure interaction between light sources and polymers [81], but no agreement has been found over whether this is a photochemical or photothermal process. Competing theories take both sides, where studies based on analytical modelling [82] favour a photothermal mechanism; whereas organic polymer photochemistry [83] has proven that the irradiation of organic molecules or polymers with UV photons leads to photochemical reactions, therefore it is likely that when irradiated with much higher fluences, sufficient to instigate ablation, photochemical reactions still take place. When ablating a polymer temperature elevation, chemical decomposition, vaporization, fragmentation, ejection and the generation of a shockwave can all be observed using a range of experimental techniques. The difficulty lies in interpreting how these electronic excitations of molecules in materials evolves to morphological changes [84].

It is important to note that polymers can be split into two critical groups in terms of laser machining nature: those that can depolymerize upon irradiation and those that decompose into fragments [81]. The classification of a polymer into one of these two groups amounts from its synthesis: polymers that are formed by radical polymerization from monomers which contain double bonds are classical candidates for depolymerization upon irradiation, whereas polymers that are formed by reactions such as polycondensation will not decompose into the monomers upon irradiation. It is also worth noting that any photochemical decomposition which alters the chemical structure of a polymer will result in a modification of the polymer's refractive index [85]. Typically polymers that can depolymerize during irradiation fall into a class of polymer that have become known as 'laser ablation polymers'. To be classified as one of this select group the material in question must meet three criteria [75]:

1) High absorptivity at the irradiation wavelength in use;
2) Exothermic decomposition at well defined positions on the polymeric backbone; and
3) Mostly gaseous ablation product (no solid or liquid debris).

The last of these criteria is critical, as a material that mostly produces gaseous ablation products will carry away any solid of liquid products that are produced by entrapment.

1.2.4 Methods of examining ablation mechanisms

There are three commonly practised methods for attempting to identify and understand the ablation mechanisms at work between a laser beam and a material [81]: the modifications to a polymer

structure can examined following ablation; time resolved measurements can be made during ablation; or the laser pulse lengths and wavelengths can be modified and the differing effect they have upon a specific material can be examined following ablation.

Modifying the pulse lengths and wavelengths is typically implemented whilst using the other two experimental techniques; however, it is a powerful tool in helping the practitioner to gain an understanding of the mechanisms at work.

A relevant example of investigations made to the polymer structure of a material have been conducted by Lippert *et al* [86]. Excimer lamps were alternately employed to study the effect of low fluence irradiation at 222 and 308 nm wavelengths where linear photochemistry could be expected; that is, without ablation. Excimer lamps emit incoherent, quasi-continuous radiation at the same wavelength as an excimer laser; however, these emit far lower photon fluxes and so multi-photon processes can be neglected. This experiment showed that the triazene-chromophore decomposes at a fluence well below the ablation threshold and is clearly the most sensitive chromophore in the triazene-polymer that decomposes directly during irradiation at 308 nm. As a consequence the possibility of a photochemical interaction during ablation at these wavelengths is deemed to be likely.

A wide choice of time resolved methods to examine the ablation mechanism are available: picosecond anti-Stokes coherent Raman scattering spectroscopy [87]; time resolved transmission [88]; nanosecond shadowgraphy [81]; nanosecond surface interferometry [89]; nanosecond photoacoustic analysis [11] and time-of-flight mass spectrometry (ToF-MS) are all common. Time resolved measurements are useful in examining the transient processes in laser ablation. The shadowgraphy method, described in detail by Hauer *et al* [90], has been used by Lippert [81] to image the shockwave and ablation products at different times during and after the pulse. Lippert's results confirm the absence of solid products in the ablation plume for irradiation of a triazene-polymer, at 308 nm; this was a result expected by Lippert due to the lack of re-deposited material found after ablation. But, further investigation found that the use of different wavelength-material combinations can generate solid ablation products. The shadowgraphy technique can also yield an insight towards the nature of the shockwave; being found to be wavelength dependent [81]. The use of surface interferometry, has been used alongside shadowgraphy to examine changes in surface morphology on ns timescales both during and after the laser pulse [89]. This imaging technique demonstrated that when machining a triazene polymer at 193, 308 and 351 nm [89], etching begins and ends with the laser pulse; however, use of the same wavelengths with other polymers, such as PI [90], PMMA and PS [84] results in pronounced swelling, followed by material removal that continues for several μs after the laser pulse has ended. Masubuchi *et al* [84] note that the expansion starts in the initial half of the excimer laser peak and reaches a maximum value at around 50 ns, before beginning to contract back to a flat surface. These workers explain that the contraction process should be controlled by the thermal dissipation of the material; however, the time taken for contraction is of the microsecond order and this is outside the scale of thermal dissipation predictions, and thus the contraction mechanism is unexplained. Photothermal ablation is often associated with pronounced surface swelling and delayed material ejection and photochemical ablation is considered to yield less swelling and instantaneous etching [81].

The work conducted by Lippert [81] reviewed here suggests that both photochemistry and photothermal reactions take place during ablation. The difficulty is in specifying the proportion of each mechanism is active in a particular situation. The material has been shown in Lippert's work to be critical in this balance: photochemistry being more dominant in photoactive polymers than for other more typical polymers, such as Teflon®.

1.2.5 Ablation product trajectory

Equally important as the phase and chemical composition of the ablation product is the speed and flight path of the material. Knowledge of this issue allows prediction of where to concentrate efforts towards material removal for a given situation.

Weisbuch *et al* examine the ablation products of a KrF laser with microcrystalline PET [80]. A subsequent review of the samples machined during these experiments demonstrate an apparent melt phase ejection from the ablation zone, with spatter patterns extending radially from the shot area. The work of Weisbuch *et al* [80] is supported by Yung *et al* [77], who explore the interaction of a 355 nm wavelength pulsed beam with Vectra A950, a liquid crystal polymer (LCP) and the topographical and chemical modifications caused by this interaction. At low fluences, close to and just above the threshold value, no surface melting is evident suggesting that in this situation photochemical decomposition dominates the ablation process. However, melting becomes more apparent in the samples as fluence is increased. Melt is indicated by solidified radial spatter surrounding the ablation zone. This result suggests that photothermal reactions become more dominant in the ablation process with increasing fluence. Yoo *et al* [91] postulate a reason for the ejection of materials from the ablation zone: evaporation is thought to take place both on the irradiated surface and in the superheated melt produced during the initial period of the pulse. This event has become colloquially known as 'explosive evaporation'. This process is covered in detail by Dyer *et al* [11] who investigated the interaction of a KrF beam with a metallic ceramic film and also site the explosive evaporation mechanism as being responsible for the debris created in that scenario. Firstly strong superheating of the surface liquid layer occurs under the non-isotropic conditions of pulsed laser irradiation. Heat loss by boiling within the liquid layer is prevented as the local vapour pressure is too low to support bubble growth from atomic scale voids. Secondly, ablation commences at a maximum superheating temperature, where the tensile strength of the liquid falls to zero. Pressure fluctuation in the liquid then instigates explosive boiling.

The recoil pressure developed by the evaporation of the superheated liquid expels mass molten material from the ablation zone. The depth and shape of the crater are critical in the angle of ejection of the materials, as described in Figure 1-4, where the ejection angle (a) for the shallow crater is smaller than the ejection angle (b) for the deep crater. The depth of a crater is directly related to two variables; the ablation rate and the number of pulses over the same area. Bauerle [92] has formulated a relationship to predict the ablation depth of a single pulse. This model of the ablation rate was found to closely approximate the experimental results of tests conducted, except for low fluences, where the absorption coefficient fluctuates with laser fluence.

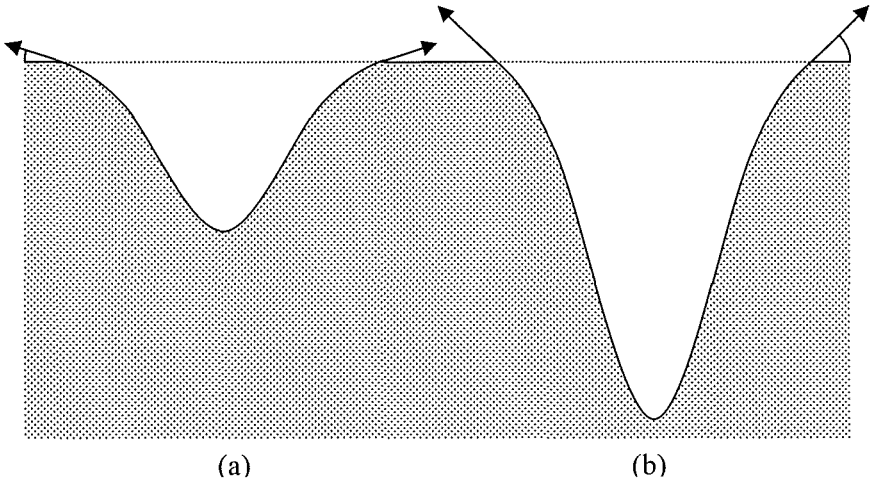

Figure 1-4: Graphical representation of the relationship between ejection angle and crater depth for a Gaussian laser beam profile [77].

Torrisi *et al* [93] examined the normalized yield of ablation products at a range of angles away from the normal to the target surface, which in this case is a copper plate. The results clearly show that over half of the ablation products are ejected in a 40° range around the normal to the material surface; furthermore, at angles greater than 30° from the normal to the copper plate, as shown in Figure 1-5 there is very little possibility of ablation products being ejected through that angle. This distribution would tend to support the theory of Yung *et al* [77] described in Figure 1-4. This is important as this knowledge allows for the assumption to be made that control of debris is only important at a 90° range around the normal to the surface being machined.

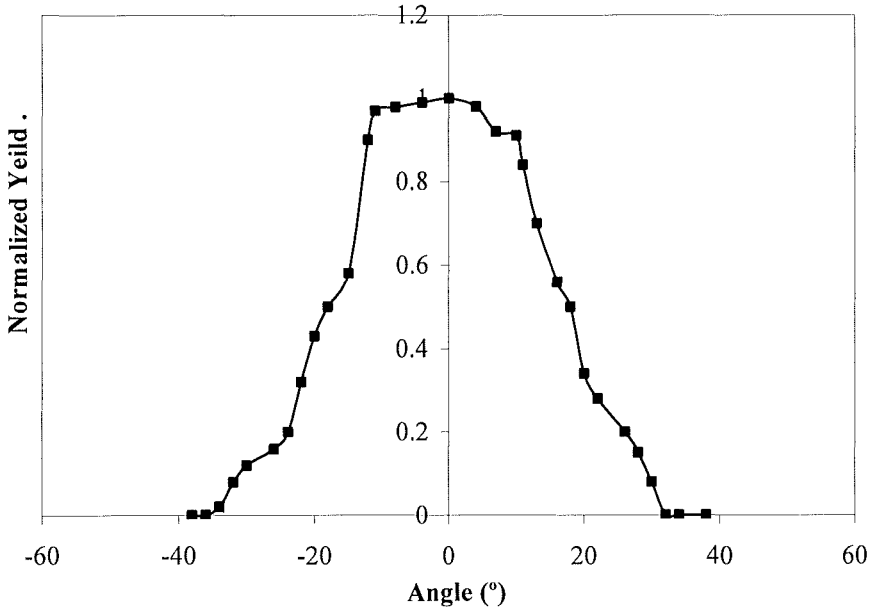

Figure 1-5: Plot depicting the yield/trajectory angle of particles flying away from the ablation spot [93].

1.2.6 *Size and form of ablation products*

As discussed in Section 1.2.3, during ablation large amounts of gaseous products are ejected, but these carry both liquid and some solid products *via* entrapment. Some research has used lasers specifically to produce particulate debris for use in other research fields. Ullmann *et al* [94] examine the relationship between laser parameters and the debris produced from various ceramics and metals in a number of carrier gasses, claiming that the purity of particles produced is governed by the purity of the carrier gas and target material itself. Gartner *et al* [95] generated Y_2O_2, SiO_2 and Cs_2O_3 nanoparticles with mean primary particle size between 4 - 40 nm dependant upon gas pressure and velocity over the ablation zone. Sasaki *et al* [96] achieved control of particle size and composition of calcium-iron oxide particles by varying the gas pressure from 0.133 to 133 Pa, particle size increasing with pressure from 2 to 26 nm; whilst the Ca/Fe reduced from 0.9 to 0.2 during the same pressure change. Ogawa *et al* [97] showed that an increase in flow rate produces smaller aggregates and smaller primary particles, but at an increased number concentration. Also increased pulse energy results in an increase in aggregate size; similar effects were achieved with increased pulse frequency.

Larger particles can form from coalescence of multiple smaller particles [94] or from the solidification of molten ablation products [77, 80]. The collision of primary particles at a high temperature early in the cooling process leads to coalescence. As the gas cools, coalescence ends and further particles that collide with the new body tend to adhere themselves to the main body and form aggregates; this aggregation process can then continue to build larger composite debris. The aggregation process could also perceivably occur for melt products that solidify before landing back on the substrate surface.

The work of Bereznai *et al* [98] supports the claims of Ullmann *et al;* B_4C was ablated with an ArF beam. Low fluences produced mostly particles of less than 20 nm diameter; increasing the fluence up to approximately 2 J/cm^2 the size of the particles produced did not change, however the amount produced did increase. Above this fluence the mean size of particles produced begins to increase, with the population of smaller particles produced becoming smaller.

1.3 Increasing Machining Efficiency and Quality

Traditional techniques of machining both mechanically and *via* the use of imaged laser optics are constantly striving to produce finer, smaller and more repeatable products for many applications, ranging from printer heads to hard drive platter patterning. New commercial applications will require improved ablation rates and control of undesirable surface effects [81]. In this Section two emerging techniques are briefly reviewed and their differences and advantages are highlighted over traditional pulsed laser ablation (PLA) in gasses.

1.3.1 *Pulsed laser ablation in gasses*

PLA in gaseous media is the most common technique used for thin film deposition, synthesis of nanoparticles, removal of micron scale particulate debris from solid surfaces and subtractive manufacturing of microstructures and nanoscale patterns on the surface of solid targets since its

emergence in the early 1960s [76]. PLA has been widely adopted because of the localized heat affected zone (HAZ) resultant of the short laser pulses in comparison to other techniques [74].

Yang [76] explains that the formation of ablation products during PLA in gasses is a result of condensation of the plasma plume generated by the ejection of ablated gaseous products from the solid target. In this scenario, there are three critical stages, generation, transformation and condensation.

It is worth remarking that the ablation kinetics for nanosecond pulses and other shorter pulse lengths significantly differ. For the ablation caused by a nanosecond pulse material ejection is likely to be dominated by thermal reactions [99]. Photons couple with both electronic and vibrational modes of the target material; this leads to electron-electron coupling and an immediate rise in temperature to the point of vaporization of the target. For ablation caused by ultra-short laser pulses (picosecond and femtosecond), heating, plasma plume formation and material ejection all occur after the pulse has ended. It is the photon absorption depth, not the thermal diffusion of the material that is critical for these short pulse lengths [76]. In this review the action of a short pulse (nanosecond) will be examined.

(a) Generation. The initial phase of the pulse will instigate ablation; the gaseous materials ejected from the target will form a plasma, as depicted in Figure 1-6(a). The plasma formed will be partially confined by the surrounding gaseous environment; however continued ablation and excitation of the plume will cause the plume to expand, as shown in Figure 1-6(b).

(b) Transformation. The ablated species originating from the target material are not suspended in the plasma plume. Because both the plasma and the surrounding environment are gaseous in nature, the two tend to mix. The high energy and temperature state of the plume allows chemical reactions to occur between molecules from the two substances to form new compounds. The latter part of the pulse adds energy to instigate these reactions; the mixing of the gas and plume continues after the pulse has ended as the next phase begins, as described in Figure 1-6(c).

(c) Condensation. The heat contained within the plume begins to diffuse into the surrounding environment at the end of the pulse. The intense thermal diffusion of the species in the plasma plume can result in collisions; leading to aggregations. Thus thermal diffusion is also critical in transformation, before eventually leading to condensation of the new mixed species into melt form and finally to solidification resulting in particulate matter as shown in Figure 1-6(d).

It must be noted that this entire process is completed in just a few nanoseconds, being complete in time for the beginning of the next pulse and the start of another of these cycles.

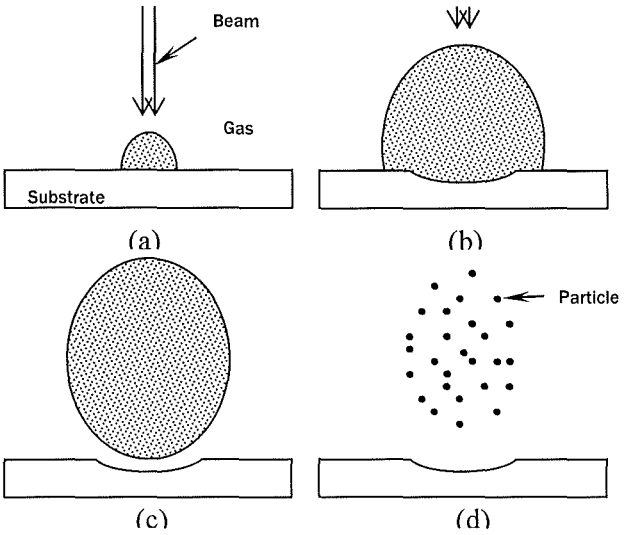

Figure 1-6: Schematic diagram of the four stages of PLA in gasses: (a) initial phase of the beam interaction; (b) further irradiation; (c) pulse ends; and (d) plume condenses to form multiple nanoscale particulates [76].

1.3.2 Vacuum ultraviolet (VUV) laser machining

This is a blanket term for a method of machining in either a vacuum, as the name would suggest, or in an inert atmosphere, commonly N_2, whilst using lasers of very short wavelength. In the commercial environment this is typically 157 nm. Due to the differing optical interface between the material to be machined and the environment surrounding it along with the short wavelength of the beam, a greater number of materials are opaque to VUV than to traditional machining in air. High photon energies, such as 7.9 eV at 157 nm, can rapidly break chemical bonds; thus minimizing the thermal loading on the target surface [81]. The use of such a short wavelengths also makes it possible to image smaller minimum feature sizes than would be achievable with traditional laser machining. The drawback of using VUV is the requirement to machine in either a vacuum or an inert gas, which adds significant complexity to tooling for these applications. Furthermore, few materials are highly transparent to the short wavelengths used in VUV processing. These materials are difficult to machine and are therefore costly, this proves to be a significant barrier to the widespread adoption of the VUV technique.

1.3.3 Liquid confined ablation

Another much less popular technique is to ablate a target material in a liquid medium. Yang has published a review of great depth in this field and its application for the synthesis of nanocrystals [76]. Yang reports that this lack of popularity has a simple reason; the ablation of solid materials is relatively easy to conduct in a conventional chamber filled with gas or evacuated to form a vacuum medium. Not only is it more of a practicable challenge; the ablation process is more complex to understand when confined by a liquid [73]. This means that studies into the application of laser ablation in liquids for material processing are not well established.

The fundamental aspects of laser ablation of liquids [33], the laser ablation mechanisms of biological tissue (mostly water) [100], underwater laser drilling and welding at the solid-water

interface using a Gaussian profile beam and laser-material interaction at a liquid-solid interface have been covered for the applications of laser cleaning, cutting and non geometry controlled etching [101].

This thesis is concerned with controlled geometry pattern etching techniques and the control of debris developed during these processes. A number of techniques have been developed that are of interest to this thesis [76]: laser induced surface patterning has been achieved by the wet etching process originated from laser irradiation of absorbable solution at the liquid-substrate interface; laser irradiation at the liquid-solid interface has been employed to prepare surface coatings on substrates; steam laser cleaning has been developed to remove small particles from surfaces using the mechanism of entrapment in vapours developed by laser irradiation in liquids; and a variety of nanocrystals and nanostructures have been synthesized by PLA of solid targets in various confining liquids.

1.3.4 Physical and thermodynamic characteristics of liquid immersed machining

The mechanism of ablation in liquids has some significant differences with ablation in gases or a vacuum. The most important of these is that the liquid confines the expansion and movement of the plasma plume due to its higher density and viscosity. This confinement can greatly influence the thermodynamic and kinetic properties of the plasma and therefore the evolution of the plume. This can give rise to distinctly different scenarios both during vaporization and condensation compared to ablation in gaseous or vacuum environments [76]. A plasma plume will be generated by the initial period of the incident laser pulse during irradiation of a solid target in a liquid medium in exactly the same manner as in a gaseous or vacuum environment; however, unlike the near uninhibited expansion of the plume that is granted by a vacuum or gaseous environment, the expansion of the plasma plume is restricted by the confining fluid.

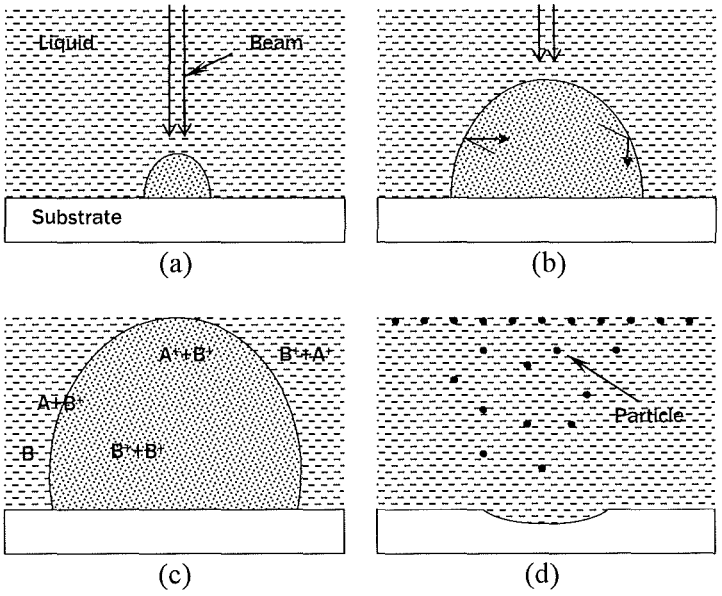

Figure 1-7: Schematic diagram of the four stages of ablation in a confining fluid: (a) pulse commencement; (b) end of pulse, confining liquid limits expansion; (c) four different reactions occuring in and around the plasma; and (d) condensation phase creates particulate debris which floats to top of confining liquid film.

Fabbro *et al* [102] found that a shockwave was induced by the laser induced plasma and was confined to the extents of the plume by the surrounding liquid. The laser induced plasma adiabatically expands when the plasma absorbs the latter part of the laser pulse and receives a further supply of vaporized mass from the target material at a supersonic velocity to create a shockwave as described in Figure 1-7b. This shockwave will generate increased pressure within the laser induced plasma plume. This increase in pressure generated by the shockwave has become known as the 'plasma induced pressure'. Thermodynamically, the increase in pressure will be coupled to an increase in temperature of the plasma, causing the laser induced plasma under the confinement of the surrounding liquid to have a higher temperature, pressure and density than that of a plasma generated in a gaseous or vacuum environment. The plasma induced pressure is dependant upon the wavelength and fluence of the beam involved [101], with the maximum pressure achievable decreasing with increasing pulse length [103].

Fabbro *et al* [54, 102, 103] have been involved in a wide range of research to understand the nature of the plasma induced in a solid-liquid system and produced an analytical model to predict the maximum pressure, p_{max}, generated by the laser induced plasma in water:

$$p_{\max} = 0.01\sqrt{\frac{\Omega}{\Omega+3}}\sqrt{Z}\sqrt{P_i} \tag{8}$$

where, Ω is the fraction of internal energy released as thermal energy (typically $\Omega \approx 0.25$), P_i is the incident power intensity and Z is the reduced shock impedance between the target and the confining liquid (water), defined as

$$\frac{2}{Z} = \frac{1}{Z_{water}} + \frac{1}{Z_{target}} \tag{9}$$

where, Z_{water} and Z_{target} are the shock impedances of the water and target respectively. The non-adiabatic nature of the plasma plume means that the relationship between temperature and pressure is not consistent with the ideal gas theory.

During the short life of the plasma plume four different types of reaction can occur, as described in Figure 1-7(c). These can occur purely in the plasma, purely in the surrounding liquid or at the liquid-plasma interface. In the laser induced plasma, two differing reactions can occur:

1. The laser induced plasma has high density, pressure and temperature allowing metastable phases to form from the molecules released from the target.
2. Reactant species could originate from the target and the confining liquid. The high temperature and pressure of the plasma promote evaporation of the confining liquid at the interface between the liquid and the plume; creating a new plasma of liquid molecules, this is termed the 'plasma induced plasma'. The two plasmas can then mix and the necessary mixed species are available to form new molecules from both liquid and target sources.
3. At the interface between the laser induced plasma and the liquid; in this case the plasma's thermodynamic properties give a good opportunity for target species to bond directly to liquid molecules, without needing them to evaporate to form a plasma.

4. Lastly, the high pressure in front of the laser induced plasma will cause ablation species from the target situated close to the plasma-liquid interface to collide with liquid molecules inside the main body of the confining liquid. This will promote the opportunity for the ablation species to react with the liquid molecules inside the liquid.

Three of these four possible scenarios involve interaction between two differing species, therefore the possibility of new, complex materials is presented by liquid confined laser ablation of solid targets.

The final stage of the evolution of the laser induced plasma plume in a confining liquid is the cooling and condensation process, depicted in Figure 1-7(d). A proportion of the plume will condense and settle as a film back onto the target material during plasma quenching by the confining liquid. This would be encouraged by the pressure applied on the plume by the confining liquid and a thin film will be deposited. The rest of the plume will condense and become entrapped by the confining liquid. This results in the synthesis of small particles that rise to the surface of the liquid film due to the action of surface tension.

The difference in ablation kinetics between liquid and gas immersed ablation of most importance is the apparent advantage liquid immersion produces in the form of increased ablation rate of the solid target [76]. The confinement of the plasma plume and the resulting high temperature, pressure and density of plume generates the ability to contribute to the etching process alongside the energy supplied by the laser beam, as reported by a number of authors [56, 104].

Further to this general observation, Zhu *et al* [56] report that the ablation rate of Si varies with the thickness of the water film above the target when using a KrF source with a pulse duration of 23 ns. The optimum water film thickness (for maximum ablation rate at a fluence of 3.1 J/cm^2) was found to be 1.1 mm. The ablation rate was found to be lower for thinner and thicker films, suggesting that a number of mechanisms are at work in this interaction. Zhu *et al* [56] claim the reason for this optimal film thickness is simply that increasing film thickness causes greater plume pressure, thus higher plume etching rates; however, increasing film thickness results in increased beam attenuation, reducing laser ablation, and therefore ultimately the size of plume generated. A compromise between attenuation and plume pressurization appears to be met at 1.1 mm in water at 248 nm wavelength. Kim and Lee [104], claim that covering a solid target with a liquid film results in the reduction of ablation threshold and the enhancement of ablation yield. Both the existence of plasma etching and the lowering of the ablation threshold in liquids suggest that laser etching can be achieved using lower pulse energies when the target is immersed in a liquid rather than in a gaseous environment. Lastly, it is known that the immersion of the target in a confining liquid leads lead to shorter plume quench times, resulting in a reduction in thermal conduction compared to traditional gas atmosphere ablation [76].

1.4 Laser beam plume shielding contributions

When a laser beam with sufficient fluence couples with a material, ablation occurs. A significant proportion of the solid material illuminated changes to a melt or gas phase over a short duration. This rapid change in state is combined with a rapid decrease in material density. The sudden change in density causes the irradiated material to expand away from its original position at

high velocity as an 'ablation plume' [8]. From this point, the plume itself can interact with either the end of the laser pulse that produced it, or the following laser pulse when using a high laser repetition rate. This shielding effect has been found to be resultant of four primary effects that will be covered in this section.

1.4.1 Inverse bremsstrahlung interactions with the incident beam

Atoms ejected from the material surface residing in a gaseous state within the plume become excited by further interaction with photons supplied by the laser beam resulting in further charge being added to the atom in the manner of ionization. bremsstrahlung interactions describe the electromagnetic radiation that is produced by the acceleration of a charged particle, such as an electron, by trajectory deflection effected by another charged particle, such as an atomic nucleus; also, the process of producing the radiation is described by this term, which is the German combination of the terminology "to brake" and "radiation". The action of absorption of electromagnetic radiation to produce charged particles is the opposite to the bremsstrahlung effect, thus attenuation of electromagnetic radiation by ionized atoms in a plasma plume is known as 'inverse bremsstrahlung interactions'. The propensity for the atoms in a gas plume to become ionized (and therefore become a plasma) greatly effects the level of the inverse bremsstrahlung interactions [105]. The degree of ionization is known to be dependant upon the plume temperature and this relationship can be predicted by use of the Saha equation [105]. The degree of ionization with respect to plume temperature has been plotted for a number of metals and elements by Lancaster [107], which shows that the degree of ionization follows a logarithmic relationship with plume temperature. No specific experimental data describing the relationship between the degree of ionization and the plume temperature has been found in the literature; nevertheless, it can be assumed from the general trend of other, more simple material structures, that the use of 'cold' ablation, as is commonly associated with excimer laser ablation will result in reduced inverse bremsstahlung interactions compared to that experienced should one use an increased laser wavelength [8]. Mróz [108] supports this relationship, stating that reduced inverse bremsstahlung interactions at short wavelengths results in the characteristically low surface roughness of deposited hydroxyapatite layers when using excimer lasers for the surface deposition technique.

Despite the commonly proposed reduction to the inverse bremsstrahlung interactions when using shorter laser wavelengths, experimental evidence has been found showing that the inverse bremsstrahlung effect is still significant when laser etching sodium, magnesium and aluminium using a beam with 308 nm wavelength and a short pulse duration of 12 ns [109, 110].

1.4.2 Beam interception by large non-gaseous species

Solid and melt phase species existent in the in the ablation plume that are significantly greater in cross sectional diameter than the wavelength of the laser beam used, the debris will absorb the photons that meet it as described in Figure 1-8(b). This localized interception of laser light *en-route* to the sample surface will significantly modify the surface topography of the feature machined in the sample, as displayed in Figure 1-8(c). The high photon energy processed by short wavelength laser beams such

as those produced by excimer lasers dictate that photochemical bond breaking dominates the etching process in gaseous media. Therefore the large debris required to intercept the beam in the manner described in Figure 1-8 are few.

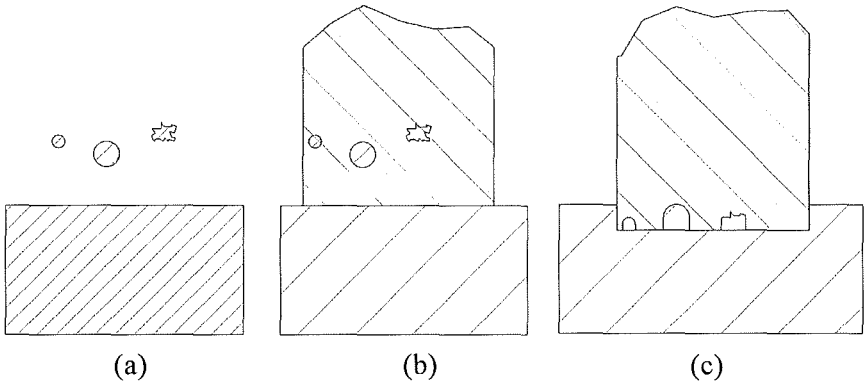

Figure 1-8: Schematic diagram describing the interception of laser light (b); by large ejected particulates (a); and the resulting effect on the feature surface topography (c).

1.4.3 Mie scattering of the incident beam

The majority of melt or solid phase species existent in the laser ablation plume will be molecular, as the photochemical etching process will tend eject groups of atoms linked by high energy bonds rather than single atoms [9]. These atomic clusters (monomers, if laser machining a polymer sample) are equal in scale to that of the laser beam wavelength. This means that the refractive limit of the electromagnetic radiation is exceeded and the photons are scattered when the collide with such small species contained with the plume. This modification to the trajectory of a travelling photon is described by the Mie theory [111, 112]. This effect results in significant attenuation of the supplied electromagnetic radiation. The magnitude of attenuation is inversely proportional to wavelength; indeed, for excimer laser wavelengths Schittenhelm *et al* [113] have shown that that the contribution of Mie scattering is markedly greater than the attenuation contribution of inverse bremsstrahlung effects.

1.4.4 Plume shockwave refraction of the incident beam

A shockwave is caused by a rapid modification to the density of a medium, causing a pulse of kinetic energy to be transferred through the atomic matrix of the medium by sequential transmission of the energy from molecule to molecule. This pulse emanates from the site of propagation at the speed of sound of the medium concerned. The rapid, short term movement of the molecular matrix causes a brief but significant modification to the density of the medium. This modification in density causes variation to the refractive index of the material at the location of the shockwave [114]. This modification to the refractive index of the medium local to the shockwave allows the use of illumination techniques to allow imaging of the shockwaves progress or position at a specific point in time by use of techniques such as Schlieren [115-117] or shadowgraphy [118]. The fact that these techniques are possible is proof that the shockwave significantly refracts electromagnetic radiation, this characteristic has been used to image the expansion of the laser ablation plume [119, 120]. This

refraction has been shown to cause attenuation of the incident beam during laser etching and contribute to the overall attenuation of the beam by the laser ablation plume [121].

1.5 Applications of Liquid Immersed Solid Ablation

A number of processes already use liquid environments for solid targets whilst laser machining for a broad range of applications. Surface patterning in the form of LIBWE, surface cleaning by means of laser steam cleaning and nanocrystal synthesis all use liquids to aide in containment, thermal control, liquid entrapment and maintenance of regular deposition respectively [76].

1.5.1 Surface patterning

Wang *et al* [122] have developed a unique technique of wet etching on the basis of laser ablation in a liquid now known as LIBWE. In this process the image is projected from a mask, then focused through to the far side of the substrate which is immersed in liquid as described graphically in Figure 1-9. It is the liquid that interacts with the beam at the solid-liquid interface and becomes superheated softening the substrate. Further energy absorption results in evaporation of the now superheated liquid and the resulting high local pressures act to etch the surface. This process has many advantages; thermal damage of the substrate is limited as it is the liquid that absorbs the laser energy, it has a high etching rate at a low fluence, it is simple to achieve, it has a high resolution and is easy to control. LIBWE has been shown to reduce laser ablation threshold fluence for wavelength transparent materials, such as quartz for excimer laser applications, by more than an order of magnitude [123, 124] and has been found by others to provide an increased ablation rate when compared to that achieved on the same materials by direct machining in ambient air [125, 126]

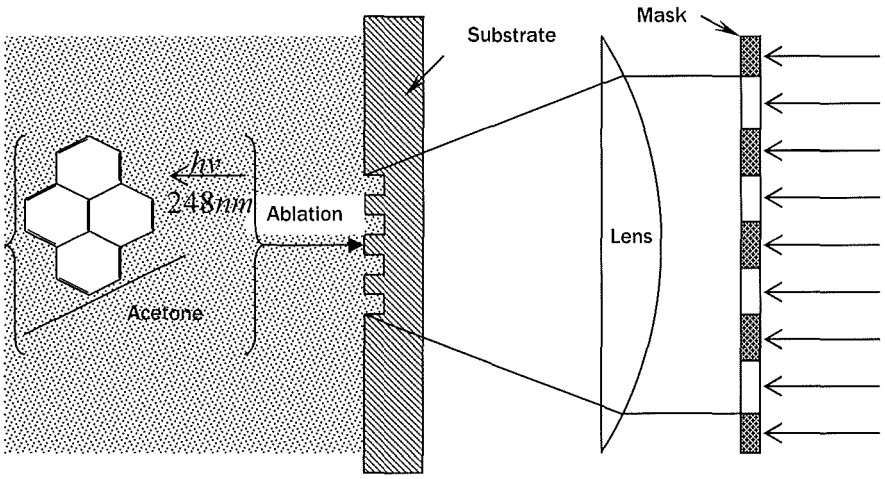

Figure 1-9: Schematic diagram describing the arrangement and method of LIBWE [122].

1.5.2 Surface cleaning

As has been well documented already in this body of work, cleaning micrometer and sub-micrometer particles from the surface of semiconductor and optical devices is a major technological challenge.

This is a view shared by Yang [76], who has highlighted recent developments in laser steam cleaning, promoting its application over traditional techniques such as ultrasonic agitation and plasma cleaning.

Laser steam cleaning was developed by Zapka *et al* [127], who observed adherent particles on a solid surface being removed efficiently when immersed in a thin film that is irradiated with a laser beam. The mechanism for this process is claimed to originate from thermal diffusion between the solid surface and the liquid film. The liquid film becomes superheated at the liquid-solid interface and heterogeneous nucleation of bubbles at the interface occurs. The heat transfer between the solid and the liquid is directly related to the bubble growth rate and size achieved. These bubbles rapidly expand and explode, causing a dramatic enhancement in the local pressure at the liquid-solid interface which acts as a cleaning force to remove particles when it exceeds the adhesion force acting between the particles and the surface. Yang's review of liquid immersed ablation [76] cites a number of studies claiming that a number of particles, including Au, SiO_2, Al_2O_3, Fe_2O_3, Si and polymers have been shown to be efficiently removable from a range of solid surfaces, including Au, Mo, Si, membranes, polyamide and traditional polymers, using this laser steam cleaning technique. All studies reviewed indicate that steam laser cleaning has higher efficiency than that of dry laser cleaning.

1.6 Nanoparticle Synthesis

The production of nano and micro particles has also caused immersion of the sample during lasing to be experimented with, proving to entirely capture all ablation-generated debris [53, 55], so use of a liquid medium to control ablation-generated debris during machining appears achievable. Sattari *et al* [53] used ablation of ceramics immersed in 4 to 6 mm of distilled water running at a constant flow rate of 116 ml/min to produce controlled collection of nanoparticles at the surface of the immersing liquid. Particle productivity has been shown to be proportional to liquid flow rate [50]. The dependence of particle size is less clear, Sattari *et al* state that laser fluence was inversely proportional to the size of nanoparticles produced (supporting the dominance of a photomechanical etching mechanism of a confined ablation plume as described by Berthe *et al* [54]). Katto *et al* [55] found that particle size is governed by the wavelength of the laser (a result common with traditional laser machining in gaseous media) and is proportional with the fluence of the beam. Once generated, debris particles experience drag force that is proportional to the viscosity and velocity of the flow surrounding it [128]. The particles are ejected away from the substrate surface at high velocity [102], and so considerable work must be imparted on the travelling particle by the surrounding liquid to transform the particles original vector to that of the fluid flow. Elaboudi *et al* [50, 51] used 248 nm excimer pulsed radiation to ablate polymer targets including polycarbonate to go about explaining the specific ablation mechanism at work during a liquid (ultra-pure water) immersed ablation event. Their work supported the findings of previous authors [54, 56] insofar as the ablation threshold decreased when using liquid immersion compared to traditional ablation in ambient air, the photomechanical interactions driven by thermal evaporation are primarily responsible for the ejection of debris material and the debris generated typically had a diameter of 50 nm and a chemistry close to that of the original material - supporting a 'cold' or photomechanical removal mechanism. Elaboudi *et al* [52] also

postulated that in addition to photochemical degradation, some debris was generated by a hydrolysis reaction as an explanation for the decreased ablation threshold of ultra-pure water immersed polyethylenetelephthalate (PET).

1.7 Liquid Application for the Function of Debris Control

A laser machining and surface modification technique that not only uses a liquid medium in its application, but relies upon it has been developed [48]. This technique delivers long wavelength laser light by use of a fine jet of water, where the water jet is effectively used as an optical fibre from the laser optics to the substrate surface. This technique is not used for transmission of a coherent image, instead delivering a concentrated, high intensity laser beam to a well defined spot on the substrate surface. This liquid then goes on to suspend debris and form flowing streams of liquid to transport debris away from critical machined areas. This technique demonstrates that the use of such media does not pose unacceptable attenuation of the beam, despite the fact that this laser light was of the opposite end of the spectrum to that produced by Excimer lasers. Also this technology shows that use of liquid media can support laser coupling with a solid medium. This is an important lesson for further development of a technique that can be used for laser beam imaging, as is used extensively in excimer laser ablation micromachining technologies.

A liquid jetting system has been developed by Scaggs [12] for use in debris control. In this arrangement a nozzle is mounted between the laser optics and the material surface, this nozzle is coupled to a liquid reservoir that is presumably pressurized to propel a fine spray of the liquid onto the substrate before, during and after laser processing has taken place. Scaggs stipulates that the reservoir contains a liquid, such as water, that is not substantially photoabsorbing around a primary UV wavelength. A schematic of this equipment is given in Figure 1-1. Little has been published detailing its performance as a technique.

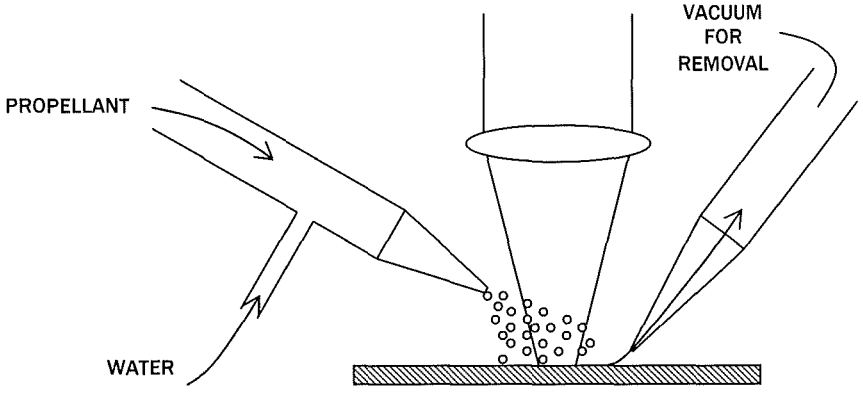

Figure 1-10: Schematic diagram describing the arrangement of equipment proposed by Scaggs [12].

1.8 Current Technological Performance Boundaries for Excimer Machining

The principles involved in laser profile machining are very simple; however, due to the scale of items being processed and the quality demands placed upon resultant products there are issues that add significant complexity to the process. There are three major areas of performance limitation:

1.8.1 Photomask resolution

To etch masks a digital plasma etching tool is used and is controlled in the x-axis and y-axis by encoding strips similar to those used to control stages on laser micromachining tools [129]. Due to the accuracy of these encoders' profiles, small curved profiles are represented as stepped interpretations (see Figure 1-11) [130]. It is easiest to visualize this as a bitmap computer graphic representation of a circle; when drawn and viewed at 1x magnification on screen it looks like a smooth, perfect representation of a circle. Yet when the viewer zooms into 6x or 8x magnification suddenly the pixel steps are apparent. The same is true of excimer laser masks. This effect can be reduced by 500% simply by increasing the size of the mask by 5 fold then shrinking the beam image using optics [2]. To use the bitmap analogy, this is akin to increasing the screen resolution greatly and drawing the circle to be (apparently) the same size on screen so that many more pixels are now utilized and the stepping effect is reduced.

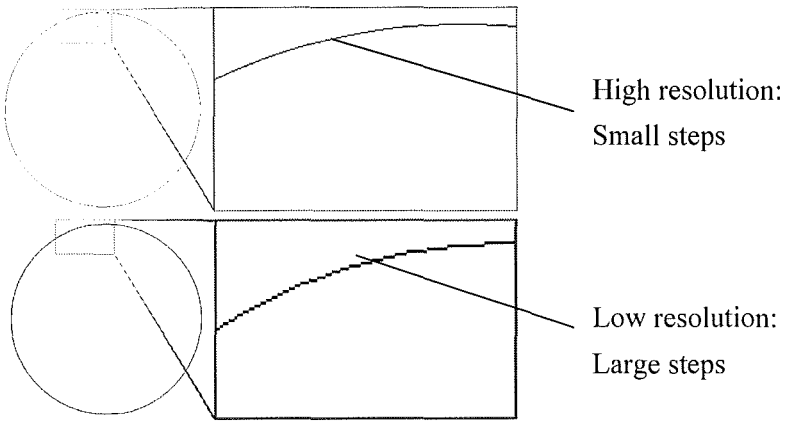

Figure 1-11: Graphical illustration of the effect of resolution upon the crispness of an image; in this case a simple circle.

This stepping is an artificial cap to the minimum feature sizes achievable using micromachining since the image can become 'pixelated' and produce a low resolution representation of a desired profile down at small scales (currently this threshold would be crossed by a circle of 1 μm diameter at the wafer [130]). This phenomenon is presently posing problems for techniques such as 'feathering' used to smooth machining seams and the half tone technique which is limited to using square apertures due to their extremely small scale [131]. Having said that, it must be stressed that this is a problem that is being incrementally overcome by generational improvements in encoder strip design and control software for the etching tools [129, 130]. Soon the minimum feature size for a chrome-hoya on quartz mask will fall below 1 μm which means it is

approaching the diffraction limit of excimer laser radiation. This diffraction limit is the natural cap of resolution. The only method to reduce this is to utilize masks of greater magnification or shorter laser wavelengths.

1.8.2 Lens effects

The next limiting factor for laser micromachining is presented by de-magnification lens resolution, because all lenses used are mechanically manufactured. Ideally a lens could focus a larger image down to an infinitely small spot. In reality there is a limit to the resolution of a lens for a given magnification; thus posing a limit to the size of an individual feature that can be machined accurately or crisply with this process [58]. A lens must be formed *via* a mechanical process of shaping, grinding and then finally polishing. The level of polish is ultimately always going to be limited to the molecular scale roughness of the material; hence there will always be an ultimate limit to focus for any lens, although currently this has not been reached. Impurities in lens materials and the techniques used to polish them still leave room for improvement [58]. Recently a lens manufacturer has developed a 6x magnification lens that can achieve the resolution desired for the laser micromachining technique [132]. This is significant as it opens the door to the use of larger masks and therefore greater overall image resolution.

Both of these limiting parameters are being incrementally improved upon over time and will continue to become less of an issue until the ultimate boundaries of performance discussed above are reached. There are many manufacturers of both masks and lenses; hence progress is almost guaranteed. This increase in performance is primarily driven by industrial competition.

Other lens effects become important when using high magnification, near field optics. High power lenses suffer from high levels of spherical aberration which makes complex imaging of objectives through a laser system limited. The result of spherical aberration is a reduction to the effective depth of focus and large deviation from focus immediately once past the limits of the depth of focus [58]. This can cause significant difficulties when machining large areas with fixed optics laser processing systems.

1.8.3 Performance limitation by debris

Debris is one limiting factor that has remained unresolved up until this point in laser micromachining despite some concerted attempts by its developers. Debris causes many issues for the industrial practicality of this process for mass production use. It can cause low production yield rates due to the effects of debris during machining or being left on the product after machining as well as contaminating the clean room environment [133]. Debris generation and distribution are virtually random occurrences and are incredibly difficult to predict. Debris production depends upon the wafer material composition at a particular location and the quality of the beam during a particular shot, along with its precise wavelength - all of which vary slightly [1]. Polymers suffer greatly from debris production when being machined using short wavelength pulsed laser ablation because of the complex molecular structure of polymeric materials. The complex structure of bonds that form the molecular matrix of polymeric materials causes scission of groups of atoms from the mass of the material at the

bond of lowest energy, these monomers then exist as solid debris items. The distribution depends upon a multitude of variables, including localized wafer material composition; machining medium viscosity and chemical inertness; shot quality; energy density; duration; wavelength and medium conditions (for instance flow rate or turbulence levels) [1]. Finally a crucial factor in the spread of debris produced by a laser shot depends upon the surrounding terrain of the wafer. For the first shot of the machining process the wafer is relatively flat and debris spread is not impeded. Towards the end of a machining cycle the topography will have developed, perhaps into a non uniform profile, which may impede flying debris by differing amounts depending upon the particular particle's vector.

This non-uniformity of debris makes the issue of debris doubly important. If debris levels were to remain at current levels, but always yield uniform or predictable coverage, it would pose a smaller problem to industry. Currently, manufacturing with the laser micromachining process is very much a system of trial and improvement [1], often relying upon the individual skill of the tool operator. This is not acceptable in many circumstances where quality issues are paramount to a product's viability.

CHAPTER 2

ADHESION THEORY

2.1 The Stages of Adhesion

Before individual force interactions are explored, the adhesion process needs to be examined as a basis for complete understanding. Reed [134] states the three significant processes that govern the interaction of two bodies: First, Particles arrive at surfaces through long range attraction forces such as van der Waals and electrostatic image forces. Second, once together the nature of the impact is governed by the nature of the deformation of the bodies and the number and strength of interaction forces in a given medium. Finally, the environmental conditions: medium parameters, the geometry of the particle with respect to hydrodynamic drag and the strength of the adhesion interaction of both long and short range in nature - govern the possibility of re-suspension.

2.2 Thermodynamic Work of Adhesion

2.2.1 *Surface forces between a two body system*

As an initial step, the simplest system possible must be considered: two particles in contact in a total vacuum labelled 1 and 2 respectively. This takes the form of a simple balance of the surface energies, γ, and the interfacial energy, γ_{12}, between the two, which can be described as the work of adhesion, W_A, [135, 136]. γ is also known as the Dupré energy of adhesion. Specifically it is a measure of energy per unit area, representing the work done to completely separate a unit area from contact with another body [137].

$$W_A = \Delta\gamma_{12} = \gamma_1 + \gamma_2 - \gamma_{12}, \tag{10}$$

The typical approach for representing solid surface energies is to express surface tension or surface energy (usually against air) as the sum of the components due to the dispersion forces, γ^d, and polar forces, γ^p; such as hydrogen bonding [138]. Thus the interfacial tension between two phases 1 and 2 can be expressed as

$$\gamma_{12} = \gamma_1 + \gamma_2 - 2\sqrt{\gamma_1^d \gamma_2^d} - 2\sqrt{\gamma_1^p \gamma_2^p}. \tag{11}$$

2.2.2 *Surface forces between a two body system in a medium*

Next a medium must be added to the system to make it replicate a liquid immersion situation more closely. The work of adhesion between two bodies in a medium, labelled '3' is given by a simple balance of interfacial free energies [139]:

$$W_A = \gamma_{13} + \gamma_{23} - \gamma_{12}. \tag{12}$$

It must be understood that this apparently simple relationship is greatly complicated by the fact that the third medium can be a liquid, vapour or gas, with each of these causing a variation on the surface force interaction. The interaction of interest for the research in this thesis is for identical bodies 1 and 1 in a liquid medium 3. In this instance [140]

$$W_A = \gamma_{131} = 2\left[\gamma_3 - 2\left(\sqrt{\gamma_1^d \gamma_3^d} + \sqrt{\gamma_1^p \gamma_3^p}\right) + \gamma_i^d + \gamma_i^p\right]. \tag{13}$$

2.2.3 *Variables that effect the surface energy interaction*

The Johnson, Kendal and Roberts (JKR) theory, which examines material deformation (discussed fully in Section 2.7), shows the link between the contact radius and W_A. Separation of the two surfaces can be treated within the formalization of linear fracture mechanics. The mechanical energy made available through the crack growth is known as the energy release rate ,G, and is described by the Gibbs equation [141]. This value is equal to W_A. It must be noted that this relationship can only be used with the JKR system since it requires the apparent applied load to remain positive

$$W_A = G = \frac{(P_1 - P)^2}{6\pi r_e P_1} = \frac{\left(K r_a^{\,3} / r_e - P\right)^2}{6\pi K r_a^{\,3}}. \tag{14}$$

where P and P_1 are the applied load and apparent applied load respectively which are defined in Section 2.7.3.; K is the geometric deformation ratio, defined in Section 2.7.; r_a is the contact radius after deformation, defined in Section 2.7 and r_e is the effective radius, defined in Section 2.7. This relationship can only be used with the JKR system since it requires the value of P_1 to remain real.

A model for use with and dependant on the RMS description of surface roughness has been developed by Rabinovich *et al* [139], and declares that surface topography has a large effect on W_A. Experimental investigation has demonstrated that increased smoothness lowers the net W_A, but increases the variance of its effect [142].

2.3 Van der Waals Force

The force most commonly identified as an adhesion force bears its discoverer's name: van der Waals, F_{vdW}, also known as the secondary valence force [143]. This is the primary force of adhesion acting upon small (less than 50 μm diameter) particles lying upon a dry surface [16]. Increases in the strength of this force can be caused by deformation of the particle, the surface or both as both increase the contact surface area between bodies [16]. Particles less than 1 μm diameter can be held to surfaces by forces exceeding 100 dynes or roughly 10^9 dyn/cm^2.

Even at absolute zero temperature solids can retain local electric fields that originate from polarisations of their constituent atoms and molecules. Above zero degrees additional contributions come from thermal excitations of the atoms and molecules. F_{vdW} include forces between molecules possessing dipoles and quadrapoles, caused by the polarisations of the atoms and molecules of the material. This can include both natural instantaneous dipoles and quadrapoles [16]. Non-polar attractive forces [144] known more commonly as London – van der Waals dispersion forces are the

primary contributing phenomena in van der Waals interactions. Non-polar attractive forces were associated optical dispersion, that is, spontaneous polarisations, by London [35].

2.3.1 *The Hamaker constant*

Hamaker [145] calculated F_{vdW} using a macroscopic approach that starts with interactions between individual atoms or molecules and calculates the attraction between larger bodies as an integration over all pairs of atoms and molecules in that body, a technique that has been used commonly by others [23, 144, 146, 147]. This integration is made using the following assumptions [144]: (i) The total interaction is obtained by the pair-wise summation of the individual contributions of each molecule; (ii) The summation can be replaced by an integration over the volumes of the interacting bodies, meaning each atom occupies a specific volume with a density, ρ, in a continuous medium; and (iii) The atomic volume density and London's interaction constant are uniform across the volume of the bodies. This pair-wise summation of intermolecular forces is now known as the Hamaker constant, A, and ranges from about 10^{-11} to 10^{-14} ergs. Some examples for materials are listed in Table 2-1.

Table 2-1: List of material specific Hamaker constants in a vacuum and water [145].

Material	Vacuum – $A/10^{-20}$J	Water – $A/10^{-20}$J
Gold	40	30
Silver	50	40
Copper	40	30
Water	3.7	-
Quartz (fused)	6.5	0.83
Quartz (Crystalline)	8.8	1.70
Fused Silica	6.6	0.85
Calcite	10.1	2.23
Calcium Fluoride	7.2	1.04
Sapphire	15.6	5.32
Al_2O_3	16.75	4.44
Polystyrene	7.9	1.3
Polymethylmethacrylate	7.1	1.05
Polyvinylchloride	7.8	1.30
Polyisoprene	6.0	0.74
Polytetrafluoroethylene	3.8	0.33
Hexadecane	5.2	0.54
Pentane	3.8	0.34
Decane	4.8	0.46

From inspection of this table it becomes clear that the use of water immersion drastically reduces A for most materials. If this system were to comprise two similar bodies in a third medium A for this system can be approximated using an interpolative combination of the Hamaker values of individual materials, listed above [145]:

$$A_{1,3,1} = A_{1,1} + A_{3,3} - A_{1,3} = \frac{\left(A_{1,1} - A_{3,3}\right)^2}{A_{1,1} + A_{3,3}} \approx \left(\sqrt{A_{1,1}} - \sqrt{A_{3,3}}\right)^2 \qquad (15)$$

Unfortunately this approach is not accurate as it does not consider cross-correlation of charge [22, 148]. Second order quantum perturbation theory [149], upon which A is based, is only an approximation that is useful for initial demonstration of the adhesion force lowering properties of liquid immersion. In reality the internal states of molecules will be modified by the proximity of all

other molecules in the system. Hence pair-wise summation of all molecules cannot be correct as the *i* and *j* components of each molecules' states will fluctuate depending upon position and surrounding. This inaccuracy is confirmed by the experimental results of Menon *et al* [150], showing large discrepancies between experimentally measured force and calculated predictions using *A*.

2.3.2 *The Lifshitz - van der Waals approach*

A more satisfactory macroscopic approach has been developed by Lifshitz [36], who started directly from the bulk optical properties of interacting bodies. This approach examines the interactions between electromagnetic waves emanating from the macroscopic bodies of molecules. The initial calculation is highly complex and requires a great deal of computation to achieve a result [151]; however, more recent translations have yielded more accessible models [152, 153]. The Lifshitz - van der Waals constant, *h*, is defined as an integral function of the imaginary parts of the dielectric constants of the adhering materials [22, 154, 155]. This function describing adherence is also readily applicable to systems involving a third medium, rather than two bodies in a vacuum [37] with need for interpolation. *h* is dependent on material combination, generally ranging between 0.6 eV for polymers to 9.0 eV for metals [148]. *h* is related to the optical absorption constant of a material - materials with high optical absorption have strong spontaneous fields and therefore should be bound by greater forces of adhesion due to F_{vdW}.

If F_{vdW} is treated as the force necessary to separate two items, then F_{vdW} per unit area between two parallel flat surfaces in contact can be calculated [16] using

$$F_{vdW} = \frac{hr_P}{8\pi L_S^{\,2}} \tag{16}$$

This calculation technique shows F_{vdW} to be dependent upon *h* and the denominating separation distance, L_s, of the two surfaces. This separation distance is small, measured in Å. For a spherical particle, the particle radius, r_p, becomes a critical numerator in this relationship [136].

Since the composition of the particle adhered to a surface influences the effect of F_{vdW} in the adhesion system, it now becomes important to identify this parameter for any given material. For ablated debris, particle is likely to be either identical to that of the surface if the particle results from a surface stress generated explosion, or a chemical compound formed from the combination of constituent reactive elements of the medium with those of the particle material *via* heating.

In practice many researchers have found compelling evidence to prove Lifshitz's method of atomic interaction summation is fundamentally correct, furthermore it is now known that Lifshitz - van der Waals forces are the predominant component of most adhesion systems. Ibrahim *et al* [156] explored the variance in adhesion of differing batch composition of lactose particles to gelatine capsules for the pharmaceutical industry. A direct, linear correlation between particle size and adhesion force was observed. The slope of the increase was in acceptable agreement with the Lifshitz - van der Waals model prediction to prove that the interaction was from increasing molecular contact between the particle and surface, since the number of real contacts on a molecularly rough surface tends to increase linearly with contact area size [157].

Also, when the primary adhesive forces were electrostatic or capillary the resultant force / size relationship was not linear, because the contact area increased exponentially with increasing particle diameter.

2.4 Electrostatic Forces

In a dry system electrostatic forces act to hold particles to surfaces in partnership with F_{vdW}. They can also play a prominent role in attracting the particles to the surface before adhesion [16]. There are two main electro static forces that act between particles and surfaces: electrostatic image forces and electrostatic double layer forces.

2.4.1 *Electrostatic image forces*

Before contact between two bodies is achieved, bulk excess charges present on the surface and/or particle produce a coulombic attraction known as an electrostatic image force, F_i. This is a long range force, acting to draw a particle to a surface. A number of literature sources have been found offering models for differing components of this phenomenon. Leenars [158] proposes a generalized solution which is supported by Bowling [16] to calculate the force that arises from different surface charge densities interacting *via* long range force law. These surface patch charges occur due to variation in the work function on a materials differing surface regions [159].

$$F_i = \frac{q^2}{4\pi\varepsilon_0\varepsilon_M L_C^2} \tag{17}$$

where ε_M is the dielectric constant of the medium between the particle and surface, ε_0 is the permittivity of free space, q is the charge and L_C is the distance between charge centres measured in Å. As this is a system formed of a particle and surface, L_C is approximately equal to $2r_p$.

Leite and Herrmann [37] support a solution proposed by Hao *et al* [160] derived from experimental testing using a sphere ended conical atomic force microscope (AFM) tip on a flat surface. Two conditions are described: (1) When the particle radius is much greater than the separation between the two, F_i is proportional to the separation distance between particle centre and the planar surface, r_p; and (2) When the particle radius is much smaller than the separation between the two bodies, F_i is proportional to the square of r_p. The voltage difference between the particle and the surface is equally critical in both cases.

2.4.2 *Electrostatic double layer force*

For small particles of differing material to the surface to which they are adhered, the electrostatic force of greater significance is electrostatic contact potential induced by double layer forces. Two differing materials in contact develop a contact potential caused by differences in the local energy states and work functions [16]. Electrons are transferred from one solid to another until an equilibrium is reached where the current flow in both directions is equal. The resulting potential difference is called a contact potential difference, U, which generally ranges from 0 to 0.5. This generates a 'double layer charge region'. The electrostatic double layer force, F_{el}, has been shown to be dependant

upon the square of the contact potential difference [22, 38, 161].

$$F_{el} = 8r_p U^2 \tag{18}$$

When particles are immersed in an electrolyte solution, any charge on the particles will attract a layer of ions of the opposite sign. This second layer of ions will themselves attracts a further layer of opposite polarity ions in a diffuse layer. This phenomenon is characterized by the *Zeta* potential, which is the potential at the fluid shear plane [16]. When two bodies are immersed in a liquid medium the resulting three component double layer interactions results in a repulsion force between the two bodies. This is important for Derjaguin, Landau, Verwey and Overbeek (DLVO) theory, described in detail in Section 2.5.

When there is a liquid medium surrounding the interacting bodies, the effects of surface tension at the body - liquid interface causes separation of the two bodies by mode of a film similar to that shown in Figure 2-1(a).

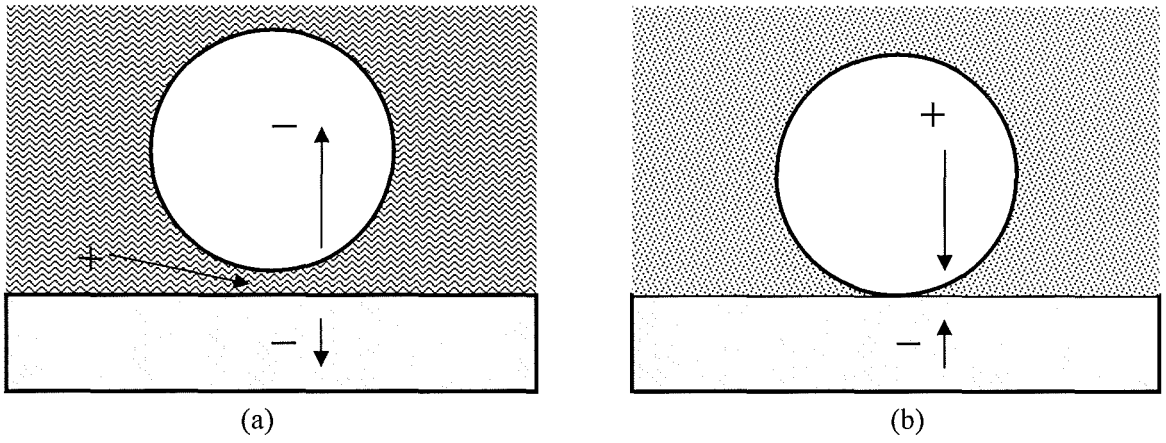

Figure 2-1: Schematic representation of the electrostatic attraction of a particle to a surface: (a) particle separated from a surface by a liquid film; and (b) a gaseous medium unable to penetrate the interface between particle and surface.

If the medium is dry and gaseous this film is not developed, as described in Figure 2-1(b), such and interaction is not possible, and adhesion is maintained. When the two bodies are separated in the manner described in Figure 2-1(a), repulsion is generated through a double layer of counterions. Counterions are the ions that accompany an ionic species in order to maintain electric neutrality. The counterions of the surface induce an opposite and equal charge upon those of the medium film between the particle and the surface. The liquid medium is now charged in a polarity that is conducive to that of the surface. Because of the medium's large bulk, it then induces an opposite and equal polarity to its own on the particle; hence the particle has the same polarity as the surface so these will now repel each other. It must be noted that DLVO theory does not consider the adhesive forces generated by the capillary action of the fluid. This is a significant limitation to the model. The force of repulsion is predicted using the Yukawa repulsion model, which is complex, but highly dependant upon the magnitude of charge occurring between the two items, the Bjerrum length (approximately 0.7 nm, dependent upon medium) and the distance between charge centres measured in Å [41]. The

combination of all of this work demonstrates that the surface topography amplitude of the surface that the particle is adhered to is highly critical in the magnitude of the electrostatic adhesion force [38].

Hays [162] measured the fields required to detach toner particles approximately 13 μm in diameter from nickel carrier spheres that had a 250 μm diameter. He then measured the charge left on the particles that were detached to calculate the force used to detach them. Particles on a conductive surface will acquire a charge proportional to the particle surface area and the electric field. These particles will experience a net force in the field proportional to the field multiplied by the charge [163].

2.5 Derjaguin, Landau, Verwey and Overbeek Theory

The interaction of two surfaces is usually dictated by the balance between the fundamental forces such as the van der Waals and the electrostatic forces as described by the DLVO theory [164, 165]. This is a simple combination of two known bodily interactions: the van der Waals attraction and the electrostatic repulsion arising from double layer counterion formations. Since this theory relies upon double layer counterion effects this model is only applicable in a liquid medium.

Nevertheless, it is well known that the adhesion phenomena is not restricted to just these two interactions: any given particle-surface system may involve specific forces such as salvation, hydration, structural (such as Derjaguin, Muller and Toperov (DMT) or Johnson, Kendal and Roberts (JKR) deformation interaction effects) and hydrophobic effects. These interactions are commonly termed non-DLVO forces [166]. On top of these direct adhesion forces, steric, hydrodynamic and frictional forces may need to be considered for a particular system.

2.6 Surface Roughness and Asperity Effects

Surface roughness is crucial to almost all of the component adhesion forces since it governs the number of 'real contacts' achieved in a contact patch between two bodies [167]. In AFM the pull-off force of particles adhered to surfaces has become easy to measure directly and from these measurements the work of adhesion due to surface energies can be calculated [168 - 170]. To do this the area of surface contact must be known. This is most simple if the contact patches, as both bodies are ideally flat and smooth, effectively making the problem two dimensional. Surface deformation immediately increases the complexity of the problem, taking it into the third dimension (various methods for approximating this effect will be discussed in the next Section). The other variable in real situations is the surface roughness.

Modelling the true contact area between a micron scale particle and a substrate is difficult. Surface asperities which exist on all real surfaces can either reduce or increase the total contact area of interacting bodies. Often varying contact areas are experienced between repeated measurements of a system, giving rise to the common reporting of data as a distribution of adhesion values [156, 171, 172]. In the same way, variance in local surface roughness across the entirety of a particle-surface interface is represented by a single roughness constant, making the model inaccurate for predicting shear or roll tendencies during removal [167].

2.6.1 *Modes of contact*

Surface asperities lead to 'contact modes' between particles and surfaces [173]. This shows the direct importance of relative asperity size between the particle and the surface. It is often the case that a particle is of the micrometer scale, and the surface has asperities spaced by more than a ⅓ of the particles diameter. In such a situation, there are only three contact modes, as depicted in Figure 2-2. Assuming a relatively spherical overall profile for the particle, the number of contact points between two bodies affects the contact area and therefore the molecular interaction between the two bodies. As has already been discussed, greater molecular interaction leads directly to greater F_{vdW}. The settling arrangement of a particle on a surface is totally random, and generally non-repeatable; hence these 'contact modes' lead directly to the variation in pull-off force experienced in many AFM experiments. In extreme scenarios, when the particle is in contact only with the top of an asperity (Figure 2-2(a)), the pull off force required to remove the particle will be much lower than (b) where the particle is touching the sides of the asperities, or entirely penetrates the inter-asperity valley. If the particle is of approximately the same scale as the surface asperities of the substrate it is settling upon, the random nature of its contact mode can cause the adhesion force to increase or decrease depending upon the location of the interaction [173]. This theory was supported by AFM examination the relationship between adhesion and topography by Mizes *et al* [174], who confirmed that areas with raised topography (and therefore fewer possible asperity contact points) offered lower adhesion. Furthermore, it was found that greater surface smoothness not only offered lower adhesion forces, but also greater variation in the pull-off force as the contact between the particle and the surface can contrast greatly between no asperity, large area contact and single point contact. The Derjaguin approximation can be use to predict the Derjaguin force of adhesion, F_{Der}, between a rigid particle on a rough and rigid surface. Here the radii of curvature of the irregularities for the particle and surface are central to the approximation, that relates these to the work of adhesion [175].

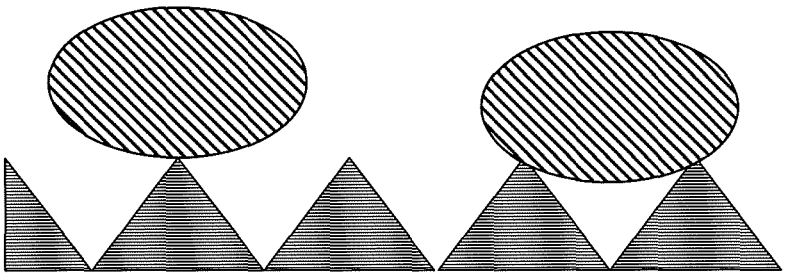

Figure 2-2: Schematic diagram of the two possible settling positions for a particle in contact with a substrate featuring comparatively large asperities: (a) the particle sits balanced upon just one asperity contact patch; and (b) the particle sits supported by two asperities.

$$F_{Der} = 2\pi\left(\frac{1}{K_p + K_s}\right)W_A \tag{19}$$

where $K_p = 1/r_p$ and $K_p = 1/r_s$ are the radii of curvature of the irregularities for the particle and surface respectively.

2.6.2 *The role of surface roughness in capillary adhesion*

Capillary adhesion, another key component of the adhesion phenomenon is also directly affected by surface roughness of a material. Ata *et al* [176] examined the role of surface roughness in relative humidity related adhesion forces. It was found that there was significant difference in adhesion force measured in dry and humid conditions at low roughness levels. Adhesion forces at just 0.2 nm roughness were measured as 130 and 100 mN/m for humid and dry conditions respectively. This significant variance is due to the surface roughness in this experiment being low, close to an ideal surface. The variance between the two results is arising purely because of capillary action. Large capillary patches are formed in high humidity conditions between the particle and the surface, adding significant adhesion force to the system. In dry conditions there is no fluid available to supply a meniscus and the resulting adhesion system is smaller. At high roughness levels, both dry and humid adhesion conditions provide results within 10% standard deviation of each other. On account of the fact that in this case the meniscus is formed between asperities and the particle, rather than a constant smooth wafer surface. This means that the meniscus formed is always very thin, so humidity affects adhesion force less with rough surfaces.

2.6.3 *Statistical methods of representing surface roughness*

A method of representing the roughness of a material across a specified area is the average roughness, R_a, which is most commonly taken across the entirety of a wafer surface. The surface size is simulated as a matrix of dimension M x N containing height data, $z(i, j)$. R_a is simply the mean of all the height data contained within the matrix. This approach can often lead to distorted results from single large values and so the most common development of R_a is the RMS roughness, R_q. This measure represents the standard deviation of the heights of peaks and troughs relative to a reference plane across a surface [177].

Useful studies have been conducted by Rabinovich *et al* [139], developing the simple flat geometry system described by Equation (20) to be correct for a particle attached to a surface, given the approximate geometry described in Figure 2-3. This model suggests that measuring the RMS roughness along with the asperity sizes and distribution of both bodies can be used to predict the adhesion contact and account for the decrease in adhesion force that arises from such surface features. For a spherical or elliptical particle the RMS roughness can be calculated with:

$$R_q = \sqrt{\frac{32\int_0^{r_1} z_{eff}^2 r_2 dr_2}{L_{asp}} k_p} \tag{20}$$

where k_p is the surface packing density for close packed spheres ($k_p = \pi(\sqrt{12})^{-1} \approx 0.907$)), r_1 is the macroscopic orthogonal radius of the particle (see Figure 2-3(a)), r_2 is the parallel planar radius of the particle (see Figure 2-3(a)) and L_{asp} is the surface wavelength of the particle (see Figure 2-3(b)). The W_A is directly related to the surface roughness and asperity characteristics and Equation (13) is key in calculating this parameter. Because this is a standard deviation value it filters out extreme values, which can contribute significantly in an adhesion contact interface. The extreme values can be expressed in terms of the peak valley height, R_t, and the ten point height, R_z. R_t is simply the height difference with respect to a centreline between the highest point recorded in the matrix M x N, and the lowest.

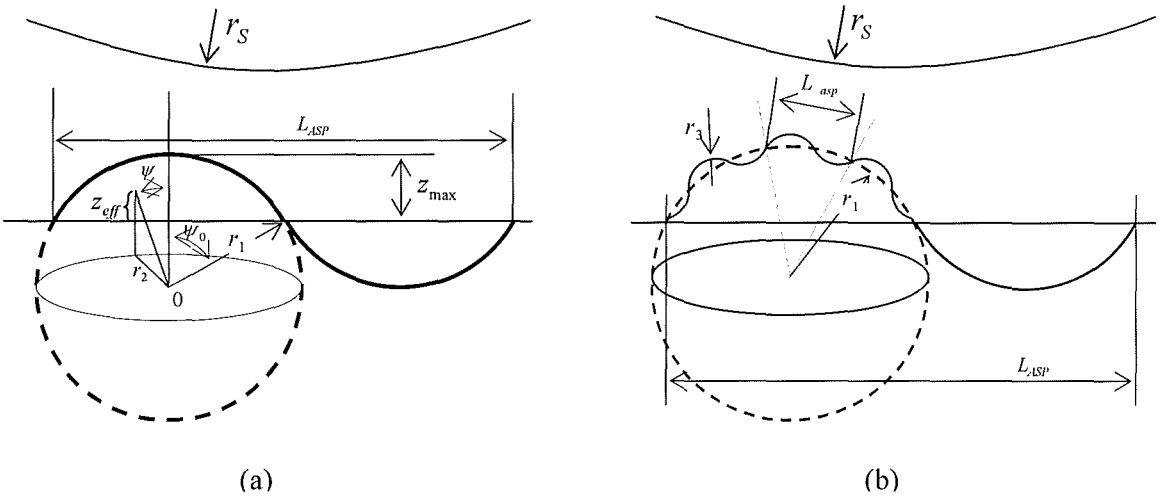

Figure 2-3: Schematic diagram showing the model geometry for Rabinovich model [139]. The notation is for use with Equation (20).

2.6.4 *Statistical methods of representing the nature of a roughness value*

Simple averaging techniques for surface roughness measurement can lack resolution, it only takes a single 'spike' to distort the true nature of an entire surface when searching purely for the largest height difference, hence R_{var} has been developed. This value is equal to the average height of the five highest local maxima and the five lowest local minima [177]. For the data presented in matrix form, a local maximum is simply defined as a cell surrounded by eight neighbouring cells that are lower in value, the converse is true for a local minimum.

The asymmetry of any given height distribution histogram can be expressed as a numerical value, often referred to as the surface skewness, R_{sk}. The use of this parameter can discriminate between different surfaces with the same R_a and R_q values. A zero value for R_{sk} indicates a symmetric height distribution [177].

A method for checking whether the surface roughness value is caused by many similar data points or if it is heavily distorted by just a few extreme values is to measure the surface kurtosis, R_{ku}, which is equal to the normalized fourth moment of the height distribution [177]. A Gaussian surface will give an R_{sk} of zero, indicating a symmetric height distribution. The R_{ku} value will increase if the variance is due to infrequent extreme values.

Finally, there is the probability function of the surface height, $P(z)$. This identifies the fraction of the surface having a height less than z with $P(-\infty) = 0$ and $P(\infty) = 1$. It can be calculated from the integral of the probability density function, $P(z)$ [177]:

$$P(z) = \int_{-\infty}^{z} P(z)dz \tag{21}$$

$P(z)$ represents the fraction of the surface with a height between z and $z + \Delta z$.

In summary, it is generally believed that increasing surface roughness results in increased adhesion force variance and most importantly, a general decrease in total adhesion force [177, 173, 176]. This is due to asperity contact decreasing body contact area [177] and reduces the contact angle of capillary meniscus formation [176]. There are a range of statistical roughness measurement tools in existence, which should aide in prediction of true contact area between bodies.

2.6.5 *Use of statistical roughness representation in force prediction modelling*

The PERC model is the result of these statistical analysis techniques [139, 140]. This was developed through theoretical analysis of surface topography measured experimentally using AFM. The surface topography is described using both the height and breadth of the asperities, expressed as RMS roughness and the peak-to-peak distance, L_{ASP}, illustrated in Figure 2-3(b). F_{vdW} has been calculated to be directly proportional to particle radius, contact area and inversely proportional to the separation; however, the interference of the peak to peak distance has also been included in this thesis, acting as a highly numerating parameter [166]. This model consistently predicts F_{vdW} to within 50% of the experimentally measured value, which is considerably better than previous models, such as the Rumpf model.

2.6.6 *Impact of surface roughness on component adhesion forces*

Roughness has been shown to be a critical factor in particle adhesion. The surface roughness of two bodies governs the total contact between them [167]. High roughness means large asperities, which in turn mean large inter-asperity troughs or valleys in which comparatively small particles can become lodged with two contact points with the substrate. Conversely low roughness means small asperities and lower adhesion in general as the total actual contact patch between the two bodies is reduced; however, the adhesion force can vary greatly on 'smooth' surfaces as the number of contact points between the two bodies has a greater possible range when the particle is large compared to the asperities. The actual contact area between a particle and a surface is critical in the interaction of surface energies [169]; thus W_A is directly affected by surface roughness.

Capillary adhesion also depends upon the surface roughness of two interacting bodies; in this

case rough surfaces offer lower adhesion potential: the meniscus formed by capillary action can only form between the asperities and the particle; on smooth surfaces the asperities are too small to support a meniscus of their own, the meniscus is formed between the mean surface profile and the particle therefore tending to be larger and stronger than would be achieved from an asperity-particle meniscus [176]. The relationship between surface roughness and adhesion force generated by capillary and other contact interactions oppose each other. Table 2-2 offers easy reference for each scenario.

Table 2-2: Comparison table for the effect of surface roughness on individual adhesion mechanics.

Adhesion mechanic	High Roughness	Low Roughness
Work of adhesion critical	High	Low with high variance
Meniscus critical	Low	High
Electrostatic image critical	High	Low with high variance

2.7 Surface Deformation Effects

It is sensible to consider the contact of two rigid spheres that have a contact patch radius of zero. The total adhesion force, F_{ad}, between these two is given by the Bradley theory [178]. This relation demonstrates the high criticality of the W_A and the effective radius, r_e, a value determined from the radii of the particle and surface of the two bodies modelled, as illustrated in Figure 2-4. It must be noted that for a flat surface the radius is deemed to be equal to ∞.

In reality no material is totally rigid, therefore some deformation at the contact patch will always take place in such an interaction [179]. The ability to directly measure the contact area between two measured bodies is solved through the use of a number of contact mechanics models. Firstly, the Derjaguin, Muller and Toperov (DMT) model [175] for small, rigid particles interacting with highly smooth, rigid substrates of low surface free energy. Secondly, the Johnson-Kendall-Roberts (JKR) model for larger particles with higher surface energies [180].

2.7.1 The Hertz model

The Hertz model [181] was formulated in 1881 to represent the mechanics of contact between a spherical body on a planar surface. This model makes three assumptions: (i) The spherical particle is considered to be elastic with a smooth surface; (ii) The surface is assumed to be rigid and smooth and so the deformation system would resemble that shown in Figure 2-4(a); and (iii) No surface forces are taken into account.

When two bodies are brought into contact both deform due to repulsive forces known as 'Born repulsion' within the contact area. This occurs at the contact area perimeter and locally around the outside of the perimeter; attraction takes place in the form of short and long range forces to balance the system. Due to the steep gradient of the born repulsion - attraction force, inter-atomic distances within the contact area differ little and the area is considered to be a flat circle for a spherical particle on a flat surface [13, 181]. Therefore, the Hertz model states that, in a repulsive-only system,

$$F_{ad} = 0 \tag{22}$$

$$r_a = \left(\frac{r_e P}{K}\right)^{1/3} \tag{23}$$

$$r_b = 0 \tag{24}$$

$$\delta = \frac{r_a^{\,2}}{r_e} \tag{25}$$

where r_a is the contact radius after deformation, P is the load applied normal to the contact plane, r_b is the contact radius when the normal load is zero and δ is the one-dimensional deformation of the system [13, 135, 175]. Those listed above that are geometrical in nature are labelled in Figure 2-4. K can be calculated if the Young's modulus, Y, and Poisson's ratio, υ, are known for both body materials [13]:

$$K = \frac{4}{3}\left(\frac{1-\upsilon_P^2}{Y_P} + \frac{1-\upsilon_P^2}{Y_S}\right)^{-1}. \tag{26}$$

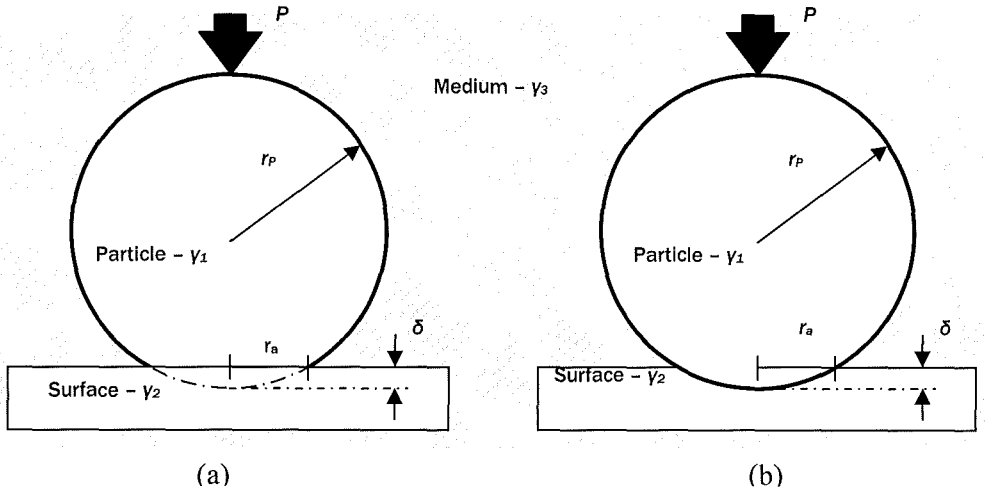

Figure 2-4: Schematic depiction of the mechanism of the effect of an applied load, *P*, normal to the surface with (a) rigid particle and elastic surface and (b) rigid surface and elastic particle. Note the allocation of surface free energy, *γ*, values to each item in the system.

Hertzian mechanics are only applicable to systems with very low surface forces along with high loads applied to the particle. These have been found to accurately describe the contact area between elastic bodies that are not experiencing adhesion forces [182]. Most real systems involve surface forces; many experimental and theoretical results have shown that the surface-to-bulk ratio becomes significant at small ratios [183] and the contact area of the bodies is much larger than estimated using the Hertz model, especially when the load P diminishes to zero [158, 182, 183]. For predictions of real systems a more advanced approach is needed [135, 175]. To include more realistic parameters is not straight forward, as interaction force depends on the intermolecular separation of the two bodies, which in turn depends upon the interaction force. Obviously the difficulty in predicting the outcome occurs because the parameters are not mutually exclusive of each other. To decouple the force-surface profile dependency either DMT or JKR models can be selected for use, each with their

own differing assumptions [13].

2.7.2 *Derjaguin, Muller and Toporov model*

This interpretation builds upon the Hertz model by taking surface forces into account [175]. This model accounts for surface forces in both the particle and the surface but maintains the Hertz models limitation of only allowing a the scenario shown in Figure 2-4(a), where the particle is elastic and the surface rigid. It maintains many of the assumptions dictated by the Hertzian model, consequently relationships are similarly simple. It adds to the Hertz model by assuming that the profile does not change because of the presence of attractive forces outside the contact zone. The contact area is calculated by adding the Bradley adhesion force

$$F_{adhesion} = 2\pi W_A r_e \tag{27}$$

to the Hertz contact relationships given in Equations (22) – (25) [13, 135, 175]. Thus a significantly more complex description of r_a and r_b is generated, now including consideration of W_A, and the added normal load this will bring about.

$$r_a = \left\{ \frac{r_e}{K} (P + 2\pi r_e W_A) \right\}^{1/3} \tag{28}$$

$$r_b = \left\{ \frac{r_e}{K} (2\pi r_e W_A) \right\}^{1/3} \tag{29}$$

The DMT model is best applied to systems with small particle radii, low surface forces and where both bodies are rigid. The DMT model may underestimate the true contact area of a system because of its Hertzian constraints (see Figure 2-4(a)). Even so, for small, hard particles on hard surfaces, the model has been found to be the most accurate [184].

So far, only small deformations for regular or simple geometries have been discussed, but nothing of the inevitable deformation of the multitude of the asperities that make up any real surface. Now both surface roughness and deformation science will be combined. Tormoen and Drelich [185], describe the use of the deformation term, δ, as calculated for both DMT and JKR deformation models as a tool along with asperity size description tools explain the combined effect of deformation of a rough surface. The surface asperities of soft materials will deform when in contact with another body. In the case of an adhesion contact area, the deformation is sometimes sufficient to result in uninterrupted contact between the two bodies. The maximum height of deformation achievable for a particular system when using DMT theory is identical to that given in the Hertzian regime, as its constituent components are the parameters modified by inclusion of the Bradley adhesion force. This means that any asperities smaller than δ are totally deformed to form a uniform contact between the two bodies, and result in no reduction in the van der Waals interaction. Any asperities larger than this value are reducing the contact area between the two bodies and affecting the total adhesion force achieved. This model only applies for an elastic system, where the material deforms in a predictable and repeatable fashion, as is the Hertzian case illustrated in Figure 2-4(a).

When the force applied to a visco-elastic material is great enough to cause permanent plastic flow, which for small particles has been found to be a common occurrence [136, 142], rather than temporary elastic deformation a different approach is required. Maugis and Pollock [186] developed a system to describe both an elasto-plastic model for when there is plastic deformation around the peripheral zone of contact, and begins much earlier than further elastic deformation, along with a fully plastic mode of deformation for an individual body with material yield strength and the body has a known radius. Further to this, Tormoen and Drelich [185] have developed a model to predict the maximum size of asperity that can be totally deformed to leave uninterrupted contact patch. This model is correct in all instances, as plastic deformation is not taken into account by either DMT or JKR, and is effectively a 'bolt-on' addition.

The loading an unloading of systems is assumed to be a smooth process with no adhesion hysteresis effects for both the Hertz and DMT models. This is not realistic, since most systems involve elastic response [175]. This has led to the development of more complex models.

2.7.3 *Johnson, Kendal and Roberts model*

This prediction method is currently one of the leading models. Like the DMT model, JKR is based on Hertz theory, this model distinguishes itself by assuming that attractive forces act only within the contact area and involves 'zero range forces'. The JKR model extends on the capabilities of the Hertz and DMT models by being able to consider the scenario described in Figure 2-4(b), which is an important distinction. To do this, JKR requires that the external load, P, as used in the Hertz and DMT models, is substituted by an apparent load, P_1, [13, 187]. P_1 is related to P, but includes consideration of the three dimensional work of adhesion over r_e [136]

$$P_1 = P + 3\pi r_e W_A + \sqrt{6\pi r_e W_A P + (3\pi r_e W_A)^2} \tag{30}$$

In contrast to Hertz and DMT theory, JKR applies a more abrupt loading and unloading process and considers adhesion hysteresis. The greater detail that this model takes into account causes greater model relationship complexity [135, 175]. It must be noted that the JKR model is believed to underestimate the contact area and therefore must also underestimate the total adhesion force that is resultant [133].

$$r_a = \frac{r_e P_1}{K} \tag{31}$$

$$F_{adhesion} = \frac{3}{2}\pi r_e W_A \tag{32}$$

$$r_b = \left\{\frac{r_e}{K}(6\pi r_e W_A)\right\}^{1/3} \tag{33}$$

Hysteresis has been experimentally found to be a significant factor in adhesion and is postulated to occur due to 'necking' between the particle and surface when the two are pulled apart as described in Figure 2-5 [174]. The neck has been found to emanate from the deformation of the

surface rather than the particle theoretically by Tabor [188], assuming linear elastic deformation across the contact patch and negligible interfacial forces outside the contact region. Experimentally this theoretical proposal was supported by Rimai *et al* [136] and DeMejo *et al* [189] who found that Tabor's predictions was one order of magnitude too small due to limitations in the assumptions made. This neck joins the two bodies together until the neck is ruptured abruptly at high negative loads. Separation occurs when the contact area radius, r_c, area falls to a value that is a multiple of 0.63 of r_a.

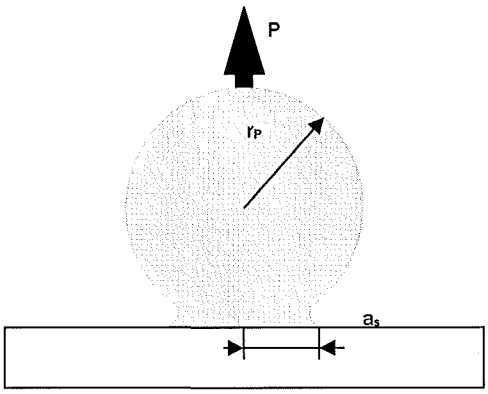

Figure 2-5: Schematic diagram of the development of a 'neck' around the contact area between particle and surface; necking is the source of adhesion hysteresis and requires large negative force P to overcome.

JKR theory is best suited for deformation prediction of systems with high surface energies, large particle radii and compliant materials [175]. The major limitation of this model is that it always predicts an infinite stress at the edge of the contact area, since it only accounts for forces within the contact region the stress at the edge must be infinite to balance the model.

2.7.4 *Maugis - Dugdale model*

Initially Maugis set about developing a tool with which a user could choose a suitable contact mechanics model [136, 141]. A dimensionless parameter, λ, is used to determine which competing model was appropriate for a particular system. This theory is said to be the most versatile description since it does not assume any limit to material properties, instead the material properties important to adhesion are summarized *via* the dimensionless parameter λ, that is defined by the relationship

$$\lambda = \frac{2.06}{z_0}\left(\frac{r_e W_A^{\ 2}}{\pi K^2}\right)^{1/3} \tag{34}$$

Where z_0 is the separation distance calculated using the Lenard - Jones potential [190]; Maugis [141] used the Dugdale approximation (MD) where the adhesion stress has a constant value of theoretical stress, σ_0, until a separation $z_0 = w/\sigma_0$, as illustrated in Figure 2-6, which is reached at radius r_{MAX}. A large λ value characterizes large radii particles along with highly elastic materials and those with high surface energies. Small values of λ represent small radii particles that are rigid and have low surface energies. λ has a range of $0 \rightarrow 1$, for each extremity:

$\lambda \rightarrow 0$, use DMT

$\lambda \rightarrow 1$, use JKR.

However, this leaves a problematic transition area where neither DMT nor JKR are satisfactory. After a great deal of debate in literature, numerical calculations based upon the Lennard-Jones potential showed that DMT and JKR are both good at predicting results for differing conditions, each set conditions lie at opposing ends of a spectrum of a non-dimensional parameter, Θ, [13, 175, 191].

$\Theta \leq 0.1$, use DMT

$\Theta \geq 5$, use JKR.

This model is accurate for adhesion in the presence of a liquid meniscus, assuming a constant pressure within that meniscus.

The MD model is complex and difficult to implement and use to provide predictions that correlate with experimental data. This issue has been addressed in the form of the Carpick Ogletree Salmeron (COS) generalization of the MD model which closely approximates the MD solution and fits experimental data for contact area friction [192]. The Tabor parameter can then be obtained from the fitting parameter, ξ, which can be related to λ by approximation using [188]

$$\lambda = -0.924 \times \ln(1 - 1.02\xi) \tag{35}$$

When $\xi = 0$ corresponds exactly to the DMT case and $\xi = 1$ to the JKR. For intermediate cases ($0 < \xi < 1$), the generalized transition equation corresponds very closely to Maugis' solution for the transition regime.

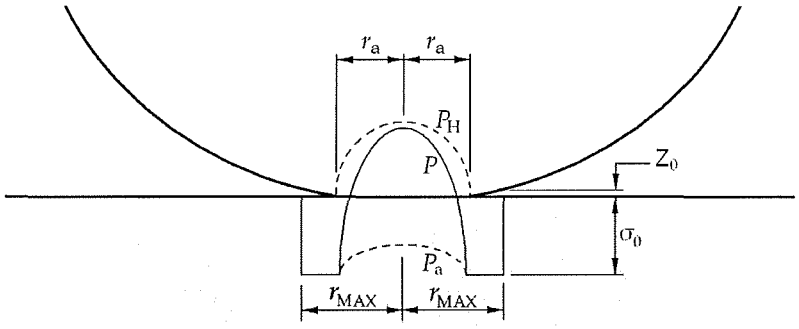

Figure 2-6: Schematic diagram of the Maugis-Dugdale stress distribution is a sum of two terms: The Hertz pressure, P_H, acting on the area with radius, a, and adhesion tension, P_a, acting on the area confined by the maximum radius, r_{MAX}.

2.7.5 *Summary of surface deformation modelling*

There are a wide variety of contact mechanics models, here those that appear most accepted and successful have been cherry picked as a basis to further research. It is generally accepted [13] that each of these differing models, including that developed most recently by Carpick *et al*[192], are best used for differing system parameters. To aide the ease of prediction for a particular system, Johnson and Greenward [193] went as far as to compile an 'adhesion map'. Shi *et al* [135] have compiled a table of some of the contact mechanics models listed in this review. This table lists the assumptions and limitations of these models, The model raised by Carpick *et al* has been added in Table 2-3, but has the same assumptions as those of the MD model.

The Hertz model considers purely the adhesive force of two particles in pure repulsion without any surface energies or external forces. Later models develop on this regime. DMT model is most appropriate for a system where both bodies are rigid, small and have low surface energies; importantly DMT only considers the particle to be deformable, the surface is assumed utterly rigid. The JKR model is best suited to large particles with a low modulus of elasticity and high surface energies and considers deformation of both materials [135, 179]. The MD model was initially developed as a tool to choose the most appropriate of DMT or JKR to use for a system, but developed into a more complete contact mechanics model that dealt with the transition range where DMT and JKR are not useful; however it is difficult to use due to its requirement for simultaneous equation solutions and iterative calculation. The COS method is an approximation of the MD model removing the need for simultaneous solution and iterative calculation [137].

Table 2-3: Comparison of contact mechanics models.

Theory	Assumptions	Limitations
Hertz	No surface forces Elastic particle, rigid surface	Not valid for low loads if surface forces are present
DMT	Long-ranged surface forces act only outside contact area Elastic particle. Rigid surface	May underestimate contact area due to restricted geometry Applies to low λ systems only
JKR	Short-ranged surface forces act only inside contact area Rigid particle, elastic surface Contact geometry can deform	May underestimate loading due to surface forces Applies to high λ systems only
MD	Periphery of contact patch modelled as a crack that fails at a given load	Analytical solution but parametric equations Applies to all values of λ Does not tend to give good correlation with experimental results.
COS	See MD	Better correlation to experimental results than MD.

2.8 Particle Impact Theory

One of the most influential factors in the interaction between a particle and a substrate is the particle's initial approach and subsequent impact with the substrate. The initial velocity of a particle before its trajectory is affected by long range adhesion forces and the subsequent acceleration generated by the long range adhesion forces along with the particles mass govern the kinetic energy stored by the particle during impact with the substrate. This kinetic energy can result in a rebound from the substrate if sufficiently large and the substrates deformation properties are conducive to such an event. This Section explores the variables critical to this initial debris event.

2.8.1 *Initial velocity, kinetic energy and critical impact velocity*

Particle impact is commonly represented and solved *via* the use of energy balances between a spherical particle and a planar surface of infinite size [134]. The mass, but more importantly initial velocity of the particle towards the surface imparts a kinetic energy upon the particle, Q_I. This initial energy is then added to in the form of further velocity as the particle accelerates towards the surface under the influence of attractive forces, Q_A. Thus the total energy involved at impact can be summed as $Q_I + Q_A$. During impact this sum of energy is transferred from kinetic movement into a

mixture of elastic energy, Q_{el} and dissipated energy loss, Q_L. This interaction represents a simple energy balance, that is dependant upon the impact velocity of the particle and the material properties of the bodies involved.

After impact the proportion of energy remaining stored as elastic energy is converted back to kinetic energy. If this converted remaining energy is greater than the energy of the short range attractive forces, Q_A', the particle will rebound. However if Q_{el} is smaller than Q_A', the particle will remain adhered to the surface. Thus a critical rebound velocity, v_C, can be defined at the point $Q_A' = Q_{el}$. Impact velocities greater than v_C will result in a rebounding particle. If there is plastic deformation involved in the impact, the yield strength of the material is also vital to the critical velocity for plastic deformation, v_{CP} [133]

$$v_{CP} = \left(\frac{2}{m}[Q_{el} - Q_A']\right)^{1/2} \tag{36}$$

where m is the mass of the particle involved in the collision.

Energy losses for non plastic deformation impacts can be assumed to lose energy only through elastic wave propagation [134]. Any impact between a sphere and a flat surface will involve only elastic deformation as long as the maximum pressure between the interacting bodies never exceeds the elastic yield point of the softest body. For a sphere with density ρ_p impacting a smooth surface, it can be shown that the elastic yield point is only achieved by impact velocities greater than a threshold velocity, v_{el}, [194].

$$v_{el} = \left(\frac{2\pi}{3K}\right)^2 \left(\frac{2}{5\rho_P}\right)^{1/2} Y^{5/2} \tag{37}$$

If the velocity of the particle before it is accelerated by the long range adhesion forces is known, the final impact velocity, after acceleration due to long rage attraction forces can be defined using a Pythagorean relationship between the initial velocity and the attraction force tempered by the initial distance of separation. Using a simple substitution, it can be said that the impact will be purely elastic if initial velocity remains beneath a system dependant threshold velocity. Given the prediction of such yield velocities, the energy loss due to elastic wave propagation can be calculated if the impact velocity, v_{impact}, density, ρ_S, and Young's modulus, Y_S, of the surface being collided with are known [195]:

$$Q_A' = \frac{p(p_1^{2/3} + 2p(p_1^{-1/3})}{3K^{2/3}R_C^{1/3}} + \pi W_A\left(\frac{R_C p_1}{K}\right)^{2/3} \tag{38}$$

2.8.2 *Plastic-elastic behaviour*

Plastic elastic deformation is more complex as the energy lost is caused by pure plastic deformation, Q_P, in some areas and the propagation of elastic waves in other areas that deform with pure elasticity and plastic deformation, Q_W. This relationship can then be used in the initial definition of the impact energy balance to create a more general description of a particle impacting a surface.

Doing this allows calculation of the total deformation energy, Q_E, of the system, which can be defined as the sum of the elastic deformation energy stored in elastic regions of the material, Q_{elE}, and the elastic energy stored in the plastic region of the material, Q_{elP} [196]. In turn, these parameters have been shown to be equivalent to pure kinetic energy in the case of Q_{elE} and a more complex relation defined by the multiple of Q_e and Q_p in the entire system for Q_{elP}.

The energy lost due to the propagation of elastic waves away from the impact zone in a plastic-elastic impact has been evaluated by Reed [134]. Summation of the interactions listed above and interpolation with respect to the action of kinetic energy leads Reed to define that:

$$\frac{1}{2}mv^2 + Q_A Q_K = Q_e + Q_{pe} v_{impact} + \frac{4Q_{pe} v_{impact}^{\ 2}}{15Q_e} + 0.05291\Lambda v_{el}^{\ 3/5} \frac{m}{2}\left(v^2 + \frac{2Q_A}{m}\right)\frac{I(v_{loss})}{v_{loss}^{\ 2}} \tag{39}$$

2.8.3 *Calculating adhesion energy*

Adhesion energy, Q_A', that combats particle rebound is a short range interaction. The long range attractive energy, Q_A, acts to attract particles to towards a surface. These are the last two parameters in the impact models to be defined and are uniquely linked, as their relative magnitudes define the propensity for a particle to rebound from a surface after collision. Q_A is simply the kinetic energy added by the acceleration due to long range attractive forces and can be defined to be one eighth of the square of the total force of adhesion over the fourth power of attraction time:

$$Q_A = \frac{1}{8} F_{adhesion}^{\ 2} t^4 \tag{40}$$

The short range adhesion energy is rather more complex, and is the sum of the mechanical energy, given as the first component of Equation (41) and the surface energy, given as the second component in Equation (41). The mechanical energy is a material property based parameter and the surface energy is dominated by the work of adhesion. The local radii of curvature of the two surfaces in contact are important for Q_A', these are taken into account by use of an interpolation between the two [134]:

$$Q_A' = \frac{p(p_1^{\ 2/3} + 2p(p_1^{-1/3})}{3K^{2/3}R_C^{1/3}} + \pi W_A\left(\frac{R_C p_1}{K}\right)^{2/3} \tag{41}$$

2.9 Capillary Forces

A liquid film can be formed due to immersion and subsequent removal from a liquid or due to high humidity conditions surrounding particle - surface system by capillary condensation or capillary action between the particle and the surface [23, 186, 197]; this occurs when an annulus of capillary

condensate forms around the base of the particle where the contact angle is highly acute [198, 199]. The resulting capillary force can make a large contribution to the total force of adhesion, or even exceed the contribution of other adhesion interactions such as van der Waals and electrostatic unless the surface is hydrophobic [176].

2.9.1 *Conditions conducive to capillary adhesion*

It must be noted that capillary condensation adhesion can only be generated in a primarily gaseous, highly humid system environment, but is known to remain after baking of the surface and particle above the liquid boiling point for many hours [16, 200]. These forces can also lead to chemical bonds being formed between particles and surfaces with some materials. Silicone particles adhered to a silicone surface have been shown to oxidize and become physically linked through the oxide produced [22]; however, this bonding is not generally active at room temperature [16]. In total submersion of a liquid medium, the boundary layer between the meniscus and the medium is too weak to apply a significant adhesion force to the particle [176, 2 01]. It must also be noted that the generation of capillary adhesion force at zero humidity is negligible [178, 201] and does not have a great deal of participation in adhesion until a critical humidity is achieved [176], which varies depending upon the materials involved but as an example has been found to be approximately 60% RH for a system of glass particle on a flat glass surface [199, 201]. Once above this threshold RH value, adhesion force on small particles is generally expected to increase by a factor of between 5 and 7 [40, 201]; however, it must be noted that the increase is generally to expected to become less prominent for smoother surfaces due to lower numbers of large asperities [40]. Once above the threshold RH, for spherically shaped particles on flat surfaces, it is believed that further increase in RH has no further effect on the adhesion interaction between the two bodies [37].

2.9.2 *The mechanism of capillary adhesion*

The reason for capillary adhesion occurring after passing this threshold value is the capillary force acting due to the liquid meniscus formed near the contact area. The pressure difference across the curved meniscus creates an attractive force, bonding the two bodies [201]. The liquid film is in a state of tension, thus the pressure inside the meniscus is lower than that of the gaseous atmosphere surrounding the system. The total force can be split into the low pressure capillary force and the interfacial tension force originating from the meniscus' surface tension acting upon the two bodies tangentially to the point of meniscus contact with each body [176, 202], this combined interaction is illustrated in Figure 2-7. At low RH values, a capillary interaction does exist; however, it is not sufficiently substantial enough to significantly affect the total adhesion force at close range. Yet it has been found to affect the long range interaction between two bodies [201] as it produces an attachment between the two bodies out to significant separation distances. A simple approximation can be used to describe force due to capillary adhesion, F_{CAP}, between a spherical particle and a flat surface. F_{CAP} can be simply defined as the sum of the adhesion force generated by the force due to the pressure difference between the meniscus and the atmosphere, $F_{\Delta P}$, and the force due to the meniscus surface tension, F_T. $F_{\Delta P}$ is the result of the Laplace

pressure due to the meniscus (which can be found by using the Laplace - Young equation [203]) over the area of flat surface coated by condensed liquid [176]. The Laplace - Young equation defines the Laplace pressure by relating the liquid surface tension to the Kelvin radius and the radii of curvature measured in two planes that are 90° opposed to each other. The force due to surface tension, F_T, for a smooth, spherical particle resting on a smooth, flat surface of exactly the same material is given by the multiple of the particle r_e and the surface tension, T, of the liquid surrounding the particle and 4π [16].

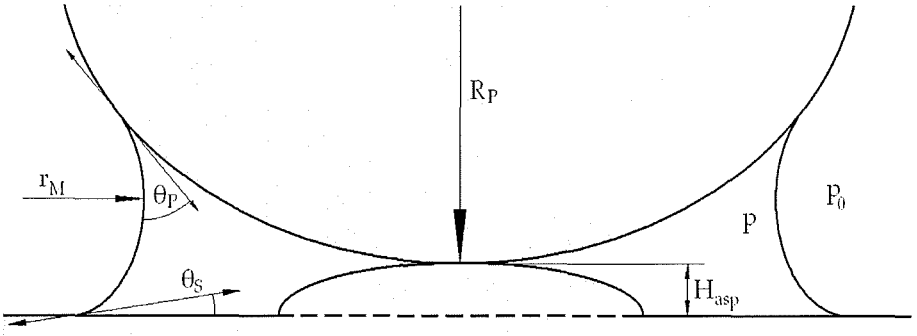

Figure 2-7: Schematic representation of a capillary interaction between two bodies. Note the inclusion of the asperity for use with Equation (42) [202, 204].

2.9.3 *Calculating the force generated by capillary condensation*

The simple model described above can be extended to make predictions for the more complex case of a smooth spherical particle and a flat substrate with nano-scale roughness as depicted by the asperity in Figure 2-7. This is a key development as surface roughness is widely believed to be critical in meniscus development [40]. Marmer originally developed a highly complex and unwieldy expression to describe such a scenario [204] which has since been simplified by de Lazzer *et al* [202].

$$F_{(\vartheta)} = 4\pi\vartheta r_e \cos\theta\left(1 - \frac{H_{asp}}{2r_M \cos\theta}\right) \tag{42}$$

where ϑ is the liquid surface tension, $\cos\theta = (\cos\theta_P + \cos\theta_S)/2$. It should be noted that this model only applies when the meniscus is large enough to span the distance between the adhering particle and the average surface plane, i.e. $H_{asp} < 2r\cos\theta$, and when the radius of the meniscus is small compared to that of the adhering particle.

Although this was derived for rough surfaces, it can also be used to describe the capillary adhesion of a smooth particle and a smooth substrate separated by a defined distance [205]. However, in this case the radius of the meniscus is fixed because the effective radius is determined solely by the relative humidity (RH) through Kelvin's equation. It is clear that Marmer's and de Lazzer *et al's* model is markedly superior to the initial relationship discussed in this review as this initial step includes no dependency upon RH, which has been shown to be a key factor in practice [40, 201 - 204, 206].

A more general equation has been developed for the case where the materials of the particle and the substrate are not identical. When the Laplace pressure acts upon a known meniscus contact area, Leite *et al* predict that the capillary adhesion force is defined by the meniscus tension including the angle of meniscus contact with the particle and the surface.

$$F_{CAP} = 2\pi r_P \vartheta(\cos\theta_1 + \cos\theta_2) \tag{43}$$

This solution, much like the more simple solution discussed earlier does not explain the force transition experimentally observed in several papers as a function of the relative humidity.

Capillary forces are known to be dependent upon contact time; capillary condensation which occurs after contact can add to any liquid already present in surface layers to increase the adhesion force [207]. Particle adhesion forces can be lowered by immersion in liquids; however if the particles are not removed by the liquid, the added capillary forces generated by the evaporation of cleaning fluid post immersion can increase the total adhesion force [16]. Experiments have also shown that the force required to begin separation of two bodies is the maximum force required to break the meniscus link, and the force required drops with increased separation, also increased removal force will result in increased separation velocity due to the liquid viscosity [199].

2.9.4 *Capillary induced particle repulsion*

To complicate the liquid immersion and capillary adhesion subject, the addition of a liquid to a system is known to induce large repulsive forces in the form of electrostatic double layer repulsion for certain pairings of materials [13]. This is a chemical related issue and brings into play PH interactions. It is plausible that capillary condensation could generate a meniscus of liquid that is conducive to powerful electrostatic repulsion, which counteracts the effects of not only the capillary interaction, but all others too. Ironically, for some materials capillary condensation of a specific medium could be beneficial to particle removal. This effect can be calculated simply by relating the change in energy release rate to the change in separation distance, but is highly complex [37].

2.10 Bridging Nano-bubbles

For AFM adhesion experiments conducted over hydrophobic surfaces; that is, those that cause water droplets to lie upon them with a high meniscus contact angle, adhesion force has often been considerably higher before contact occurs than traditional long range adhesion forces could predict. Curiously, that this force often increases in large steps, rather than in a linear climb. Parker *et al* [208] has proposed that the cause of this additional attraction were sub-microscopic bubbles present on the hydrophobic surfaces becoming attracted to the tip of the AFM cantilever and 'bridging' the two; thus the sudden increase in attraction generated by the bubble's surface tension with every new bubble to bridge the gap. It was then suggested that these bubbles then spread along the two surfaces, becoming shorter and fatter, dragging the particle towards the surface. This new theory was in good correlation with experimental data, since it did not require any new adhesion parameter to be conjured for its sake, it was just an extension of capillary theory. Plus, the fact that the varying heights of the bubbles which are governed by the local surface properties of the hydrophobic material mean that bubbles bridge the

gap consecutively rather than simultaneously; thus matching the nature of the stepped response of experimental measurements [209].

Further proof that these nano-bubbles exist is generated by following experiments involving purified, de-gassed media. The use of these caused the expected reduction in the range of attractive force, as there were less nano-bubbles lying on the hydrophobic surface and a restriction to their size as the source of the gas available for their formation was minimized [210, 211]. Wood and Sharma [211] showed that the force was also of shorter range for surfaces that had never been introduced to a gaseous material; that is ultra high vacuum (UHV) class materials. This suggests that these nano-bubbles become attached to defects on the surfaces when they pass through the atmosphere - liquid interface [209].

Using a colloid sphere attached to an AFM cantilever, the attraction force generated by a single nano-bubble has been obtained, and from this significant theory work undertaken to predict the interaction force generated by this phenomenon. However this is highly complex and still in its infancy, and is the source of many thesis' itself and beyond the scope of this review. For more detailed information consult the works of Attard [209] and Carambassis *et al* [212].

2.11 Chemistry and Adhesion

2.11.1 Effects of PH

It is well established that changing the PH of a surrounding liquid or gaseous medium has a significant effect on the overall adhesion force acting between two bodies [213, 214]. General consensus agrees that high PH media result in a reduction of total adhesion force and it is accepted that PH has no effect on van der Waals interactions [213 - 216]. Instead the key to this variance is suspected to be alteration of electrostatic double layer forces [213, 214]; however, these are not the only factors [213].

Christendat *et al* [213] discuss the cause of PH related variation of electrostatic forces acting outside the contact area between two bodies. The system can be best understood by examining the complex chemical compositions for the surfaces in the system. The chemical composition is critical for the nature of the electrostatic interaction; in this case an Amine surface and a silicon example are focused upon. For Amine surfaces, the usual pK_a value is in the range of 7 to 8 [217]. For a hydrophilized silicone wafer in water a pK_a of only 2 to 3 [213] can be expected. Hydrolyzed silicone become silanol groups, obtaining a pK_a of approximately 6 [213]. As a result, silica wafer surfaces display zwitterionic due to significant changes of electrostatic interactions caused by shifts of the acid-base equilibrium of different types of surface groups [218]. It is known, however, that the actual pK_a values for chemical groups on surfaces are usually lower than the values of the same groups in solution, this difficulty being attributed to the difficulty of forming a charged state for the ionisable groups on surfaces due to the influence of neighbouring charged sites [219]. Considering the pK_a values and adhesion force, amine surfaces can be assumed to exhibit strong positive charges in the PH range from 3 to 6, then becoming mostly neutral in a solution with PH between 8 and 10. The silica surface is quite different, due to its zwiterionic behaviour, it is predominantly negatively charged in a solution with PH between 3 and 6, increasing until becoming fully negative in solutions of between 8

and 10. So it is apparent that alteration to the PH of the medium will affect the surface charges, and thus the electrostatic double layer interactions of many surfaces useful in industry, especially that of the microelectronics sector. To compound this chemical complexity, local material variations in the particle surfaces and local PH fluctuations can cause non linearity in the force generated across an area [213].

In the case of the system of silica and amine bodies discussed above, studied by Christendat *et al* [213], low PH causes a reduction in the electrostatic double layer repulsion interaction, resulting in smaller compensation for strong F_{vdW} and so the resulting total adhesion force is larger. Jacquot and Takadoum [220] found that using water as a medium appeared to increase the total adhesion force between silica particles and surfaces and accredited this occurrence to a similar mechanism. As the PH increases the electrostatic double layer interaction is re-established and adhesion force decreases. For some interactions with a small contact area due to geometry, orientation or material hardness, submersion in high PH media can result in the electrostatic double layer force being greater than the adhesion forces it opposes, and therefore the particle is repelled from the surface, this is a general trend in adhesion force response to PH change shared by many sources of literature, including Attard's work [209].

2.11.2 *Covalent bonding*

Covalent bonding provides a more permanent relationship between a particle and a surface. Instead of contact forces such as F_{vdW} or electrostatic, where the particle and substrate remain separate entities that will revert to an original, individual form when separated, covalent bonding forms a physical, chemical link between the two bodies. For hydrophilic materials covalent bonds are a major cause of adhesion [213].

2.11.3 *Ionic Binding*

For hydrophilic materials, the effects of hydrogen bonding can counteract expected high repulsion forces caused by electrostatic double layer repulsion as discussed previously. In highly acidic solutions, the medium causes the surfaces of both bodies to maintain the same polarity, causing strong electrostatic repulsion, however Christendat *et al* [213], noted that for systems involving two hydrophilic materials the pull off force remained high. The explanation is thought to be hydrogen bonding occurring between the two bodies, chemically tying them together. Although the negative charges of the two bodies causes electrostatic repulsion between them, it also causes attraction to positive ions of the hydrogen atoms in the solution, which bond with first one surface, then the other when another of its ions becomes sufficiently attracted to it, hence a physical, atomic link is formed. This theory is supported by further experimentation by the same author, where the addition of $CaCl_2$ to the solution to decrease the PH, the calcium has a positive charge and is thought to have lowered the specific negative charge on the surfaces of both bodies and therefore the potential for hydrogen bonding to occur, and the adhesion disappeared. Not only this, but prevention of 'ionic binding' between surfaces as it has become termed means that the medium solution can penetrate the interface between the

bodies, separated by the electrostatic double layer force, uninterrupted; thus the contact patch that is so important to van der Waals interactions is reduced, further reducing the total adhesion force.

It appears that the scenario is not a simple one, just because two bodies are in a high PH solution does not mean that there is guaranteed to be lowered total adhesion, the chemistry of the surfaces is also significant. It is worth noting that wherever there is potential for hydrogen bonding, strong adhesion is likely to be experienced.

2.11.4 Temperature dependence

It has been remarked upon by several authors that increased temperature could result in increased adhesion. Rimai *et al* [136] note that deformation increases with temperature due to softening of the materials involved. Most plastics are in a rubbery state at room temperature, having glass transition temperatures, T_g, in the low Kelvin's (T_g < 200K). Christendat *et al* [213] briefly point out that increased temperature results in fast chemical bonding due to thermal excitation of atoms, thus again increased temperature leads directly to increased chemical bonding between two bodies. Temperature may also be important in the development of meniscus in capillary adhesion, but no literature exists that explored this avenue.

2.12 Friction Generated by Adhesion

Particles can be removed in more than one way. So far in this review, the only method that has been explored is direct, perpendicular removal of the particle from a surface; however, if a fluid drag system were used for removal, this upward force would not be accurate, instead a transverse force across the surface would be the prominent means of removal, thus friction and rolling of particles and parameters that effect his process become key.

First, it is wise to consider nano-friction in the same way that friction is modelled at a larger scale *via* use of Amonton's law, as done by Attard [209]. Here the coefficient of friction, a surface parameter, and the load forcing the particle onto the surface generate the friction force. For adhesion, a negative load is required to separate the two bodies, it is known that the friction is high when the separation load, F', is zero. Thus for nano-scale interactions Amonton's law may be slightly modified:

$$F_f = \mu\left(F_{adhesion} + F'\right) \tag{44}$$

where $F' > 0$ is the adhesion, i.e., the absolute force required to pull the two bodies apart. This modification to the relationship reflects the assumption that friction only occurs when the two bodies are in contact. Using contact mode AFM Attard experimentally measured friction as a function of the applied load at various PH levels [209]. It was shown that friction is proportional to load, a predictable result, given the assumptions made by Amanton's law. This implies that reducing the PH of a surrounding medium will increase the adhesion, and therefore the friction. This is important for fluid drag removal mechanisms. Also, in repulsive interactions, where the particle is being pushed away from the surface by electrostatic double layer interactions, Attard found that friction is negligible, but for any level of adhesive contact, friction is non-zero. Attard concludes from this that

friction is a function of the local separation of two interacting bodies and is independent of the force law. Friction occurs between two bodies when energy can be transferred from one to another, thus the two bodies have to be close enough together for this interaction between atoms to be comparable in size to the thermal energy. This is the role of adhesion in friction; to bring them close enough together for atomic interaction.

The general consensus of previous experiments in this area is that the friction force between two solid bodies in nano-contact with each other is proportional to the true contact area. This has been demonstrated by experimentally measuring both the friction force between the two bodies and the if the interfacial shear strength of an interaction is known; the interfacial shear strength represents the friction force per unit area of a pair of materials, one can also consider it to correspond to the intrinsic frictional dissipation per interfacial atom. The interfacial shear strength is not necessarily a constant, and can more generally be described as a constant along with a pressure dependent term [137]. It must be noted that this relationship is environment sensitive, i.e. variation in temperature and chemical composition of the medium and body materials will directly affect the friction between two bodies.

Finally, in this Section it has been noted by Feiler *et al* [40] that friction between a particle and a surface is inversely proportional to RH. This is an interesting observation, as high RH normally causes an increase in adhesion force. One would expect that the friction force would increase accordingly, but, this is not the case and so some new mechanism must be at work. Importantly, the reduction in friction is not as drastic as the corresponding increase in adhesion in the same experiments. This reduction in friction is attributed to lubrication between the bodies by the accumulated film between the two.

2.13 Contact Time

It is commonly accepted that contact time and adhesion force are proportional to one and other. Many of the constituent adhesive forces covered in this review are time dependent. Surface deformation, capillary interaction, chemical bonding and adhesion friction are all related to mechanical parameters, such as viscosity or stress, and are therefore operational in the time dimension.

Capillary adhesion is dependent upon the size of the meniscus generated, which forms over a period of time [201]. The meniscus formed can then operate as a medium for transfer of ions in a chemical reaction to create a physical bond or increasing strength with time [221]. Surface deformation is not an instantaneous process, as infinite acceleration is not a real possibility; the surface deforms in from zero to an asymptote point of equilibrium with the material hardness of the materials involved over a period time [175]. Time is also crucial for the removal mechanisms commonly applied such as fluid drag removal or surface acceleration, whilst it is also integral in friction interactions [137].

2.14 The Effect of Geometry in Adhesion

In much the same way that surface roughness and deformation effects can affect the total adhesion of bodies to one another, the initial geometry of a particle and surface can have a huge effect on the adhesion interaction of a system. This is as a direct consequence of the contact area dependence of

available volume to compress through deformation. This is recognized by Méndez-Vilas *et al* [222] who explore various situations relating to geometry. If the particle is of an irregular shape, for instance sitting on large asperities, each with small corner radii, the total contact area will be very small. Similarly an ellipsoidal particle lying with its largest radius wall in contact with a dished substrate, a very large contact area is likely; hence adhesion interactions will be large for a particle-substrate system of this nature, this is supported by the work of Vezenov *et al* [13]. This is important, as particle shapes maybe dependent upon machining parameters and therefore aide in prediction of surface interactions.

CHAPTER 3

STATE-OF-THE-ART IN DEBRIS REMOVAL

3.1 An Overview of Debris Removal Practices

First, it is worth noting the conventional cleaning techniques that are not believed to be effective at small particle removal. Bardina [19] lists those that are known to be ineffective: air and gas jets; mechanical abrasion; chemical displacement and emulsion; electrostatic elimination; aqueous; vapour degreasing; strippable adhesive coatings; polishing and buffing; heat treatment; ion bombardment and combustion; and leaching. These methods are deemed ineffective because they are either grossly inefficient, or simply will not remove small particles.

Ghosh and Ryszytiwskyj [223] list a set of particle removal techniques used in industry. Some of these techniques are analogous with the scientific measurement techniques listed in Section 1.2 of this review because often removal techniques have been demonstrated through an attempt to discover the adhesion forces occurring upon particles of varying sizes [149], materials, geometries and whilst immersed in varying media. This is because by the very nature of an adhesion force, when it is exceeded the particle is removed from its resting place. Those techniques listed in Table 3-1 that are not used for measurement of adhesion force shall be explained in this Chapter.

Table 3-1: List of particle removal techniques [223].

Chemical Removal	Mechanical Removal	Thermal Removal	Miscellaneous
Alkaline cleaners	Wiping	Vapour Degreasing	Application of electric field
Acid cleaners	Scrubbing	Bake-out and fire-polishing	Laser debris removal
Hydrofluoric acid	High pressure jet		
Water	Ultrasonic		
Surfactants	Megasonic		
	Centrifugal		

3.2 Chemical Removal Techniques

Non-mechanical contact removal techniques rely mainly upon two central concepts: etching and jetting/spraying, and Bardina [19] has listed four of these. Low pressure surfactant spraying, etching and centrifugal spray cleaning all rely upon chemical removal of the particles. Etching simply dissolves the unwanted particle substances and leaves the substrate material untouched [19, 43]. This is one of the most common techniques used in industry today. This system is useless for the laser micromachining industry as the particles and substrate are very similar in composition. Low pressure surfactant spraying also relies upon a chemical method of removal, using a detergent to reduce the surface tension of water and remove soils through emulsification [19] - its success depending on the effectiveness of the detergent. This means that the detergent must be compatible with both the particle material and the surface; forming a bond with the particle material whilst being repelled from the surface material, again for laser micromachining this system is not suitable. Centrifugal Spray cleaning is a step forward

upon surfactant spraying, as the use of centrifugal force removes contaminated cleaning solution from the surface entirely [146].

Water based cleaning is often conducted using one of two mechanisms; sonication or shear, or a combination of these [224]. Shear simply involves use of water flow over a surface to be cleaned, imparting drag upon particles it passes whilst naturally negating capillary and electrostatic forces and significantly reducing van der Waals interactions. Sonication will be covered later in this Chapter.

One of the greatest problems in the use of chemical surfactants in the modern industrial climate are the restrictions placed on them by the Montreal Protocol Agreements, which have resulted in the complete worldwide banning of chlorofluorocarbons (CFC's) and methyl chloroform (1,1,1, trichloroethane – (TRIC)) due to the devastating effect these had on the ozone layer. Most industrial surfactants were based upon these chemicals [225]. Considerable efforts have since been made to find ozone friendly substitutes for the restricted chemicals, but replicating the cleaning ability of them has been difficult. Perfluorinated liquids are generally seen as the future for ozone friendly surfactants; which are made by replacing carbon bound hydrogen atoms with fluorine atoms in a variety of organic compounds, examples include perfluorooctane (C_8F_{18}), FC-75 and FC-77 Fluorocarbon electronic fluids [7]. It has been found that carboxylic acids can stably suspend a wide range of submicron particles [226].

Skidmore [227] advises of the difficulties generated by submersion and drying of wafers in liquid particle removal media, sighting particle transfer from the liquid surface to the wafer as the liquid is drawn off it (or the wafer is drawn out of the liquid bath). Koppenbrink *et al* extend this by advising that fluids with lower surface tensions are likely to leave behind few droplets. Further to this, evaporation of liquid remaining on the wafer can lead to streaking and spotting of the surface along with particle deposits, especially when using water, which is aggressive towards the wafer surface and can dissolve traces of silicone and silicone dioxide, before leaving residues of the solute material behind when the water evaporates.

Instead Koppenbrink *et al* [228] propose two methods termed as 'chemical or steam drying'. The first drying process consists of immersing a wafer carrying vessel in tanks of DI water and then suspending the wafers above a tank of boiling isopropanol (IPA). The wafers are then extracted from the water and then clear of the IPA vapour, which pulls the water droplets off the surface. The second method is formed of two steps. First any rinsing or cleaning fluid is driven off the wafers and replaced by a non-aqueous drying fluid; second the non-aqueous fluid is evaporated using a pre-dried gas, preferably of an inert nature, such as nitrogen, blown across the wafer a low velocity.

3.3 Mechanical Contact Cleaning

The use of non-contact cleaning becomes ineffective for use on particles of less than 2 μm in diameter, whilst also being inefficient for the range from 2 to 20μm diameter particles [16]. Unfortunately the use of contact cleaning is not suitable for many functions, including modern silicone wafers[7] or optical components for the booming audio-visual industry; this is due to the danger of the cleaning process creating unwanted scratches in the surface of the work-piece being cleaned. All mechanical removal techniques are prone to causing damage to a sample either through excessive repetition of the

process or through excessive use of force or power. The prospective success of mechanical cleaning techniques depends greatly upon the nature of the material being cleaned, typically harder materials fair better, hence polymers which are common in laser micromachining are not best suited to this range of techniques [224].

Some examples of contact cleaning are given by Bardina [19], wiping is a common method of cleaning optical components *via* dragging a solvent saturated lens tissue across the affected surface; it is limited by its inefficiency, Musselman and Yarbrough [229], point out that it takes eight man-hours to clean just one square foot. Along with this slowness, this process would not be easy to mechanize. Particles can be deposited back from the tissue, posing further issues [224].

Brush scrubbing is a mechanical method that has a great deal of contradictory material written about it [44, 230, 231]. Generally it has now fallen out of favour. This process is most effective when camel hair, mohair, nylon or polypropylene fibres are used for the brush, shaped like a cylinder. The brush hair never actually touches the surface due to the hair's hydrophilic nature, instead a thin film of water-based scrubbing solution separates the two [19]. Limitations in this process arise from contamination issues; The brush can become infested with particles removed previously and become a source of re-contamination itself; thus making this an inefficient process [231].

High pressure jet scrubbing is seen as one of the most gentle processes in the mechanical group of techniques [224]. It relies upon shear stress developed at the particle/surface interface generated by the force of a high pressure jet dragging upon the particle. The liquid commonly used is static free DI water, sprayed at high velocity [229], sweeping across the surface at pressures ranging from 100 to 4000 psi [19]. The application of fluid drag on a particle to act as a removing force (such as Air and gas jets), as employed currently by many laser micromachining tools, has been discussed and explored by Zimon [197], who examined the effect of drag produced by both air and water. He derived a function to describe the force required for the detachment of small particles from a surface that simple: the drag force had to be equal to or greater than the friction force based upon Amonton's law. The drag force, F_{drag}, is given by

$$F_{drag} = C_d a_1 \frac{v'^2}{2} (\rho_P - \rho_M) \tag{45}$$

where, C_d is the drag coefficient, v' is the fluid viscosity, a_1 is the cross-sectional area of the particle and ρ_p and ρ_M are the densities of the particle and medium (a fluid) respectively. Zimon goes on to add that for a linear distribution of velocity in the boundary layer of the substrate, Stokes' can yield predictions that have been experimentally ratified.

Air and nitrogen guns are usually effective in removing large particles (>10μm) from the surface, but ineffective in removing smaller particles [149, 163]. This limited scope for particulate removal and control by gas jetting (either by use of positive pressure jetting or vacuum motivated gas evacuation over the feature) is highlighted by the attempted application of such techniques during excimer laser micromachining [2, 131, 132]. These techniques were found only to be capable of modification to the deposition location; the use of low viscosity media jets did not provide sufficient suspension or retention of the debris produced during laser ablation and the action of the long range adhesion forces were large enough to cause deposition of the debris down stream of the ablation

despite the high flow velocities used for the gas jetting were sufficient to require technicians using the system to require ear protection. This equipment evolved from cross flow jetting to a vortex flow in attempts to remove the debris from close proximity to the sample surface and avoid deposition, but all techniques attempted using gas jetting were only successful in producing differing debris deposition patterns on the sample surface [45, 46].

Ultrasonic devices have been used for effective measurement and industrial cleaning of surfaces in liquid media for years [16], however these devices do not operate at their optimum frequency of 20kHz due to noise issues [42, 224]. It is known that the cleaning mechanism; cavitation intensity, depends upon three variables: Rheological properties of the medium, colligative properties of the medium and the amplitude & frequency of the radiating wave [43]. Some critics have claimed ultrasonics useless for small particle removal [229, 230], or that incorrect use can cause damage to the sample being cleaned [229]. Ultrasonic methods have been used in air experimentally; Mullins *et al* [232] reported that 85% of 11.5μm diameter particles were removed from the surface at an acceleration of 16.5m/s^2. This experiment also looked at the use of media other than air, such as water and Freon TF, the results reinforcing the belief that the use of a liquid medium lowers adhesion forces. In this case up to 90% of the same glass particles were removed at only 7.5m/s^2.

Derjaguin *et al* [161], used a vibrational method to produce accelerations of approximately 10^4g, however they continue to explain that through the use of frequencies in the megahertz range, accelerations of approximately 10^6g are possible. Mullins and Renade[30] have also used an ultrasonic horn to study the adhesion forces of micron sized metal flakes to a surface.

Megasonic techniques have also been used by Schwartzman *et al* [233]. This system operating in the frequency range 850kHz to 900kHz. Suspected to produce a high pressure wave as a mechanism for particle removal [231]; this device was shown to be effective at removing 0.3 μm particles using a hydrogen peroxide solution. Water alone did not work as well. Others have also had similar success with this method [229]. Megasonic cleaning is now a common method of industrial cleaning for silicon wafers, only taking 15 minutes to clean a batch of 100 wafers [233]. Megasonic cleaning offers many advantages over ultrasonic cleaning, since it causes very few scratches, breakages or chips, since the substrates being cleaned are not put under mechanical stress. However from the survey of literature for this review, applications that do not use a liquid medium have not been found.

One simple technique employs centripetal force. Another removal technique used experimentally is submersion; the creation of electrical double layer forces between bodies *via* the immersion of a particle - substrate system in a liquid.

Ranade *et al* [149] note that only the use of centrifugal, aerodynamic, hydrodynamic and vibration removal techniques are effective for micron sized particle removal. Visser [234] used a hydrodynamic method to measure the adhesion forces between sub-micron carbon black particles and cellophane surfaces in rotating concentric cylinders. He states that the hydrodynamic force, is proportional to the revolution speed of the cylinders used and the radii of the particles involved. To successfully complete his experiments Visser managed to produce rotational speeds of 8,000rpm.

Hotaling and Dykeman [235] have developed a contamination removal device for the USAF Rome Laboratory involving a gas/solid jet spray, electron and ion guns along with lasers for optical

equipment for the space industry. This system involves laser or jet removal of particles, which is not novel, but crucially the use of a metal mesh supported 'aerojel', which is simply a hydrophilic, organophilic and porous foam like substance that retain the ability to flow and thus requires support from the course wire mesh, described as having "10 pores per inch or varying geometry". The pores of the aerojel are cylindrical in geometry and range in size from nanometres to microns depending upon the density of the particular gel chosen for use. This gel captures particles removed by the jet or laser, whilst having a high absorptivity and retention of particles to prevent it from rapidly becoming a source of debris rather than a removal mechanism. However, this system is designed for use in space, where contact with micro-particles is much less common than for the application intended for this thesis, so its use in micromachining technology as proposed by Hotaling and Dykeman is questionable.

3.4 Miscellaneous Removal Techniques

Degeest [236] recognized the possibility of removing particles from a surface using electric fields. As discussed in Section 2.4 of this report, a high field is desirable for the removal of particles in this method. This means that the system is limited by the dielectric breakdown point of the medium immersing the particle - surface system. The dielectric breakdown of gas is dependent upon the geometry containing the gas, along with the density, atomic and molecular properties of the gas involved. For air at normal temperature and pressure (21°C, 1 atm.) breakdown occurs at 30kV/cm.10 Further to this Cooper *et al* [163] Conducted an experiment to remove particles from a sample using large electric fields (>200 kV/cm) inside a 10^{-6} Torr vacuum environment to avoid electrolytic breakdown issues. They found that using this method all particles 15μm diameter or less were removed within a minute, usually within a second of experiencing the electric field. The values gained from this experiment confirm that adhesion force is inversely proportional to particle size in a zero humidity environment; whilst again confirming the belief that particle/substance material is an important variable, nickel being adhered by more than four times the force of a similar sized glass particle (and therefore needing a larger field to be removed). Although this method could be useful for effective reduction in active adherence forces and cause a more even distribution of particles across the substrate (since the authors found lateral movement of particles away from one another); this method as a means of removal is not suitable for laser micromachining use. It is not viable to machine in such a high vacuum environment. Furthermore, the authors admitted that the removal electrode had to be covered with an insulator to prevent particles from exchanging charge and becoming repelled back to the initial surface. Such materials (acrylic varnish, for instance) are not stable in the high radiation environment of a laser and would out-gas, causing damage to optics. The authors conclude that they expect sub micron diameter particles to require fields of MV/cm^2 magnitude; however with optically satisfactory, affordable and plentiful media for laser machining; this is unlikely to be achievable.

Laser cleaning is a well established means industrial cleaning, most famous for removal of carbon particles from air pollution on stone statues and buildings in highly developed cites. It is a broad and varied sector of technology with a wide range of applications [16]. A well established technique for removing micron scale particles from surfaces using laser radiation is by using short

pulsed high fluence excimer beams in a dry gaseous atmosphere. Typically the particle and substrate materials differ. systems of carbon, silica, ferric oxide, calcium sulphate, magnesium oxide [237], silicone [238] and organic particles [239] on silicone [237, 238], Al-coated silicone [237], quartz, optical mirror [237] and nickel phosphorous surfaces [240]. This research established that these particles could be ejected from a surface using short pulsed laser radiation due to the optical absorption of either the particle or the surface over a short interval and the resulting rapid thermal expansion producing an acceleration great enough to eject the particle from the surface. However, this method has drawbacks: some surface materials can be damaged by the high fluence required for particle ejection; some of the particulates tend to melt or even coalesce instead of being ejected; once ejected the particles have a tendency to resettle on a different part of the surface; and the particle must not be of the same material as the surface to prevent melt fusing or ablation of both.

Another novel removal technique has been postulated and tested by others [241, 242] and involves a similar process of short pulsed excimer laser irradiation, described by the author as "steam laser cleaning." In this technique the laser cleaning process is enhanced by the ablation of a thin film of fluid deposited on the contaminated surface, or the top layer of the contaminated surface itself causing a rapid super heating of the liquid film. This rapid heating of the liquid film causes large transient forces to act upon the particles, which can overcome the adhesion interactions at work. Tam *et al* preferred the mode of heating both the substrate and the liquid film, as this produced very efficient heating of the liquid - substrate interface and explosive evaporation of the film and successful removal of particles. It is noted that the use of a liquid film in this way has clear advantages in efficiency over the dry system described by Zapka *et al* [237], as it can remove more particles of smaller size with less shots at a lower fluence. This is beneficial for the cleaning of delicate substrates, damaged by high fluence irradiation. Furthermore, water is put forward as a better liquid than pure ethanol, as high super heating temperatures can be achieved with water and thus greater explosiveness in the evaporation of this liquid.

This is a promising technique for laser micromachining, as excimer lasers are already the tool of choice for profile machining. However questions remain over the interaction of liquid media with the beam for high definition profile machining. This is an area that will be explored experimentally by this thesis.

Two In-line debris and recast control techniques during laser processing have been experimented with [243-244]. One technique involves the application of an anti-spatter composite coating (ASCC) prior to laser machining in the form of a tape applied to the substrate to be machined [243]. This technique was applied using a 400 W Nd-Yag laser at 1.06 μm for metallic sample drilling in media of O_2, air, N_2 and Ar. This is a long wavelength machining technique where temperature is critical to the removal process and the application of ASCC proved to greatly reduce the melt spatter; yet, this technique introduces sample contact to the process. Also the application of a flowing salt solution liquid over the sample surface has also been attempted during Nd:YVO_4 laser processing of metallic surfaces at 532 nm [244]. Green wavelength light produces less heat than infrared, but is not short enough to remove the issue of melt and spatter altogether; the salt solution immersion was found to markedly reduce melt spatter and increase the removal of debris by 300%. Shorter wavelength pulsed laser machining (355 nm) has been attempted coupled with the application of a micron thick

film of ultra pure water to aide in debris removal from hard disk platters [245]. This technique used the viscosity and meniscus of the surface layer of liquid to retain debris as the liquid was ejected and atomized from the substrate surface with some success. This further demonstrates that liquids can be introduced to laser machining environments with successful results.

3.5 Debris Issues Following Removal from a Machining Site

Although not strictly within the remit of this thesis, it seems sensible to recognize that the debris problem does not end once the particles cease to pose a threat to the substrate being machined. The debris must be transported from the machining head then separated from the machining medium and collected into a safely disposable source that can be easily and rapidly accessed for regular service.

The first of hurdle in this process is that of extraction tube clogging; tubes and pipes offer an even higher possibility of debris settlement than the machining area, as the critical surface area to be lined compared to the volume of contaminated medium flowing increases when multiple tubes are used; thus more surface is available to be lined with debris, resulting in a constriction in the tube with time requiring lengthy maintenance. A number of papers have been located that cover various issues in this topic.

One possible method for micron and even sub micron sized particle removal has been accidentally noted by Bowling [16]. The bending of air extraction lines taking samples to optical particle counters. When these tubes are flexed, even slightly, a spike of particles is detected by particle counters, suggesting that the bending of the tubing dislodges particles that have become adhered to the inner surface of the pipe at the point of flexure. This is thought to be the result of physical forces applied to the inner surface of the tubing at the point of flexure, such as stress, which are large when compared to the force of adhesion holding a particle to that section of the surface.

Alberg [17] has explored the prominence of debris collection at pipe joints, testing several common pipe joining methods using a rudimentary and potentially unreliable technique; Alberg's method of delivering a vibration to the system being provided by "dropping the handle of a screwdriver from 3 inches height" is not seen as repeatable. However, this research did highlight some basic ground rules to avoid debris bottlenecks at tubing junctions: dead volumes in the flow should be avoided as debris will collect in these at an accelerated rate; insert rings (such as malleable olives) should be avoided as particles can collect both in front and behind such a constriction; and the use of flared type connection fittings are recommended, as the interface between the tube and the connector is smooth, as described in Figure 3-1.

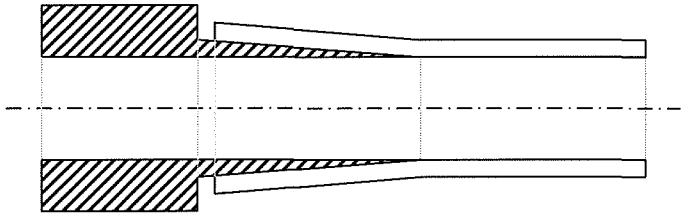

Figure 3-1: Schematic diagram of a flared tube connector fitting as recommended by Alberg [17].

Part II

Open Thin Film Regime Flowing Liquid Immersed KrF Excimer Laser Ablation of Bisphenol A Polycarbonate.

CHAPTER 4

EXPERIMENTAL EQUIPMENT DEVELOPMENT, PROCEDURES AND ANALYSIS FOR OPEN THIN FILM FLOWING LIQUID IMMERSED ABLATION

The basis of all experimental work must be the requirement to generate reproducible and stable results. To do this a number of criteria must be met to ensure that this goal is successfully achieved: repeatable input parameters; thorough recording of method and materials used; unobtrusive equipment; and robust data sampling. In the case of open thin film flowing DI water immersed KrF excimer laser ablation the laser type, specification and delivery method are critical, as new equipment is required to introduce DI water to the sample with minimal interference to the machining interaction between photons and material. The packaging of this equipment is difficult due to limited clearance between the de-magnifying lens and the sample mounting stage. Also, novel analysis techniques are required to produce discrete data for robust interpretation of results. This Chapter will detail the steps taken to fulfil these requirements.

4.1 Laser details

For this thesis an excimer laser was used (EMG 203 MSC; Lambda Physik, GmbH); a variety that is common across industry and is a well established and understood source of UV radiation. This laser could be filled with a KrF gas mixture to produce 34 ns, 400 mJ pulsed UV light with a wavelength of 248 nm at 250 Hz, resulting in a peak stated operating power of 100 W. The precise settings and output of the laser, both reported by the laser control unit (LCU) and by direct measurement at the image will be reported individually for each set of results.

4.2 Material details

The material used in a given experiment will undoubtedly have a dramatic influence on the results produced. Materials are typically made in batches and the physical properties of any sample within a batch will normally be near identical to that of any other sample from that batch [246]. However the use of differing batches, or worse, brand of supplier will inevitably have an impact on the linearity of results between experiments. This Section explores both of these factors. To make this thesis relevant to industry the materials used in this study are common in industrial processes, but in particular the displays sector. PC, amongst other polymers with similar properties are now becoming adopted as a durable and lightweight substitute for glass with particular relevance for the portable display sector [247]. Amorphous polymers lend themselves well to laser machining due to the chain like nature of their structure [46]. This is true of PC and is elucidated in Figure 4-1 [248], where the chemical layout of bisphenol A polycarbonate (better known commercially as Lexan) is given. This schematic shows that prediction of the photon energy required to totally destroy this molecule chain is complex. To achieve the process typically accredited as scission, a minimum

photon energy of 330 eV is required [248], which would result in large monomer particles being produced. These monomer particles exist as solid or melt in the plume and are left to be deposited back on the unmachined surface of the sample following the laser machining process or to interact with following laser pulses. These residue monomers can be clearly witnessed optically as a yellow tinge to laser machined Bisphenol A polycarbonate [45]. The high visibility of deposited laser ablation generated debris, coupled to the good laser ablation removal characteristics of PC materials, makes Bisphenol A polycarbonate an excellent candidate material for assessment of in-line debris control techniques. This is because the performance of the control technique both for debris control and it's impact on the machining process can be easily assessed using this material.

Bisphenol A polycarbonate (Holbourne Plastics, Ltd), was as received in 1200 x 1000 mm^2 sheets of 0.5 mm thickness. Prior to KrF excimer laser processing, the bisphenol A polycarbonate sheet was cut into rectangular sections of 8 x 12 mm^2 using scissors - a shear cutting technique which avoids production of debris. Protective cover sheets were then peeled off each sample.

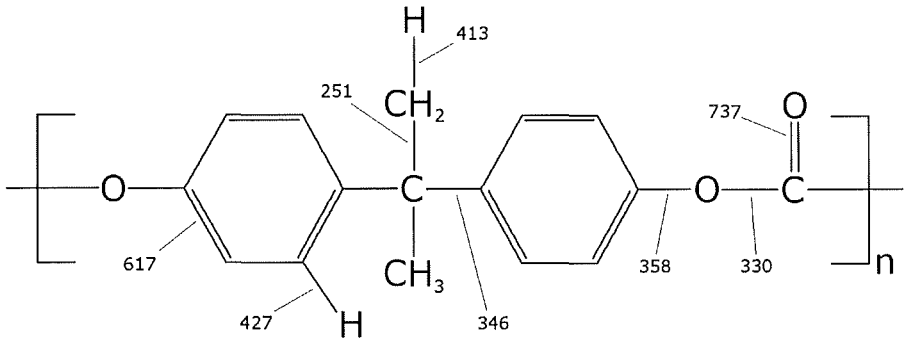

Figure 4-1: Chemical structure of bisphenol A polycarbonate, including chemical bond strengths in eV. [248].

In the same way physical changes to the polymer surface during repeated laser pulses can effect the interaction between the beam and polymer. An increase of surface roughness at the interface will result in a decrease of fluence within the beam. This is because the surface area irradiated by the beam is proportional to surface roughness. This could even result in the fluence level falling beneath the ablation threshold for processes operating just above this fluence level in ideal conditions [249]. These minor details can lead to large differences in results for what initially appear to be identical experiments. The exact conditions and materials used must be carefully examined and recorded when examining and presenting results respectively. To this end all samples used in this thesis emanate from the same batch of Lexan.

4.3 Beam Control

4.3.1 Gaussian energy profile

Typically, excimer lasers will produce a beam (typically square) of a dimension predetermined by its manufacturer. One major limitation of excimer lasers is the Gaussian-like profile of their beams [1]. The energy density of the beam varies depending upon position, being high in the centre and low at the edges, as described in Figure 4-2(a). The beam of an excimer laser is not actually Gaussian

because excimer lasers produce beams that do not have a single phase across the wavefront, but instead have a pitted and rough wavefront due to the many transverse modes present [9]. To machine a predictable layer of material with uniform thickness a linear energy density profile is required. The closest that can be achieved to this perfect case is the 'top-hat' energy density profile, where the energy density is uniform across the beam except at the very edges as described by Figure 4-2(b). To achieve the transition from Gaussian-like to 'top-hat' energy density profile the beam must be modified using special type of lens – a homogenizing lens [58].

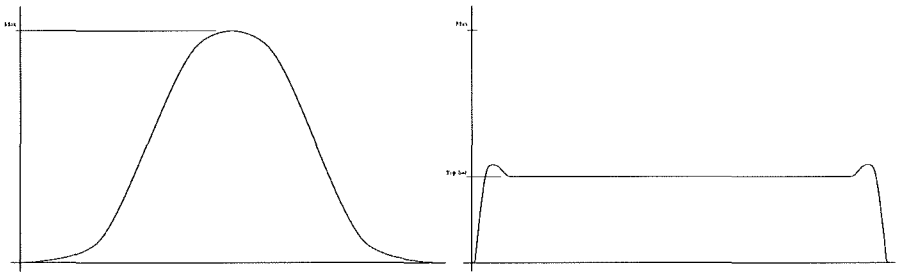

(a) (b)

Figure 4-2: Diagram illustrating the profile of: (a) Gaussian fluence; and (b) 'top-hat' fluence.

4.3.2 Homogenizing lenses

For course alteration of a beam homogenizing lenses are used to either spread or gather the beam in one plane. They must be used in couples, one to alter the localized path of the beam; then a second optic of opposite and equal magnification to collect the beam at a desired point and allow it to continue without further convergence or divergence, as displayed in Figure 4-3. These lenses are of a complex geometry that cause interference within the beam: multiple overlapping light paths combine to give a virtually even spread of energy at a specific image plane [58], as indicated in Figure 4-3 by the variation in shade of the beams. The use of homogenizing lenses also aides in homogenizing energy density across poor beams [9]. Manufacturing imperfections cause the 'top hat' signature profile, due to slight distortions and malformations of the lens profiles. It must be noted that to fully homogenize an excimer beam two sets of lenses are needed in opposing planes. Use of homogenizing lenses leads to outer fringes of light that are described as lower order functions of the lens; these are edge beams that have become separated from the desired main beam. This can be seriously exacerbated by poor calibration of a pair of homogenizing lenses, where a beam is gathered by the second lens before or after it has passed the image plane point of the initial lens. The beam used for the work presented in the next three chapters showed a mixture of homogenizing success as shown in Figure 4-4, that shows that the beam was well homogenized across the y-axis (Figure 4-4(a)) and poorly homogenized across the x-axis (Figure 4-4(b)).

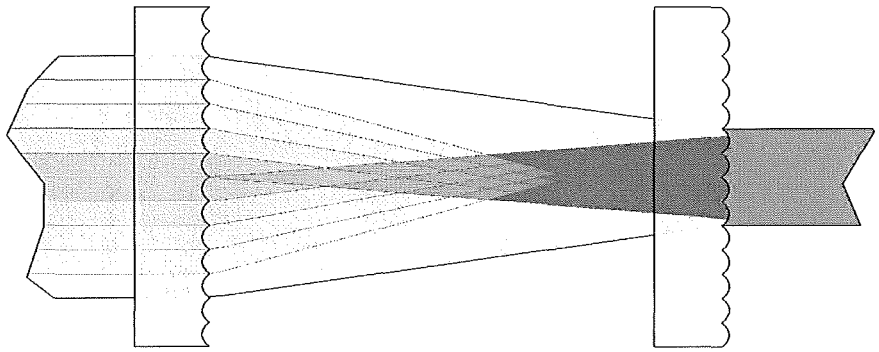

Figure 4-3: Schematic diagram to describe how homogenizing lens A splits the original Gaussian-like excimer beam, making all the split components cross, resulting in a uniform energy density across one plane. This is then collected by lens B at the focal length of the first.

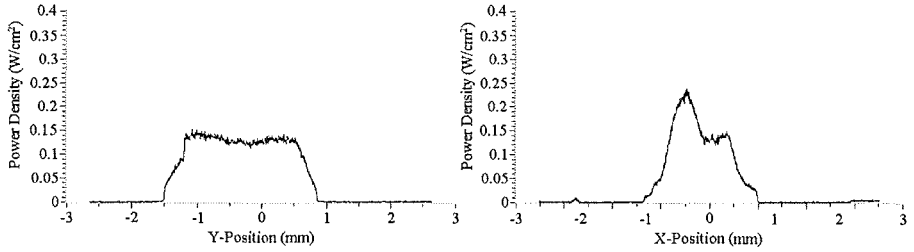

Figure 4-4: Trace representing the cross-sectional profile of the raw homogenized beam used. Here the beam is well homogenized across the y-axis (a); but, poorly homogenized across the x-axis (b).

4.3.3 Image plane control

As with all laser machining techniques, the workpiece had to be moved around in relation to the beam to allow even the simplest of machining regimes to be performed. No material is perfectly flat or planar parallel, so as the material was moved around in x- and y- directions, the cross-sectional thickness of the material varied. Due to the high magnification and resolution of the final lens used, the depth of focus (DoF) of this system was just 6 μm. To maintain the workpiece surface position inside the DoF of the laser micromachining de-magnifying lens, an in-house manufactured feedback loop control system was designed to drive the z-stage and hold the workpiece surface at a predefined position deemed to be in the centre of the system DoF at room temperature. This system was capable of maintaining the substrate surface position to within one micron by dynamically driving the lift stage given logical interpretation of the deflection of a reflected reference HeNe beam. In the case of this tool, burdened with thermal movement problems, small amounts of thermal expansion or contraction can cause the image plane to drift significantly when considered alongside the small DoF of the laser optics used. The image plane could foreseeably move outside the boundary of the calibrated DoF, making any lift stage correction futile as the feedback loop would correct to the wrong point in space. Since this was a thermal problem, maintenance of the surrounding environment temperature negated the thermal expansion variance occurring over short time periods. The issue of thermal expansion could have become an issue if some samples were machined in the cold of winter

and others in the heat of summer, the non-climate controlled environment of the laboratory was liable to change with outdoor temperature. To this end all samples were machined in a single month-long time window during July 2008.

Thermal drift of the micromachining centre was a minimal issue when compared to the packaging issue raised by mounting the open thin film flowing liquid immersion equipment to the micromachining centre. The inclusion of the Perspex enclosure for these experiments meant the reference beam used for measuring level change was obstructed and this dynamic focussing method could not be used. Instead the stability of the stage had to be trusted. This can be taken with some assurance, as the stages were a screw drive type and were therefore stable and sturdy. Before the commencement of any experiment, the sample height was set to being as close to the centre of DoF as possible. The feedback system was then overridden and the enclosure installed before the experiment was instigated. This obviously left these experiments open to poor focus repeatability. The DoF also plays an important role in limiting the tilt angle - a feature critical to the immersion experiments, this was achieved using a method covered in detail in Section 4.4.1. A 100 μm diameter spot allowed a maximum tilt angle of 3.4° whilst maintaining the entire image within DoF tolerance.

4.3.4 Fluence measurement

When conducting any group of experiments, there must be a maintenance of key input parameters to present a set of results that are contextually similar to each other. This can be achieved through rigorous maintenance of methodology and the detailed recording of any changes to this methodology where necessary. In all the work presented, detailed explanation of the laser beam fluence will be presented. The values stated are mean values generated from a large number of individual data values for each sample. A procedure for collecting such data was developed and adhered to for all fluence data presented in this thesis. Fluence data was calculated from pulse energy data taken using a pulse energy head (J50LP-2; Molectron Detector, Inc.) positioned above the focal point of the laser, and enumerated by a laser energy meter (EM400; Molectron Detector, Inc.). The fluence was calculated using the mean beam energy measured (averaging techniques were employed for experimental rigour: beam pulse energy was recorded five times before and after machining each sample, every value recorded was the mean value measured over 100 pulses)

4.3.5 Micromachining centre details

For this thesis the open thin film flowing liquid immersion rig was built to be mounted onto an externally developed excimer laser micromachining tool (EX-PS-500; Exitech, Ltd). The optics were contained within an optically sealed cabinet for safety. This arrangement is shown schematically in Figure 4-5. As one can see from Figure 4-5, homogenizers and magnifying lenses were used to generate a beam that had an even energy distribution. Thereafter the beam was shaped by the use of a stainless steel mask to produce a 7.5 mm square or a 7.5 mm diameter circular objective beam that was a 15x magnification of the desired image at the image plane.

This use of a single rigid optical layout for all experiments offered the obvious benefit of relative beam shape and profile repeatability. Despite this, there were still some phenomena that had

to be addressed to assess the true reliability of the optics system: the condition of the optics and the absolute position of the optics relative to one another.

Optic condition is dependant upon two variables, one being a result of singular incidents and the other being time and usage dependant. Damage occurs unpredictably and instantaneously, either by misuse, accidental impact or contact with other materials, this is a variable that can be prevented, and to do so the laser cabinet is tamper sealed. Wear and cleanliness of the optics is more difficult to avoid and is exacerbated by the lack of access to the optics caused by tamper prevention. Cleanliness can change rapidly and have a dramatic effect on the energy level and beam uniformity delivered at the image.

This tool had a major weakness: the optics cabinet was formed from aluminium. Being an aging tool manufactured in the late 1980's, modern developments in optical stability, such as a granite chassis, had not been implemented on this system. The use of aluminium made this tool highly susceptible to thermal movement, which may have caused drift in the beam energy and uniformity at the image over a time scale of minutes.

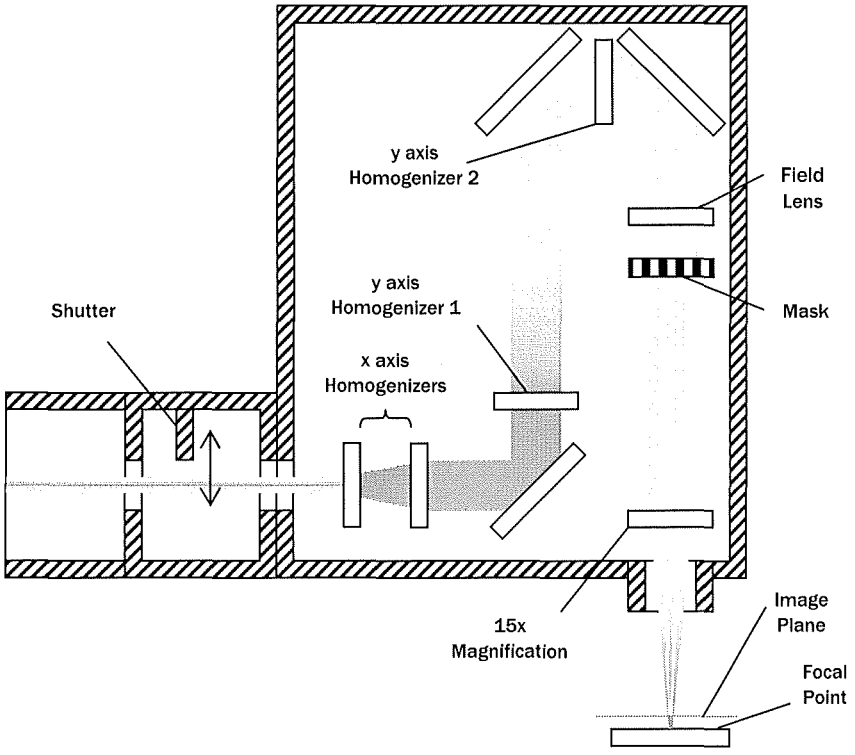

Figure 4-5: Schematic diagram of the layout of the optics box.

4.4 Equipment Used to Facilitate Open Thin Film Flowing Liquid Immersed Ablation

4.4.1 Sample mounting rig

A secure and locatable jig was manufactured that allowed new samples to be mounted and located in a single position under the beam. The jig was located to the top of the x- and y-position controllable stages, as shown in Figure 4-6. A recess had been machined to act both as a basin to collect used liquid and to accommodate the sample table and pitch control mechanism, as highlighted in red in

Appendix 1-1. The sample table was supported by a cradle that hinged on two dowel pins (Item N° 7, in Appendix 1-1). These dowels sat in two aligned and precision ground v-grooves, highlighted in green in Appendix 1-1. Each dowel was retained by a copper strip which was screwed to the basin. The tilt angle could be checked by use of a miniature spirit level bulb, removed from a camera tripod c-mount; thus level could be assured and the magnitude of tilt could be monitored to a maximum of ±6°. The cradle's resistance to tilt could be altered by changing the torque on the copper strip retaining screws (Item N° 13, in Appendix 1-1). The cradle is shown in Detail View B in Appendix 1-1. It featured two powerful magnets (Item N° 12 in Appendix 1-1), a location dowel pin and a ridge to provide retention, axial alignment and longitudinal position respectively for the sample table. The sample table shown individually in Detail View A in Appendix 1 was machined flat and planar parallel from a magnetic grade of stainless steel which provided the necessary level of corrosion protection against the liquids intended for use. An M3 x 0.5 threaded thumb adjustor (item N°s 8 to 10, in Appendix 1-1) could be screwed into the basin. The top of this thumbscrew was machined to a cone, ensuring that only a single point in the centre of the thumbscrew was in contact with the base of the sample table. This thumbscrew could be used to maintain or adjust the tilt of the sample table as required by each experiment. This arrangement was designed to hold the top surface of a 500 μm thick sample close to the image plane of the KrF excimer laser system and therefore allow easy adjustment *via* control of the tool's z-stage. The sample was mounted on the stainless steel table by means of the capillary action of IPA which was applied to the sample table before the sample was mounted.

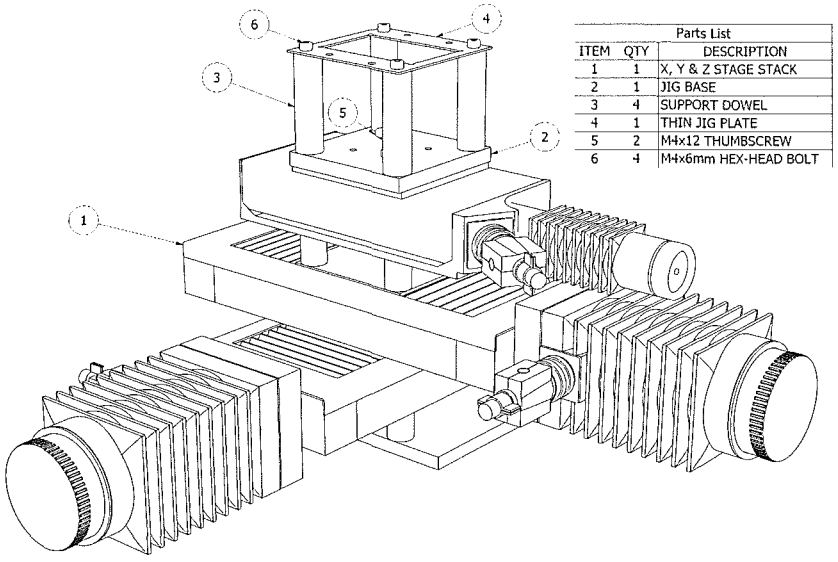

Figure 4-6: Perspective view of the position controllable stage stack and sample spacer.

4.4.2 Shroud design

A simple shroud was required to enclose the sample to ensure control of the environment around the sample and capturing all products of ablation both for the benefit of rigorous results and to protect the final optic of the tool. As high speed imaging was originally a desirable target for use in this body of work, the shroud was manufactured from acrylic, a material that is transparent at visible wavelengths.

Also, this material was cheap, readily available and easy to machine. The shroud was designed to slide together and form a stiff box from five laser cut panels, shown in Appendix 1-2. This box also provided support and location for two utilities: filtered air was directed down the length of the shroud chamber (details of the filtration technique are covered in Section 4.4.3); liquid was supplied by a ⅛" copper tube (as detailed in Section 4.4.4). The air filtration equipment was mounted by use of bulkhead fittings on the end walls of the shroud and a slotted opening, highlighted in red in Appendix 1-2, was provided at the bottom of each of the side panels to afford a contact fit against the top half of the liquid supply tube, constraining the tube in two axis by trapping it against the mounting plate of the jig.

4.4.3 Environmental control and fume filtering inside the shroud

Two inline gas filter holders (XX4002500; Millipore, Inc.) could be mounted to the shroud using 6 mm diameter stainless steel bulkhead fittings to isolate the internal volume of the shroud from the external atmosphere. Both filters had a maximum particle permeability of 0.8 μm. The filter holders featured National Pipe Threads (NPT) an American standard which was not commonly available in Britain. As such, specialist fittings were used to mount the filters. Inside the holder the filter was supported by a fine mesh, dictating that the gas to flow through the filter assembly from the female-thread end to the male-thread end, as illustrated by the red arrow in Figure 4-7. To mount the filter holders two differing 6 mm outer diameter bulkhead fittings were required; one being to a ¼" Male National Pipe Thread (MNPT), and the other to a ¼" Female National Pipe Thread (FNPT). The inlet filter holder was screwed into the FNPT bulkhead fitting; the outlet filter holder was screwed onto a MNPT bulkhead fitting. To draw air through the filters and shroud a vacuum pump was used, providing 0.006 l/s volumetric flow rate through the shroud. This flow rate was sufficiently high to evacuate the shroud of unfiltered air, but insufficient to markedly impact the geometry or trajectory of any ablation plume or ejected debris respectively. To attach the vacuum a pipe fitting was mounted to the outlet filter holder. Teflon sealant tape was used on all threads to ensure a leak-free installation.

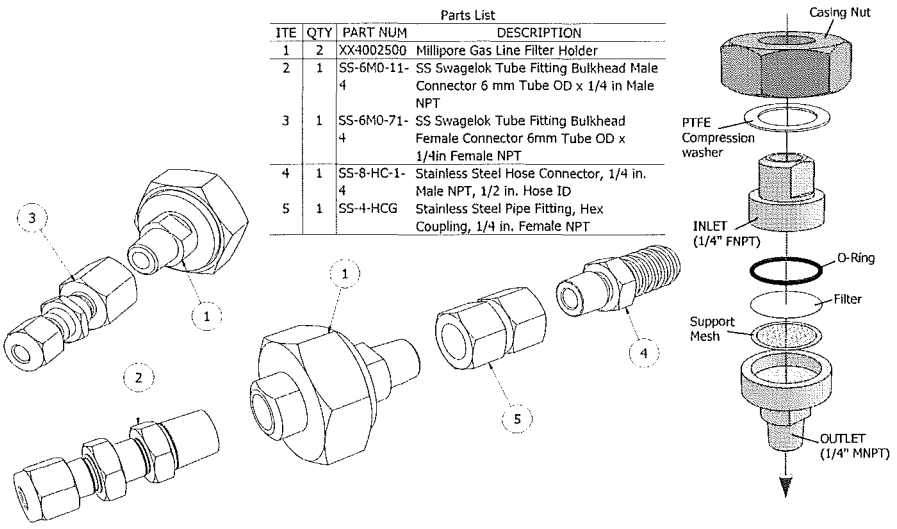

Figure 4-7: Technical exploded diagram showing the air filtering arrangement used.

4.4.4 *Liquid supply*

Due to the limited space available under the final optic of the KrF excimer laser and the complexity of installation, only a small diameter tube could feasibly be used, so a 1/8" outer diameter copper tube (Flotec, Ltd) was installed. As copper is a malleable material the tube was flattened over an 18 mm length and notched to form a flat nozzle for produce a wide, thin jet of water over the sample surface, as shown in the detail views in Figure 4-8. To maintain a relatively uniform flow rate across the width of the opening the nozzle was supplied from both ends. This was useful as it afforded simple mounting and location of the nozzle *via* use of notches in the shroud side-walls, as discussed earlier in Section 4.4.2. The copper tube was bent to loop up and away from possible contact with the location screws for the liquid basin and allowed to rest on one of the gas filter supply tubes; hence the 3° angular dimension given in Figure 4-8. This design of liquid supply used minimal elevation, an attribute that was in short supply in the arrangement resultant from installing this equipment in the laser micromachining centre used. Importantly, this design allowed repeatable location.

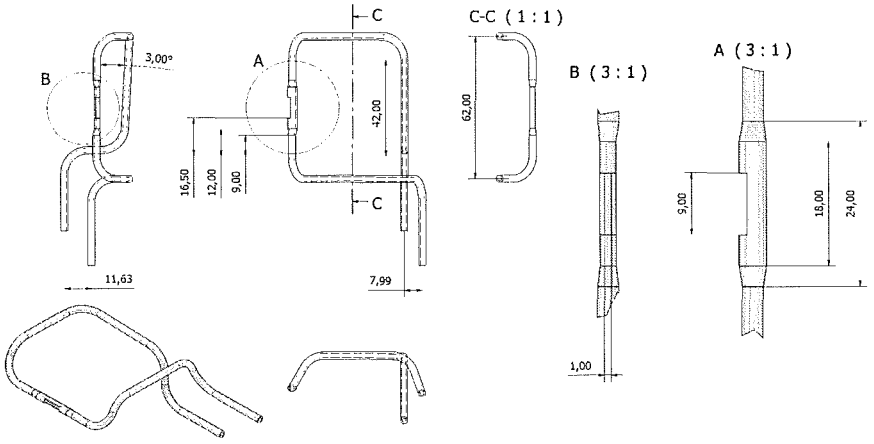

Figure 4-8: Technical diagram showing the geometry formed into 1/8" outer diameter copper tube used to supply water inside the shroud, and produce a flat nozzle for shaped water flow.

For this thesis liquid was supplied by use of gravity feed from a butt supported at a constant height, thus a single flow rate was used for supply that was measured using a flow metre (F4500; Key Instruments, Inc.) to be 0.015 l/s. For this thesis the sample table tilt angle was left at 90° to the incident beam, as this arrangement explores the most simple arrangement, easily reproducible for an industrial application. The supply was gated by a valve to allow rudimentary control of liquid flow before being delivered though a flat nozzle, described above, mounted 0.5 mm above the sample. As measured using a graticule and magnifying optics, the film thickness achieved with this arrangement was 0.8 mm,

4.4.5 *Full Assembly*

The constituent items covered in this Chapter were assembled to construct a modular solution providing environmental control, fluid supply and sample positioning with a high degree of repeatability. The provided spacing jig was mounted to the system stages; the shroud was a push fit

onto the top plate of the spacing jig as shown in section C-C of Appendix 1-3, which maintained a satisfactory air seal. Once in place the shroud provided strong location for the liquid supply tube and the filtration system that had been devised. This design enabled the assembly to fit between the stages and the final optic of the tool, as described in Appendix 1-4.

4.5 Error Analysis

The recording of accurate results is obviously critical to any practical research. However, choices must be made at the outset to maintain a level of accuracy with an understanding of the errors likely to be encountered. These errors will come from many sources; the filters used for larger debris, the resolution of the vision systems used to analyse debris smeared across shroud walls and the vision systems' resolution when observing any debris trapped in liquid. The measurement of filtered and liquid entrapped debris pose the greatest scope for error. The maximum particle permeability size of the filters will vary from filter to filter. To measure particles in fluids a traditional optical microscope will be needed; this leaves the measurement process open to error from both the low magnification of the optics in use and human error of the user. The shroud will be inspected using an electron microscope, ensuring that the errors from this sample of results will be much smaller than those of the other two samples.

4.6 Experimental Design

A schematic of the entire experimental arrangement is given in Figure 4-9. This diagram demonstrates the compact nature of this arrangement, and in particular the limited height for the open thin film flowing immersion rig due to the dimensions of the height detection laser and the quadrant detector. Also, in an attempt to limit the risk of water damage to the laser micromachining system in the event of a leak, the volume of water stored for use in the liquid butt was minimal, giving enough flow for approximately 20 seconds of machining. This limited water supply, coupled with the lack of 'fire on demand' capability available on the micromachining system, meant that contrived techniques had to be employed to achieve large numbers of pulses in the limited immersion time available. For more samples requiring more than 15 pulses, the number of laser pulses at high repetition rates was measured by the knowing the laser repetition rate and controlling the duration that the laser micromachining centre's shutter was held open by manual switch activated solenoid. For lower pulse numbers the laser repetition rate was set to 1 pulse per second and the pulses were manually counted whilst the shutter was held open by the manual switch. The second technique was used for all debris samples, as it removed error from the pulse number count and therefore offered a fair comparison between the volume of debris generated across all features.

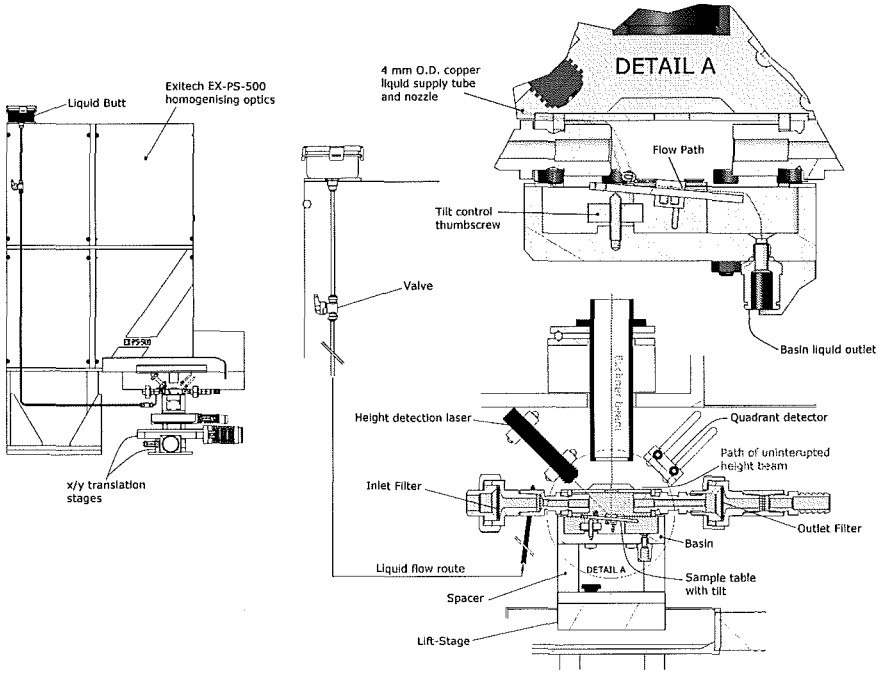

Figure 4-9: Technical diagram describing all supplies to the sample and the position of the sample relative to the beam during machining.

The lack of a truly programmable PSO stage control also meant that only one feature could be machined into each sample as it was sensible that each sample should only be used for a single feature, to stop cross contamination. After lasing has ended the enclosure was removed and the sample was then placed into the cell of a sealed sample tray to protect it from atmospheric dust. The open thin film flowing liquid immersion equipment was cleaned, reset and loaded with a new sample, the image plane position was found, the enclosure was reinstalled and a following sample was manufactured.

For measurement of laser ablation threshold, the laser fluence had to be modified between samples to produce features over large numbers of pulses. The fluence level of this system, although measured accurately using the technique described in Section 4.3.4, was controlled by modifying the lasing voltage of the laser; consequently, high precision control of the laser fluences used was difficult using this equipment.

4.7 Debris Deposition and Feature Characterization Procedures

All of the items that are of interest to this thesis were small, occupying the sub millimetre scale. This made fine measurement difficult. Further challenge was provided by the nature of the measureands to be investigated. A length or depth is simple to measure in a highly discreet manner; the only uncertainty lies with accuracy. This is true of the depths measured for this work as will be described in Section 4.8, where modern techniques were used to great effect. Population density of multiple small items is more challenging as the data is likely to be gathered in a highly indiscrete, analogue fashion. This Section describes novel and representative techniques developed to allow quantitative, rather than qualitative analysis.

4.7.1 Sample imaging arrangement

Raw images of KrF excimer laser machined features and the surrounding debris affected zones were captured using a combination of 10x magnification through an optical microscope (MeF3; Reichert-Jung, GmbH.) fitted with a charge coupled device (CCD) based digital camera (HC300Z; Fujifilm, Fujix, Inc.), which had a resolution of 2560 x 1920 pixels. This arrangement allowed items greater than 1.1 μm^2 to be resolved; this value is half the calibrated pixel size (measured by counting the pixels imaged over 1mm on a graticule through the same imaging arrangement), it follows that this vision system at this magnification cannot realize the dimension of any feature smaller than 2.2 μm in diameter.

4.7.2 Image collation

Samples remained in the enclosure until a sample tray was prepared and ready to quickly accept them, the enclosure was then removed from the basin and the sample was swapped to the sample tray as fast as possible before being sealed from the external atmosphere once again to protect it from atmospheric dust.

For inspection, samples were mounted to a smooth black surface by the use of IPA capillary adhesion. This technique ensured even lighting and a minimum of background optical abhorrence. The data to be used was gathered in the form of images, using the arrangement described in Section 4.7.1. The Samples were illuminated by reflection, images being obtained from light that was supplied above the sample and reflected by the sample. The size of the area of interest was large but the level of detail required was high to allow for accurate particle identification. These are conflicting needs when imaging; the camera used had a resolution of 2560 x 1920 pixels. Over a wide area each pixel would effectively describe a large spot, giving poor definition to the results gained. A technique to provide wide imaging and a high data resolution as required.

To achieve both of these requirements, a 10x magnification was used to grab a number of sector images that could later be digitally stitched together in the manner shown in Figure 4-10. The images were stitched together automatically using an automatic image alignment tool (Photoshop CS3; Adobe, Inc.) to give repeatable stitching without human error. Figure 4-10 demonstrates the wide surface area surveyed and the high resolution, as stated in Section 4.7.1, afforded simultaneously by use of this technique.

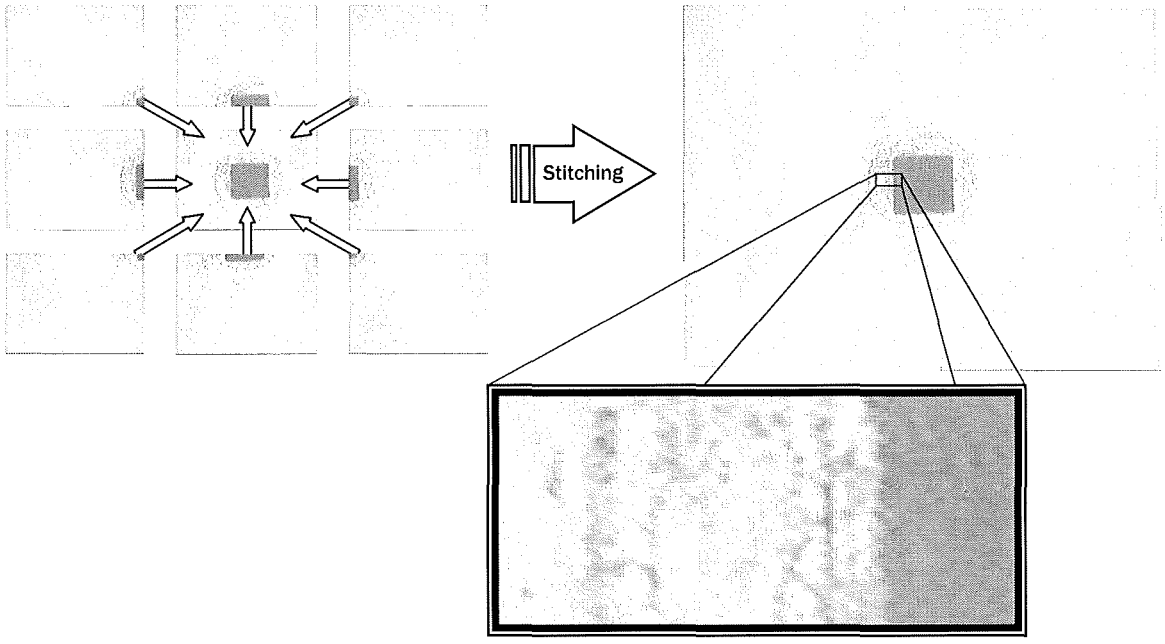

Figure 4-10: Schematic diagram describing the process and advantages of the image stitching technique used for this thesis.

4.7.3 Image analysis and interrogation to produce discreet data

Once stitched, the image is interpreted using mage analysis software (Visilog 6.6 Xpert; Noesis, SA.). A number of techniques are used to convert a colour image, as developed in Section 4.7 and displayed Figure 4-10, into a binary map of debris across an area. The steps required to do this are listed below and sample images of each step are displayed in Figure 4-11:

(a) The colour image was separated into the constituent Red, Green and Blue (RGB) channels. The channel giving best contrast between debris and surface was chosen. For these samples, was the red channel, since the raw images had a high saturation of blue.

(b) The new greyscale intensity map of the red channel of the original image was inverted to give a negative. Debris was now a high response, appearing close to white to the viewer, and the clean surface had a low response, appearing darker.

(c) Local equalization, a process known in Visilog as "lequalize" was used to match the average intensity of the entire image with respect to the localized contrast of a user specified cell size. For equality of analysis in this thesis, the cell size used was chosen and maintained. It had to be small: debris particles often only populate a few pixels. Cells had to occupy a multiple of 4 pixels; a cell area of 16 pixels was chosen. This gave a well equalized light gradient across the entire image and still allowed relatively large local contrast for debris identification.

(d) Thresholding was now employed to convert a digital representation of an analogue image into a purely binary format. Thresholding is a logical method of setting high and low light intensities; The best method for this thesis is a logic named "top hat", where there are three intensity ranges:

i. Low intensity, this can be set to encompass all intensity levels that are below that of interest; that is, the entire 'clean' surface; this will now be replaced by a high response (blue).
ii. High intensity: in the same way, there could be features that are not debris such as microscratches, or the boarders of the shot image, which once inverted appear too bright – these are not debris and so are not of interest to the analysis. Any of these 'high' areas can also be replaced with the same colour as the 'low' intensities (blue).
iii. If the high and low thresholds have been set correctly, the medium intensities will be the signals generated by the debris and are interest to this analysis, these can be selected as a second, different colour.

In this way the image was split into two colours, hence the term 'binarization': one colour of interest and one colour for contrast. For this thesis, top hat thresholding intensity values were set so that any intensity lower than 104 (out of a maximum 256) was judged to be too low, and any intensity greater than 116 was considered too high. Hence, the intensity window for debris identification was 12 wide, resulting in the image displayed in Figure 4-11(d). This was maintained throughout the work in the interest of continuity of results – reliable comparison is critical as the process did not achieve accurate particle counting but did accurately represent population trends.

(e) Any borders, as can be seen in Figure 4-11(a-c) should have been caught by the top hat binarization process. However, for any fine borders that remain, Visilog can use programmable logic to remove regular shaped features from binarized images, this is known as 'border_kill', and prevented any unwanted points being identified and skewing the results at a later stage; however, first the binarization polarity needed to be swapped using a tool known as 'regiona_extrema', since the border_kill command looked for 'high' signals.

(f) Finally the binarized image can be analyzed logically to generate statistical information concerning feature area, position and circumference; data is output in a spreadsheet format and has a corresponding output image that identifies different features by colour and shown in Figure 4-11(f).

This technique did have one drawback: any features captured in the initial micrographs would have had edge geometry that was beyond the scope of the resolution of the technique uses. This led to poor debris feature edge definition. As a result, multiple small debris lying in close proximity to each other could be identified as a single large item. These could be removed by using programmable logic within the software to remove any features that were over a specified area from the output data. For this thesis, the upper limit of debris size analyzed was 1000 pixels. This filtering technique has been implemented in Figure 4-11(f) and is the reason the apparently reduced number of debris from the preceding images. Although this was a limitation that prevented accurate enumeration of the complete population size of debris generated on any given sample, this technique was highly repeatable, and therefore is a true reflection of the relative debris population density between samples.

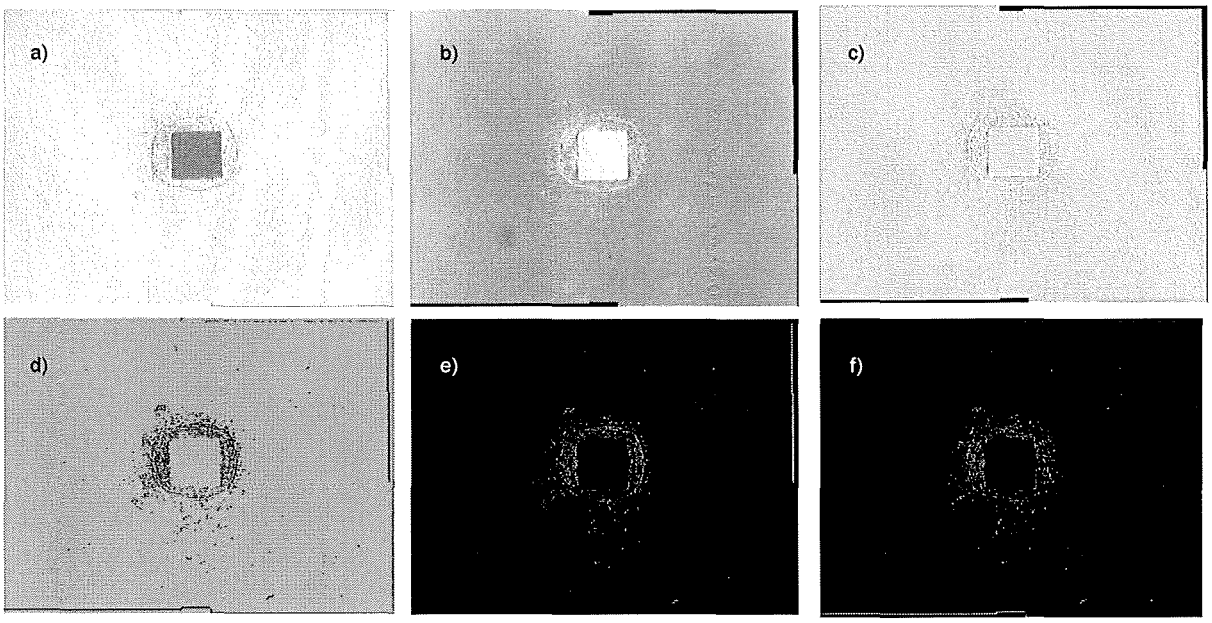

Figure 4-11: Six stages of image processing using Noesis' Visilog 6.6: (a) 'RGBtoMONO' - separates the raw image to an intensity map of the three component signals, the one with highest contrast must be chosen; (b) negative: an inversion of the intensity map; (c) lequalize – the gradient of the entire image is set to a common; (d) top hat – thresholding technique; (e) border kill – logically removes edge signals present from the camera system; and (f) analyse – logically generates statistical sizing and position data.

4.8 Physical Analysis Techniques

4.8.1 Feature depth measurement.

The ablation depths were measured using a dragged needle profiler (CM300 Talysurf; Taylor-Hobson, Ltd). Five passes were made across the surface of the sample and into each feature at 50 μm intervals. To minimize the possibility of profile error the mean average depth of each sample feature was then calculated from a selection of three profiles for each sample feature. To guard against outlier samples being produced and effect the ablation threshold measurements taken, all data plotted for interpretation in these results are mean average values taken from the data produced by three sample features machined using each flow velocity.

4.8.2 Surface topography analysis

To examine the surface roughness and waviness of the machined samples a selection of samples machined in ambient air and under open thin film flowing DI water immersion were selected. Each sample was then vacuum coated with a thin layer of Al to ensure sample surface reflection. Thereafter the samples were placed into a white light interferometer (WLI) (New View 5000; Zygo, Corp) to measure the surface roughness using a camera resolution of 640 x 480 pixels, imaged through magnifying optics of 10x. Thus each sample analysed has an area of approximately 250 μm^2. Software (Mountains; Taylor-Hobson, Ltd) was used to process and interpret the raw data generated. The samples were compared by means Robust Gaussian elimination to separate data waviness and roughness signals. Waviness specifies the macroscopic drift from a planar ideal and roughness specifies the microscopic drift from the planar ideal. All data was levelled in software, using the un-

machined sample surface as a reference plane; this action reduces the interference of data slope with waviness results. The areas investigated must be large enough for the cut-off filter between surface roughness and waviness to be implemented, but small enough to fit independently inside the feature area. To achieve this two 150 μm square regions of interest were selected from opposite corners of the bottom surfaces of the machined areas of the samples. It is this data that has been examined and will be reviewed in this thesis. This technique provides data to guard against anomalous values being generated from a sample.

A Gaussian data sampling filter of 8, 16 and 32 μm was used. The use of these filters allowed differentiation between microscopic roughness and macroscopic waviness deviations from the planar average, taking into consideration the idea that the definition of the scale of roughness and waviness of features can change dependent on point of view and user requirements. This idea can be illustrated with use of this simple analogy: if a pilot was flying over a desert covering mountainous terrain at high altitude, his eyesight would resolve the large amplitude, long wavelength undulations of the mountains and the smaller amplitude and wavelength undulations of the desert sand dunes and waviness and roughness respectively; a man standing on the desert surface would see the dunes as large wavelength and amplitude undulations but recognize the smaller, short term wind generated ripples in the sand as relative surface roughness; an insect on the desert surface would recognize these short term wind generated ripples as large undulation waviness and classify the texture of the sand grains as surface roughness. The RMS amplitude value in μm is quoted in this thesis for waviness, W_q, and roughness, R_q, as a measure of the deviation from the planar average. These values are calculated from four separate samples machined and analysed separately to guard against error.

CHAPTER 5

DEBRIS MODIFICATION AND CONTROL

Hitherto, all attempts to remove debris from an excimer laser machined sample has been conducted by use of a post process cleaning technique, and debris control attempted during excimer laser machining has been attempted using gas jetting or vacuum techniques, as described in detail in Part I of this thesis. In this Chapter, the debris control performance of a novel in-line technique is presented in terms of deposition limitation, deposition positional trend modification and deposited debris size is compared to the debris generated during KrF excimer laser ablation of bisphenol A polycarbonate.

5.1 Introduction

Micro particulate ablation debris produced during excimer laser beam interaction with a material are highly excited objects of very small mass. This means that these particles need a large force to decelerate them, yet only have a very small surface area available for a decelerating force to be applied. Traditionally, excimer laser machining has been conducted in gaseous media: these are easy and cheap to contain, regulate and supply. These media, however, have very low viscosities and consequently cannot provide high drag force to the small, highly excited particles moving through them. Conversely, liquids have a much higher viscosity than gases; thus the small particles will face much more resistance. Additionally, liquids are better conductors, dissipating electrostatic forces whilst completely removing capillary adhesion problems by swamping condensation sites, which in turn promotes surface cleaning. Despite these benefits to debris control there are potential problems posed by liquids to the beam path: reflectance, uneven refraction, micro-bubbles, transmissivity and heat related effects are all possible.

Two feature geometries have been chosen as the deposition pattern of the debris appears to be geometry dependent: circular and square sets of features, machined in ambient air and under open thin film flowing DI water immersion, are machined with the sample table lying at a normal to the vector of the beam. This way all samples produced are not affected by the possible effects of incident beam angle. It must be noted that the mechanism of ablation is significantly modified by the implementation of a liquid medium, explained to in Section 1.3.3. The ablation threshold is modified, dependant upon film thickness, along with ablation rate. A circular feature has been chosen with the intention of producing debris deposition in an annular pattern to give a reasonable indication of mean range with respect to fluence. A square feature has been chosen to represent the modal trend of debris deposition for features with acute angle corners.

5.2 Circular Feature Geometry

The debris distribution of the sample machined in ambient air displays areas of localized high debris density as can be seen in Figure 5-1 and Figure 5-2. Given the five variables available from the body

of literature, one can say that there are three possible explanations for this occurrence; either working exclusively or in combinations thereof. The beam profile may have caused an uneven ablation rate across the image, creating an uneven pressure profile in the ablation plume; thus debris is consistently expelled with positional tendencies. Also, the surface profile of the original material may have generated localized changes in the beam incident angle; thus modifying the local trajectory of the debris. Finally, the material composition of the polycarbonate will not be completely homogenous across the whole image; thus some areas within the image may produce more debris than others. Inspection of the original optical micrograph displayed in Figure 5-1(a) in concert with the Visilog analysis in Figure 5-2 would tend to support the postulation that the deposition of debris is dominated by the shape of the ablation plume: two curved 'horns' can be seen extending with a large radius, symmetrically from the centre of the image.

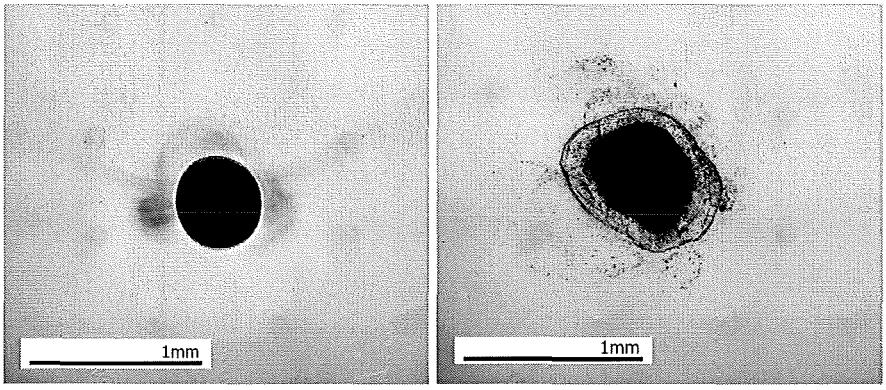

Figure 5-1: Stitched section optical micrograph images of circular features KrF excimer laser machined (a) in ambient air and (b) under open thin film flowing DI water immersion.

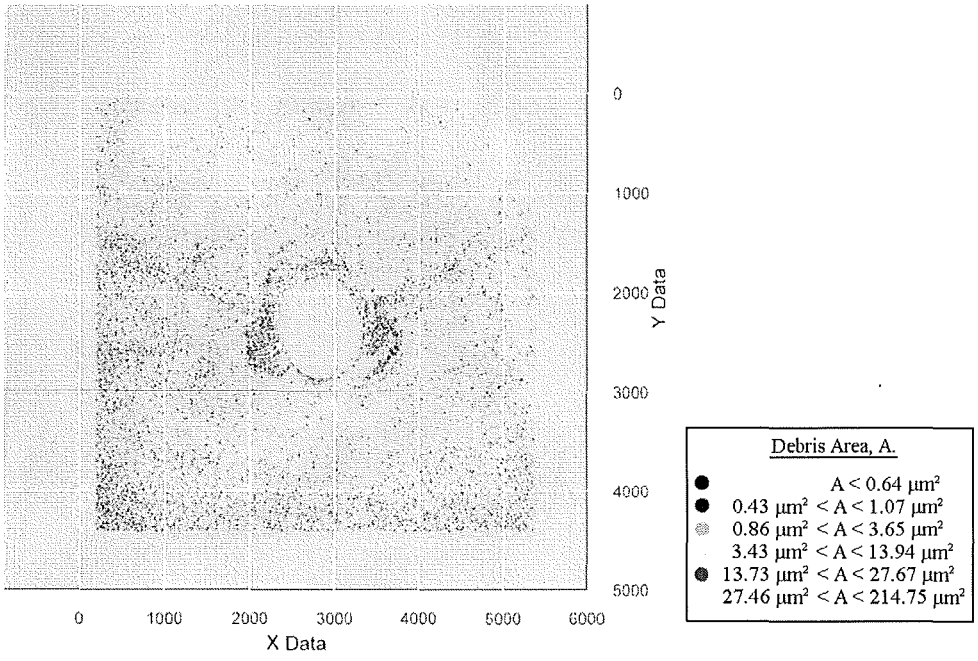

Figure 5-2: Plot for a circular feature showing debris size against position for a sample KrF excimer laser machined in ambient air.

The majority of the debris deposited lies within 180 μm of the centre of the image. The largest of the debris produced (areas between 3.43 μm^2 and 13.94 μm^2) has very little range, lining the edge of the feature, large intermediate debris (areas between 0.86 μm^2 and 3.65 μm^2) appears to have less range than smaller species and lies in radial streaks from the edge of the feature. Both of these results are contrary to expectation; however, large intermediate debris also occurs in increased concentration along the horns, suggesting that debris is transported on the edge of the ablation plume, providing support for the theories of Dyer *et al* [11, 24 - 27].

When compared to the sample machined in ambient air, the sample produced under open thin film flowing DI water immersion shows a more homogenous distribution of debris. It must be noted that the dark line of debris surrounding the machined feature clearly visible in Figure 5-1(b) have been filtered out of the data plotted in Figure 5-3 - these separate debris items were generating signals with areas greater than 214.75 μm^2, as the low contrast between individual items made groups appear to be single objects after the binarization process. Nevertheless, the raw image displayed in Figure 5-1(b) is still useful as it clearly shows a boundary range from the feature edge of between 75 to 150 μm. Outside this boundary the concentrations of debris drops significantly. This represents a significant reduction in range of the debris when machined under open thin film flowing DI water immersion, supporting the theory proposed by Fabbro *et al* [102] that liquid immersion constricts the growth of the ablation plume. Even so, the use of DI water in this experiment has not prevented deposition of the debris back onto the substrate. According to Bowling [16], this could be a result of the lack of electrostatic conduction offered by the liquid medium chosen for this experiment, allowing the debris to be attracted back to the substrate surface by long range electrostatic forces. The trails of debris that do lie outside the perimeter boundary evident in Figure 5-1(b) follow what appear to be liquid flow lines and only lie downstream of the sample; thus it would appear that a low flow rate, provided by just 0.1 bar of standing head pressure has affected the deposition pattern of the debris. The occurrence of these ripple patterns of debris deposition support the result of Sattari *et al* [53], that proposed increased flow rate promoted production rate of laser ablated nanoparticles, claiming increased flow rates remove particles from the path of oncoming pulses more efficiently. Because of this, it is proposed that the use of higher flow rates will be interesting in combating debris deposition.

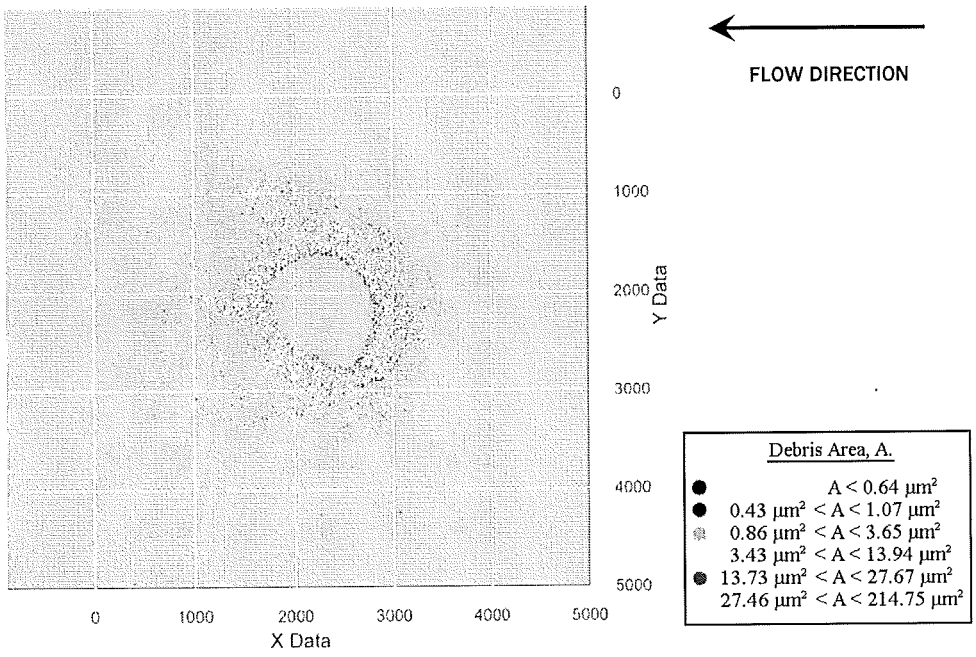

Figure 5-3: Plot for a circular feature showing debris size against position for a sample machined under open thin film flowing DI water immersion.

5.3 Square Features

Figure 5-4 shows that when KrF excimer laser machining in ambient air, the geometry of the feature being machined is critical to the positional deposition trend of the debris produced. To this end, machining square features is useful in illustrating the effect immersion machining has upon the homogeneity of the deposition distribution of debris. The difference between the data plot of the sample machined in ambient air (see Figure 5-5) and the sample machined under open thin film flowing DI water immersion (see Figure 5-6) is even more pronounced than that of the circular features described above.

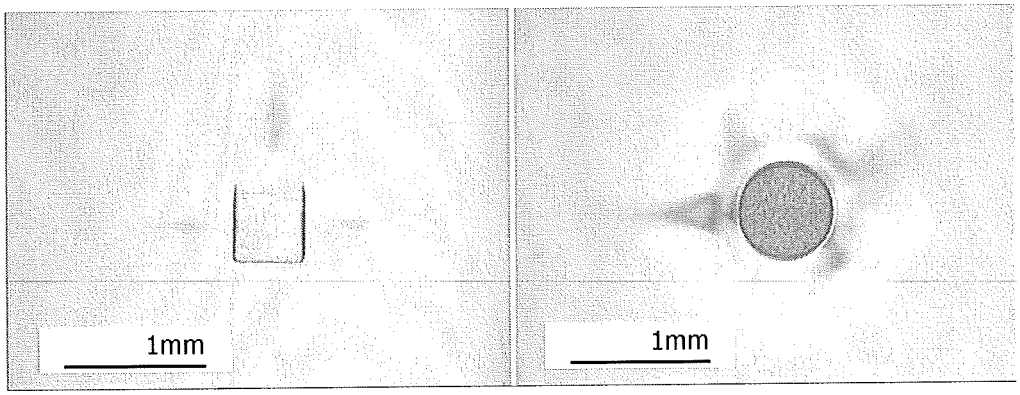

Figure 5-4: Optical micrograph images of a square and round feature machined in ambient air.

As Figure 5-5 shows in detail, the sample generated in ambient air causes debris to be deposited with a modal tendency at a normal to the straight edges of the square feature. Thereafter, the debris mushroom at a distance of approximately 460 µm from the feature centre. This modal response

is highly pronounced for larger debris, the signal response of debris lying in the deposited streaks show a majority population of items between 0.43 μm^2 and 3.65 μm^2. As with the circular features discussed above, this finding supports the proposal that debris transport is governed by the shockwave that has been reported to exist at the edge of the ablation plume [11, 24 - 27]. Debris is deposited at the extent of the ablation shockwave; as debris is liberated from the substrate during ablation by photomechanical processes, the solid and liquid species become trapped in a shockwave that is motivated by the gaseous products of photochemical interactions between the beam and material [22]. The patterns generated suggest the range is either governed by the point at which one shockwave meets another, each shockwave emanating from a neighbouring corner of the feature as described schematically in Figure 5-7, or by the pulse length and fluence of the ablating beam [54, 103]. The regime of the ablation plumes that create the debris patterns with a mushroom-like geometry, as one can see in Figure 5-4(a) and Figure 5-5, and compared to the different deposition pattern of Figure 5-4(b), are represented schematically in Figure 5-7.

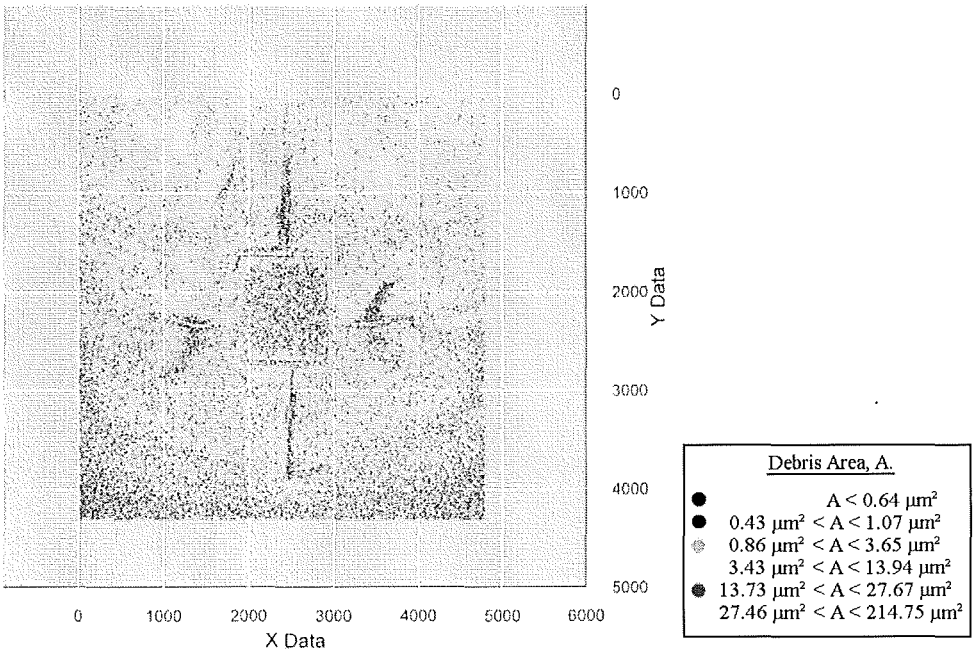

Figure 5-5: Plot for a square feature showing debris size against position for a sample machined in ambient air.

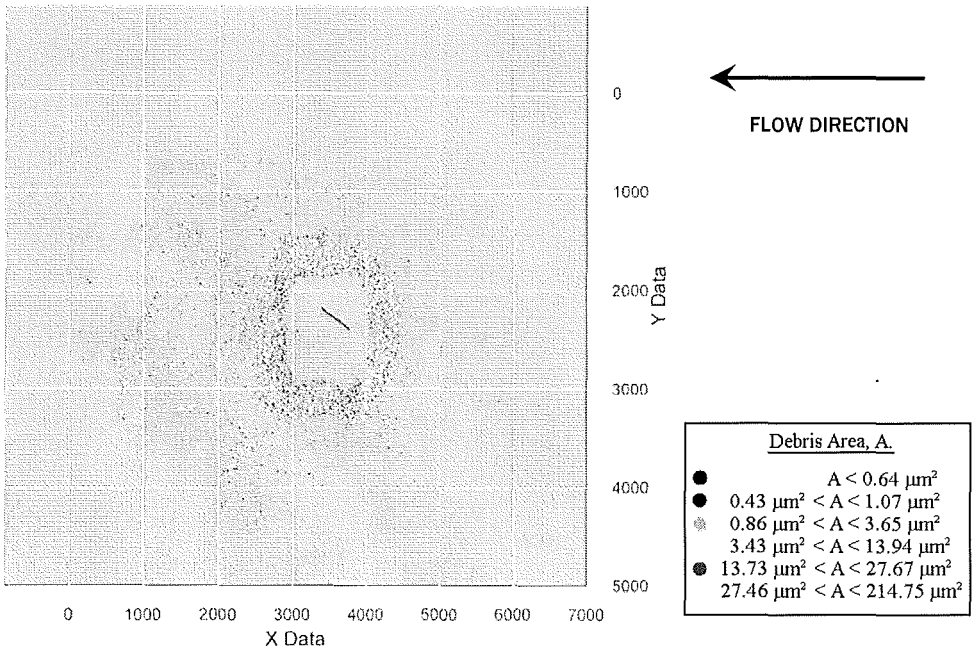

Figure 5-6: Plot for a square feature showing debris size against position for a sample machined under open thin film flowing DI water immersion.

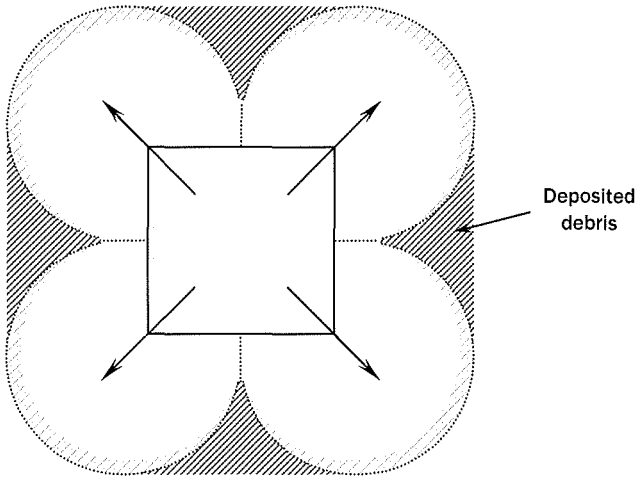

Figure 5-7: Schematic diagram illustrating four ablation plumes emanating from the corners of the square image. Debris lands in higher concentrations where they meet.

By comparison, the sample machined under open thin film flowing DI water immersion, shown in Figure 5-6, displays none of the modal trends of the dry sample, shown in Figure 5-5. The range of debris deposition is limited to approximately half that of the sample machined in ambient air for the vast majority of species deposited and the particles appear to be homogenously and randomly scattered within that range, again supporting the proposal of strong restriction of ablation plume expansion by the immersing liquid. Both the lack of deposition pattern and limited range are in agreement with the findings of Fabbro *et al* [102]. Here the action of constricting the ablation plume will lead to higher temperatures, pressures and turbulence within the plume. This in turn will lead to a more random and homogenous deposition pattern shown in Figure 5-6. The only modal trends that appear in Figure 5-6 resemble fluid flow lines, supporting the findings of the circular sample detailed

above and suggesting that the laminar flow of liquid has had an effect on the likely deposition site of generated debris. The common occurrence of debris down stream of the machined feature and very little debris upstream, observed in Figure 5-6, provide further conformation and agreement with the work of Sattari *et al* [53].

5.4 Mean Deposition Size and Size Trends

Comparison between the control sample of bisphenol A polycarbonate KrF laser machined in calm, ambient air and the equivalent sample machined under open thin film flowing DI water immersion showed marked differences. The most apparent of these was the difference in size of the debris produced by each machining method. Inspection of Figure 5-2 and Figure 5-5, together representing machining conducted in ambient air in contrast to Figure 5-4 and Figure 5-6, together representing machining under open thin film flowing DI water immersion, it is clear that the vast majority of debris generated by ablation in ambient air have areas covering less than 3.65 μm^2. In contrast, the vast majority of the debris produced under open thin film flowing DI water immersion covers an area greater than 3.43 μm^2. This is immediately apparent by the difference in colour between the two groups of plots: the dry samples, displayed in Figure 5-2 and Figure 5-5, are dominated by darker data point colours and the immersion samples, displayed in Figure 5-3 and Figure 5-6, are dominated by bright yellow data points and a large number of red data points.

This result can be illustrated in more quantitative terms by measuring the mean size of debris produced using both machining techniques. Debris generated during open thin film flowing DI water immersion ablation increases in cross-sectional area by an order of magnitude from debris generated in ambient air, which was measured to be 0.86 μm^2 and 0.64 μm^2 for circular and square features respectively, to 7.08 μm^2 and 15.23 μm^2 for circular and square features respectively, generated under open thin film flowing DI water immersion.

Figure 5-8 and Figure 5-9 plot the frequency of occurrence of debris features within 10 size classes defined by $f = 2n\text{-}(2n\text{-}1)$ for circular and square features respectively. The smallest debris detected is approximately 5 times more common on ambient air samples. Equally important is the increase in generation of large debris by open thin film flowing DI water immersion ablation. It is proposed that this is due to colloidal debris agglomeration, as described by Heim *et al* [179]. This theory offers satisfactory explanation for both the lack of small debris and the increased numbers of larger debris classes since the effects of colloidal adhesion, where micro-bubbles in the immersion medium collect populations of small debris particles at the gas liquid interface of the bubble, which are then forced together into a single, large particle as the micro-bubble collapses. This analysis supports the mean average values, with trends distributed about the mean values listed above. The numbers of small debris existent on the samples machined under open thin film flowing DI water immersion are small compared to the samples machined in ambient air, but conversely, the numbers of intermediate and large debris existent on the samples machined under open thin film flowing DI water immersion are high when compared the samples machined in ambient air. This is the expected response for colloidal agglomeration, where large numbers of small debris are used to form smaller numbers of large particles. The production of larger debris with the use of immersion *via* action of

colloidal interaction between debris items is in collusion with the results of Katto *et al* [55], who noted the production of sponge like artefacts produced at high pulse fluences for stagnant fluid immersed KrF excimer laser ablated targets.

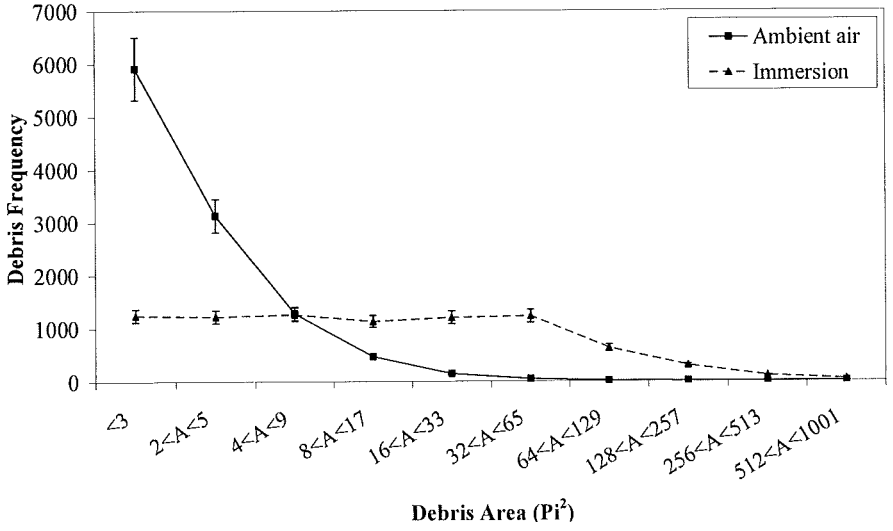

Figure 5-8: Frequency of debris lying within size classed groups for circular features

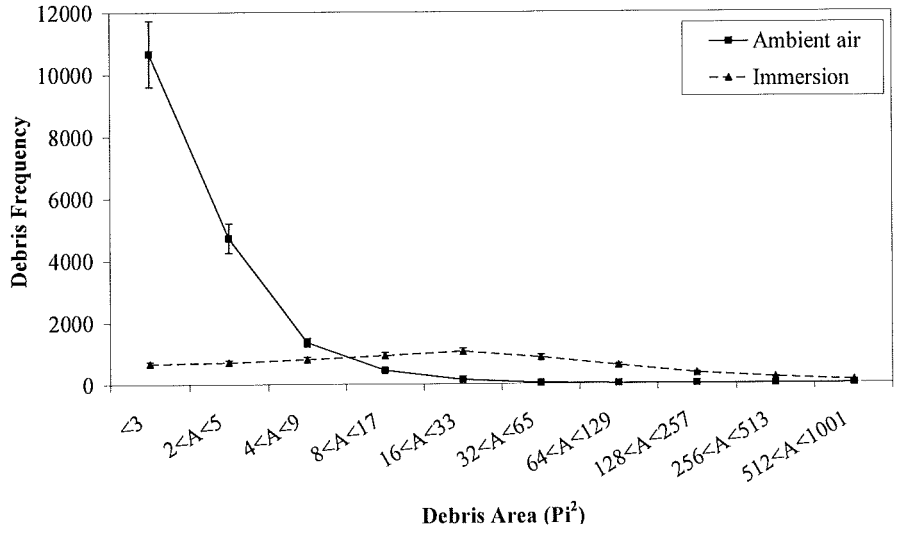

Figure 5-9: Frequency of debris lying within size classed groups for square features.

5.5 Feature Geometry Considerations

Figure 5-1(a) and Figure 5-1(b) show a marked contrast between the two features machined in terms of geometric accuracy. As detailed by Zhu *et al* [56], the ablation rate and ablation threshold of features when using liquid immersion in a thin film regime shows a significant loss in machining efficiency compared to KrF excimer laser machining in ambient air. Also, the use of open thin film flowing DI water immersed ablation has been shown to considerably affect the topography of the features machined in terms of surface roughness (see Section 7.2). This is thought to be due to a shift in primary etching mechanism. The immersing fluid has a higher density and viscosity than that of a typical gaseous machining medium, thus constricting the ablation plume expansion and therefore

providing an inversely proportional increase in plume pressure, density and temperature. This increase in plume density offers greater plume shielding to following laser pulses, reducing the laser ablation rate. Simultaneously, the increased temperature and pressure of the ablation plume acts to etch the surface of the sample in a way not possible when machining in ambient air. When using open thin film flowing DI water immersion; however, the volume of the liquid covering the ablation plume is not sufficient to constrain the ablation plume at high pressure and the plume pressure is released in the action of splashing of the immersing fluid; thus, the ablation rate achieved by thin film flowing DI water immersed laser ablation is significantly reduced when compared to a thick film regime. The action of the plume etching, coupled with the random nature of immersion fluid splashing given the rippled nature of the flow over the sample gives poor geometric accuracy. The use of a new immersion rig to eradicate the optical effect of flow ripple over the top of the sample during machining will also prevent splashing of the immersing fluid and allow an increase of flow rate which is desired for better control of debris as stated above.

CHAPTER 6

IMPACT OF OPEN THIN FILM FLOWING DE-IONIZED WATER IMMERSION ON KrF EXCIMER LASER ABLATION CHARACTERISTICS.

The immersion of a laser-generated ablation event may result in an alteration to two primary parameters used for measuring pulsed laser machining efficiency: the ablation threshold and the ablation rate. All previous research into liquid immersion assisted laser machining has involved stagnant liquid. This thesis explores for the first time the impact of laminar flow liquid immersion on ablation rate and ablation threshold, using the data gleaned to identify any differences in the machining mechanism between ablation in ambient air and under laminar flow liquid immersion.

6.1 Effects of Open Thin Film Flowing De-ionized Water Immersion Ablation on Ablation Threshold

The ablation threshold can offer insight into the nature of the ablation mechanism at work in a beam – material interaction. In the case considered herein the beam and material remain the same, but the mechanics of that interaction in terms of chemical reactions, the effects of plume shielding and the contribution of plume etching to the removal of material yield a significant modification to the ablation threshold. Two data sets (ablation in ambient air and ablation under open thin film flowing DI water immersion) are plotted in graph Figure 6-1. The plot of data for the sample machined in ambient air shows a strong linear correlation, with all the results being tightly packed around the trend line. This would suggest that the threshold value yielded for ablation in ambient air is accurate. The data plotted for immersion machined samples includes four anomalies, plotted as triangles in Figure 6-1. This is interesting as these four anomalies appear to lie in a trend, which yields an intermediate threshold fluence value between ablation in ambient air and under typical liquid immersion. The intermediate group could be caused by either one of three occurrences or a combination thereof: (i) The liquid flow changes in geometry with respect to time due to natural turbulence generated surface ripple; thus a thinner or non-existent liquid coating to the material surface may have been present for a period during the machining of anomalous results. (ii) Ablation plume generated splashing could also cause significant geometric change to the liquid flow with a similar result: the plume, which becomes compressed by the high viscosity of the immersion liquid to a pressure that is uncontainable by a thin film of covering fluid, results in liquid rupture and splashing. The result of such splashing is an uncovered section of the sample in the flow, thus allowing a following pulse unobstructed access for ablation in an ambient air interaction, surrounded by flowing liquid. This is inline with the findings of Zhu *et al* [56] (iii) The focus of the anomalous results could have been unusually good when compared to the general trend of these samples as all the anomalous results were greater than the trend. This is a situation that is a consequence of changing immersion fluid surface geometry, where

non-repeatable flow geometry could act to focus or defocus the beam with respect to time, resulting in varying fluence levels, and varying etch depths. This effect would result in a widened spectrum of depth data, rather than the clear data groupings demonstrated in this data.

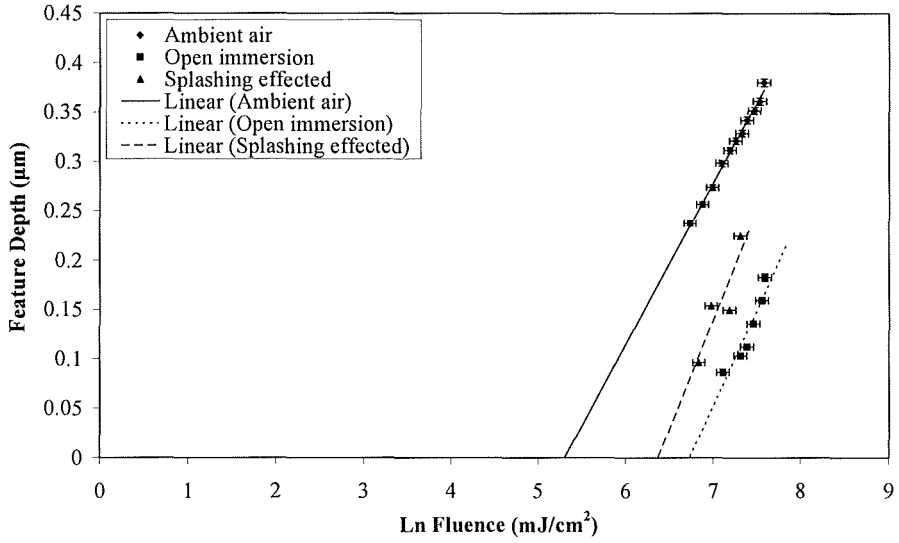

Figure 6-1: Feature depth against fluence to determine ablation threshold for ambient air, normal liquid immersion and anomalous immersion.

The threshold fluence for bisphenol A polycarbonate is only 37.7 mJ/cm^2 in ambient air, indicating the excellent machining attributes that bisphenol A polycarbonate poses for excimer laser machining. Such a finding is in accord with those of Lemoine *et al* [250]. In contrast, the non-anomalous plot for thin film flowing DI water immersion machined samples require 66.7 mJ/cm, a significant increase in threshold fluence over the sample machined in ambient air. This goes against the findings of Fabbro et. al [102] and Elaboudi *et al* [50 - 52], who found that the use of liquid immersion using thicker, stagnant films of ultrapure water greatly reduced the ablation threshold. According to Zhu *et al* an optimum flow thickness for liquid immersion ablation exists [56], occurring at around 1.1mm. Since film thickness is critical, then it is reasonable to postulate that the beam passes through the medium to the sample as normal and ablation commences, generating an ablation plume; the liquid restricts the expansion of the plume, compressing it, increasing its optical density with respect to a similar plume unimpeded in ambient air, thus resulting in greater plume shielding and lower laser ablation rates. Simultaneously, the increased pressure of the plume, in union with the thin (less than 1.1mm thickness) laminar film causes rupture of the flow, resulting in splashing of the immersion liquid and a loss of plume pressure before the plume etch threshold of the material is achieved. Hence the laser ablation rate is decreased without the addition of plume etching that normally occurs when using thick (over 1.1mm) films. This indicates that the four erroneous data points plotted in Figure 6-1 were machined in a situation where the etching contribution given by the laser beam was higher: The splashing occurred in a mode that allowed more pulses to arrive at the sample surface without having to pass through a liquid medium, thus not experiencing the shielding of the compressed plume generated by the previous pulse, giving a lower effective threshold fluence at the image.

The gradients shown in Figure 6-1 for ambient air and thin film flowing DI water immersion machining suggest that the ablation rate response of liquid immersion with increasing fluence is greater than the response of ablation in ambient air. Further inspection of the plot gradients yields support for the explanation of the anomalous results detailed above. The anomalous data points display the steepest gradient and all fall close to the trend line. This observation supports the idea that changes in liquid flow geometry gives increased ablation rate rather than the effects of randomly improved focus. The precise cause of this change in geometry can also be attributed using the gradient as evidence; for if the erroneous results were purely due to nozzle generated flow variations the gradient would have been similar to that of the non-anomalous results, but less tightly packed around the trend line as this would be a random error response. More likely is a change in liquid geometry due to plume generated splashing: as fluence rises, volumes of water removed from the flow by splashing are proportionate. Consequently, higher fluence pulses result in greater exposure of the surface to ambient air and more exposure to an ambient air level of laser etching, as alluded to in great detail in Chapter 9 of this contribution.

6.2 Effects of Thin Film Flowing De-ionized Water Immersion Ablation on Ablation Rate

The ablation rates for bisphenol A polycarbonate machined in ambient air and under thin film flowing DI water immersion are shown in Figure 6-2. The ablation rate is gives useful information concerning volumetric removal of material once above the fluence threshold of the material and will give further insight into efficiency of etching under a thin laminar flow water film. It must be noted that the plot made in ambient air is less prone to error due to the higher number of pulses used. Despite the small number of pulses used to collate data for immersion ablation, the plot generated shows that every point is close to the trend line; thus an accurate measurement of the true ablation rate has been obtained.

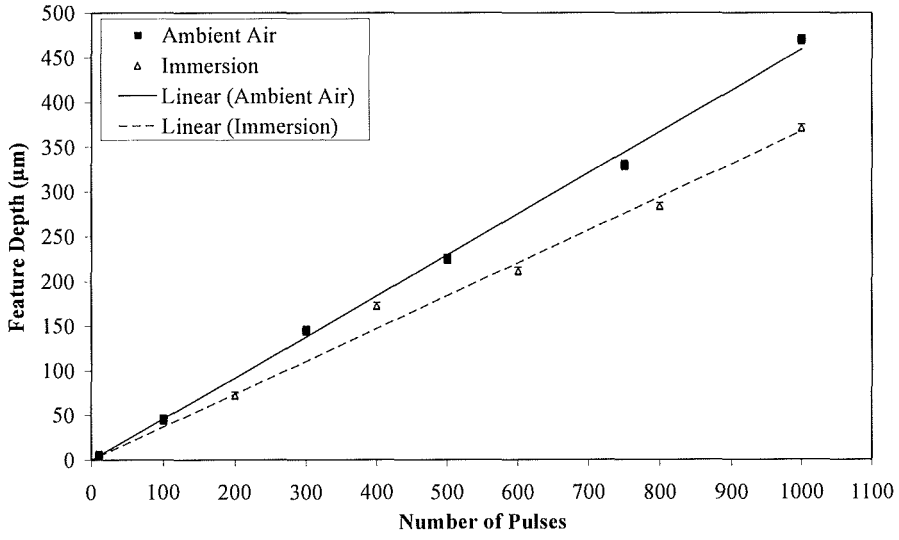

Figure 6-2: Ablation depth against number of pulses to determine ablation rate in ambient air and under DI water liquid immersion.

Figure 6-2 demonstrates KrF excimer laser machining in ambient air offers higher ablation rates than thin film flowing DI water immersion machining as would be expected given the threshold fluence values determined from Figure 6-1, but the decrease in ablation rate due to the use of immersion ablation is not significant. The difference between the gradients of the trend lines for ablation in ambient air and under thin film flowing DI water immersion is 0.09, showing a drop in ablation rate of 20%. It was expected that ablation rate in liquid would be lower than that of ambient air; if the threshold fluence for removal of material in ambient air is half that required under open thin film flowing DI water immersion, it can be expected that removal of material will continue at a similarly high rate once the fluence threshold is exceeded. Instead the difference in ablation rate is minimal (50% was expected; 20% was measured), once again supporting the proposed scenario stated above, where ablation plume motivated splashing of the immersion fluid film releases the plume vapour and allows less plume shielding of the following pulse.

6.3 De-ionized Water Attenuation of KrF Excimer Laser Radiation.

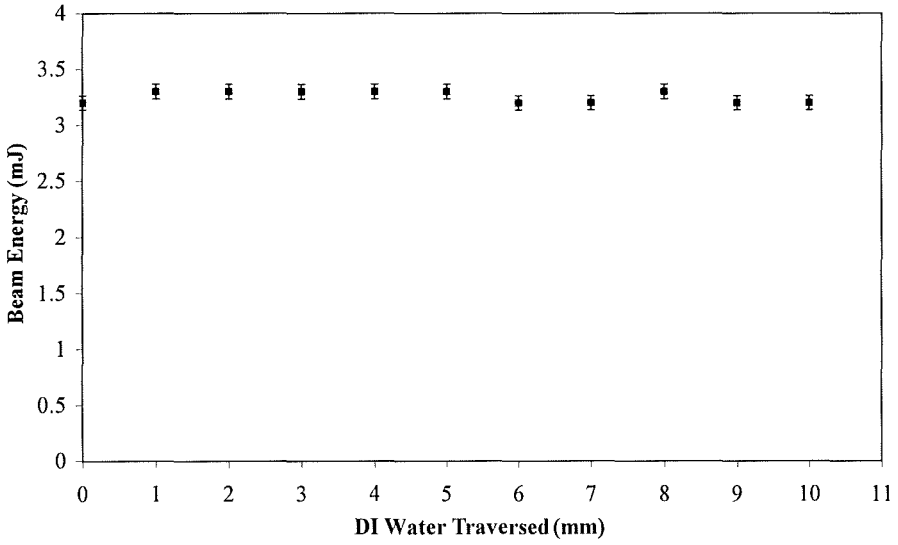

Figure 6-3: Out of focus laser beam pulse energy against thickness of DI water traversed by the KrF excimer laser beam.

The results of the ablation threshold and rate experiments detailed above are interesting; they raise two potential reasons for the response to medium change: (i) increased plume shielding generated by restricted plume expansion as described by Zhu *et al* [56], without the plume etching mechanism that normally accompanies plume compression due to vapour plume motivated splashing of the immersion film before plume the plume etch pressure threshold of the sample is achieved; (ii) the attenuation of the DI water medium is significantly different to that of air and is attenuating the beam on route to the sample and lowering the image fluence. For conclusive support for one of these possibilities the attenuation of the immersion medium was measured. A special pot has been manufactured, using a fused silica slide that has been epoxy resin bonded to a transparent acrylic tube which is internally marked with a millimetre scale. This pot was placed on top of the power meter head, both of which are a significant distance below the image plane of the optics. The mask used for this experiment would give a 500 μm diameter circular spot at focus. The water level and corresponding readings

taken are plotted in Figure 6-3. The effect of increasing water depth for the beam to pass through is small. Most fluctuations in the values can be explained by the random variations in pulse energy, pulse to pulse, inherent of excimer lasers. Thus it follows that the loss of ablation rate by use of liquid immersion must be a mechanism other than immersion medium attenuation of the KrF excimer laser beam. Hence this result gives further support for the proposal that splashing and the mode of splashing with regard to the loss of plume etching and increase in plume shielding is the reason for a loss in lasing efficiency. Indeed, the findings of Fabbro *et al* [102] and Elaboudi *et al* [50 - 52] showed for open thick film immersion lasing efficiency is increased, but Zhu *et al* [56] showed that the effectiveness of an open film is limited to a critical film thickness of 1.1mm. The findings in this thesis were obtained using a film thickness much lower than 1.1mm. It must be noted that the fluence of the beam at the surface of the liquid is insufficient to cause splashing, thus the effect of splashing to the loss of beam energy cannot be measured with this technique. It would be of interest to define a magnitude for the effect of splashing by placing a pool of water in the DoF of the laser optics and taking a set of beam energy readings for differing energies and liquid depths. Nevertheless the findings herein are insightful insofar as they show that a loss in lasing fluence, and therefore efficiency, is not the result of the DI water liquid medium when using open thin film laminar flow immersion assisted machining, but is caused by the interaction between vapour plume, beam and surrounding thin liquid medium.

CHAPTER 7

TOPOGRAPHY AND GEOMETRY OF FEATURES MACHINED INTO BISPHENOL A POLYCARBONATE USING OPEN THIN FILM FLOWING DE-IONIZED WATER IMMERSED KrF EXCIMER LASER ABLATION

All media through which electromagnetic radiation pass present resistance to progress dependent upon medium characteristics and wavelength. The use of a liquid to cover a material to be ablated poses an added complexity to the beam path. In this work the KrF excimer laser beam must pass from the de-magnifying optic, into ambient air, then into de-ionized (DI) water before colliding with a sample surface, whereafter the beam should reach focus. Until now no work has been conducted to relate the impact of ablation medium modification to the surface topography of the features machined. The rippled surface of the DI water flow across the surface may generate localized defocusing of the beam, with drastic effect on the surface topography of the sample. As such, this Chapter will present novel work that offers further interpretation of the laser ablation modification by sample DI water immersion using new surface topography information.

7.1 Effects of Open Thin Film Flowing De-ionized Water Immersion Ablation on Feature Waviness

In the first instance it is worth inspecting the trends generated by the three filters used to determine the use of each data set and also gain an understanding of the scales of surface morphological features produced by both KrF excimer laser ablation in ambient air and under thin film flowing DI water immersion. Figure 7-1(a) plots the mean RMS surface waviness measured at the six beam fluences used in ambient air. As one can see all three plots produce similar trends, suggesting all three are useful and that the waviness morphology was measureable using all three filters in this instance. As one would expect, filter size is inversely proportional with undulation amplitude; this is because less period distance is available for surface elevation change when using a small filter. Figure 7-1(b) plots the mean RMS surface waviness measured at the six beam fluences used under open thin film flowing DI water immersion. Again all three plots show similar trends, showing that all three filters generated valid data and therefore the immersion technique did produce surface morphology with a feature size of less than 8 μm.

Visual comparison of two samples produced using the highest beam fluence of 593.3 and 594.9 mJ/cm^2 for KrF excimer laser ablation in ambient air and under open thin film flowing DI water immersion respectively demonstrates that ablation in ambient air produces crisp, well defined feature shapes with steep wall angles, as shown in Figure 7-2(a) and Figure 7-2(b); when compared to the poorly defined features displayed in Figure 7-2(c) and Figure 7-2(d). However, despite these general observations, the waviness of the surface at the bottom of the features produced in ambient air and under open thin film flowing DI water immersion appears similar. This observation is further

confirmed by comparison of the profile waviness values returned from Figure 7-2(b) and Figure 7-2(d). Here Wq was taken from a two dimensional profile across the centre of the features, giving values of 0.24 and 0.286 μm for KrF excimer laser ablation in ambient air and under open thin film flowing DI water immersion respectively.

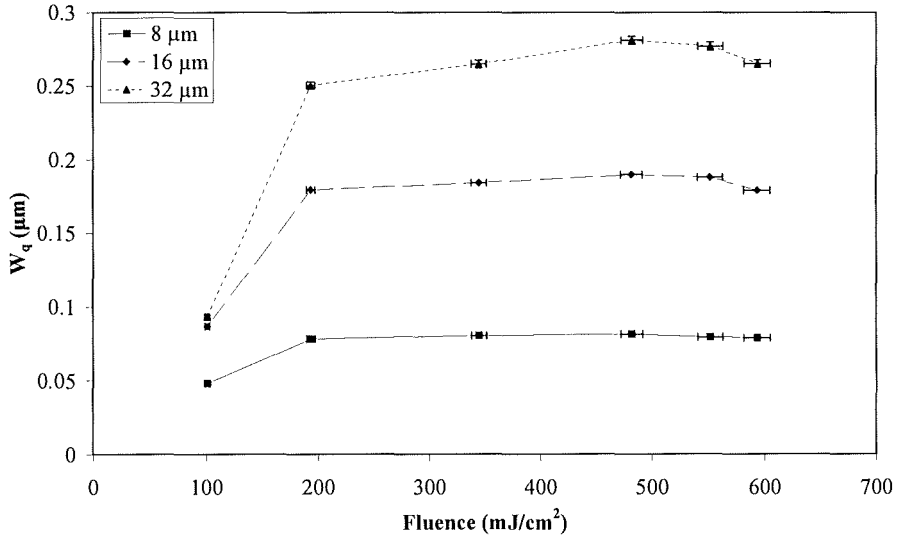

(a)

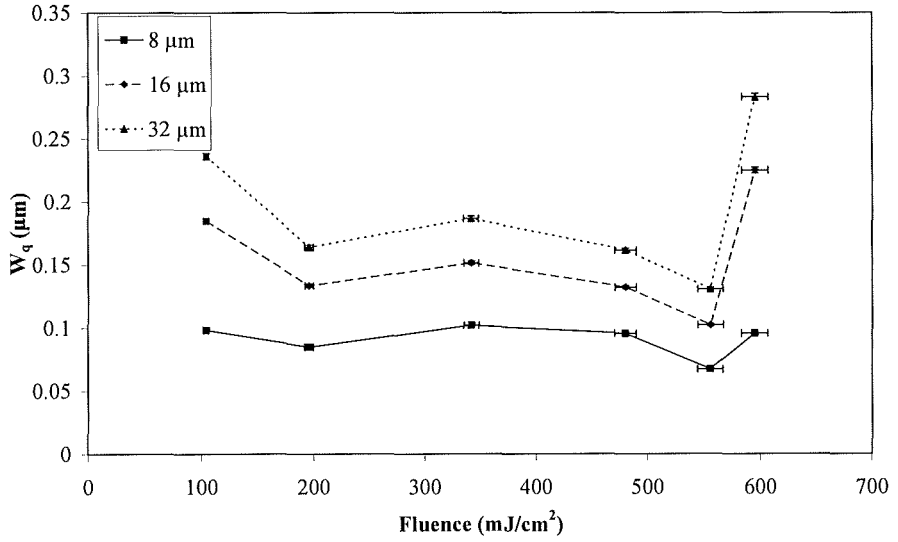

(b)

Figure 7-1: Plots for 8, 16 and 32 μm cut-off filters showing RMS surface waviness amplitude with respect to fluence used to ablate bisphenol A polycarbonate in (a) ambient air and (b) under open thin film flowing DI water immersion.

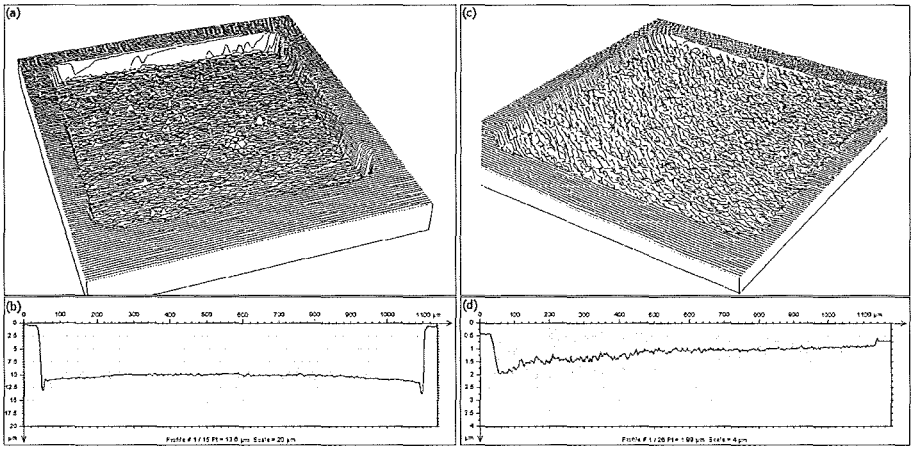

Figure 7-2: 3D views of entire features ablated in (a) ambient air and (c) under open thin film flowing DI water immersion; and 2D profiles from the cross-sections of features ablated in (b) air and (d) under open thin film flowing DI water immersion.

Use of surface analysis provides values that have less tendency to be skewed by anomalous extremities due to the filtering technique and the much larger population of data points available when compared to the profile technique offered in the previous paragraph. The filter size of 16 μm can be used (as it has been previously show to offer a reliable trend, above) the mean RMS surface waviness of samples produced using fluences of 593.3 and 594.9 mJ/cm^2 in ambient air and under open thin film flowing DI water immersion respectively are displayed graphically in Figure 7-3(a) and Figure 7-3(b) respectively. With this technique a Wq value of 0.179 μm is returned for KrF excimer laser ablation in ambient air and 0.225 μm for KrF excimer laser ablation under open thin film flowing DI water immersion. KrF excimer laser ablation under open thin film flowing DI water immersion produced a surface that had 26% more mean waviness than a similar sample produced using KrF excimer laser ablation in ambient air.

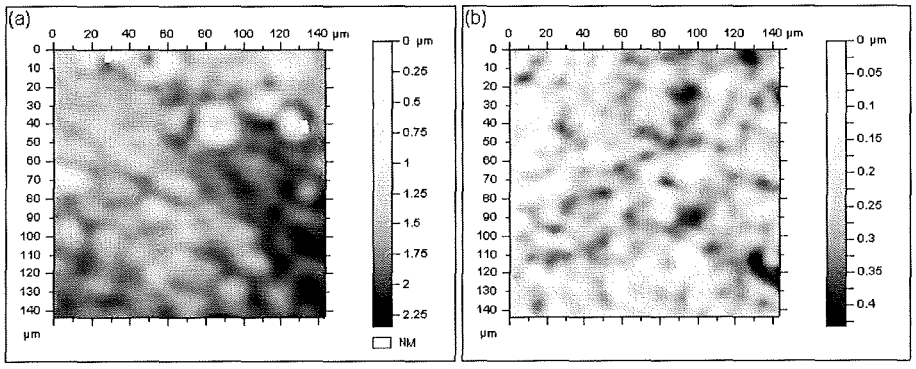

Figure 7-3: Area colour maps describing the surface amplitude undulation for features with a wavelength greater than 16 μm generated by KrF laser ablation in (a) ambient air and (b) under open thin film flowing DI water immersion.

Further detail can be gleaned by plotting the change the relationship between surface waviness and fluence. This has been done and is shown in Figure 7-4, where KrF excimer laser ablation in ambient air and under open thin film flowing DI water immersion shows that the surface waviness generated by a KrF excimer laser beam in ambient air is much more stable and predictable than that produced by a similar beam under open thin film flowing DI water. Inspection of the plot for

KrF excimer laser ablation ambient air in Figure 7-4 also shows that the fluence appears to have little impact on the RMS surface waviness of bisphenol A polycarbonate. The same could be true of the KrF excimer laser ablation in ambient air and under open thin film flowing DI water immersion, but the result is so unstable that no solid interpretation can be taken. The plot for KrF excimer laser ablation under open thin film flowing DI water immersion does demonstrate that there is little to be done to predict the machined surface waviness with respect to fluence, given the number of samples used for this thesis to guard against error. All that can be said of this immersion technique is that is produces surface waviness of a similar magnitude to KrF excimer laser ablation in ambient air. Figure 7-4 also shows that the relationship listed for the highest fluences used for this thesis, used for interpretation above are not representative of the relationship between fluence and surface waviness in general. The highly inconsistent surface profiles produced using this immersion technique is likely to be generated by the uneven film thickness resultant of film flow surface ripple.

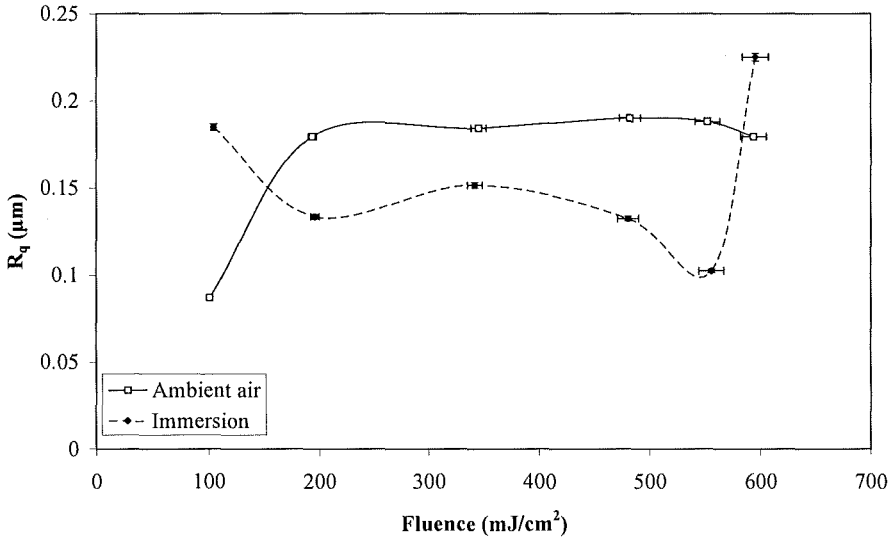

Figure 7-4: Surface waviness (features greater than 16 µm in wavelength) against fluence for features machined in ambient air and under open thin film flowing DI water immersion.

This ripple was a result of meniscus, which defined the flow geometry, thus the effect of rolling eddies alone were not responsible for the deposition patterns evidenced in Chapter 5 of this thesis, where debris distribution appeared to lie in ripple patterns downstream of the feature machined. Instead, large inertial, capillary and viscous contributions act to generate inconsistent flow geometry. This means that the covering thickness differs with respect to location and thus the containment of the plume also varies. This means that localized premature rupture can occur in some locations in the beam and not others, thus causing the uneven surfaces witness in this thesis to be generated.

7.2 Effects of Open Thin Film Flowing De-ionized Water Immersion Ablation on Feature Roughness

In the same manner as used for surface waviness, the initial step to be taken must be to consider the relevance of the data collated. Figure 7-5(a) plots the mean RMS surface waviness measured at the six beam fluences used in ambient air. It is clear from Figure 7-5(a) that the three plots produce similar trends, suggesting the roughness morphology was measureable using all three filters. As before, filter

size is inversely proportional with undulation amplitude. Figure 7-5(b) plots the mean RMS surface roughness measured at the six beam fluences used under open thin film flowing DI water immersion, showing the same agreement of trends found in Figure 7-1 and Figure 7-5(a); therefore, it can be said this immersion technique did produce surface morphology with a resolution of less than 8 μm. Figure 7-5(b) shows and interesting trend for all traces at high fluence; the roughness increases as a spike between 550 and 600 mJ/cm^2. This could be a result of a modification to the ablation mechanism as fluence increases. Excessive fluence when the ablation plume is confined by an immersing liquid could cause excessive plume heating of the feature and therefore result in increased melt. Alternatively, high fluence used in conjunction with liquid confined ablation plumes could result in increased levels of photo mechanical, shear stress dependent, material removal and surface roughness.

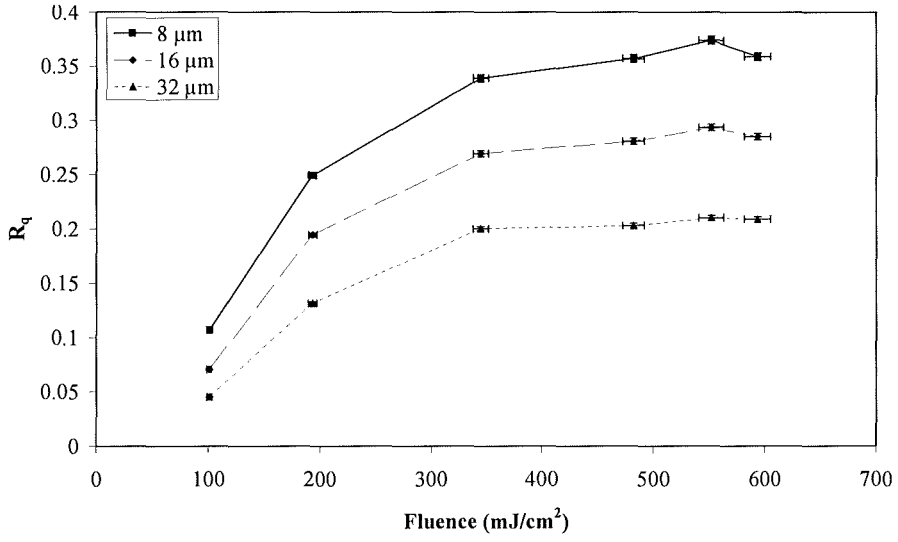

(a)

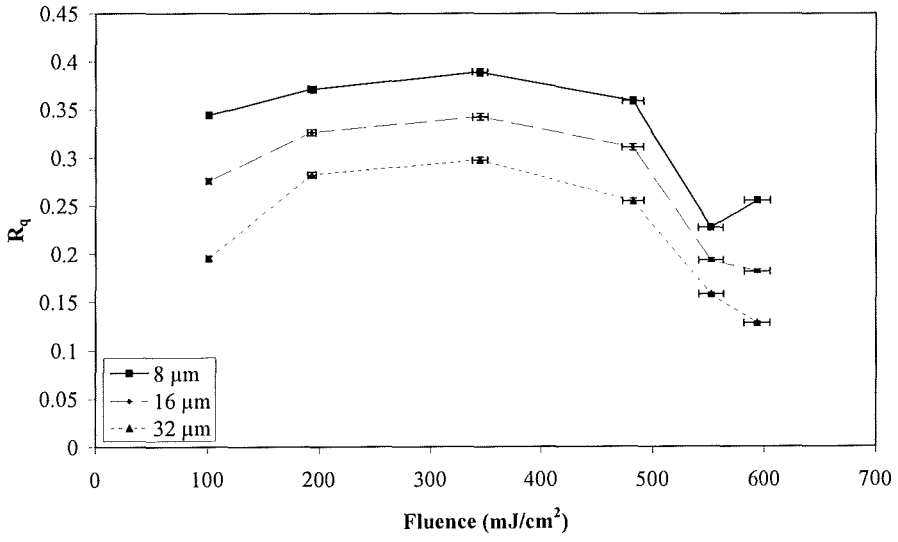

(b)

Figure 7-5: Plots for 8, 16 and 32 μm cut-off filters showing RMS surface roughness amplitude with respect to KrF excimer laser fluence used to ablate bisphenol A polycarbonate in (a) ambient air and (b) under open thin film flowing DI water immersion.

The two samples produced using the highest beam fluence of 593.3 and 594.9 mJ/cm^2 for KrF excimer laser ablation in ambient air and under open thin film flowing DI water immersion respectively can be compared initially using a simple visual comparison, as in the manner used for waviness. Ablation in ambient air appears to produce features with an even surface morphology, as shown in Figure 7-6(a), when compared to the apparently rough surfaces of the features produced under open thin film flowing DI water immersion, as displayed in Figure 7-6 (b). The roughness of the surface at the bottom of the features produced in ambient air and under open thin film flowing DI water can be measured using analysis of surface cross-sectional profile to generate a roughness value in the same manner as that used for surface waviness above. A profile of KrF excimer laser ablation in ambient air is given in Figure 7-2(a) and under open thin film flowing DI water immersion in Figure 7-2(b). Here, R_q was taken from a two dimensional profile across the centre of the features, giving values of 0.398 and 0.297 μm respectively.

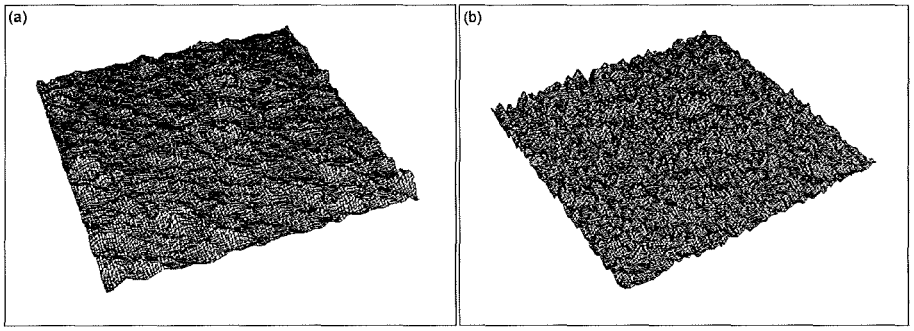

Figure 7-6: Close-up 3D view showing the small scale surface topography (roughness) of a sample produced using KrF excimer laser ablation in (a) ambient air and (b)under thin film flowing DI water immersion.

The filter size of 16 μm can be used to for analysis of a surface in terms of roughness. The mean RMS surface roughness of samples produced using fluences of 593.3 and 594.9 mJ/cm^2 in ambient air and under open thin film flowing DI water immersion respectively are displayed graphically in Figure 7-7(a) and Figure 7-7 (b) respectively. With this technique a mean W_q value of 0.285 μm is returned for KrF excimer laser ablation in ambient air and 0.182μm for KrF excimer laser ablation under open thin film flowing DI water immersion. Thus, it would appear that use of open thin film flowing DI water immersion generates a significant reduction in surface roughness from ablation in ambient air of 36%.

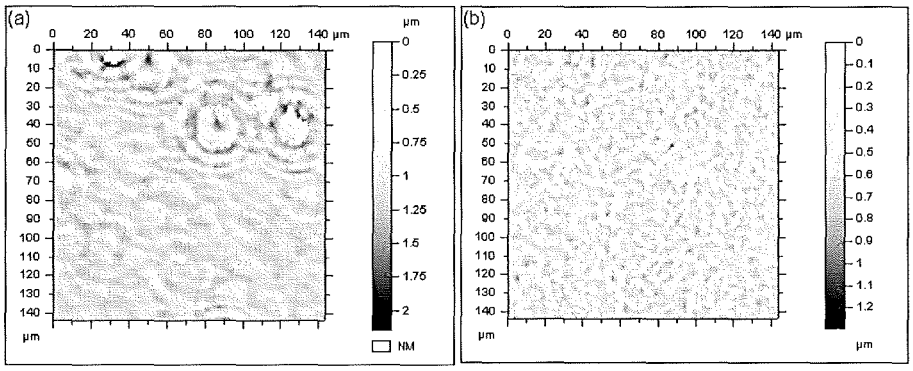

Figure 7-7: Area colour map describing the surface amplitude undulation for features with a wavelength lower than 16 µm generated by KrF excimer laser ablation in (a) ambient air and (b) under open thin film flowing DI water immersion.

The relationship between mean RMS surface roughness and fluence, where KrF excimer laser ablation in ambient air and under open thin film flowing DI water immersion is plotted with respect to the mean laser fluence used to produce each feature is given in Figure 7-8. It is evident from Figure 7-8 that there is a marked contrast in trend between the surface roughness of features produced using a KrF excimer laser beam in ambient air and under open thin film flowing DI water. Inspection of the plot for KrF excimer laser ablation in ambient air given in Figure 7-8 shows that the surface roughness is related to beam fluence by a 4th order polynomial relationship. In contrast, the plot for the samples KrF excimer laser machined under open thin film flowing DI water immersion demonstrates a less mathematically definable relationship, but has a maximum Rq of 0.34 µm at 341.4 mJ/cm^2 and a characteristic outlying point for the maximum fluence used of 594.9 µm, which does not follow the trend dictated by its counterparts. The sudden drop in roughness above 500 mJ/cm^2 could be a result of the action of ablation plume compression exceeding the level that can be contained by the thin film fluid flow and generating large volumes of film splashing, as witnessed during the experiments. The ablation plume pressure is directly related to the laser fluence. High roughness is symptomatic of the aggressive shock fracture etch mechanism at work in a photomechanical regime promoted by ablation plume confinement in viscous fluids; the drop in surface roughness to a level lower than that achieved by ablation in ambient air at a similar fluence level indicates an immersion medium dependent modification to the ablation plume. The action of splashing at high fluence halts the effect of ablation plume compression and the enhanced photomechanical etching mechanism that it promotes. The airborne fluid after splashing will then interrupt the beam *en route* to the sample surface, causing beam diffraction, diffusion and attenuation; thus reducing the concentrated laser etching ability available in ambient air. This way the surface roughness of the sample was reduced when machining using open thin film flowing DI water immersion with a similar laser fluence the case when ablating in ambient air. Importantly, the magnitude of the two plots are of the same scale. The overall roughness value generated by a KrF excimer laser beam immersed by open thin film flowing DI water was, on average, 17% greater that generated by KrF excimer laser ablation in ambient air.

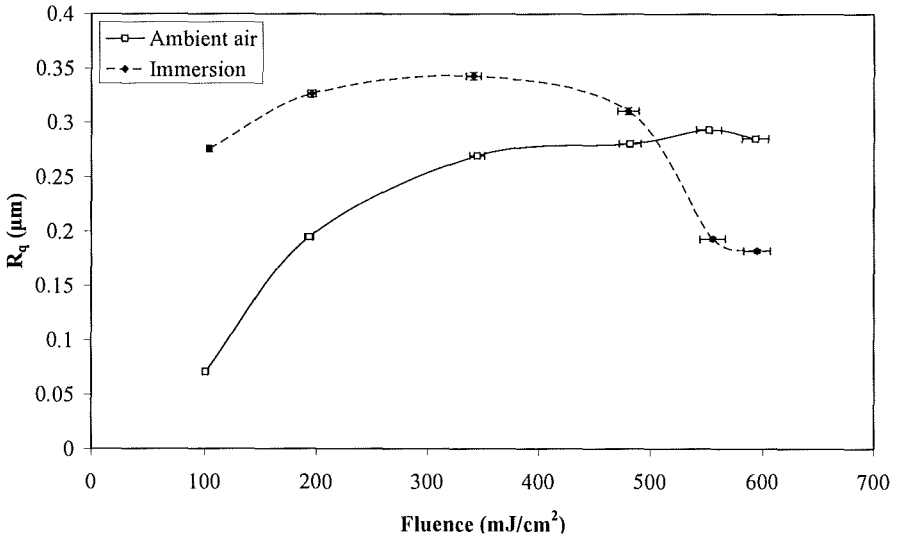

Figure 7-8: Surface roughness (features lower than 16 µm in wavelength) against fluence for features KrF excimer laser machined in ambient air and under open thin film flowing DI water immersion.

7.3 Open Thin Film Flowing De-ionized Water Immersion and the Effects Thereof on Ablation Mechanism and Feature Surface Topography

In ambient air the microscopic and macroscopic topography of a machined feature are likely to be governed by different interaction characteristics. It is known that all excimer beams exhibit poor beam profile homogeneity, even when well calibrated [9]. Indeed excimer beams do not actually produce a Gaussian beam profile as they do not have a single phase across the wavefront, rather they have a pitted and rough wavefront due to the many transverse modes present in an excimer beam [29]. As a result, any optical attempt to correct homogeneity will always be limited by this factor. This error in the beam profile will always result in a small variation in fluence across the image, generating a non-planar machined surface at a nanoscopic scale for every pulse. But, this wavefront error is not a constant feature of the beam and so errors will change with respect to position across the image from pulse to pulse. More important is the macroscopic beam shape: this will result in a deviation from planar machining at the image. This error will grow in size over a number of shots, as described schematically in Figure 7-9, due to the macroscopic beam profile being repeatable from pulse to pulse [9]. With each new pulse the cumulative error from the desired machining plane grows as the supplied macroscopic energy density error with respect to location remains similar for every pulse. The feature geometry machined by KrF excimer laser ablation in ambient air was well defined, with high wall draft angles. This would suggest that photomechanical ablation was not the dominant factor in removal in ambient air as this etching mechanism would be concentrated at the centre of the feature and be inversely proportional to radius from the centre of the feature. This in turn would result in a concave geometry, rather than the crisp geometry displayed in the results.

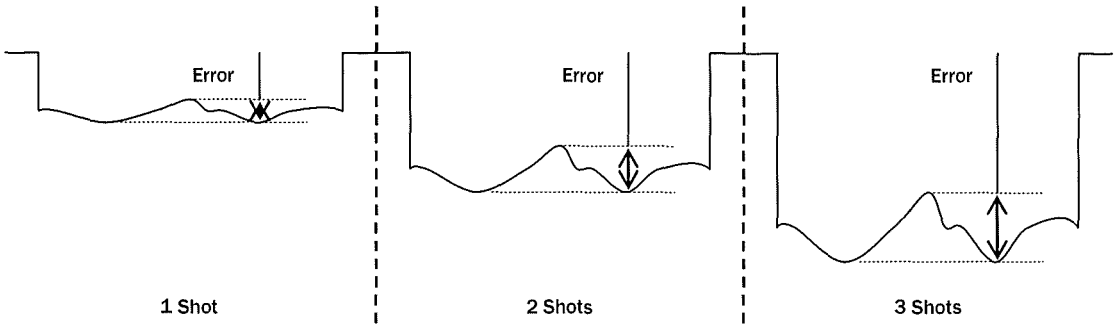

Figure 7-9: Schematic depiction of the result of repeatable errors in macroscopic beam shape over a number of pulses.

The surface roughness of an excimer laser machined feature is dependent upon the ablation mechanism that removed the material to produce the feature. This ablation mechanism is a complex and contentious subject, with recent literature alluding to a number of mechanisms that work together simultaneously [34]. The most common practice for laser micromachining is for ablation to take place in an ambient air environment, allowing simple material loading and rapid processing times without the need for time consuming gas evacuation procedures. The ablation mechanism is also material specific, with much debate surrounding the exact nature of polymer interactions with short wavelength laser beams. In the case of a 248 nm beam interacting with a polymer material in ambient air, the theory of explosive evaporation, postulated by Kelly and Miotello [30, 251], which accounts for a primarily photochemical interaction with a photothermal element active between beam photons and the material's atomic matrix. Yang [76] develops on this to explain that formation of ablation products during PLA in gasses is a result of condensation of the plasma plume generated by the ejection of ablated gaseous products from the solid target. In this scenario there are three critical stages: generation, transformation and condensation. The key stage with respect to a machined feature is the generation phase. In the case of laser ablation in gas at atmospheric pressure, the vapour plume can expand relatively unimpeded as there is little difference in density and viscosity between the vapour plume and surrounding atmosphere as described in Figure 7-10(a).

When ablating material beneath a film of liquid the interaction between beam, plume and material is different from the interaction that would take place in ambient air. The expansion of the plume is now restricted by the increased viscosity of the surrounding liquid [76], with molecules attempting to escape the plume are prevented by the plume/liquid interface as described in Figure 7-10(b). The confinement of the ablation plume has been found by Zhu *et al* [56] to etch the surface of the workpiece. Zhu *et al* claim the optimum film thickness for ablation rate to be approximately 1.1mm.

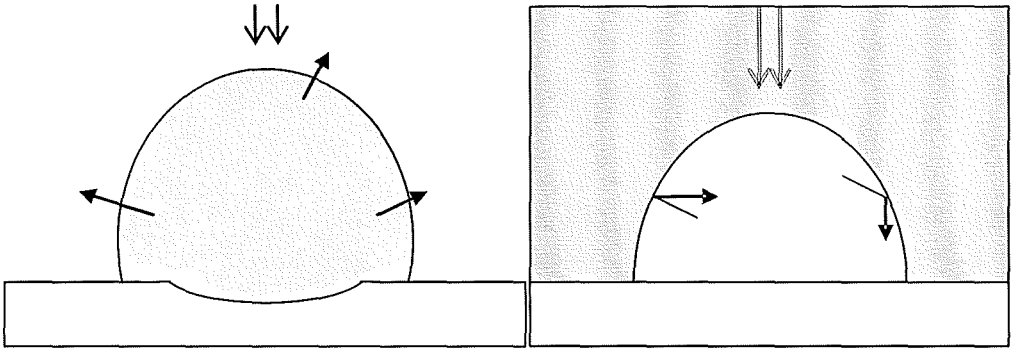

Figure 7-10: Schematic comparison of vapour plumes in air (left) and liquid immersion (right) and the impedance of the liquid to the plume expansion.

The greater mean Rq values measured for the open thin film flowing DI water immersion machined samples compared to that of the sample machined in ambient air are interesting. This result is not in agreement with the studies of Fabbro *et al* [102] and Zhu [56]. The work of these authors has shown that immersion of the ablation plume restricts plume growth, increasing plume pressure, temperature and internal turbulence. This has the action of increasing the plume etching contribution compared to a similar process occurring in ambient air. The increased optical density of the immersed plume means increased plume shielding; thus the beam had lower fluence for etching at the image during immersion ablation than it would in ambient air. It is believed the compressed, hot, turbulent plume vapour cited by Fabbro *et al* [102] will cause highly homogenous ablation rates at a microscopic scale. However, this thesis differs from the work of previous observers as it uses a thin film regime (less than 1.1 mm thick [56]) of rapidly flowing fluid. The enclosure used to seal the machining environment and protect the tool optics was splashed with water droplets with every pulse. The action of ablation plume growth restriction in a fluid medium and the greater plume pressures that result in a thin film regime flow results in flow rupture and splashing, as detailed in Chapter 8. The action of this splashing and the greatly increased complexity of the ablation mechanism that it causes results in the increased surface roughness and the unpredictable nature of the machined sample surface waviness. This action supports the idea that photomechanical etching mechanisms are promoted by liquid immersion as proposed by Elaboudi *et al* [50]. Also, splashing poses potential risk for the tool optics.

All the samples machined using a KrF excimer laser beam in ambient air display a repeated surface anomaly at a location 465 μm from the bottom wall and 630 μm from the left wall of the feature as viewed in Figure 7-2(a). This is something of interest to the casual observer, given the shockwave interaction theory proposed in Chapter 5. The interaction of localized, expanding plumes is claimed to produce the characteristic geometry dependent debris deposition trends witnessed when machining using shaped laser beams in gaseous media. Thought has not been dedicated to the result of the interaction of plumes inside the ablated feature. The near central location of the surface anomaly and its repeatable location within the feature are proposed to be a result of this plume interaction within the feature. The interaction between the separate plumes appears to make a morphological medication to the machined material surface structure. All samples machined under open thin film flowing DI water immersion also display this anomaly, but in a new position, repeatedly 430 μm from

the bottom wall and 460 μm from the left wall of the features machined as viewed in Figure 7-2(c). However, these features are markedly smaller in amplitude than those developed in ambient air. This contribution adds support to the theory that these surface morphological features are ablation plume pressure dependent, as the action of confined ablation plume by liquid immersion resulted in smaller anomaly and a change in anomaly location.

Part III

Closed Thick Film Regime Flowing Liquid Immersed KrF Excimer Laser Ablation of Bisphenol A Polycarbonate

Part III

Closed Thick Film Regime Flowing Liquid Immersed KrF Excimer Laser Ablation of Bisphenol A Polycarbonate

CHAPTER 8

EXPERIMENTAL EQUIPMENT DEVELOPMENT, PROCEDURES AND ANALYSIS FOR CLOSED THICK FILM FLOWING LIQUID IMMERSED ABLATION

The experimental and analysis techniques used in Part III of this thesis build on those used in Part II. New developments will be described and explained in this Chapter. The poor performance of the open thin film liquid KrF excimer laser ablation immersion technique in terms of the feature machining dictated that a new technique be developed to control the effect of laser ablation plume motivated rupture and the resultant splashing. To this end new equipment was designed featuring a closed duct liquid immersion flow geometry that has never been explored as a means of broad beam laser ablation etching control. This technique allowed the investigation of flow velocity variation and the resultant effects this has on the laser ablation mechanism, an interesting subject that is explored in this thesis for the first time and is of direct relevance of emerging laser ablation mechanism science.

8.1 Introduction

To continue the work carried out so far, it was important to use a similar laser energy source for the means of comparison. The KrF excimer laser micromachining centre used for the work covered in Part II was retired after that work had been completed and replaced. The work outlined in the following Chapters has been compiled using the analysis of samples machined using another KrF excimer laser based micromachining centre. As was done in Part II, the precise settings and output of the laser measured at the image will be reported individually for each set of results. However, the performance is not markedly different, the maximum achievable laser pulse energy is 150 mJ greater, but this can be controlled and the pulse duration is significantly reduced over that of the laser used previously; only this parameter could cause a noticeable difference in the ablation performance of the comparative systems. A more marked impact was made by the functionality of software control 'fire-on-demand' technology that was a feature of the newer laser micromachining tool used for this part. Substantially increased immersion durations and flow velocities that were possible due to the inclusion of a pump for liquid supply and the multifunctional character of the closed thick film immersion ablation equipment developed as an evolution of the work described previously in Part II.

8.2 Laser Details

For this thesis an excimer laser was used (LPX200; Lambda Physik, GmbH); a more modern unit than that used for the experiments in Part II. This laser could be filled with a KrF gas mixture to produce 20 ns, 550 mJ pulsed UV light with a wavelength of 248 nm at 200 Hz, resulting in a peak stated operating power of 120 W. Also, this laser had full output control by means of an

LCU; thus a requested pulse energy was supplied with more repeatability than was available using the previous arrangement.

8.3 Material Details

For the purposes of the continuity of this thesis, identical materials along with preparation and storage techniques were used for the closed thick film flowing liquid immersed KrF excimer laser ablation work that will be covered in the following Chapters. See Section 4.2 for full details.

8.4 Beam Control

The laser micromachining centre that made use of the laser specified above was markedly superior to that used in Part II in many ways as will be described in Section 8.4.1. However, it did lack one optical feature that the previous system did have in its favour: laser beam homogenising optics. As described in Figure 4-3, this optical element acts to modify a Gaussian beam profile to a much more feature profile machining conducive top-hat profile. To rectify this problem, a de-magnifying lens with low magnification, 4x optic (Francis Goodhall, Ltd), was used alongside small orifice (800 x 800 μm square and 800 μm diameter circular) laser beam masks, formed by use of femtosecond laser cutting of copper shim. Doing so allowed only a small area of the un-homogenized Gaussian beam profile to be sampled as described schematically in Figure 8-1. As proof of this technique actual measured beam profiles taken at after the laser mask, but before de-magnification, are given in Figure 8-2.

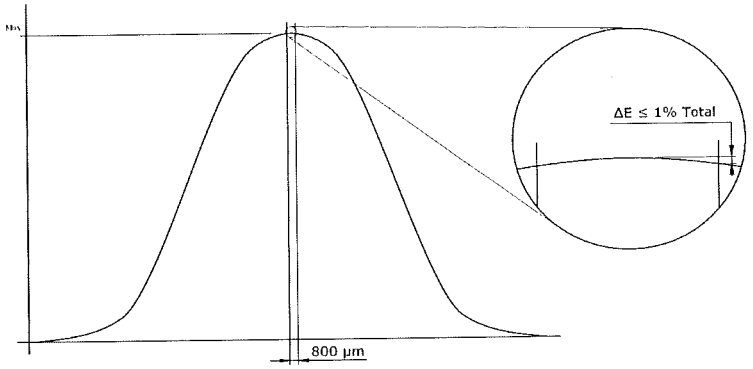

Figure 8-1: A schematic diagram describing the resultant action of sampling just a small area in the centre of a Gaussian laser beam.

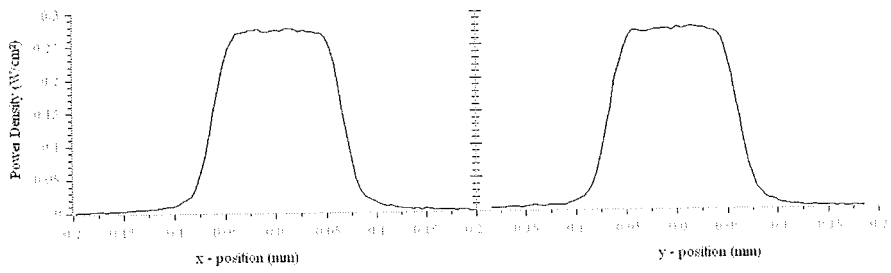

Figure 8-2: Cross-sectional x- and y-axis power density profiles taken using a CCD laser beam profiler.

8.4.1 Laser micromachining centre details

The system (M8000; Exitech, Ltd) used in this research used a granite based chassis and as such, encompassed all of the advantages that comes with this feature: greater vibrational stability; markedly reduced thermal instability; increased bearing surface flatness and the ability to use linear motor driven air stages (Aerotech, Ltd), affording this system greater positional precision and stability. This system also featured a software controllable laser beam attenuator situated in the optical arrangement described schematically in Figure 8-3. This item presented the ability to manufacture multiple features using varying laser beam fluence on a single sample in one machine run. This will be useful in a number of ways: it allows more samples to be produced for better data averaging, as is covered in detail in Section 8.4.3; it allows feature neighbour cross contamination prevention to be investigated, as covered in Section 8.6.1; and it dictates that all features compared are machined during one machine run, with identical flow parameters, further improving the scientific rigour of this thesis.

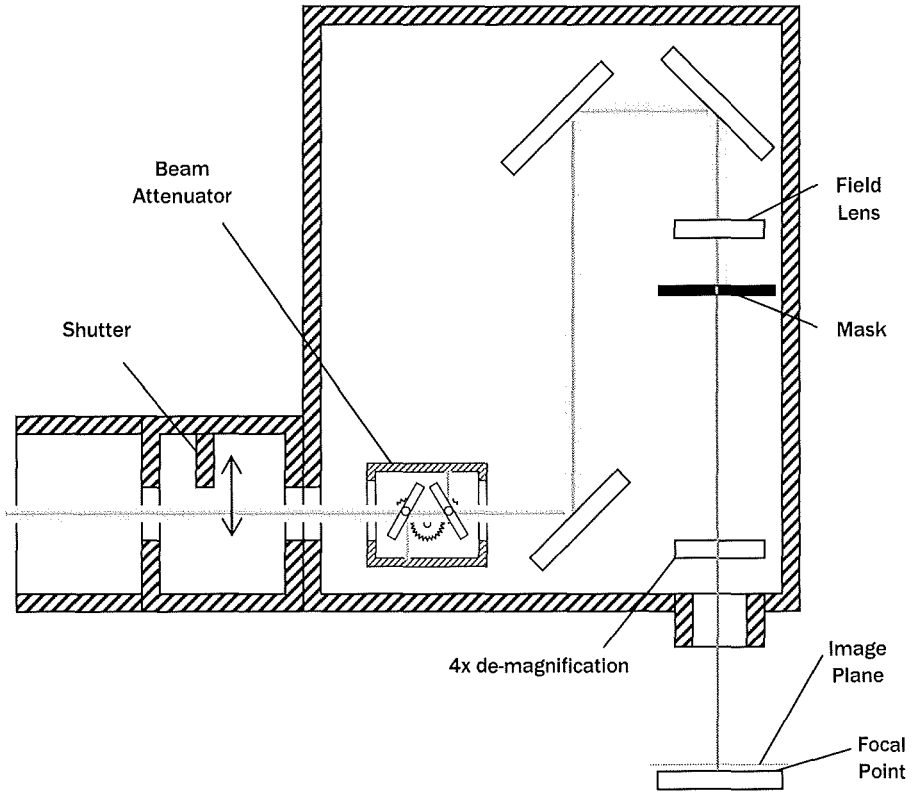

Figure 8-3: Schematic diagram of layout of the optics box.

8.4.2 Image plane control

Furthermore, this system did include the dual PSO fire on demand software controlled laser firing and stage positioning. Combined with the new fully sealed and pump supplied equipment used as will be described in Section 8.5.3, this allowed sustained machining over periods of minutes, rather than seconds as before; thus, multiple features could be produced together, on one sample, allowing feature debris contamination from other machined features to be explored.

All features examined in this thesis had two neighbours: every one lying 200 μm away from the sample on either side. Critically, these features are aligned across the direction of liquid flow. One

feature is produced before each of the samples inspected in this thesis using just three pulses, the feature inspected in this thesis is produced using six pulses, then following this, another feature is machined to the right of the feature of interest using twelve pulses. The use of neighbouring samples is important in the context of this thesis: when machining features into a sample industrially, it is common for multiple features to be machined at separate times or even during separate phases of manufacture [1]; thus the importance of preventing cross contamination of debris produced from one feature impacting the quality of another is high.

Focus was found by producing features over progressively narrowing focal rage until satisfactory focus was achieved. This was possible due to the high stability and repeatability of the laser micromachining centre used, and was not an option on the previous system due to instability.

8.4.3 Fluence measurement

This fluence data was calculated from pulse energy data taken using a pulse energy head (J50LP-2; Molectron Detector, Inc.) positioned above the focal point of the laser, and enumerated by a KrF excimer laser energy meter (EM400; Molectron Detector, Inc.). The fluence was calculated using the mean beam energy measured (averaging techniques were employed for experimental rigour: beam pulse energy was recorded five times before and after machining each sample, every value recorded was the mean value measured over 100 pulses - between readings the attenuator was reset to account for attenuator position errors) so that any changes in laser output over time were accounted for.

8.5 Equipment used to Facilitate Closed Thick Film Flowing Liquid Immersed Ablation

8.5.1 Ambient air KrF excimer laser processing

Samples machined in ambient air were produced, using the same laser and micromachining equipment as the closed thick film flowing liquid immersed ablation samples. The bisphenol A polycarbonate samples were mounted directly to the vacuum chuck inside the micromachining station. After lasing ended the sample was removed and placed into the cell of a sealed sample tray to protect them from atmospheric dust.

8.5.2 Closed thick film flowing liquid immersion sample mounting equipment

This equipment was designed with contrasting objectives to that detailed and used in Part II. The open thin film flowing liquid immersion equipment was designed to provide flowing liquid immersed KrF excimer laser ablation on samples that could be loaded and removed from the equipment with ease. This requirement dictated the need for the open flow principle. As detailed in the results given in Part II, this technique showed promise concerning the control of laser ablation-generated debris, but performed poorly in terms of machined feature quality. Figure 8-4 describes the critical experimental layout used for the results to be presented in Part III of this thesis. In Part II, the equipment used had many complex constituent features to provide environmental control (the gas filter assembly), liquid

supply (copper tubing) and protection for the laser optics from ablation motivated splashing (the shroud). The equipment described schematically in Figure 8-4 seals the sample inside an air tight chamber that is completely flooded with a controlled fluid when in use, clamps the sample in place securely and prevents ablation generated splashing; thus achieving all of the functions listed above with just one simple assembly. This equipment has far more efficient functionality than that used in Part II. The debit of this innovation is the loss of easy sample loading. The system described in Figure 8-4 is formed from three machined aluminium shims with relevant recesses to allow sample location under Figure 8-4(c) and controlled flowing liquid geometry over the sample surface by component Figure 8-4(e) that located the UV transparent fused silica laser window labelled as Figure 8-4(d). This flow rig was mounted to the side of the sample vacuum chuck of the laser micromachining centre. A water tight seal was maintained by use of o-rings and even force supplied by 8 M4 bolts indicated by Figure 8-4(f), which were time consuming to undo and re-tighten.

The sample was positioned in the centre of the flat aluminium table between the water supply and exit holes. The sample was retained by a recess in a spacer plate (Figure 8-4(c)) that lay in contact with the aluminium sample table (Figure 8-4(b)). An O-ring cord, located by a rectangular groove in the sample table, provided a seal between the sample table and the spacer plate. On the top of the spacer plate a second oval O-ring groove was machined to locate another O-ring cord. This acted as a gasket between the spacer plate and the laser beam window (Figure 8-4(d)) – a 25 x 25 x 5 mm^3 UV grade fused silica sheet (Comar Instruments, Ltd). The beam window was retained by a diamond shaped recess in a third aluminium plate (Figure 8-4(e)), that was 8 mm thick to provide stiffness to the whole sandwich assembly and prevent fracture of the laser beam window.

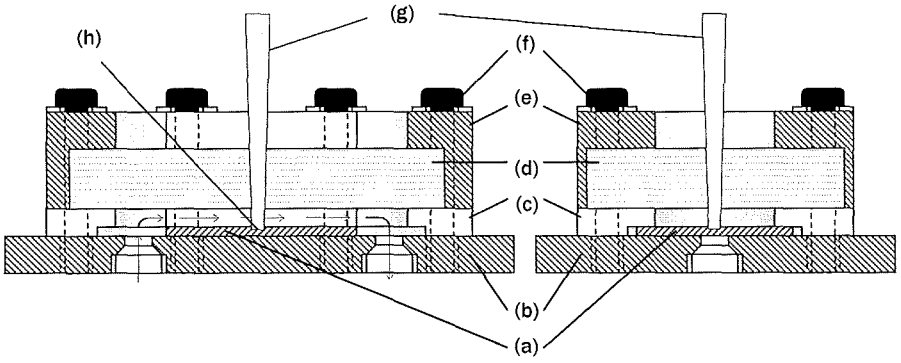

Figure 8-4: Cross-sectional assembly diagram of the closed thick film flowing liquid immersion ablation sample chamber assembly.

8.5.3 Liquid supply

Figure 8-5 shows the water filtering and supply system. Water originated from normal mains supply by wall tap. The water was poured into a domestic water filter (Britta, Inc.) situated at the top the water supply assembly to remove typical corrosive elements present in mains water. The water was then retained in a header tank located above the pump and, under the action of gravity, was forced into the 700 W pump chamber (CPE100P, Clarke Power Products, Ltd.). The pump forced the water through a water flow rate meter (FR4500; Key Instruments, Inc.) and then along a 3 m distance through a 6 mm outer diameter nylon tube to the inlet push-in elbow fitting on the bottom of the

sample table. Last, the water was returned along a further 3 m through a 6 mm outer diameter nylon tube to a collection bucket. The pump was capable of producing 4.2 bar at the outlet, equating to a maximum flow velocity through the ablation chamber of 3.89 m/s, given losses along the supply and return tubing. Precise control of the flow velocity was provided by a variable valve of the flow-meter. Flow velocities of 0.03, 0.11, 1.85, 2.78, 3.24 and 3.70 m/s were used for this thesis.

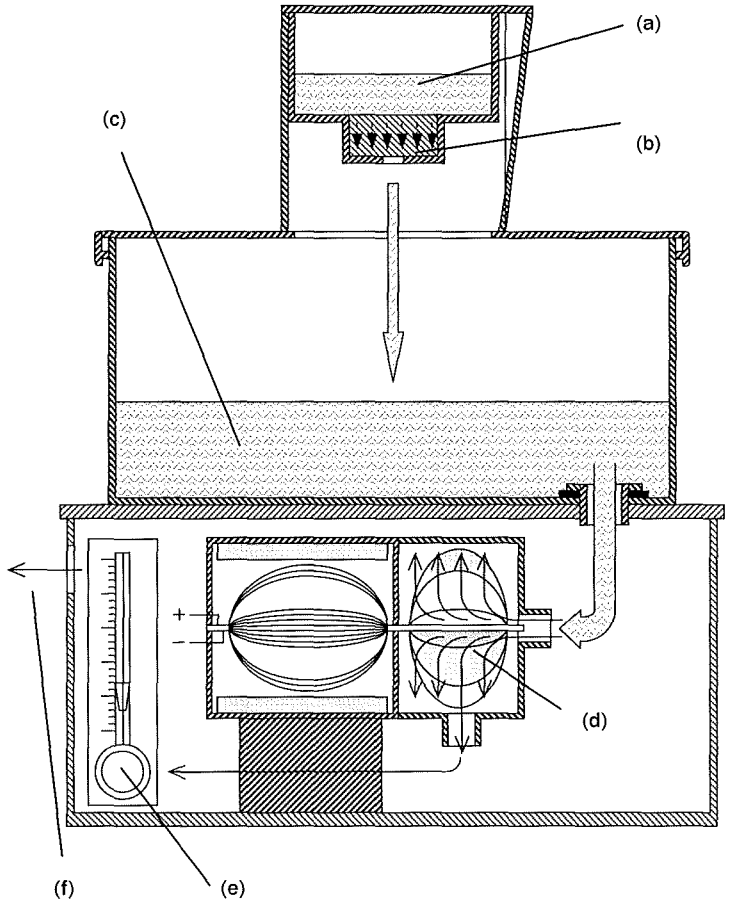

(a) Water from source;
(b) filtering;
(c) filtered water storage;
(d) centrifugal pump;
(e) flow-rate control valve; and
(f) high pressure, flow-rate controlled filtered water outlet to immersion ablation chamber (see Figure 8-4(c)).

Figure 8-5: Schematic diagram showing the arrangement of the fluid supply unit.

8.6 Key Experimental Details

8.6.1 Neighbouring features

All features examined in this thesis had two neighbours: every one lying 200 μm away from the sample on either side. Critically, these features are aligned across the direction of liquid flow. One feature is produced before each of the samples inspected in this work using just three pulses, the feature inspected in this work is produced using six pulses, then following this, another feature is machined to the right of the feature of interest using twelve pulses. The use of neighbouring samples is important in the context of this work: when machining features into a sample industrially, it is common for multiple features to be machined at separate times or even during separate phases of manufacture [252]; thus the importance of preventing cross contamination of debris produced from one feature impacting the quality of another is high.

8.6.2 *Debris Deposition Samples*

The features inspected for the production and deposition of debris were the same features machined for measurement of the ablation rate. In particular, the features machined using six pulses were interpreted in this thesis. This number of pulses again gives further continuity to this experimental work from that conducted in Part II of this contribution. As such, the same preparation and meticulous experimental methodology, described in Section 8.6.4, was adopted for these features.

8.6.3 *Threshold fluence samples*

A sample included six machined sites, each produced using 50 pulses in the same machine run with uninterrupted filtered water flow over the sample during machining. The system attenuator was used to change pulse energy by a repeatable amount between sites. The attenuator positions used were 0.5, 0.6, 0.7, 0.8, 0.9 and 1.0. Figure 8-6 shows the corresponding fluence values measured using this mask for ablation in ambient air and under closed thick film flowing filtered water immersion respectively, that produced features of 203 x 205 μm^2.

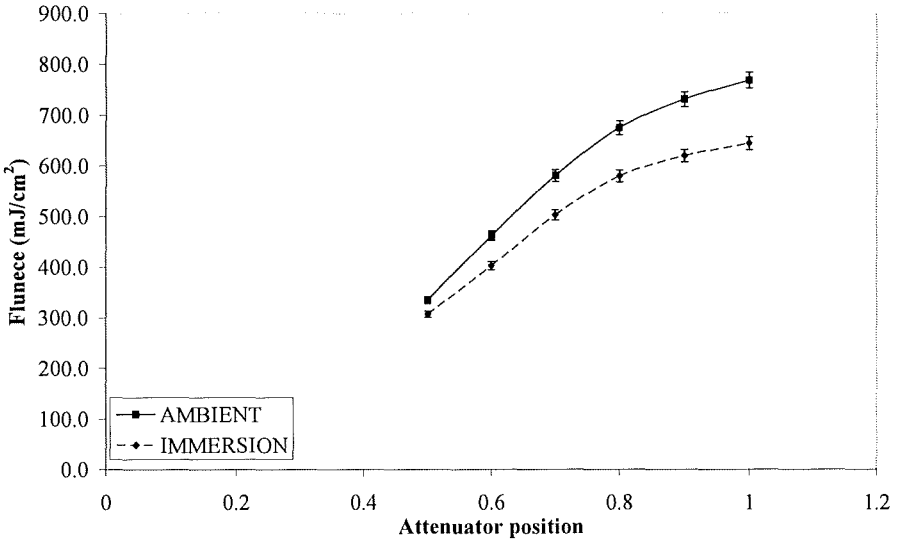

Figure 8-6: Comparison of beam fluence generated at various attenuator positions recorded for both the filtered water samples and the ambient air samples.

8.6.4 *Ablation rate samples*

Six sites were machined on all samples, each produced using an increasing number of pulses (3, 6, 12, 60, 120 and 480 pulses) to produce an ablation rate matrix. The features of interest for debris analysis in this study as the feature machined using six pulses. Six pulses were used for producing the samples that are the subject of this thesis to allow direct comparison to samples discussed in Part II. In this instance the beam was attenuated by a tool attenuator set at 126° from minimum transmission, resulting in a beam fluence of 580.7 and 578.1 mJ/cm^2 for ablation in ambient air and under filtered water immersion respectively, that produced features of 203 x 205 μm^2. This fluence data was calculated from pulse energy data collated as described in Section 8.4.3.

8.7 Analytical Procedures

Generally, the same techniques as those described in Section 4.7.1 were employed for the samples analysed in the remainder of this contribution; however, various improvements have been made to improve the depth and breadth of analysis, whilst also reducing analytical error: increased optical micrograph resolution, as detailed in Section 8.7.1; lighting gradient correction has been introduced, as discussed in Section 8.7.2; and the depth of discrete analysis of the data collated has been increased using techniques covered in Section 8.7.3.

8.7.1 Optical microscope resolution

The same reflective illumination was used as that described in Section 4.7.2, imaged through an optical microscope (Optiphot; Nikon Corp.). But, instead of the magnification used previously, 20x magnification was now employed to increase the effective resolution of the CCD photosensor (GXCAM-5; GT Vision, Ltd.), which had a resolution of 2582 x 1944 pixels. This gave a calibrated pixel area of 0.012 μm^2. A blank micrograph was also taken to account for any dirt that may have been present in the microscope optics and to record the image brightness gradient produced by the illumination technique

8.7.2 Collating images

For numerical data to be produced from solid samples, a number of steps had to be taken to achieve the resolution of data across the broad area of samples machined for this thesis as before; but now this technique was improved for higher resolution. Each sample was imaged digitally as an uncompressed bitmap in nine sectors (bottom left, bottom, bottom right, left, centre, right, top left, top and top right) as before, a process described schematically in Figure 4-10. The sector images were then digitally corrected in terms of brightness gradient and erroneous marks using software (Image Pro 6.2; Media Cybernetics, Inc.) and the blank micrograph, described in Section 8.7.1, as a datum image. The corrected sector images were then combined to a single, large, high resolution bitmap without any compression.

8.7.3 Analysing images

The same software binarization technique was used here as had been employed previously. This is described in detail in Section 4.7.3. The increased resolution afforded by the 20x magnification of the microscope has given a significant improvement in the techniques sensitivity alone. Greater breadth of analysis than was achieved in the Part II of this contribution has been made possible by the application of a matrix processing suite (MATLAB 2008b; The MathWorks, Inc.) to produce six final data sets for samples produced in ambient air and under closed thick film flowing filtered water immersion at flow velocities of: 0.03, 0.11, 1.85, 2.78 and 3.70 m/s). This final averaged data was separated into ten groups classified by area size. This data could then be manipulated to produce general population density data, local population density data by sector or displacement data, which will be presented in this contribution.

8.8 Physical Analysis Techniques

The same techniques as those described in Section 4.8 were employed for the samples interpreted in Part III and Part IV of this thesis.

CHAPTER 9

ABLATION-GENERATED DEBRIS CONTROL BY MEANS OF CLOSED THICK FILM FILTERED WATER IMMERSION

In this Chapter the debris control, modification and removal performance of a closed thick film flowing immersed laser ablation technique that has been developed following the findings presented in detail in Part II of this thesis, are presented. This new equipment allows user control of the immersion liquid flow velocity through the ablation chamber of the equipment. The effect of this new parameter on the debris characteristics of the features machined into bisphenol A polycarbonate using a KrF excimer laser are also investigated here.

9.1 Introduction

Open thin film flowing liquid immersion has successfully demonstrated control of debris from the ablation spot, with 90% of debris found deposited downstream of the ablation spot whilst using only a low flow velocity. The use of open thin film flowing liquid immersion has significant limitations: surface ripple, rolling turbulence and limited flow velocity. Zhu *et al* [56] have shown that the immersion depth has a critical influence on the interaction between the laser beam and the material. This means that particles may be both generated and ejected in different ways, dependent on the flow thickness at a specific point in the beam cross-section.

Once generated, debris particles experience drag force that is proportional to the viscosity and velocity of the flow surrounding it [55]. The particles are ejected away from the substrate surface at high velocity [24], and so considerable work must be imparted on the travelling particle by the surrounding liquid to transform the particles original vector to that of the fluid flow. If the flow is rippled, some debris will have less working distance available for the liquid to impart work on its original vector than can be offered to other particles produced at other locations in the cross-section of the beam.

Inertial, capillary and viscous effects along with the proportionally large contribution of surface tension (due to the small thickness of the film) combine within the flow at a molecular scale to generate significant flow ripple. Also, the large gradient of drag between the material-flow interface and the flow meniscus – ambient air interface causes a tendency for eddies to develop within the flow that roll into the material surface as described in Figure 9-1. In an open flow, turbulence commences following a characteristic distance measured between the contact point of a fluid on a flat plate and the point at which the flow becomes turbulent [55]; however, this case requires all dimension of the flow, including film depth, to be large compared to the characteristic distance. In the case of this flow, the meniscus defines the flow geometry, thus the effect of rolling eddies alone are not responsible for the deposition patterns evidenced in Chapter 5 of this thesis, where debris distribution appeared to lie in ripple patterns downstream of the feature machined. Instead, large inertial, capillary and viscous contributions complicated the flow path.

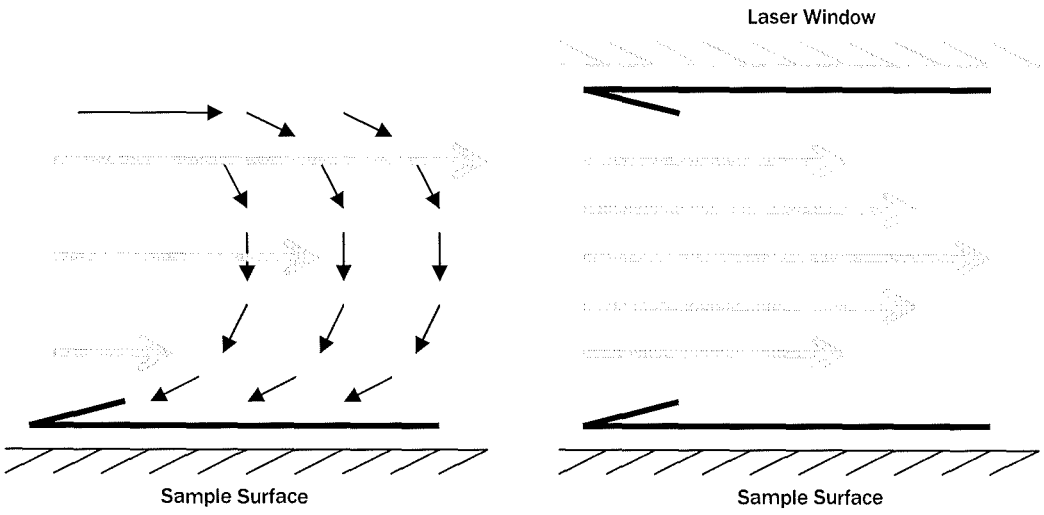

Figure 9-1: Schematic representation of the contrast of flow properties between (a) open thin film flow and (b) closed duct flow

A closed immersion technique dictates that the flow is confined within a duct. And so in turn will significantly improve the efficiency of debris control. A closed immersion technique allows control of film thickness; hence, the ratio between laser beam etching and compressed plume etching can be modified, [50 - 52, 56, 102]; thus, the ejection vector mode and velocity can also be altered. A closed geometry of immersion flow ensures the minimum traverse distance for debris to travel and have work imparted on its original vector and speed as a constant. Furthermore, there is the ability to control (and increase) the flow velocity of the fluid though the duct; this will increase the drag force imparted on a debris particle by the flow. Last, the symmetry of the closed immersion technique will remove the meniscus dominated flow characteristics present in the open immersion technique. Equal drag is imparted to all flow boundaries; hence the characteristic distance of a flow in a closed duct is described by cross-sectional dimensions. Lower turbulence means debris captured in the flow is less likely to collide with the duct walls and be deposited in an unwanted position.

9.1 Impact of Closed Thick Film Flowing Filtered Water Immersion on Debris Deposition

The distribution of debris generated by KrF excimer laser ablation in ambient air is dictated by the beam shape as described in Chapter 5 of this thesis, as one can see from Figure 9-2(a(i)), (b(i)) and (c(i)), four high density mushroom shaped deposition areas can clearly be seen extending at a normal to the edges of the square feature machined. In Chapter 5 it was shown that debris was ejected, then deposited at normal angles to the linear edges of features. This tendency for preferential debris distribution was repeated when using triangular beam shapes and a circular beam geometry. Debris has been shown to be transported in the laser ablation plume shockwave [25, 26]. The deposition patterns witnessed in Chapter 5 have a beam shape dependency on account of separate shockwaves, generated and expanding simultaneously from different locations in the beam, which then collide and

intersect as they expand, depositing debris either at the location of shockwave collision or at the periphery of individual shockwave range. For a square, four seed points form separate shockwaves, one from each corner of the feature, as described in Figure 5-7. As these expand they intersect, dropping debris as they collide in the shaded areas indicated.

The existence of a neighbour is obvious for the sample shown in Figure 9-2(a(i)), which was machined in ambient air. Debris from the sample's neighbour to the right has been deposited along with the debris of the feature being inspected to produce a significantly increased debris density to the right of the feature. The same cross contamination is not evident for any of the closed thick film flowing filtered water immersion samples (see Figure 9-2(a(ii)) to Figure 9-2(a(v))). This thesis demonstrates that the use of closed thick film flowing filtered water immersion changes the primary parameters that dictate the deposition trend of debris from a group of ablation characteristics that are difficult for a user to control, to a set of separate flow parameters that are easy for the user to control independently of the laser ablation mechanisms used for machining.

Figure 9-2(b) and Figure 9-2(c) are groups of contour plots representing the total particle population density per 486.6 μm^2 area (which corresponds to a 10000 pixel box). Figure 9-2(b) shows contour plots for all the samples seen in Figure 9-2(a). Figure 9-2(b(i)) clearly demonstrates the characteristic high density distinct deposition pattern of the sample machined in ambient air; this distribution pattern is not present on any of the closed thick film flowing filtered water immersion ablated samples shown in Figure 9-2(b(ii)) to Figure 9-2(b(v)). This removal of high density localized deposited debris smears was caused by the action increased suspension and subsequent retention of particulate debris by flowing filtered water immersion. Furthermore, drag imparted on the particles was much greater when using filtered water, a fluid offering two orders of magnitude greater viscosity than air [128], which accordingly afforded a marked increase in removal of debris from the sample.

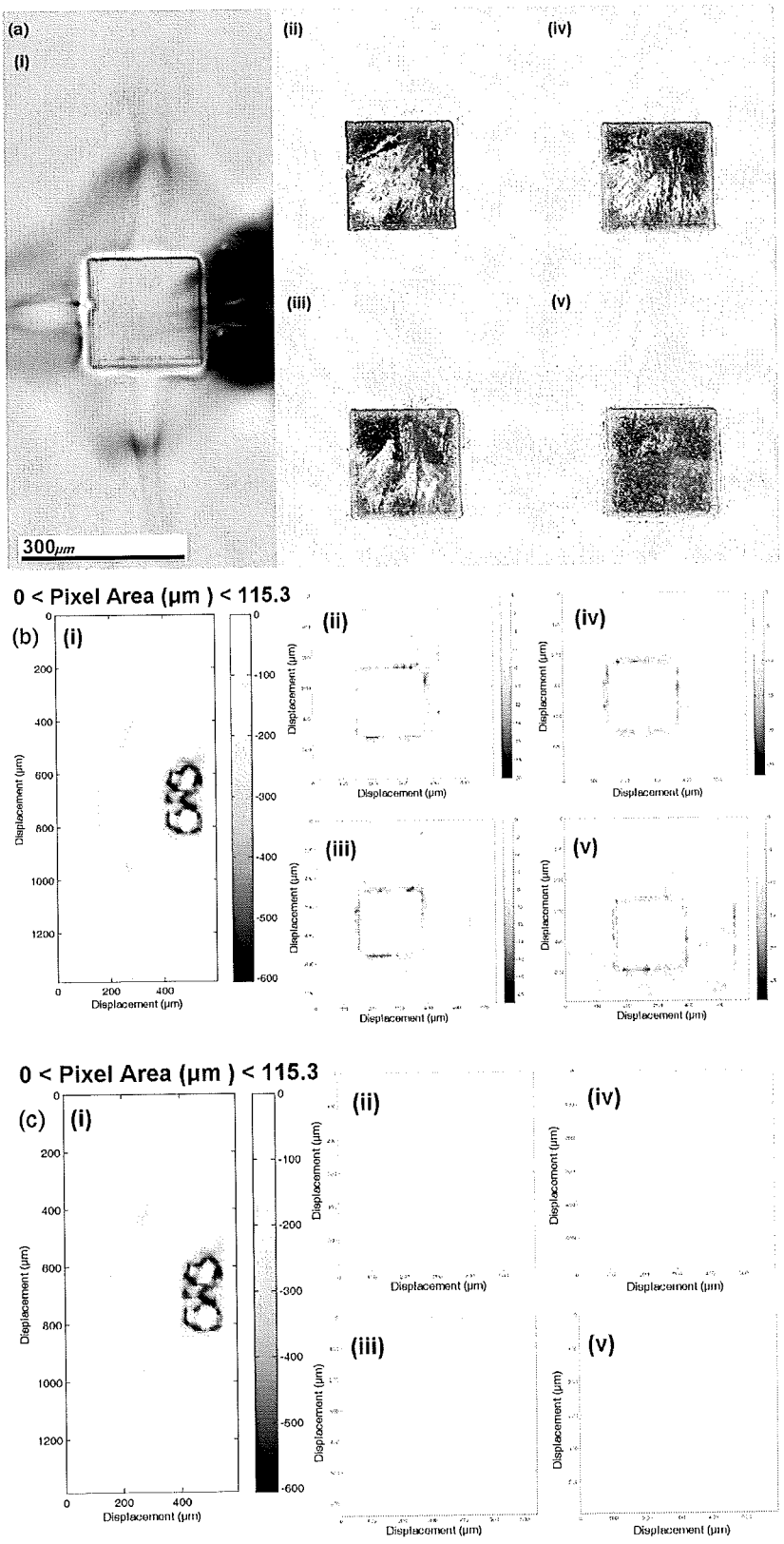

Figure 9-2: Optical micrographs, stitched and software enhanced for smooth illumination (a): (i) ambient air; (ii) 3.70 m/s; (iii) 2.78 m/s; (iv) 1.85 m/s; and (v) 0.03 m/s. Contour plots of discrete particle density measures over 100 pixel square areas (separate legends for each sample) (b): (i) ambient air; (ii) 3.70 m/s; (iii) 2.78 m/s; (iv) 1.85 m/s; and (v) 0.03 m/s. Contour plots of discrete particle density measures over 100 pixel square areas (single legend calibrated to maximum particle density measured from any of the samples) (c): (i) ambient air; (ii) 3.70 m/s; (iii) 2.78 m/s; (iv) 1.85 m/s; and (v) 0.03 m/s.

9.2 Impact of Closed Thick Film Flowing Filtered Water Immersion on Total Debris Population.

A visual comparison of particle numbers present on the samples is given by Figure 9-2(c). Comparison of Figure 9-2(c(i)) to the closed thick film flowing filtered water immersion machined samples (see Figure 9-2(c(ii)) to Figure 9-2(c(v))) demonstrates a marked difference in deposited debris population: the legends show a 96% reduction of the debris population generated by ablation in ambient air when closed thick film flowing filtered water immersion was applied.

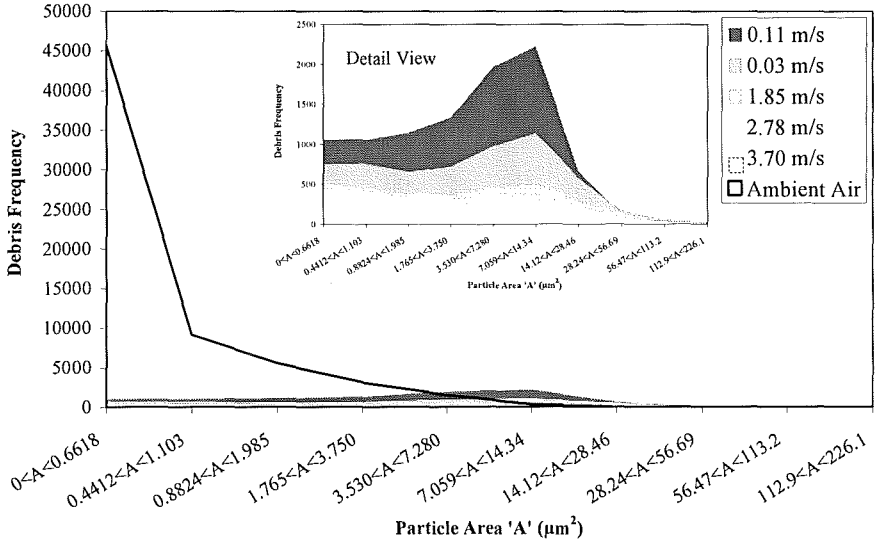

Figure 9-3: Frequency of debris particles against particle size to describe the total particle population of samples produced under ambient air and the relative population of debris produced by closed thick film filtered water immersion ablation at various flow velocities.

Part II showed that the use open thin film flowing DI water immersion ablation produced proportionally less small debris than ablation in ambient air; a greatly increased proportional population of medium debris particles and a similar, small proportion of large debris. The same analysis has been conducted on the closed thick film flowing filtered water immersion samples in this thesis and compared to samples machined in ambient air. Figure 9-3 demonstrates that the total debris population size produced when using closed thick film flowing filtered water immersion ablation across all size classes, at any flow velocity (see detail view in Figure 9-3), was 4603 compared to the 65553 produced by ablation in ambient air. This is a reduction in debris deposition across the inspected surface of 93%. The use of closed thick film flowing filtered water immersion was even more effective at reducing debris deposition in terms of frequency than the open technique described in Part II of this thesis. Once again, debris deposition for closed thick film flowing filtered water immersion is dictated by the flow parameters of the immersion liquid.

9.3 Feature Floor Characteristics

When machining using ambient air as a medium, the debris was ejected away from the feature, as evidenced by Figure 9-2(a(i)). Whereas all features machined in ambient air showed an even and clear

floor, as can be clearly seen in Figure 9-2(a(ii)) to Figure 9-2(a(iv)) and Figure 9-4(a), all samples machined under closed thick film flowing filtered water immersion ablation displayed a dark, opaque floor, as shown in Figure 9-4(b). Under flowing closed thick film flowing filtered water immersion, the debris was also ejected outwards in all direction, including the upstream direction; this debris was assumed to be forced back over the feature by the oncoming flow of immersing filtered water. It was assumed turbulent eddies, caused by the step change in surface level at the feature wall, deposited debris on the feature floor. To confirm this, a sample machined using closed thick film flowing filtered water immersion ablation was cleaned using ultra-sonic bath excitation, a well documented technique of removing a wide range of particulate sizes from a surface [46]. The result of cleaning the sample for 10 minutes in fresh DI ionized water demonstrates identical floor patterning before (see Figure 9-4 (b)) and after (see Figure 9-4 (c)) treatment. This indicates that the apparent darkening of the feature floor is not a result of debris, rather it could be the result of an alteration to machined surface topography by be action of closed thick film flowing filtered water immersion machining. The micrographs used in this thesis rely on reflective lighting, therefore increased diffusion of the light by the sample feature floor would make it appear darker. This will be investigated in more exhaustive detail in a future publication.

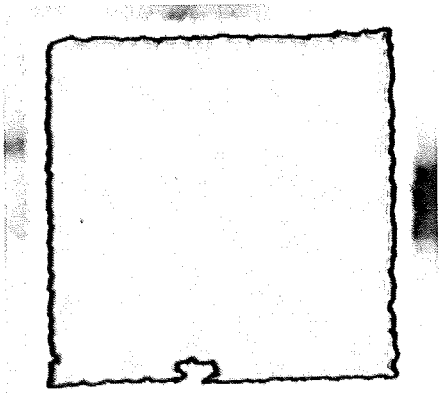

(a)

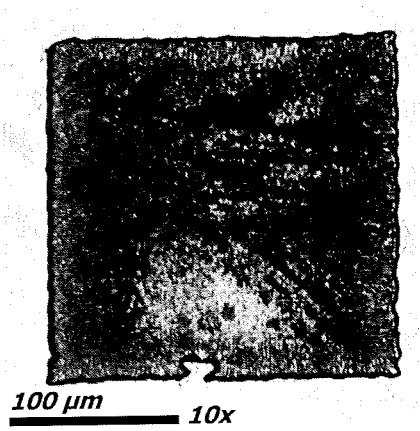

(b)

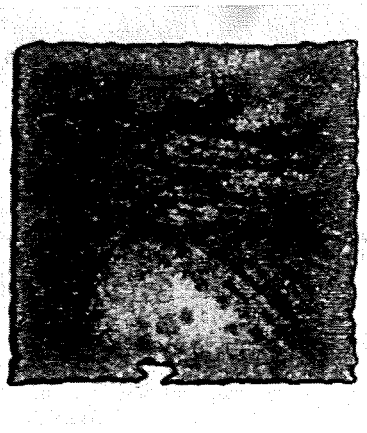

(c)

Figure 9-4: Optical micrographs of features machined into bisphenol A polycarbonate in a medium of (a) ambient air, (b) under closed thick film flowing filtered water immersion, shown before ultrasonic bath cleaning and (c) the same feature given in Figure 9-4(b) after ultrasonic cleaning for 10 minutes.

9.4 Impact of Flow Velocity on Deposition Trend

The results displayed in Figure 9-5 show the number of particles of three specific size ranges for each closed thick film flowing filtered water immersion flow velocity tested discretely by use of contour plot. Each group of result plots have been generated by taking a mean average of the deposition frequency of three separate machined samples to guard against experimental inaccuracy. The full results are split into 10 debris particle size classes, with the smallest, middling and second largest (1^{st}, 5^{th} and 9^{th}) debris size plots being given for illustration of the findings of this thesis.

Again, all closed thick film flowing filtered water immersion ablation sample results shown in Figure 9-5(b to f) show a contrast to the typical ambient air deposition tendency displayed in Figure 9-5(a). None of the closed thick film flowing filtered water immersion samples, that were all produced using different flow velocities, display either the high deposition density or the characteristic debris size distribution (that was dominated by a majority of small debris). The closed thick film flowing filtered water immersion samples (see Figure 9-5(b) to Figure 9-5(f)) all show an equal population of both small and medium size debris and a proportionally increased population of large debris deposited when compared to the samples produced in ambient air.

When inspecting and comparing the debris distribution of the closed thick film flowing filtered water immersion samples there is an obvious contrast in distribution between the three high flow velocity samples displayed in Figure 9-5(b) to Figure 9-5(d) produced using 3.70, 2.78, and 1.85 m/s respectively, and the lower flow velocity samples described by Figure 9-5(e) and Figure 9-5(f) that were produced using 0.11 and 0.03 m/s respectively. The higher flow velocity samples all demonstrate a clear propensity for the debris deposition downstream of the feature, whereas the low flow velocity samples both appear to show an even distribution upstream and around to the sides of the feature across the direction of the flow. The samples displayed in Figure 9-5(f) also show a significant population of debris upstream. This would suggest that the tendency for debris to be deflected and transported by a liquid is directly dependent upon the liquid flow velocity. This interpretation is strongly supported by close inspection of the high flow velocity samples: increased flow velocity, such as the plot in Figure 9-5(b), results in decreased debris deposition, as can be identified by the magnitude of frequencies registered in the legends for each group of plots. Flow turbulence also appears to become important, as one can see from Figure 9-5(b), where stream lines of debris can be identified for the medium sized debris to the top right of the feature.

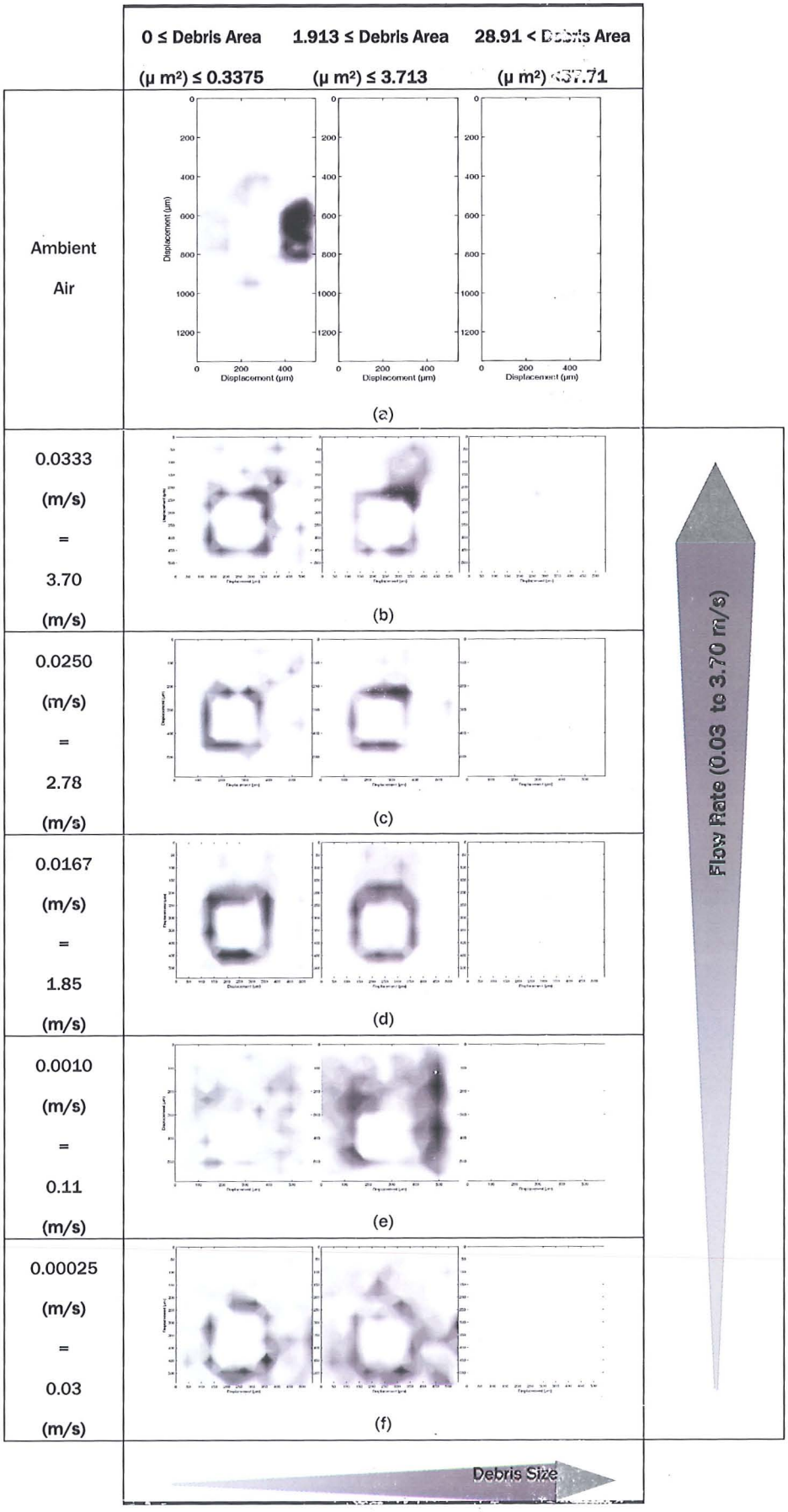

Figure 9-5: Discrete contour plots of particle density with respect to size class and flow velocity for closed thick film flowing filtered water.

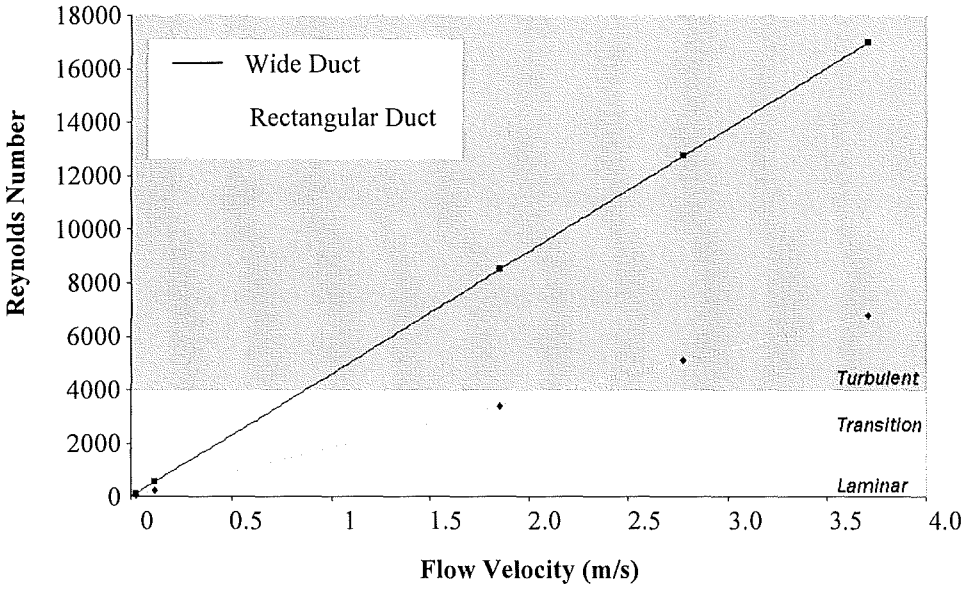

Figure 9-6: Reynolds number against flow velocity for a wide duct and a rectangular duct for specific flow velocities used in this thesis.

The Reynolds numbers of the flows in this chamber have been calculated using both rectangular duct and parallel plate approximations; these have been plotted in Figure 9-6. All of the samples machined at a high liquid flow velocity experienced turbulence in the flowing filtered water medium. The two samples machined at lower flow velocities were both machined in the laminar regime. Turbulence generated at high flow velocities may cause debris particles trapped in the flow of water to be directed back towards the sample surface downstream of its production and ejection site. Increased flow velocity results in increased turbulence [128]; thus it stands to reason that that a greater proportion of debris deposited at high flow velocities will be deposited as a result of turbulence. The results for the high flow velocity samples in Figure 9-5(b to d) support this hypothesis, showing an inverse relationship between total debris population size and flow velocity, but more localized streak pattern grouping of debris downstream of the feature as the flow velocity was increased. The samples produced using laminar flows do not show this characteristic, instead they demonstrate a more even deposition trend. Reduced flow velocity even allows deposition upstream of the feature, as can be seen in Figure 9-5(f), suggesting that this flow velocity only offers a level of control to maintain suspension of the ejected debris in the fluid, rather than providing strong positional control also.

9.5 Impact of Flow Velocity on Debris Population by Size Class

Figure 9-7 shows the population size of debris produced using immersed ablation with respect to debris size class. The results given in Figure 9-7 make it clear that increased flow velocity results in decreased deposition frequency. This is perhaps to be expected as increased flow velocity means increased drag on particulates to provide motive force upon them, despite any turbulence issues discussed above.

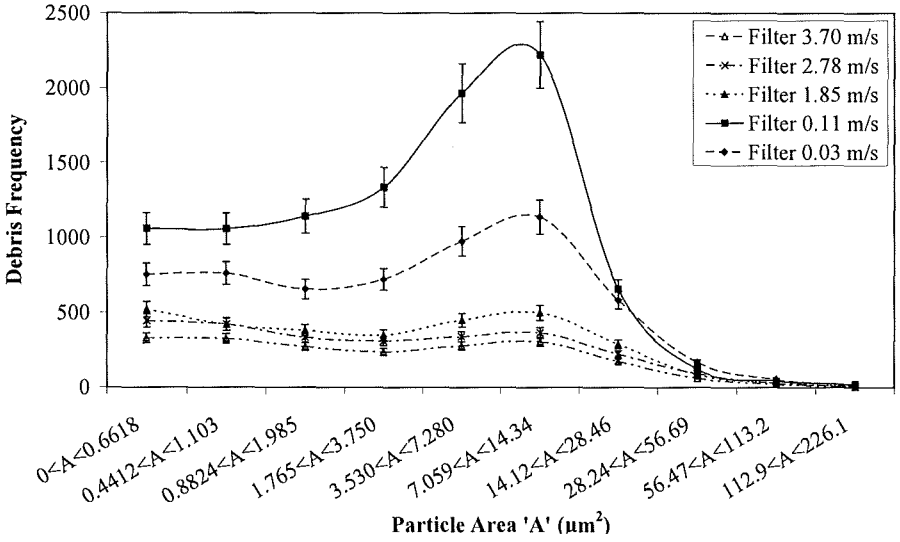

Figure 9-7: Debris frequency against debris size to give the debris distribution frequency across the whole area by size class for all immersed samples for various flow velocities.

Figure 9-7 also demonstrates that low flow velocity, laminar closed thick film flowing filtered water immersion produced a majority population of medium sized (1.765 to 28.46 μm^2) debris particles. This result can be attributed to the action of colloidal debris interaction, as described by others [38, 55]. Closed thick film flowing filtered water immersion produces a larger majority of medium sized debris than that displayed by open thin film immersion in Chapter 5 of this thesis: the closed technique provided a more stable medium geometry for particles to interact and combine within. Use of open thin film immersion caused potential cohesion to be avoided by the action medium rupture and splashing. A closed thick film flowing filtered water immersion structure allows more of the small debris to combine to form medium size colloids [16]. Large multiple colloid debris are uncommon: the adhesion forces become overwhelmed by the action of gravity and drag forces for particles larger than 5 μm in diameter [42], a value at which the population sizes drop off rapidly in Figure 9-7, instead they gather small debris, explaining the low small debris population. Generally, increased flow velocity results in reduced total debris population; however, the samples machined at the lowest flow velocity (0.03 m/s) do not follow this trend, showing a smaller population than the immediately higher flow velocity. The lowest flow velocity used was chosen as it resulted in a flow velocity insufficient to traverse the entire length of the feature between pulses, hence debris suspended in the flow produced by one pulse would obstruct the course of the following pulse, thus resulting in decreased average fluence across the feature. This would reduce the laser ablation rate and therefore the volume of debris produced by the lowest flow velocity in a way not experienced by the 0.11 m/s samples. This is what causes the abnormally low debris population of the lowest flow velocity.

9.6 Relationship Between Debris Size and Deposition Displacement

To interpret the action flowing closed thick film flowing filtered water immersion had on debris with respect to positional control of deposition is to inspect the distribution of deposition displacement

from site of production by particle frequency with respect to debris particle size and flow velocity. This can be deduced effectively using two differing techniques.

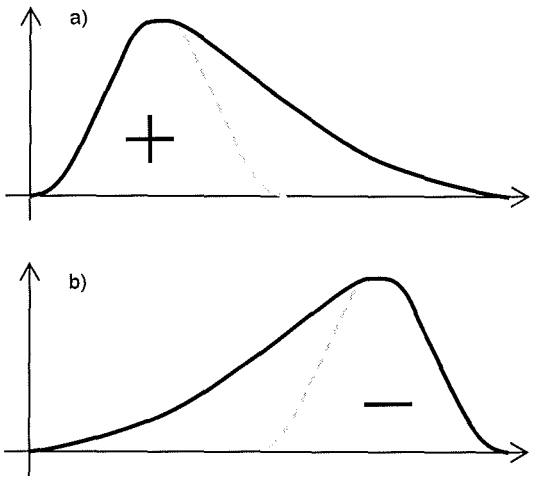

Figure 9-8: Schematic diagram demonstrating the distribution described by (a) a positive skew value and (b) a negative skew value. The magnitude of the data skew is defined by magnitude of skew value.

A statistical technique can be used: distribution skew, a numerical value that denotes the shape of the distribution about the mean of a frequency distribution. A positive skew value is the result of a distribution where a greater proportion of the population lies between the mean and infinity, as shown in Figure 9-8(a); a negative skew value is the result of a distribution where a greater proportion of the population lies between the origin and the mean, as shown in Figure 9-8(b). A large skew value denotes a strong population 'lean' about the mean, a lower skew value denotes a distribution of the population that is more evenly balanced about the mean. In Figure 9-9, plots of the magnitude of skew for all the immersed samples are displayed with respect to displacement from the top edge of the feature as viewed in Figure 9-2a. The plots of the samples machined in turbulent flow displayed in Figure 9-9 all show correlating trends. Small debris has a large positive skew, which drops away to a smaller positive skew for medium size debris. This means the displacement of debris before deposition increases with size. This finding is contrary to the expected trend, where the ratio of surface area to volume decreases with size, causing the action of drag against mass dominated inertia to reduce with increasing particle size. An explanation of this interesting trend can be given using turbulence and adhesion science: the action of turbulence does not affect large debris as easily as small debris due to the contrasting relationships between size, surface area and mass, thus large debris more readily follows the general vector of the flow than small debris and is therefore less commonly smeared onto the sample surface [56]. Also, the drag on a particle with respect to the size of the adhesion forces acting upon it will be favourable for easy removal of larger debris [16]. The samples produced using laminar flow velocities display much less predictable plots, but broadly follow those of the turbulent flow velocity samples suggesting that the immersing liquid volume provides less stable debris transportation mode than the turbulent flows, perhaps as a result of the interaction of ablation plumes generated by subsequent laser pulses with the surrounding immersion fluid before it has fully cleared the feature location. It must be noted that the skew measure is limited to

only the lower seven debris sizes as there are fewer large particles available for reliable plots above the debris particle size of 129 μm^2.

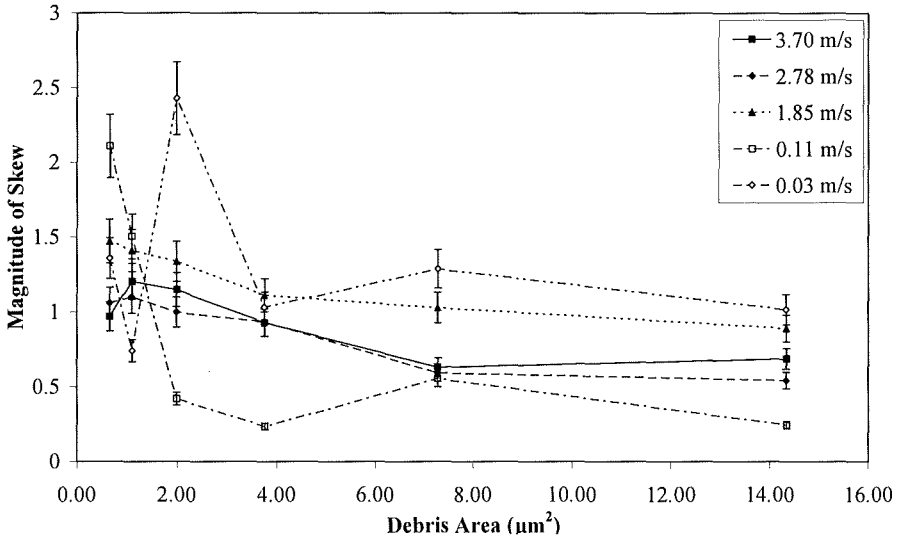

Figure 9-9: The x-position distribution skew of the frequency data for the small to medium size debris. There were too few large debris particles measured to give reliable data for this type of analysis.

Another, less simple measurement of the positional tendency was made to verify the previous statistical analysis. The centre position of the debris population density peak can be plotted for each designated debris size class. This information is plotted for each flow velocity in Figure 9-10. These plots tally well with indications presented by the skew magnitude data, where the displacement of the debris from the top edge of the machined feature increases with debris size up to a maximum debris size of 129 μm^2. However, the use of the median measure of the top 5% of the normalized frequency distribution allows interpretation of the larger debris deposition displacement. Inspection of these points shows the larger debris is deposited with larger displacement from the machined feature than small debris. The unreliable trend demonstrated by the skew measurement for laminar flow velocities in Figure 9-9 is more interpretable when plotted using the median measure of the top 5% of the normalized frequency distribution shown in Figure 9-10. This data appears to tie well with the trend of increased displacement for medium sized debris over smaller debris in the same flow conditions for debris up to 129 μm^2 in area; however, the data becomes unreliable for larger debris sizes due to small numbers making this measurement technique susceptible to significant distortion by outliers.

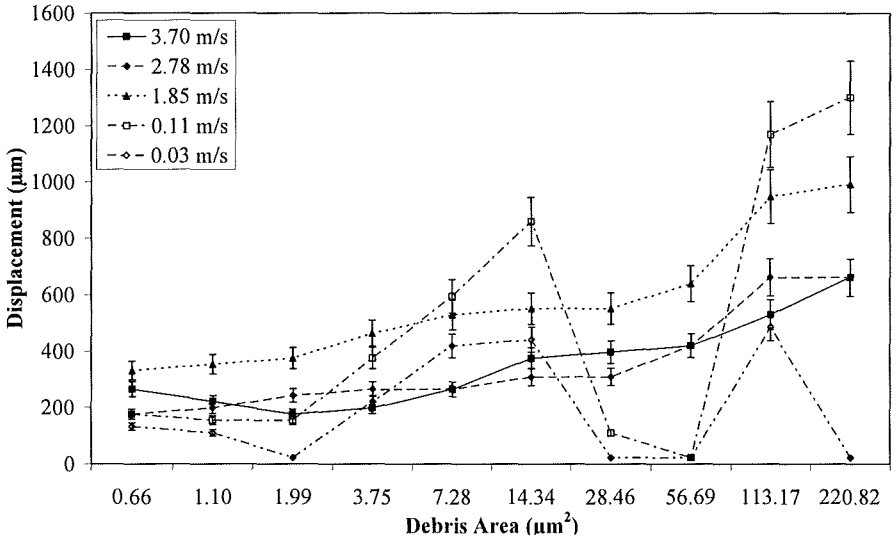

Figure 9-10: Debris displacement against particle size to demonstrate the shift in distribution of the debris with increasing debris size: this time using the median of 95th percentile of normal distribution of distribution frequency data.

In Figure 9-9 the flow velocity of 1.85 m/s has the largest magnitude of positive skew; in Figure 9-10 it has the highest displacement for every size class of debris measured. This demonstrates that the optimum flow velocity for maximum displacement of debris before deposition occurs at 1.85 m/s. The 3.70 and 2.78 m/s samples display similar displacements for each debris size class as the laminar flow samples. This can be attributed to the effect of turbulence causing unnecessary deposition at excessive flow velocities and a lack of motive force for transportation of debris species at very low flow velocities; thus leaving an intermediate flow velocity acting as the best compromise.

9.7 Modification to the Image Plane Position of the Optical System

A simplistic prediction of the change in image plane position of the laser system could be calculated before any machining was conducted, using the technique of ray tracing [257]. For a true calculation of the beam characteristics, thin lens theory states that a number of dimensions must be known for an imaging system such as that used in an excimer laser micromachining tool, as illustrated in Figure 9-11. The system described in Figure 9-11 is a simple case where the beam does not experience any change in medium. The system involved in the ablation of a substrate immersed in a closed thick film of filtered water is much more complex, requiring the beam to pass from the de-magnifying optic, into the ambient air of the system, on to enter the substrate immersion apparatus fluid enclosing window before finally leaving the window and traversing the immersion fluid itself. The changing refractive index will have the effect of modifying each ray as described in Figure 9-11. If the angle of incidence of a ray, θi, is known, the angle of refraction, θr, resultant at each stage can be calculated by rearranging the definition of the refractive index to give:

$$\theta_r = \sin^{-1}\left[\frac{\sin\theta_i}{n}\right] \tag{48}$$

The maximum angle of incidence, can be found when the distance between the beam and the substrate and the change in radius of the beam are known. The tool used in this contribution had a lens – substrate separation of approximately 65 mm (calculated to be 63.438 mm using thin lens theory); the radius of a planar wave passing the edge of the mask orifice was 400 μm and then went on to pass through the edge of the lens and being de-magnified to the image plane where the image had a radius of 102 μm, giving a maximum angle of incidence, denoted θia, described by line '*Ia*' in Figure 9-11 as 0.45°.

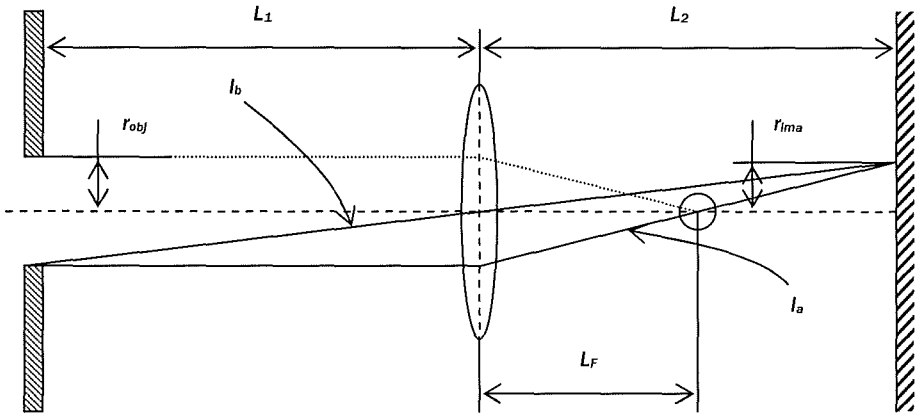

Figure 9-11: Schematic diagram describing the two defining rays, I_a and I_b, in an imaging system.

The other image defining ray passes from the edge of the mask, through the centre of the lens and onto the opposite edge of the image at the feature, labelled as 'I_b' in Figure 9-11 which will now be denoted θ_{ib}. In the case of the tool used for this thesis, the distance between the mask and the substrate was 250 mm, thus knowing the dimensions of the mask, feature and the separation of lens and substrate as stated above, gives an angle of incidence of 0.09° for θ_{ib}.

When a ray passes from one medium to another, the relationship between the refractive indices of both media must be taken into account. This is done by application of Snell's law [58], which can be written as

$$\theta_r = \sin^{-1}\left[\frac{n_1 \sin\theta_i}{n_2}\right] \tag{49}$$

where n_1 is the refractive index of the medium being passed from and n_2 is the medium being passed to.

Using Snell's law, it can be calculated that a ray passing from the medium of air surrounding the micromachining centre, that possesses a refractive index value of 1.0008 for electromagnetic radiation with a wavelength of 248 nm [258], into the UV grade fused silica, which possessed a measured refractive index of 1.5084 the same wavelength [259], resulted in the modification to the path vectors of I_a and I_b. As the light passed through the fused silica window the angle of refraction of I_a, θ_{ra}, was 0.3°, and the angle of refraction of I_b was 0.06°.

As one can see in Figure 9-12, the angle of the refraction at the first medium interface becomes the angle of incidence for the second, denoted as θ_{ii} in Figure 9-12. Again, Snell's law can be used here to calculate the final range of angles of refraction, θ_{rr}, of any rays including or between I_a

and I_b in Figure 9-11. The reactive index of filtered water on 248 nm wavelength electromagnetic radiation is 1.3787 [260]. Knowing this, and assuming the boundary between the water and the fused silica window is regular and without cavity, the angles of refraction, θ_{rra} and θ_{rrb} are derived to be 0.3° and 0.07° respectively.

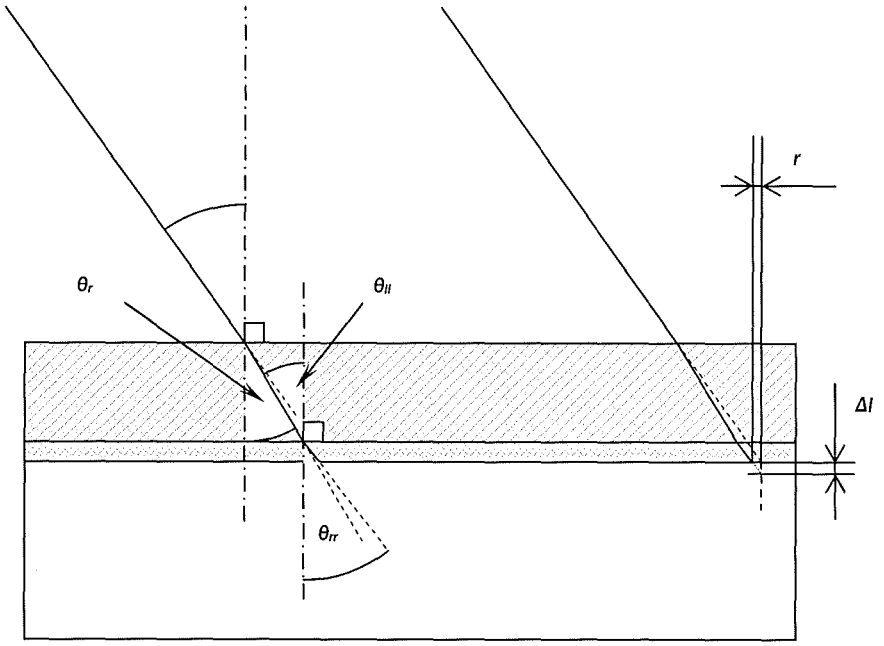

Figure 9-12: Schematic diagram illustrating the modification to the vector of a ray through changing medium, taking into account Snell's Law.

Given these the angles of modification and knowing the micromachining system was left unchanged as the laser machining was moved from ambient air to having the liquid immersion equipment mounted and filled with flowing filtered water, the change in distance to the image plane of the optical system can be calculated using successive application of simple trigonometry. The closed thick film flowing liquid immersion equipment used in this thesis was composed of 1.5 mm of filtered water covered by 5 mm UV grade fused silica. Knowing these dimensions allows the calculation of the modification to the position of the image plane of the system, denoted Δl in Figure 9-12, which was predicted to be a 2.958 mm increase.

In reality, the immersion rig sample mounting surface was mounted 1.7 mm beneath the level of the vacuum chuck. The two features machined in ambient air and under closed thick film flowing filtered water immersion with optimum focus are indicated by a square in Figure 9-13(a) and Figure 9-13(b) respectively. The stage height of the lowest sample in Figure 9-13(a) was at 3.475 mm from its home position. The stage elevation between each feature was 0.025 mm, meaning that the image plane position for machining in ambient air was found at 3.675 mm from the home position of the stage. For the closed thick film flowing filtered water immersed samples, shown in Figure 9-13(b) the lowest feature height was 2.275 mm from the homing position, meaning the image plane position was found in this case to be 2.475 mm. This gives an increased optical length by relative stage position of 1.2 mm for the immersed sample over that of the sample machined in ambient air. Coupling this value with the 1.7 mm deviation in mounting height results in a 2.9 mm increase in optical length, a value

very close to that predicted mathematically above. This result means that the modification of beam path can be easily predicted given known equipment dimensions, when using closed thick film flowing immersed KrF excimer laser ablation machining techniques.

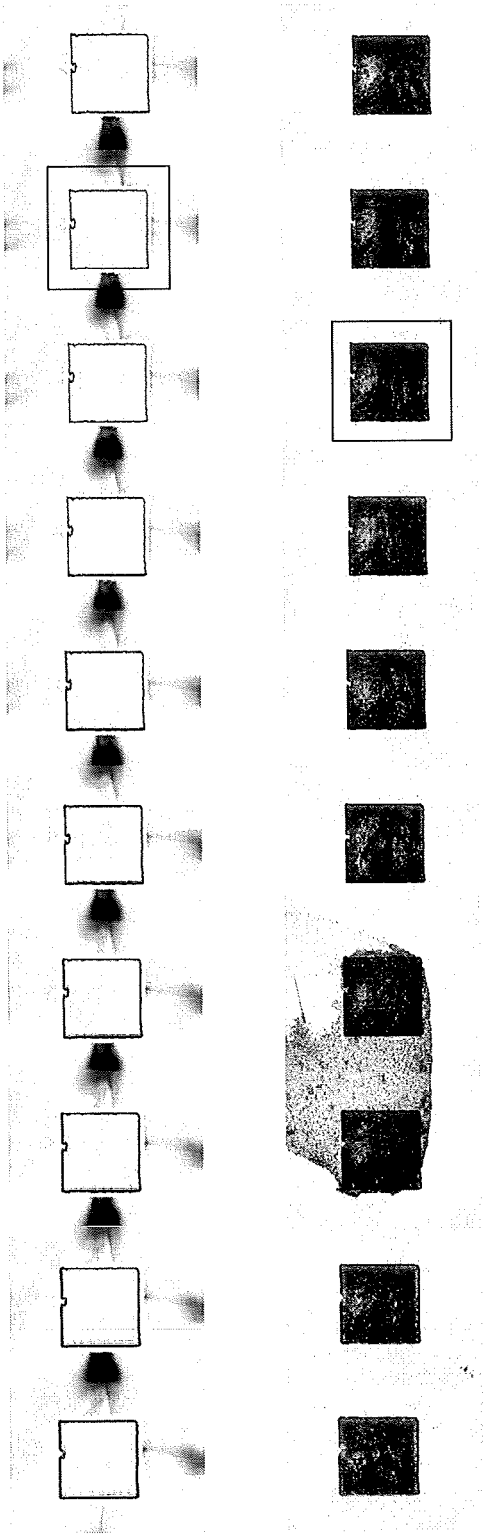

(a) (b)

Figure 9-13: A strip of features machined at 0.025 mm intervals using KrF excimer laser ablation in (a) ambient air - feature 9 (boxed) is the optimum feature and (b) under thick film flowing filtered water immersion - feature 8 (boxed) is the optimum feature.

9.8 Modification to the Depth of Focus

The DoF is the tolerance between image plane positions where the image is in focus. The objective is imaged through the optical system, which guides a laser beam from the source, through the objective, through the de-magnifying lens and onto the image. The depth of focus is defined primarily by the characteristics of the de-magnifying lens; but, the application of further optics may modify this dimension. Moreover, modifying the ablation mechanism from one that is dependent upon the laser etching provided by a beam in focus to one that can operate using the etching contribution of a compressed plume by use of a compressed ablation plume, as will be described in detail in Chapter 10 of this thesis, could present the possibility of an increased range of DoF that produces an acceptable image that can be deemed to be 'in focus'. Alternatively, the implication of such a mechanism could equally reduce the range of material surface positions that produces an equivalent feature definition to that in ambient air.

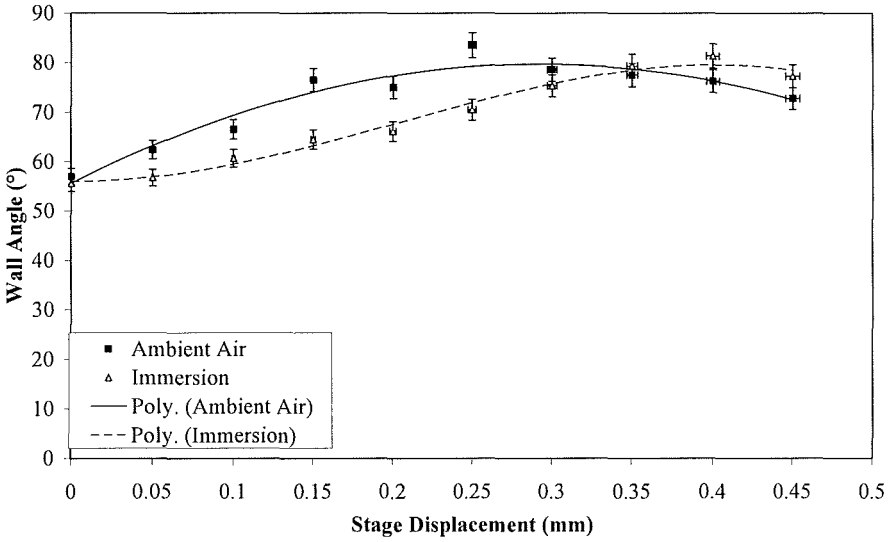

Figure 9-14: Feature wall angle against increase in optical length for features machined by KrF excimer laser ablation in ambient air and under closed thick film flowing filtered water.

Figure 9-14 plots the average wall angle, taken from 10 profiles of features machined at each image plane position, with respect to 10 sample surface displacements, separated by increments of 0.05 mm. Two plots are given, a plot describing the angle between level and the wall of ten features machined in ambient air and for a feature machined under closed thick film flowing filtered water ablation at intervals of 0.1 mm in optical length. These results show that use of immersion can produce wall angles equivalent to those achieved by KrF excimer laser machining in ambient air; however range of optical length that high wall angles are produced in is smaller when using KrF excimer laser ablation under closed thick film flowing filtered water KrF excimer laser ablation immersion. This result indicates that the depth of focus is reduced. Interpolation of the polynomial best fit lines given for each group of data identifies that a wall angle greater than 77° is achieved by ambient air over a range of 0.2 mm, but for the samples machined using KrF excimer laser ablation under closed thick film flowing filtered water immersion, this range is 0.15; this indicates a reduction in the depth of focus of the system by 25% when using immersion. This result cannot be the result of

an optical change to the beam by the immersing fluid and associated equipment UV grade fused silica window; the installation of this apparatus has the effect of reducing the separation of the rays I_a and I_b, as denoted in Figure 9-11, when the beam is 3 mm above the surface of the material, hence the actual depth of focus was marginally increased as reduced divergence between the rays was afforded. Given this knowledge, it is clear that the modification to the ablation plume by use of closed thick film flowing filtered water ablation results in reduced feature definition, when using the flow velocity of 1.85 m/s as used for this thesis.

CHAPTER 10

IMPACT OF CLOSED THICK FILM FLOWING FILTERED WATER IMMERSION ON KrF EXCIMER LASER ABLATION CHARACTERISTICS

Further to the high debris control provided by the closed thick film flowing immersion technique, it is expected that the use of this technique can also provide greater stability to the laser ablation mechanism. Two commonly used measureands of the laser ablation mechanism are interpreted in this Chapter. This work is also at the vanguard of laser ablation mechanism research, as the ability to change the flow velocity of the immersing fluid presents the possibility of modifying the proportional contributions of the individual etching mechanisms that combine to produce what is commonly termed 'laser ablation'.

10.1 Introduction

As discussed at the start of Chapter 9, a flow running across a flat plate in the open flow immersion technique allowed surface ripple to occur and thence the depth of liquid above the plume varied with respect to time and position above the sample, this results in an irregular and non-repeatable plume etch-rate and threshold. This was witnessed by the fluctuation between ablation depths with increasing numbers of laser pulses that should have produced a linear relationship in a regular, repeatable surrounding medium. The split ablation threshold values reported in Chapter 6 have been accredited to the splashing action of the open thin film immersing flow of DI water. The use of a closed ablation chamber has removed the variance of the flow geometry both with respect to time and position above the sample to be machined by ensuring the drag on the boundaries of the flow symmetrical about the centre of the flow, as described schematically in Figure 9-1, and removes the meniscus that dominates flow characteristics in open flows.

10.1 Etching Threshold

10.1.1 Impact of closed thick film flowing filtered water immersion on ablation threshold

Ablation threshold is a useful tool for measuring the effectiveness of a technique at etching a material: low threshold fluence indicates that minimal laser energy is required to remove material from a substrate. Figure 10-1 shows two plots describing the feature depth machined against the natural log of the laser fluence required. In the standard way, each plot has been fitted with a linear trend line that has been extended to predict the natural log of the minimum laser fluence required to etch the material. The solid trend line in Figure 10-1 is the etching trend for 248 nm laser radiation in ambient air of bisphenol A polycarbonate; the dashed linear trend line in Figure 10-1 is an average of the ablation etching trend of 248 nm laser radiation of bisphenol A polycarbonate

that has been immersed in a closed filtered water layer (1.5 mm thick) flowing at a number of velocities from 1.39 to 3.70 m/s.

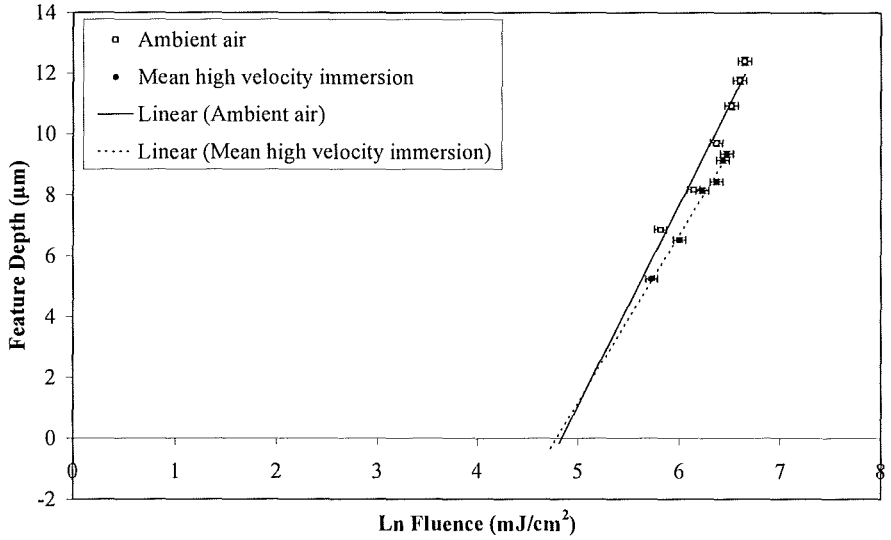

Figure 10-1: Feature depth against laser fluence achieved using 50 pulses to determine threshold fluence in ambient air and across all turbulent flow velocities tested under closed thick film flowing filtered water immersion.

This indicates that turbulent flow velocity closed thick film flowing filtered water immersion KrF excimer laser ablation has an average threshold fluence taken from all turbulent flow velocity samples of 116.6 mJ/cm^2, compared the higher value required in ambient air of 126.1 mJ/cm^2. The difference between turbulent flow velocity thick film closed filtered water immersion than KrF excimer laser ablation in ambient air at etching bisphenol A polycarbonate is small and could be explained by experimental error. This result is much closer than the open thin film flowing DI water immersion described in Chapter 6 to the findings of work by others [50 - 52, 54, 56, 102], who collectively determined that the increased etching efficiency with respect to laser fluence is due to the action of plume etching. plume etching occurs when the ablation plume is prevented from expanding by a viscous surrounding medium [54]. Under compression, the gaseous species, initially generated by photonic interaction with the sample, have increased temperature when compared to similar gases inside an ablation plume, it is therefore able to expand with ease. These gasses aggressively attack the surface of the sample, so restricted plume expansion by use of a viscous surrounding media gives rise to plume etching. This is in contrast to the effects of KrF excimer laser ablation machining under open thin film flowing DI water immersion, as described in Chapter 6, where the loss in ablation efficiency was accredited to the action a plume motivated rupture. Here, the high pressures initially generated inside the plume, that was initially restricted in growth by the surrounding thin film of DI water, rapidly become too high for the thin film of water to contain; resulting in explosive escape of gases from the immersing film. This scenario results in loss of plume etching action, but the existence of the plume during the laser pulse decreased the magnitude of laser energy arriving at the substrate by the action of plume shielding; thus both etch mechanisms available are limited by use of an open immersion technique, as described in detail in Chapter 6 of this thesis.

10.1.2 Impact of closed thick film turbulent flow filtered water immersion on ablation threshold

In Figure 10-2(a) the etch depth achieved using KrF excimer laser ablation on bisphenol A polycarbonate under closed thick film filtered water at six flow velocities ranging from 1.39 m/s to 3.7 m/s in increments of 0.46 m/s, is plotted with respect to the natural logarithm of laser fluence. This allows for the ablation threshold fluence at each flow velocity to be calculated. Table 1 lists the calculated ablation threshold fluences which are plotted in Figure 10-2 (b). All of these samples were produced in a turbulent flow velocity regime (V > 0.88 m/s), where the filter water flowing over the bisphenol A polycarbonate sample was travelling at sufficient velocity to have a Reynolds number above 4000; thus having a turbulent flow. As can be seen in the plots shown in Figure 10-2(a), the gradient and x-intercept of all the samples are similar, as confirmed numerically by the trend line gradients offered in the top left of Figure 10-2(a). This repetition of etch efficiency confirms that the experimental procedure is robust and the closed thick film flowing filtered water immersion technique provided a repeatable and stable medium that ablation can occur within. Despite the apparent similarity of all these plots, the resulting threshold fluence values demonstrate a flow velocity dependent trend that may be explained by interaction between the flowing filtered water and the ablation plume.

Table 10-1: List of ablation threshold fluences at varying flow velocities. Values are plotted in Figure 10-1(b).

Flow Rate (l/min)	Flow Rate (l/s)	Flow Velocity (m/s)	Threshold Fluence (mJ/c m^2)
2.00	0.033	3.70	115.7
1.75	0.029	3.24	111.8
1.50	0.025	2.78	114.1
1.25	0.021	2.31	113.0
1.00	0.017	1.85	118.6
0.75	0.013	1.39	126.5
0.06	0.001	0.11	125.7
0.015	0.00025	0.03	See text

The plot given in Figure 10-2(b) shows the threshold fluence of the six samples plotted with respect to the flow in which they were machined. This indicates that achieving minimum threshold fluence requires an optimum flow velocity. Turbulent flows beneath this do not significantly distort the ablation plume, as given in Figure 10-3(b), causing maximum compression of the plume and maximum traverse distance for the beam through the plume resulting in increased plume shielding. The optimum flow velocity for bisphenol A polycarbonate according to the results plotted in Figure 10-2(b) lies at 3.00 m/s, where the situation drawn in Figure 10-3(c) occurs, where the flow causes distortion of the plume to reduce traverse distance for the beam through the plume and therefore minimized plume shielding whilst allowing the existence and action of plume etching by the still compressed ablation plume. Above the optimum flow velocity, the plume is blown away before it can become fully developed, as is the case in Figure 10-3(d), reducing or negating the plume etching effect, leaving only the laser beam that now has minimal obstacles for possible attenuation to pass through, to etch the material. The small changes to threshold fluence made across this broad range of

flow velocities (which corresponds to an increase in flow velocity of 166% from the lowest value plotted in the turbulent flow velocity regime) means that the KrF excimer laser ablation threshold is not critically sensitive to the use of a non-optimum flow velocity.

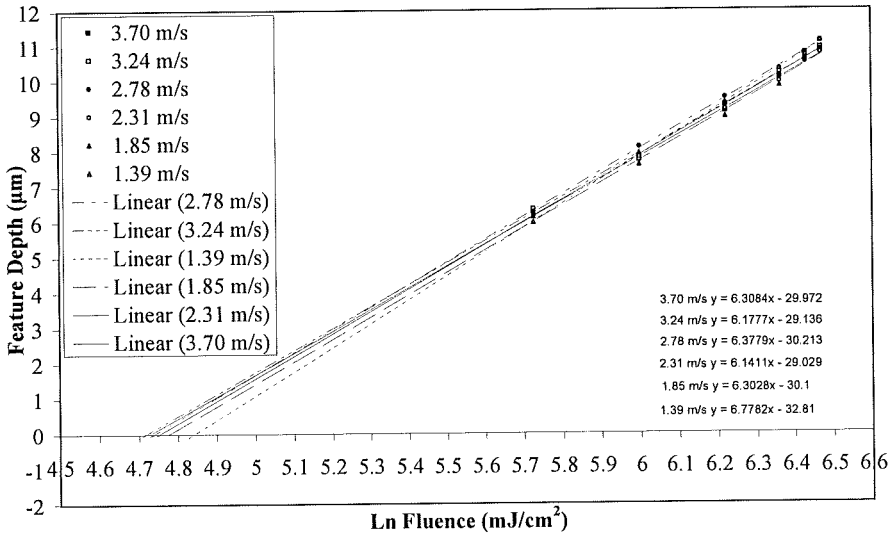

(a)

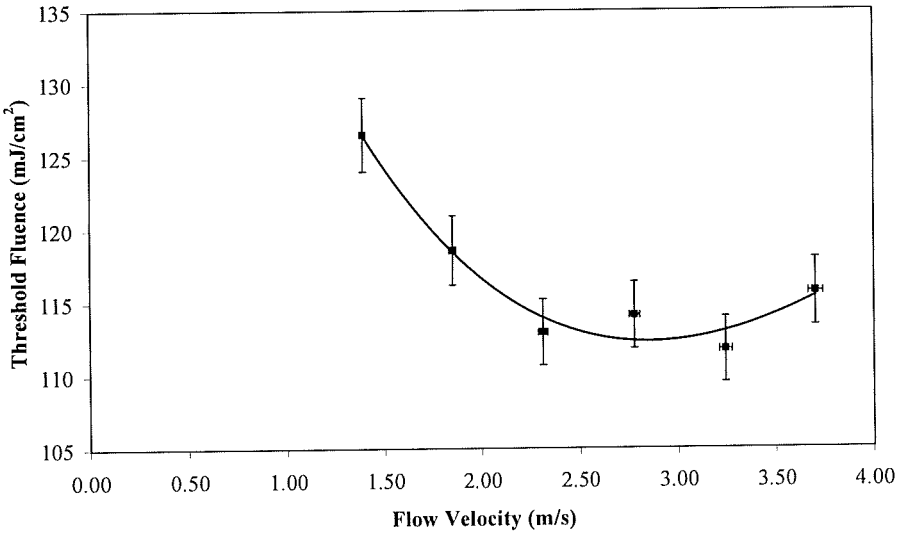

(b)

Figure 10-2: A detailed set of plots describing the ablation threshold of six different samples machined under turbulent velocity regime closed thick film flowing filtered water immersion (a) and a plot of the etch depth dependency on flow velocity of bisphenol A polycarbonate immersed in filtered water (b).

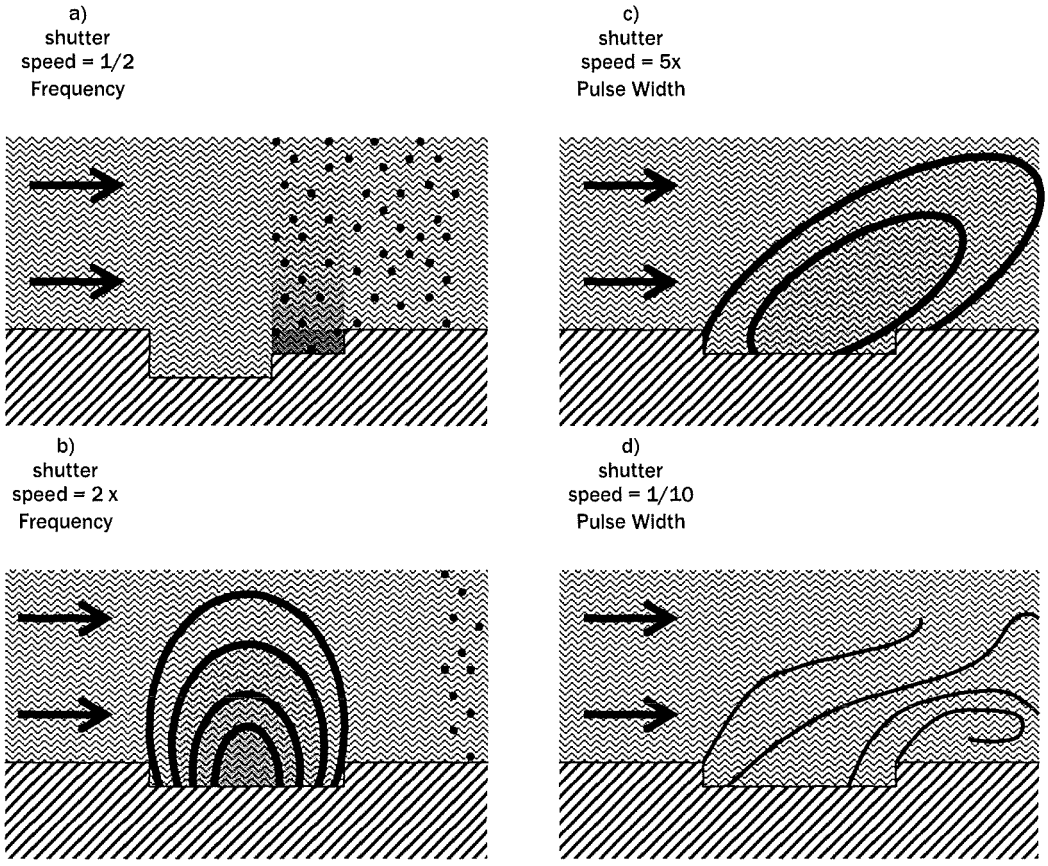

Figure 10-3: When the flow velocity is laminar and the laser pulse frequency is high, the liquid flow may not remove all of the debris before the next pulse arrives; thus the suspended debris may obscure the pulse, effecting the machined profile (a); a flow velocity lying below the optimum allows the ablation plume to fully develop, maximizing plume shielding and near compensating by uninhibited plume etching (b); the optimum condition occurs when the flowing liquid distorts the ablation plume to minimize plume shielding, without removing the action of plume etching (c); and when using a very high flow velocity with respect to the pulse width of the laser the ablation plume may become distorted by the viscosity of the fluid. This may have an impact on plume etch rate (d).

10.1.3 Impact of closed thick film laminar flow filtered water immersion on ablation threshold.

Figure 10-4 plots the etch depth of the mean average of all the turbulent flow velocity regime samples with respect to the natural logarithm of the fluence along with plots for two samples machined using laminar flow velocity regime closed filter water immersed ablation that both had flow velocities low enough to ensure laminar flow are also given. Threshold fluence values for the laminar flow velocity regime samples are given in Table 1. As has been stated above, the ablation threshold value of the average turbulent flow velocity regime samples has been calculated to be 116.6 mJ/cm^2. The sample produced at the highest laminar flow velocity had a threshold fluence of 125.7 mJ/cm^2, a value similar to that of the lowest velocity turbulent closed thick film flowing filtered water immersion flow velocity sample, which had an ablation threshold measured at 126.52 mJ/cm^2. This result supports the proposal that laminar flow velocities allow the ablation plume to become fully developed inside the liquid volume, as shown in Figure 10-3(b), producing maximum plume shielding of the laser beam. Losses in laser etching due to plume shielding are then partially compensated for by the action of

plume etching being unaffected by the action of the turbulent flow velocity. The samples produced using the slowest flow velocity of all those listed in this thesis show a very poor correlation. This poor correlation appears to support the idea described schematically in Figure 10-3(a), where the flow velocity did not have a magnitude sufficient to remove debris produced by one pulse from above the feature before the arrival of the next pulse, resulting in an unreliable laser fluence at the feature.

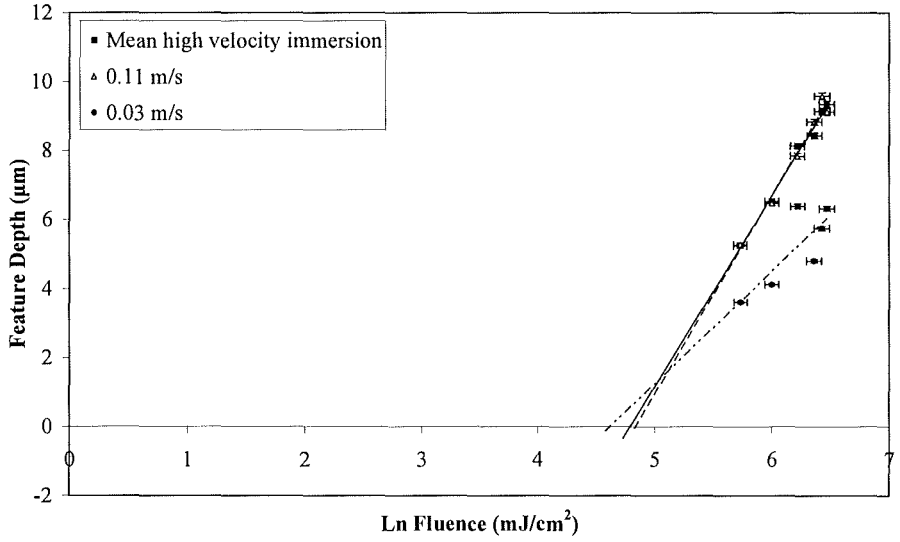

Figure 10-4: Feature depth against laser fluence to compare the average ablation threshold achieved using turbulent flow velocity regime thick film closed immersion ablation and two laminar flow velocity regime thick film closed immersion machined samples.

10.1.4 Flow - plume interaction states.

A more detailed explanation of the impact of increasing flow velocity on the ablation threshold under closed thick film flowing filtered water immersion is made clear by Figure 10-3. The premise of the closed thick film flowing filtered water immersion technique is to entirely clear the image area of debris produced by a laser pulse before the following pulse arrives, thus the velocity of the flow with respect to the pulse frequency is critical. Whereas very low flow velocities do not remove debris reliably between pulses, resulting in unreliable laser fluence at the sample surface (see Figure 10-3(a)); using a flow velocity that is sufficiently high to fully and reliably clear debris from above the feature, but lower than the optimum flow velocity, causes total ablation rate loss due to the plume shielding of the fully developed compressed ablation plume, (see Figure 10-3(b)). But, this loss is compensated for by the etching action of the plume (see Figure 10-3(b)). The optimum flow velocity is achieved when the immersing liquid washes a proportion of the ablation plume away during the laser pulse, not allowing excessive plume shielding, but simultaneously not completely destroying the ablation plume, thereby preserving the action of plume etching, a state illustrated by Figure 10-3(c). When greater than optimum flow velocities are used they allow maximum laser etching, the high viscosity of a liquid medium will deform the ablation plume during the laser pulse, reducing the plume etching mechanism described in the literature [50 - 52, 54] by removing the ablation plume before it has fully developed (see Figure 10-3(d)). These four states are described in terms of etching contribution by laser and plume by the hypothetical plot in Figure 10-5. The data generated in this thesis shows that

direct laser ablation etching is still the dominant factor in this interaction, as the curve in Figure 10-2(b) describes. When the plume becomes fully developed, plume shielding has a far greater limiting effect on the ablation threshold than high flow velocities washing away the compressed ablation plume. The optimal flow velocity for achieving minimal threshold fluence is achieved by a compromise, indicated by the dashed vertical line in Figure 10-5, where the combination of laser etching and compressed plume etching result in an increased ablation rate greater than the maximum ablation rate achievable by either of the component etch mechanisms alone. This plot shows the dependence of plume etching on the existence of significant laser etching, as laser etching is required to develop an ablation plume that can then go on to become compressed and begin etching itself. The plume etch rate declines as the immersing liquid flow velocity begins to wash the ablation plume away at higher velocities, leaving just the action of laser etching, at mechanism that relies on mechanical and chemical interactions [32, 33].

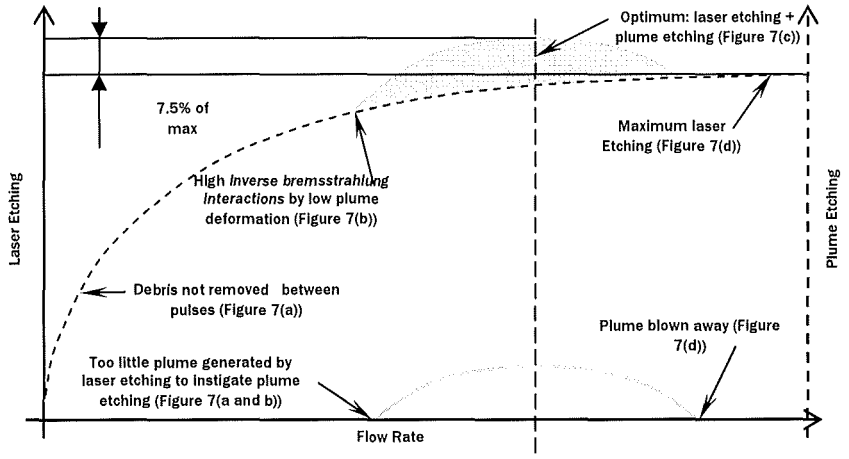

Figure 10-5: Schematic plot showing the action and combination of plume etching and laser etching and the flow velocity dependence of both. An optimum point exists and is depicted by the dashed vertical line, where the summation of both etching mechanisms combines to maximum effect.

The average ablation threshold fluence can be plotted with respect to the closed thick film flowing filtered water immersion fluid flow velocity (see Figure 10-6). Initial inspection of Figure 10-6 supports the states described in detail above. Sub optimum turbulent flow produced a maximum threshold, measured to be 126.52 mJ/cm^2, denoting poor etching efficiency, where high plume shielding limited laser etching, the size of the plume and therefore the aggressive etching action of the compressed hot gasses inside a water immersed plume, as described to the left of Figure 10-5. As the flow velocity is increased towards the optimum threshold value of 111.76 mJ/cm^2, the ablation threshold fluence drops. This is what one would expect to happen as the magnitude of laser etching and plume etching increased together. As the flow velocity rises beyond 3.24 m/s to the maximum magnitude tested, the threshold fluence begins to rise slightly again to 115.71 mJ/cm^2, where the ablation plume was beginning to be washed away before it was able to become fully developed, leaving only the action of laser etching to remove material.

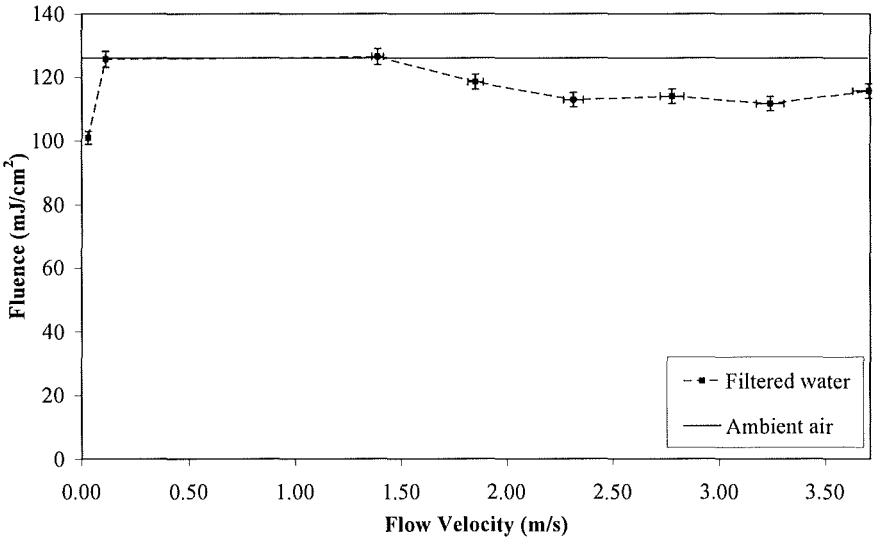

Figure 10-6: Fluence against flow velocity to give a comparison of average threshold fluence measured at all thick film closed immersion filtered water flow velocities against the ablation threshold in ambient air.

10.1.5 Closed thick film flowing filtered water immersion equipment laser beam attenuation.

The previous discussions only take into account the average ablation threshold measured across all laser fluences. If the data is split to high fluence data and low fluence data, two plots can be generated; these show a clear contrast to each other. In Figure 10-7(a) high laser pulse fluence data is plotted. This data shows the turbulent flow velocity regime samples had significantly lower threshold fluences than high fluence ambient air samples. The threshold fluence increased drastically to a value of 399.16 mJ/cm^2 for the lowest flow velocity. In contrast, the low laser pulse fluence data, plotted in Figure 10-7(b), had significantly reduced threshold fluence for the very low flow velocity and greatly increased threshold fluences for the turbulent flow velocity regime data. The two filter water plots appear to be mirror images of each other about the threshold fluence of bisphenol A polycarbonate in ambient air. This can be explained by returning to the theory of confined ablation plumes [54] and the drag imparted onto it by the liquid flowing over it. At laminar flow velocities the plume generated was not removed, it was able to become fully developed and etch the sample as it lay under compression. High fluence resulted in significant plume shielding, hence a high threshold fluence. Low fluence laser pulses always perform well for etch efficacy in ambient air because they do not produce large plumes and waste energy with heating *via* multi photon interactions [9] a fact demonstrated by the magnitude of the threshold fluence in ambient air in Figure 10-7(b). Any etching provided by the plume to supplement this efficient removal by low fluence pulses significantly increased the ablation rate with respect to the laser energy supplied, causing the low threshold fluence recorded for the lowest flow velocity. As the flow velocity increased to the turbulent flow velocity regime, the ablation plume was removed, allowing maximum laser etching without any plume shielding that limits high fluence pulse efficiency in air. This was of no aide to power pulses, that lost the supplementary action of plume etching with the deletion of the ablation plume, removing any advantage over ablation in ambient air. Losses due to attenuation of the equipment, such as the flow

chamber window, which was 5 mm thick and the immersing filtered water itself, resulted in the increased recorded threshold fluence for turbulent flow velocity closed filtered water immersion ablation evident in Figure 10-7(b).

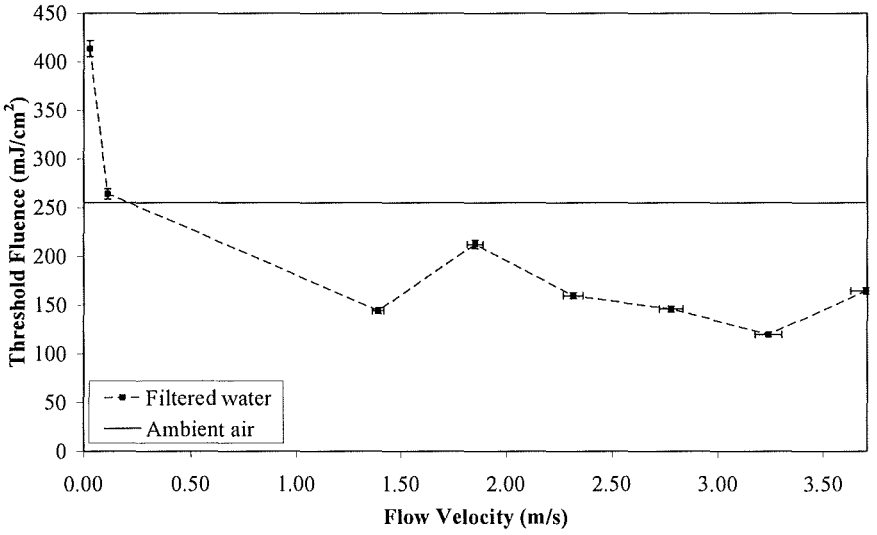

(a)

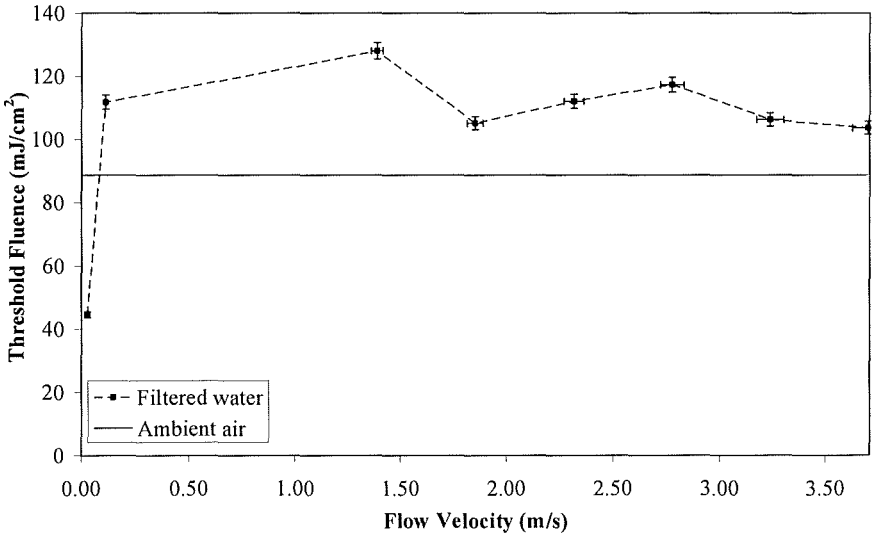

(b)

Figure 10-7: Comparison of the average threshold fluence measured for high fluence pulses at all closed thick film flowing filtered water immersion flow velocities against the ablation threshold in ambient air (a) and a comparison of the average threshold fluence measured for low fluence pulses at all closed thick film immersion flow velocities against the ablation threshold in ambient air (b).

10.2 Ablation rate

The use of a closed ablation chamber removes the variance of the flow geometry both with respect to time and position above the sample to be machined. If a thin film regime closed flowing immersion technique (less than 1.1mm in thickness [56]) is implemented, the compressed ablation plume will extend through the flowing liquid from the sample surface to the bottom surface of the chamber

window potentially plume etching the window, damaging a critical component in the optical path of the beam. This means that the experiments conducted in this thesis used a thick film regime to prolong the life of the chamber window.

10.2.1 Impact of flow velocity on ablation depth

The variance of fluid velocity used for closed thick film flowing filtered water immersion for removal of machining debris during laser ablation has a direct impact on the ablation rate achieved. The clearest demonstration of this is given graphically in Figure 10-8. In Figure 10-8 the feature depth achieved using a nominal number of laser pulses, identified in the plot legend, through the immersing closed thick film filtered water. Firstly, the depth achieved is proportional to the number of pulses fired, which is an expected and logical result: every pulse removes material, thus the cumulative effect of 'n' pulses will approximately be 'n' multiplied by the etch depth of a single pulse, for 3, 6, 12, 60 and 120 pulses, this linear relationship is borne out, as an example, examining the depths machined at 2.78 m/s gives 0.512, 1.046, 2.205, 10.03 and 19.25 μm. However, the use of 480 pulses, does not follow this trend; instead the depth etched is 36.65 μm, a value that falls below the expected depth given the relationship described above. When machined, there was no allowance made in the stage control algorithm to correct the optical length of the beam as the feature was machined ever deeper (this could be done by moving the sample towards the de-magnifying optic by the single pulse etch depth after every pulse). Figure 10-8 illustrates that the bottom of the machined feature falls out of the DoF of the micromachining system between 120 and 480 pulses. Therefore, with this knowledge, the rest of this thesis will not include 480 pulses in the calculation of ablation rates. More significant to this thesis, the simple plot of feature depth with respect to immersing liquid flow velocity given in Figure 10-8 demonstrates that low flow velocities cause 'n' pulses to machine less material than high flow velocities. A rapid but smooth increase in etch depth generated by 'n' pulses is followed through the laminar flow velocities (0 to 0.27 m/s), through intermediate flow velocity (0.27 to 0.47 m/s) and into the turbulent region (0.47 m/s and upwards). The results show that once using turbulent flow velocities there is little increase in etch efficacy.

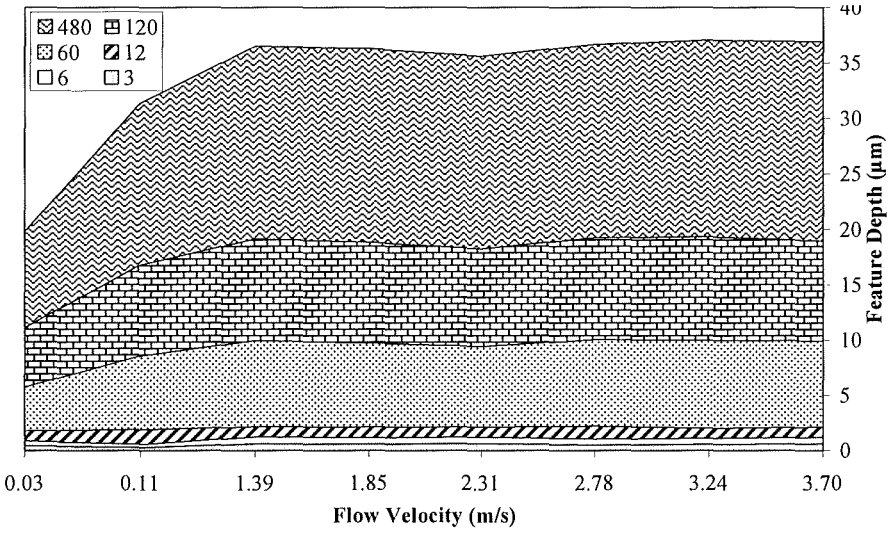

Figure 10-8: Filled line graph plotting the depth machined under closed thick film flowing filtered water

immersion by 3, 6, 12, 60, 120 and 480 pulses at 0.03, 0.11, 1.39, 1.85, 2.31, 2.78, 3.24 and 3.70 m/s.

10.2.2 Impact of turbulent flow velocity on ablation rate

The ratio determined by comparing the number of pulses used to machine a measured feature depth gives the ablation rate, that is the mean depth machined by a laser beam at a measured fluence in a single pulse [28]. In Figure 10-9 the ablation rate of a laser beam measured to be within 2% of 578 mJ/cm^2 for every sample machined, as indicated by the error bars given for every point plotted in Figure 10-9; thus, the ablation rates plotted for each closed thick film flowing filtered water immersion flow velocity can be compared. Figure 10-9 demonstrates that the turbulent flow velocities used (1.39 to 3.70 m/s separated by increments of 0.46 m/s) made little difference to the ablation rate of bisphenol A polycarbonate using KrF excimer laser pulses. This fact is demonstrated by the gradients listed for each flow velocity in Figure 10-9. These gradients, that are equivalent to the numerical ablation rates of the material vary by just 7% of the lowest ablation rate achieved, measured as 150.2 nm/pulse, achieved at 2.31 m/s.

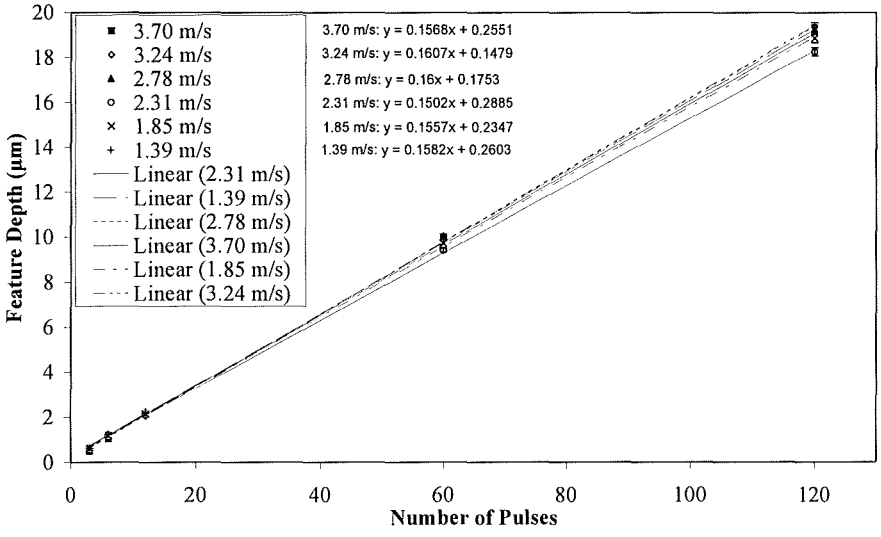

Figure 10-9: Ablation depth against number of pulses to determine ablation rate under closed thick film flowing filtered water immersion for five turbulent regime flow velocities.

The mean performance of KrF excimer laser ablation immersed under closed thick film turbulent flow velocity regime filtered water can be compared to the performance of a similar beam measured to have a fluence of 581 mJ/cm^2, making this comparable to those used for the immersed samples, machining the same bisphenol A polycarbonate sample in ambient air in Figure 10-10. The plot points of the mean ablation rate generated under turbulent filtered water flow include the 9% error bars required to represent the 2% variance of the measured fluences of the beams used to machine the turbulent flow samples and the 7% range of from highest to lowest recorded ablation rate. Inspection of this plot shows that the mean ablation rate centre line, indicated by the small dashed linear trend line in Figure 10-10, is 13 nm/pulse greater than that of ablation in ambient air, this is an 8.5% increase in ablation rate when using closed thick film turbulent flow velocity regime filtered water immersed ablation over ablation conducted in ambient air.

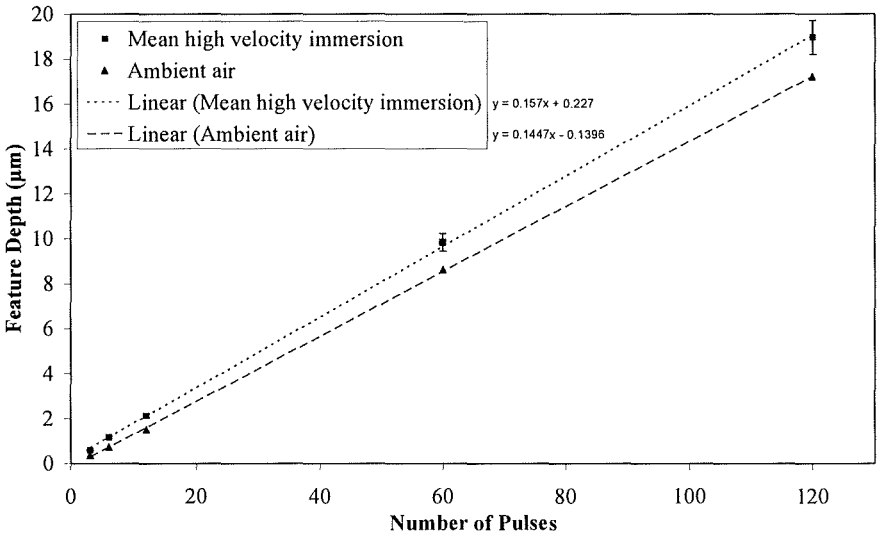

Figure 10-10: Ablation depth against number of pulses to determine ablation rate in ambient air and under closed thick film flowing filtered water immersion for a mean turbulent regime flow velocity.

10.2.3 Impact of laminar flow velocity on ablation rate

Figure 10-11 gives three plots. The plot described by the solid black linear trend line is the mean of all the ablation rates measured to be achieve in the turbulent flow velocity regime discussed in the previous Section; this is plotted to act as a reference for the two plots of interest in Figure 10-10. Two flow velocities were used in the laminar regime: 0.03 and 0.11 m/s. However, the laser repetition rate was increased by a multiple of four to 200 Hz. This was done with the intention of raising the pulse repetition rate above the frequency that the volume of liquid covering the feature is completely renewed. The reason for this action was to cause the possibility of debris to remain suspended above the feature as the following pulse occurs. The samples machined at the flow velocity of 0.11 m/s all had a fluence within 3% of 579 mJ/cm^2, as indicated by the error bars in Figure 10-11. The linear trend line for 0.11 m/s flow velocity is marked by a close dashed line and gives an ablation rate of 141.1 nm/pulse, thus giving a decrease in ablation rate of 15.9 nm/pulse, a drop of 10% from that achieved by mean ablation under a closed thick film turbulent flowing filtered water immersion. The samples machined for the 0.03 m/s flow velocity were all machined using a beam fluence within 4% 578 mJ/cm^2. The trend for 0.03 m/s flow velocity is represented by a double - dot - dashed linear line that has a gradient of 89.2 nm/pulse, a value that is 43% lower than the ablation rate achieved under a turbulent velocity filtered water flow and 37% lower than the ablation rate achieved using a flow that was 72% slower than the 0.11 m/s laminar flow velocity. The difference between the two laminar flow velocities is marked compared to that between 0.11 m/s and the turbulent flow velocities. This is caused by dramatic change in the refresh rate of the immersing fluid over the machined feature. This must be compared to the pulse repetition rate of the laser. For the 0.11 m/s sample the repetition rate of the laser was 50 Hz and the refresh rate of the immersing filtered water was 556 Hz, giving a ratio of 11.1 new liquid volumes between laser pulses; compared to a ratio of 0.695 new liquid volumes between laser pulses, as the liquid volume was only refreshed 139 times every

second for the 0.03 m/s flow velocity. Clearly, this significant disparity has directly resulted in a marked reduction of ablation rate.

Comparison of the mean ablation rate achieved by KrF excimer laser ablation under closed thick film laminar flow velocity regime filtered water immersion and in ambient air is given by Figure 10-11. The mean plot of ablation under closed thick film laminar flow velocity regime filtered water immersion is given with error bars indicating the 37% difference between the two flow velocities used. The mean ablation rate of these two is plotted by a long dashed linear trend line in Figure 10-12, giving a mean ablation rate of 115.2 nm/pulse. Ambient air is plotted without error bars as all the features used to measure the mean ablation rate were machined into a matrix of features in one machine run, thus the laser fluence, measured to be a mean value of 581 mJ/cm^2, is taken to be uniform for all feature groups, thus an error is not quoted. The ablation rate recorded for KrF excimer laser ablation of bisphenol A polycarbonate in ambient air was 144.7 nm/pulse. The mean ablation rate achieved by KrF laser ablation under closed thick film laminar flow velocity regime filtered water immersion is 20% lower than the ablation rate achieved in ambient air. This is a shift in performance from the turbulent velocity results. Furthermore, the error bars in Figure 10-12 indicate that the ablation rate in a laminar flow would not exceed that of ambient air in any case.

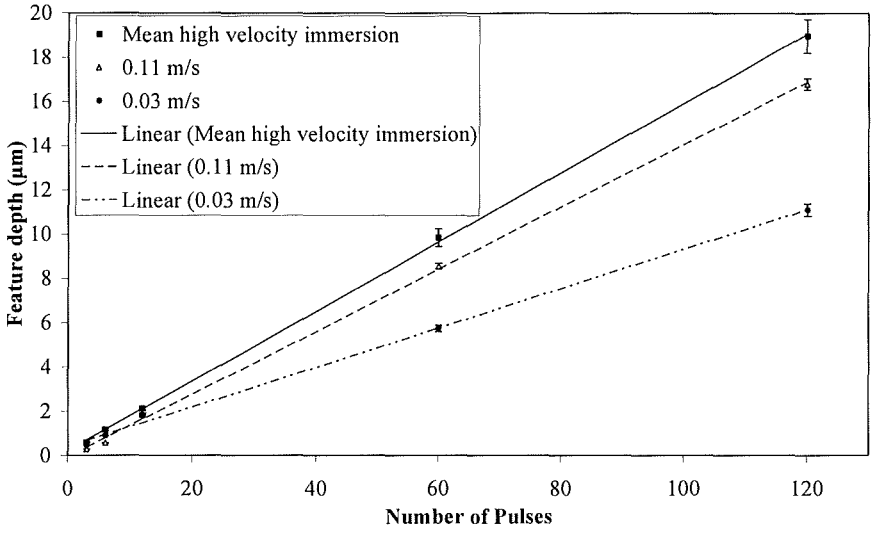

Figure 10-11: Ablation depth against number of pulses to determine ablation rate under closed thick film flowing filtered water immersion for a turbulent regime mean high flow velocity and a laminar flow velocity regime of 0.03 and 0.11 m/s.

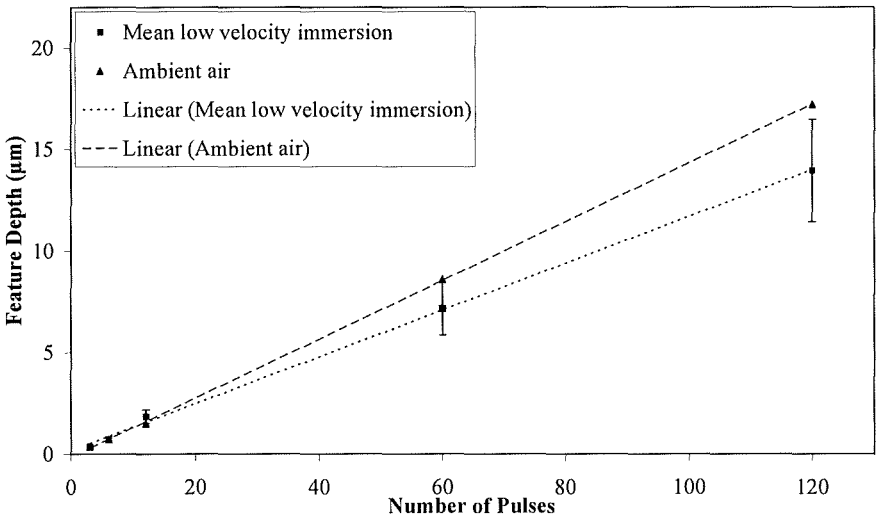

Figure 10-12: Ablation depth against number of pulses to determine ablation rate in ambient air and under closed thick film flowing filtered water immersion for a mean laminar flow velocity regime.

10.2.4 Flow – plume interaction states: The action of flow velocity on laser ablation

The dashed line in Figure 10-13 represents the ablation rate of the closed thick film flowing filtered water immersed samples and the solid, horizontal line represents the ablation rate measured for the samples machined in ambient air. Use of a range of flow velocities in a closed thick film flowing filtered water immersion ablation technique, from laminar to turbulent has resulted in a distinct trend that is described graphically in Figure 10-13. These two plots clearly demonstrate the change in typical ablation rate at laminar flow velocities (when the refresh rate of the liquid volume covering the laser machined feature is lower than the laser repetition rate) that drop sharply beneath the ablation rate produced in ambient air with a trend that follows a high power law, smoothing with increased flow velocity that causes a liquid volume refresh rate that is significantly greater than the laser repetition rate.

This can be explained by the interaction of the flowing liquid and the debris suspended within that flow on the laser beam and the ablation plume generated in the same way as it explains the variation in threshold fluence described in the first half of this Chapter. At very low flow velocities, where the ratio of fluid volume refresh rate with respect to laser repetition rate is less than 1, debris particles, that were ejected from the machined feature in all directions, including upstream, were still suspended in the flow above the entirety of the feature when the following pulse arrived. These particles intercepted the beam *en route* to its destination, lowering the fluence of the beam arriving at the feature, as described in Figure 10-3(a), reducing the etching efficacy of the laser energy originally delivered by the laser this is a result plotted schematically in Figure 10-5, which also identifies that a threshold level of laser etching is required to instigate a plume to add a contribution to the etching. As the frequency ratio between laser and fluid volume increased past 1 to 11.1, the debris was removed from the site of the machined feature before the second pulse arrived. This left the full quota of beam fluence to pass onto the sample surface; expect the highly viscous nature of the immersing filtered water constrained the expansion of the ablation plume. The flow was still not rapid, as it was

travelling in the laminar regime, and was not travelling with sufficient velocity to distort the ablation plume as it expanded over a short time frame within the flow as described schematically in Figure 10-3(b). This compressed ablation plume has a greater optical density when immersed in filtered water than it would in ambient air. This caused the ablation plume to provide increased plume shielding to the continuing laser pulse compared to the situation of ablation in ambient air, reducing the laser energy arriving at the sample surface. However some etching contribution was given by the ablation plume, reducing this perceived hindrance [50 - 52, 102] as denoted schematically in Figure 10-5, where the plume has now been allowed to develop and begins to aide in the etching process, although the laser etching possible is still not optimum.

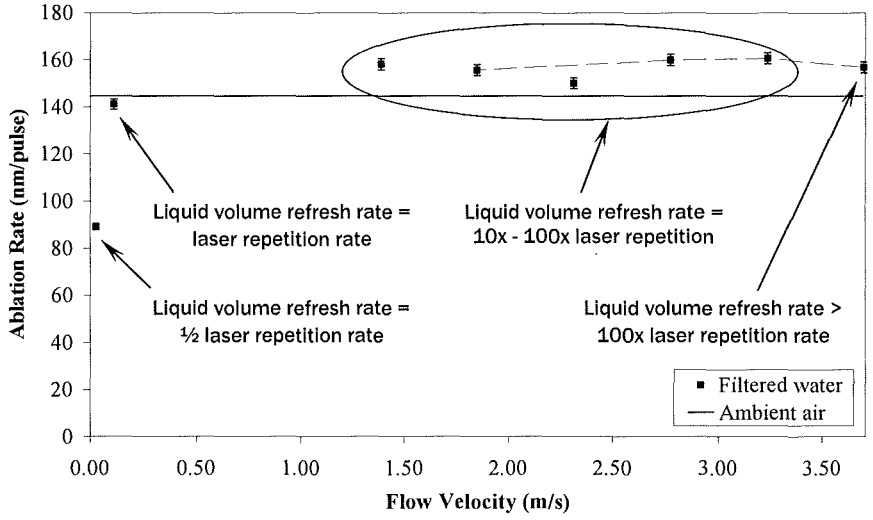

Figure 10-13: Measured ablation rates against flow velocity for ablation conducted in ambient air and under closed thick film flowing filtered water immersion, using 20 Hz laser repetition rate.

As the flow velocity moves into the turbulent regime the ablation plume begins to become distorted and lean due to the drag on it imparted by the rapid flow velocity of the high viscosity flow past it. This reduced the optical path length of the ablation plume for the laser beam as described schematically in Figure 10-3(c). The plume was merely distorted in shape at this point, and could still provide a significant etching contribution, at some flow velocity, shown in Figure 10-13 to be between 2.78 and 3.24 m/s, the distortion of the plume reached a maximum before the flow velocity became so high it began to destroy the plume and reduce the plume etching contribution. This was the optimum ablation rate point, where the laser had good access to the material and the plume is still etching effectively, and is indicated in Figure 10-5 by the dashed line. In Figure 10-5 the accumulative effect of laser etching and plume etching is presented in the grey area at the top of the diagram.

A flow velocity of 3.70 m/s is shown to have a reduced ablation rate compared to that measured at 3.24 m/s in Figure 10-13. The cause of this is illustrated in Figure 10-3(d). Here the flow velocity was so rapid that it was destroying the ablation plume before it was able to become fully developed and provide an etching contribution. Nevertheless, the lack of an ablation plume means that the laser beam has almost unopposed access to the material surface. This point is plotted to the right of Figure 10-5. Figure 10-5 is also useful in describing the criticality of the two etching processes.

Figure 10-5 shows that the peak ablation rate was only 2.4% larger than that of samples machined at non-optimum turbulent flow velocities, this value is marginal, but critically, larger than the maximum experimental error calculated of 2%. This is because the contribution of plume etching is small compared to that of laser etching, as indicated by the schematic plot in Figure 10-5.

CHAPTER 11

TOPOGRAPHY AND GEOMETRY OF FEATURES MACHINED INTO BISPHENOL A POLYCARBONATE USING CLOSED THICK FILM FLOWING FILTERED WATER IMMERSED KrF EXCIMER LASER ABLATION.

The surface topography of a feature machined using KrF excimer laser ablation can present evidence useful to the identification of the proportional contributions of the constituent etching mechanisms that combine in the grouped term 'laser ablation'. The novel equipment developed for this thesis allows the control of the flow velocity across the laser ablation event. Chapter 10 explains that this flow interacts significantly with the ablation plume and modifies the proportional contributions of the etching mechanisms taking place. Further evidence of this can be found when inspecting the feature surface topography of the samples machined using thick film flowing filtered water immersed KrF excimer laser ablation.

11.1 Introduction

This thesis has shown that modifications in surface topography were the result of immersion and not simply by variations in fluence level in Chapter 7. Surface topography characteristic modification or increased debris control could yield benefits for micro lens array manufacture, where profile accuracy and light diffusivity is key [261]. The open thin film laminar flowing DI water immersion technique pioneered by this thesis has limitations insofar as surface rippling caused inconsistent, large surface topography. This Chapter will explore the implications of confining the boundaries of the immersion fluid used in the work described in previous Chapters. This way the action and effect of ablation plume motivated rupture and splashing of the immersing film on the feature generated topography produced by closed thick film flowing filtered water KrF excimer laser ablation can be interpreted.

11.2 Effects of Closed Thick Film Flowing Filtered Water Immersion Ablation on Feature Waviness

In the first instance it is worth inspecting the trends generated by the three filters used to determine the use of each data set and also gain an understanding of the scales of surface morphological features produced by both KrF excimer laser ablation in ambient air and under closed thick film flowing filtered water immersion. This is a logical test for the data collated and is conducted here in the same way as it has been previously in Chapter 7 of this thesis. Figure 11-1(a) plots the mean RMS surface waviness measured at the six beam fluences used in ambient air. As one can see, all three plots produce similar trends; however, the plot taken for the 32 μm roughness – waviness cut-off filter shows a markedly exaggerated plot, suggesting that the surface waviness of features above 32 μm varies from that of deviations with lesser undulation in wavelength. All three filters display a similar outlying data point for 675.2 mJ/cm^2 that appears large. Critically, filter size is inversely proportional

to undulation amplitude; this is as one would expect because less undulation wavelength is available for surface elevation change when using a small filter. Figure 11-1(b) plots the mean average of mean RMS surface waviness data at the six beam fluences used under closed thick film flowing filtered water immersion flowing at the velocities of 0.11, 1.85 and 3.70 m/s. The trends demonstrated by this data are more similar across all filters than for the data collated for ablation in ambient air. Although the 579.9 mJ/cm^2 data point appear to be high with respect to surrounding points for all three filters. The high fluence waviness data for ablation in both ambient air and under closed thick film flowing filtered water is irregular, thus it would appear that high fluence laser ablation causes unpredictable large wavelength undulation surface topography. For further progression of this thesis, data will be interpreted from the 16 µm waviness-roughness filter cut-off, as this data demonstrates a good representation of the trend offered using all three filters.

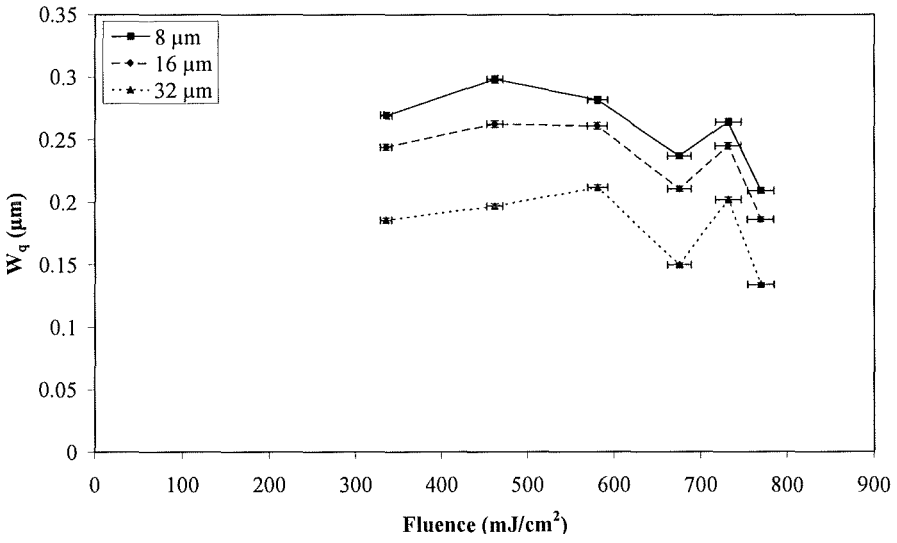

(a)

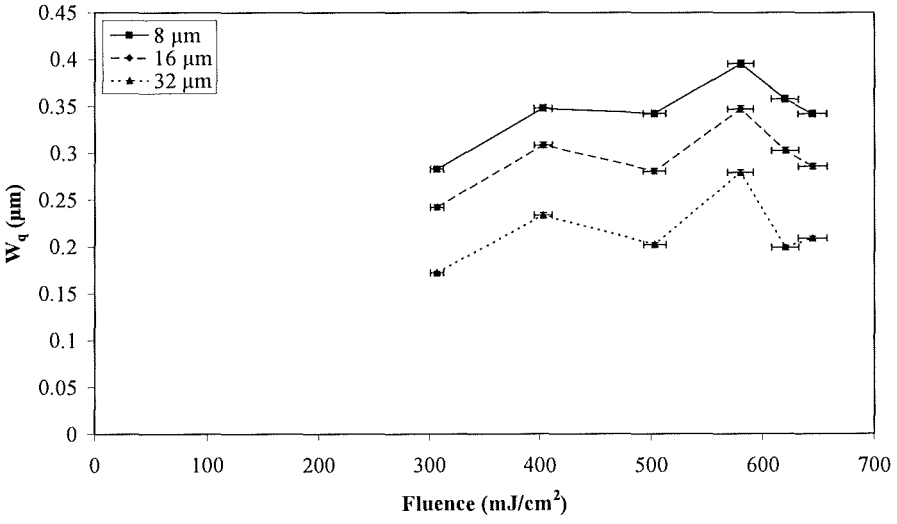

(b)

Figure 11-1: Plots for 8, 16 and 32 µm cut-off filters showing mean RMS surface waviness amplitude with respect to fluence used to ablate bisphenol A polycarbonate in (a) ambient air and (b) under closed thick film flowing filtered water immersion across three flow velocities.

Visual inspection of three dimensional WLI collated magnified models of two samples produced using the beam fluence of 580.7 mJ/cm^2 for KrF excimer laser ablation in ambient air, as shown in Figure 11-2(a), sets a benchmark for definition of machined geometry. The wall angles produced are high, as indicated by the cross-sectional profile shown in Figure 11-2 (a), and can be measured to average 82.1°. The feature floor in Figure 11-2(a) is close to level; however, it is noticeably domed. KrF excimer laser ablation using a beam with a fluence of 617 mJ/cm^2 under closed thick film flowing filtered water immersion flowing at 0.11 m/s, shown in Figure 11-2(b), the geometry is markedly less crisp and the feature floor is 1.6° from level, and the wall draft angles are significantly lower, averaging 66.2°. Ablation taking place in a flow velocity of 1.85 m/s (see Figure 11-2(c)) produced a feature with improved definition to geometry over the 0.11 m/s flow velocity feature (see Figure 11-2(b)) and has a floor angle of 1.2° and an average wall angle of 81.6°. Ablation under a flow with a velocity of 3.70 m/s results in a feature that has the finest geometry achieved in this thesis, as can be seen in Figure 11-2(d). This feature has a floor angle of just 0.5° and none of the floor curvature observed in Figure 11-2(a) for the samples machined in ambient air. Also, the wall angles achieved using 3.70 m/s flow velocity are the highest recorded, being 84.4°. These results illustrate that the feature geometry is affected by use of differing medium surrounding the ablation event, with increased viscosity results in decreased feature geometry definition. This is proposed to be caused by the significantly increased contribution of plume etching promoted by the confinement of the laser ablation plume afforded by immersion in viscous media [50 - 52, 56, 102]. This thesis also demonstrates that both the geometrical definition and wall angles of features machined are proportional to flow velocity, as both increased with flow velocity.

Profile waviness values were calculated using the cross-sectional profiles for each feature given in Figure 11-2 and used in combination with values taken from similar samples to reduce error. KrF excimer laser ablation using a fluence of 580.7 mJ/cm^2 in ambient air was measured to have a mean waviness magnitude of 87.2 nm in Figure 11-2(a). Features machined using a KrF excimer laser beam with a fluence of 617 mJ/cm^2 under closed thick film filtered water flowing at 0.11 m/s was measured to have a waviness of 214 nm, reflecting the poor geometry definition identified above generated using this flow velocity in Figure 11-2(b). Using a flow velocity of 1.85 m/s resulted in profile waviness of 121 nm in Figure 11-2(c) and using 3.70 m/s flow velocity gives a similar mean profile waviness of 115 nm in Figure 11-2(d), a value 34 nm greater than that produced using half the flow velocity. Both 1.85 and 3.70 m/s flow velocities lie in the turbulent flow regime for the cross-sectional geometry of the equipment used, and the waviness is measured to be markedly lower than that produced at a flow velocity of 0.11 m/s that lies in the laminar region for this equipment. As well as the flow parameters, it is worth noting the ratio between the distance covered during the duration of laser pulse and the traversing length of the feature being machined (in this case 203 μm) shows that the number of times the fluid volume is refreshed in the laminar regime is significantly lower than that achieved at the turbulent regime; thus, debris removed in previous pulses could be interfering with following pulses at laminar flow velocities, causing localized high beam attenuation and therefore increased surface waviness. Furthermore, the flow velocity of a fluid with the viscosity of water (approximately two orders of magnitude more viscous than ambient air) will impact the geometry of the ablation plume. This could result in mere compression of the plume at

laminar flow velocities and total destruction and removal of the plume at rapid flow velocities. This is described in detail in Chapter 10 of this thesis. Another noteworthy outcome of this data is the significant improvement in machined feature geometry definition is significantly improved using the closed thick film flowing technique over that achieved using an open thin film flowing immersion technique given in Figure 7-2(d).

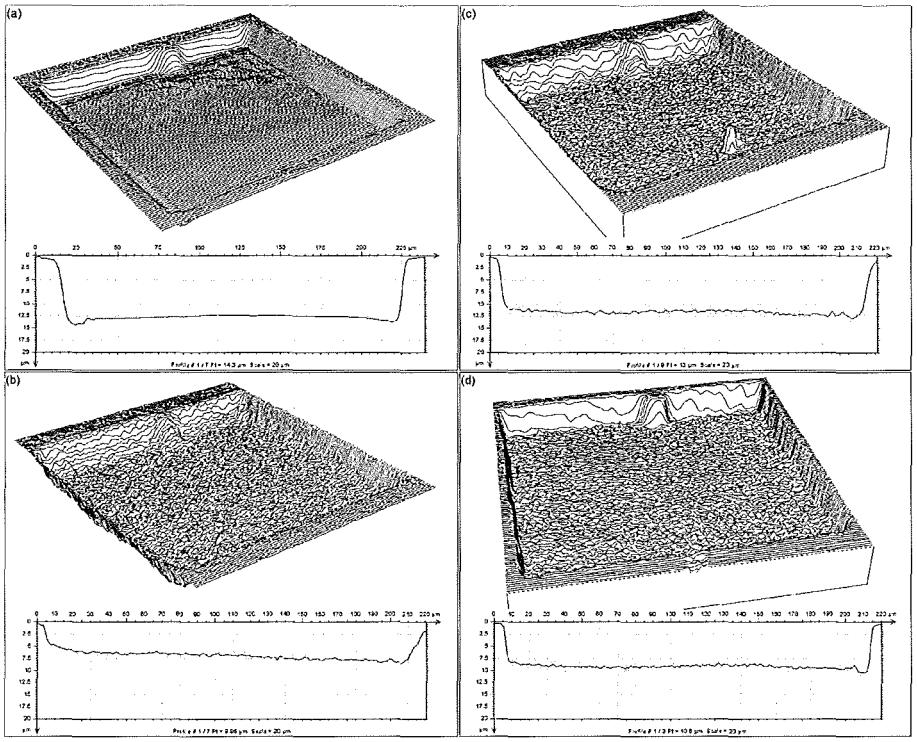

Figure 11-2: 3D views of entire ablated features and 2D profiles from the cross-sections of features ablated in (a) ambient air and (b) under closed thick film flowing filtered water immersion flowing at 0.11 m/s, (c) under closed thick film flowing filtered water immersion flowing at 1.85 m/s and (d) under closed thick film flowing filtered water immersion flowing at 3.70 m/s.

Further detail can be gleaned by plotting the change the relationship between surface waviness and fluence. This has been done and is shown in Figure 11-3, where KrF excimer laser ablation in ambient air and under closed thick film flowing filtered water immersion at the flow velocities of 0.11, 1.85 and 3.70 m/s shows that the surface waviness generated by a KrF excimer laser beam in ambient air is much more stable and predictable than that produced by a similar beam under closed thick film flowing filtered water at any flow velocity. The data is most inconsistent for the lowest flow velocity of 0.11 m/s. Although the waviness values returned at this flow velocity are the lowest of those produced using closed thick film flowing filtered water immersed ablation; indeed the mean waviness returned across all fluences when using an immersing fluid flowing at 0.11 m/s is 8.3% lower than that generated by ablation in ambient air. The highest mean waviness generated over all fluence values tested was by the flow velocity of 1.85 m/s, at 346 nm. The flow velocity of 3.70 m/s produced the most stable plot of the three immersed samples, as can be seen in Figure 11-3. The mean waviness amplitude generated at this flow velocity was 323 nm. Also the data for the two flow velocities in the turbulent regime reflect an agreeing trend: the waviness is proportional to fluence. The plots given in Figure 11-3 for closed thick film flowing filtered water immersed ablation also

indicate that predictability of surface waviness with respect to fluence is proportional to flow velocity. This is proposed to be due to decreasing impact and interruption to flow geometry by the explosive nature of the laser ablation plume as flow velocity increases. This is a logical interpretation, as increased velocity will result in increased liquid volume passing the ablation plume area per second, thus the ablation plume will have a smaller disruption effect on the flow passing per second.

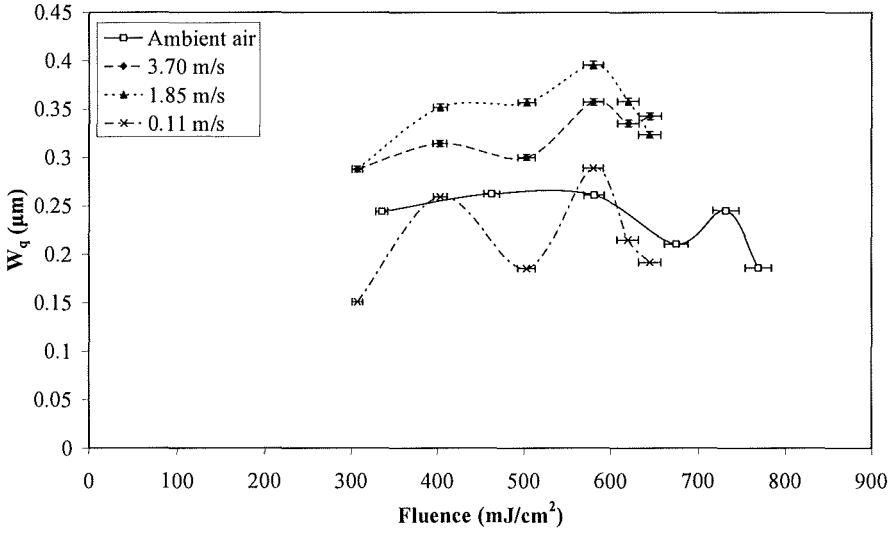

Figure 11-3: Surface waviness (features greater than 16 µm in wavelength) against fluence for features machined in ambient air and under closed thick film flowing filtered water immersion.

11.3 Effects of Closed Thick Film Flowing Filtered Water Immersion Ablation on Feature Roughness

In the same manner as used for surface waviness, the initial step to be taken must be to consider the relevance of the data collated. Figure 11-4(a) plots the mean RMS surface waviness measured at the six beam fluences used in ambient air at 8, 16 and 32 µm roughness-waviness cut of undulation wavelength filter. The three plots show good agreement, suggesting the roughness morphology was measureable using all three filters and that asperities were produced that have smaller area than 8 µm^2. Figure 11-4(b) plots the mean average of mean RMS surface waviness data at the six beam fluences used under closed thick film flowing filtered water immersion flowing at the velocities of 0.11, 1.85 and 3.70 m/s. This data shows the same agreement of trends that were witnessed in Figure 11-4(a); therefore, it can be said the immersion technique did produce surface morphology with an area lower than 8 µm^2. This is a result in agreement with findings from KrF excimer laser ablation conducted under open thin film flowing DI water immersion, as detailed in Chapter 7. Filter size is inversely proportional with undulation amplitude, which is in contrast to the relationship displayed by waviness filtering. This can be explained using the same undulation wavelength logic: increased undulation distance provides greater scope for large variation in surface amplitude.

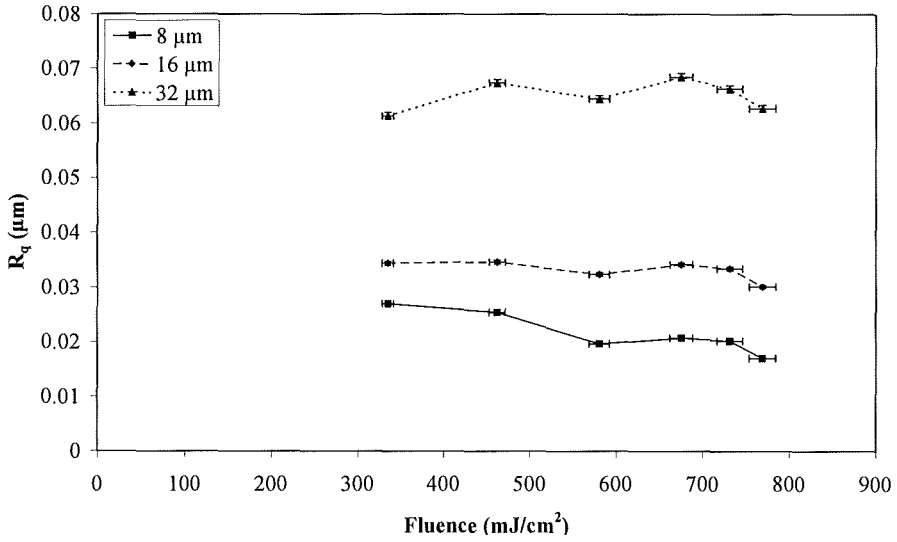

(a)

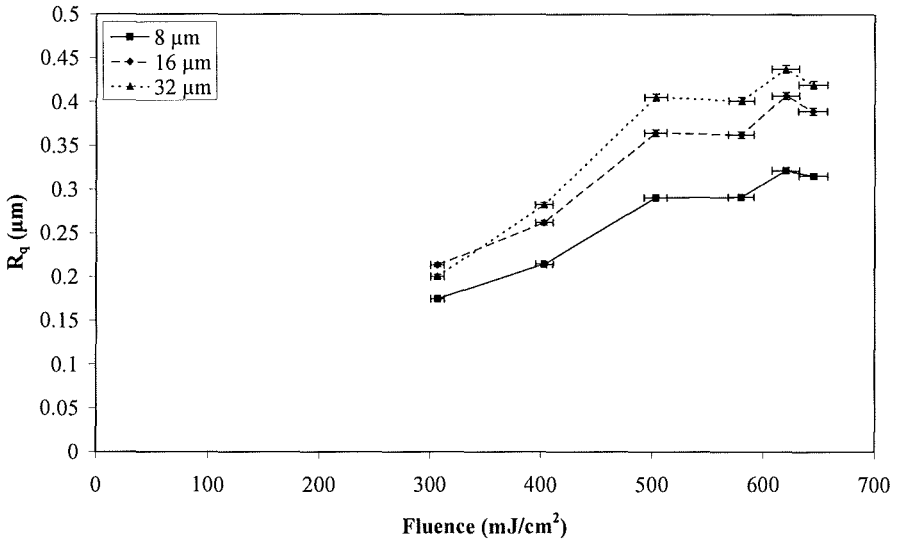

(b)

Figure 11-4: Plots for 8, 16 and 32 µm cut-off filters showing RMS surface roughness amplitude with respect to KrF excimer laser fluence used to ablate bisphenol A polycarbonate in (a) ambient air and (b)under closed thick film flowing filtered water immersion.

Figure 11-5 shows four similar 3D reconstructions of WLI data viewed over an identical area of 81 µm^2 and with visual topography amplification of 15%; thus, all four can be directly compared to assess relative surface roughness. The surface roughness of a sample produced using a beam fluence of 580.7 mJ/cm^2 for KrF excimer laser ablation in ambient air, shown in Figure 11-5(a), is noticeably smoother than the surfaces shown in Figure 11-5(b), Figure 11-5(c) and Figure 11-5(d) for samples machined using a KrF excimer laser with beam fluence of 617 mJ/cm^2 to ablate bisphenol A polycarbonate under thick film closed filtered water flowing at 0.11, 1.85 and 3.70 m/s respectively. The roughness of the three immersed samples appear to have similar amplitude; however, the surface area covered by asperities appears to decrease with increasing immersing fluid flow velocity.

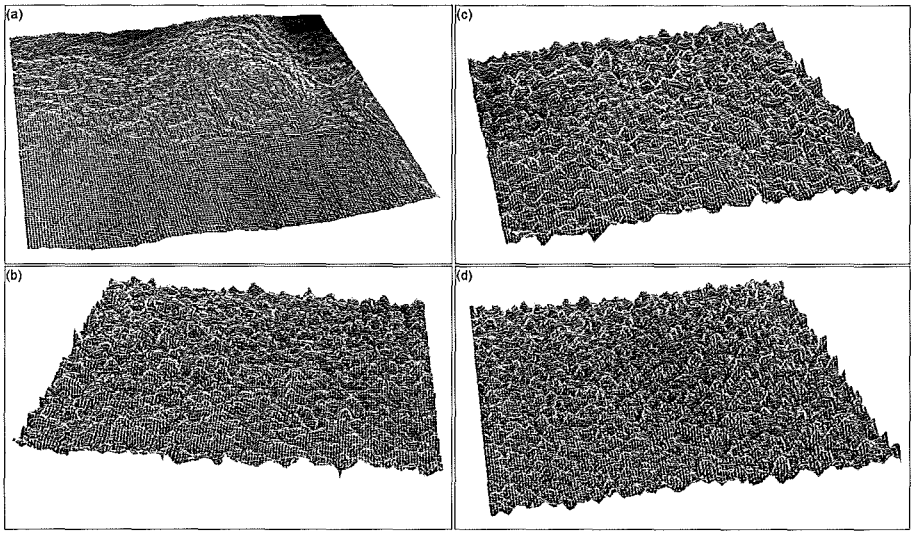

Figure 11-5: Close-up 3D views showing the small scale surface topography (roughness) of a sample produced using KrF excimer laser ablation in (a) ambient air, (b) under closed thick film immersion flowing at 0.11m/s, (c) under closed thick film immersion flowing at 0.11m/s and (d) under closed thick film immersion flowing at 0.11m/s.

This observation from a 3D view is supported by inspection of the gradient maps given in Figure 11-6, where surface height appears to change more rapidly at a flow velocity of 3.70 m/s, shown in Figure 11-6(d), than for the sample produced using a 0.11 m/s flow velocity, shown in Figure 11-6(b). This can be observed by inspecting the sharpness of contrast between deep (dark) points and high (bright) points. The 3D image of the sample machined in ambient air, shown in Figure 11-5(a), does clearly show the large waviness undulations discussed in Section 11.3 of this thesis. The rippled effect of surface melt, cited as a significant contributor to the ablation mechanism [262], is evident in the sample machined in ambient air, shown in Figure 10(a). The relationship between mean RMS surface roughness and fluence is plotted for the four cases investigated in this contribution are offered in Figure 11-7. This graph clearly shows the low level of surface roughness measured from the surface machined using KrF excimer laser ablation in ambient air compared to the significantly increased levels of fluence achieved using flow velocities of 0.11, 1.85 and 3.70 m/s under closed thick film flowing filtered water immersion. The trend plotted for ablation in ambient air is very regular and close to continuous. The gradients are of interest; the projected fluence required to produce a surface roughness with zero amplitude when using closed thick film immersed ablation flow velocities of 0.11, 1.85 and 3.70 m/s were -769, -21.29 and 38.75 mJ/cm^2 respectively. Since the data collated at the laminar flow velocity has already been stated to appear unstable, the value for this flow velocity can be disregarded. This leaves two values that are sufficiently close to zero as to be regarded as having origin intercepts. Hence the trend lines plotted in grey in Figure 11-7 have been plotted to intercept the origin. Doing this shows that the gradient (which represents the rate of increase in surface roughness with respect to fluence) has a power law proportionality to flow velocity: The increase in gradient from 0.11 to 1.85 m/s (an increase in velocity of 1.74 m/s) is much greater than the difference between 1.85 and 3.70 m/s (and increase of 1.85 m/s). This relationship supports the ideas proposed in Chapter 10 of this thesis where the nature and result of the ablation plume was defined by the velocity of the flow passing it.

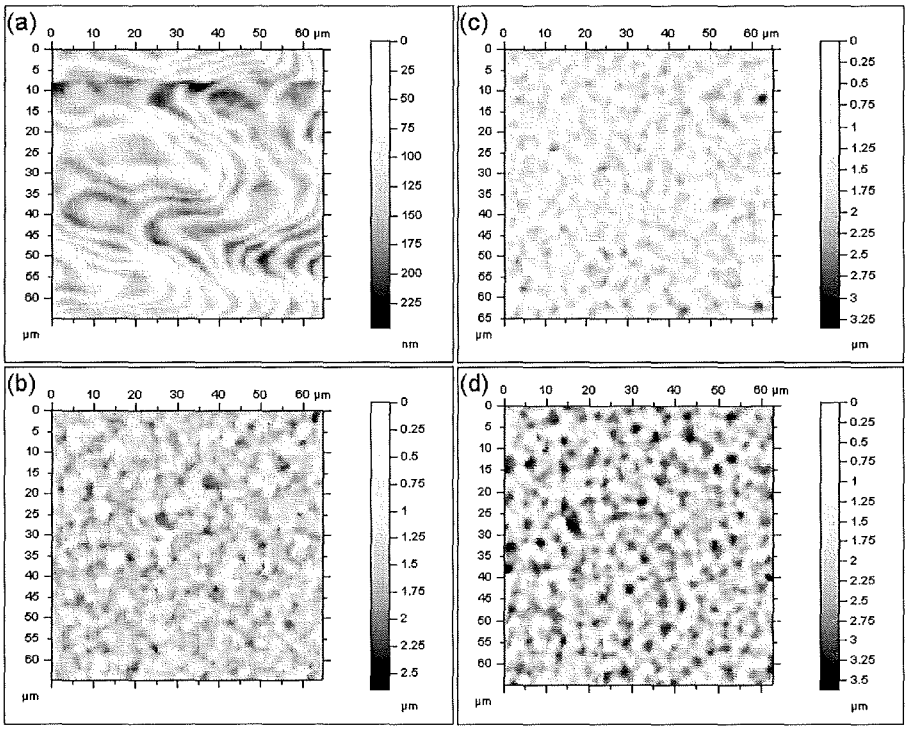

Figure 11-6: Greyscale maps showing the small scale surface topography (roughness) of a sample produced using KrF excimer laser ablation in (a) ambient air, (b) under closed thick film immersion flowing at 0.11m/s, (c) under closed thick film immersion flowing at 0.11m/s and (d) under closed thick film immersion flowing at 0.11m/s.

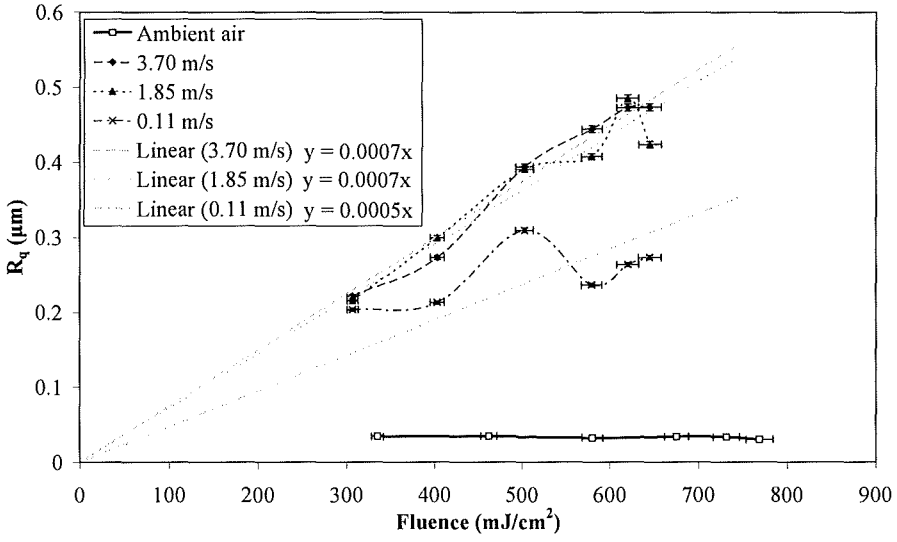

Figure 11-7: Surface roughness (features lower than 16 µm in wavelength) against fluence for features KrF excimer laser machined in ambient air and under closed thick film flowing filtered water immersion.

11.4 Closed Thick Film Flowing Filtered Water Immersion and the Effects Thereof on Ablation Mechanism and Feature Surface Topography

It has been shown that ablation in air is a complicated interaction between a number of contributing etching mechanisms [28 - 31, 77, 262, 263]. Of these, one that is of interest and has been proven to exist is that of photomechanical etching [30, 31]. This etching mechanism is dependent on beam fluence, beam wavelength (as the internal stresses causing acoustic type stress that are termed "photomechanical" are claimed to be initiated by thermal load), pulse duration and substrate chemistry when machining in vacuums or low viscosity media such as ambient air [31]. In ambient air, the laser initially couples with the material surface without interruption. An ablation plume then develops rapidly between the sample surface and the laser source for the remaining during of the laser pulse. The low viscosity of air allows the plume to expand almost without constraint, thus the shock on the surface is minimal, and the course removal of the raw beam is softened by the mask of the ablation plume. As a result the surface waviness and roughness are low.

The use of increased viscosity media adds another critical component to this recipe: ablation plume pressure [102]. The action of a viscous medium, such as filtered water, as used in this contribution, acts to suppress the expansion of an ablation plume during and after the laser pulse. This means that similar levels of evaporate and gas are contained in a smaller volume when machining under a liquid immersed sample than when machining in ambient air, where the plume can expand more freely. This results in increased plume pressure by a level that can be calculated using the work of Berthe *et al* [54]. In the case of filtered water, where shock impedance is approximately 3500 times greater than ambient air [264], this increase is approximately a multiple of 70 in pressure over laser ablation in ambient air. Previous work, covered in Chapter 7, using open thin film regime flowing DI water immersion of laser ablation resulted in film rupture and splashing observed in Part II of this thesis. Using a closed thick film immersion regime prevented this rupture and splashing, which in turn resulted in an increase in ablation rate and threshold [56]. Having said that, The work described in Chapter 10 of this thesis found that the application of flow velocity control caused noticeable variation in the KrF excimer laser ablation rate and fluence. This was proposed to be due to the proposed flow - plume interaction given schematically in Figure 11-8.

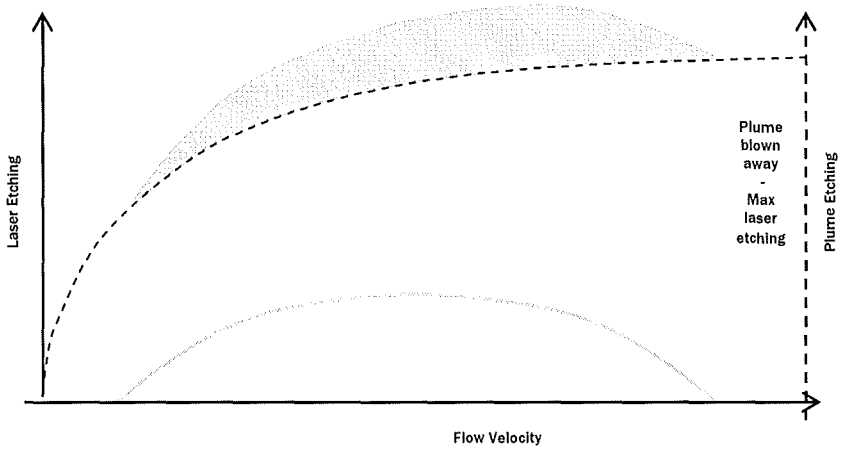

Figure 11-8: Schematic proposal of the compound interaction of laser and etching plume etching resulting in increased roughness. Roughness and waviness are proportional to waviness.

At the laminar flow velocity used in this thesis, the distorting drag force applied to the plume by the passing flow of filtered water was minimal and thus the photomechanical contribution was large, but this high pressure gas strongly attenuated the beam by plume shielding, limiting the impact of laser etching on the surface of the sample, as indicated by the large compound bulge shaded in grey in Figure 11-8. The plume, unable to expand in the viscous water in the same manner as in air aggressively attacks the surface of the material resulting in increased surface roughness over the sample machined in ambient air, where photomechanical etching can only occur briefly. The dense plume also protects the feature from further attack by the raw laser beam.

As the immersing fluid flow velocity was increased to a turbulent regime, the drag of the flow on the plume distorted the plume in proportion to the flow velocity. Distortion of the plume in the flow afforded the beam a shorted traverse distance through the highly shielding plume, increasing the level of laser etching taking place per pulse and consequently increasing the exposure of the feature to the laser beam with less plume masking to soften its profile. Also the plume is not removed by the plume merely distorted, causing further coarse material removal by means of compressed plume etching as indicated by continued growth in size of the plume etching mechanism in Figure 11-8. This explains the large roughness values witnessed in Figure 10 for the closed thick film flowing filtered water immersion velocity of 1.85 m/s.

At 3.70 m/s drag on the plume was so significant as to have begun complete removal of the plume (that act to partially mask the feature from the beam, with a softening effect) before the 25 ns pulse has ended, this allowed maximum laser etching of the surface as asserted in Chapter 10 of this thesis. Simultaneously, no plume etching can take place as the plume is removed too rapidly. This result would result in a vastly reduced photomechanical etching process and therefore a much lower surface roughness that has not been indicated by these results. This is the combination described schematically to the right of Figure 11-8. This scenario also explains the peak waviness reported by this thesis, as plume etching should have a less defined profile than a laser beam.

11.5 Modification of the Ablation Pressure: A Cause for Feature Floor Darkening

It is sensible to consider PLA in gaseous media first. Three distinct phases have been identified to occur during such an interaction. The initial phase of the pulse will instigate ablation, and is termed 'generation': the gaseous materials ejected from the target will form a plasma, as depicted in Figure 11-9(a). The plasma formed will be partially confined by the surrounding gaseous environment; however continued ablation and excitation of the plume will cause the plume to expand, as shown in Figure 11-9(b) [76].

The ablated species originating from the target material are not suspended in the plasma plume. Because both the plasma and the surrounding environment are gaseous in nature, the two tend to mix. The high energy and temperature state of the plume allows chemical reactions to occur between molecules from the two substances to form new compounds. This chemical modification is termed 'transformation'. The latter part of the pulse adds energy to instigate these reactions; the mixing of the gas and plume continues after the pulse has ended as the next phase begins, as described in Figure 11-9(c) [76].

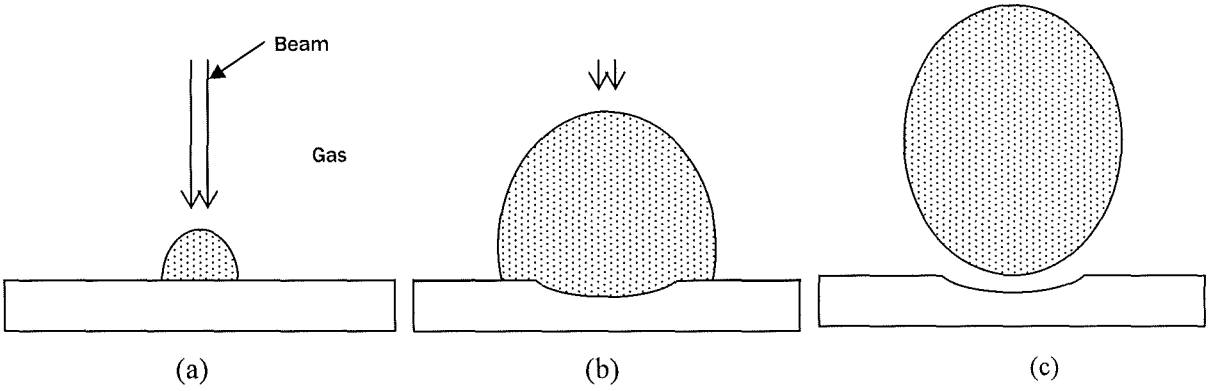

Figure 11-9: Three stages of PLA in gasses: (a) initial phase of beam creates a small, rapidly expanding plasma plume; (b) further irradiation ablates more material and energizes plume, causing further plume expansion; and (c) pulse ends, plume quenching period beings.

The heat contained within the plume begins to diffuse into the surrounding environment at the end of the pulse. The intense thermal diffusion of the species in the plasma plume can result in collisions, leading to aggregations. Thus thermal diffusion is also critical in transformation, before eventually leading to 'condensation' of the new mixed species into melt form and finally to solidification resulting in particulate matter [76].

Fabbro *et al* [102] found that a shockwave was induced by the laser induced plasma and was confined to the extents of the plume by the surrounding liquid (see Figure 11-10). The laser induced plasma adiabatically expands when the plasma absorbs the latter part of the laser pulse and receives a further supply of vaporized mass from the target material at a supersonic velocity to create a shockwave as described in Figure 11-10(b). This shockwave will generate increased pressure within the laser induced plasma plume. This increase in pressure generated by the shockwave has become known as the 'plasma induced pressure'. Thermodynamically, the increase in pressure will be coupled

to an increase in temperature of the plasma, causing the laser induced plasma under the confinement of the surrounding liquid to have a higher temperature, pressure and density than that of a plasma generated in a gaseous or vacuum environment. The plasma induced pressure is dependent upon the wavelength and fluence of the beam involved [101], with the maximum pressure achievable decreasing with increasing pulse length [103].

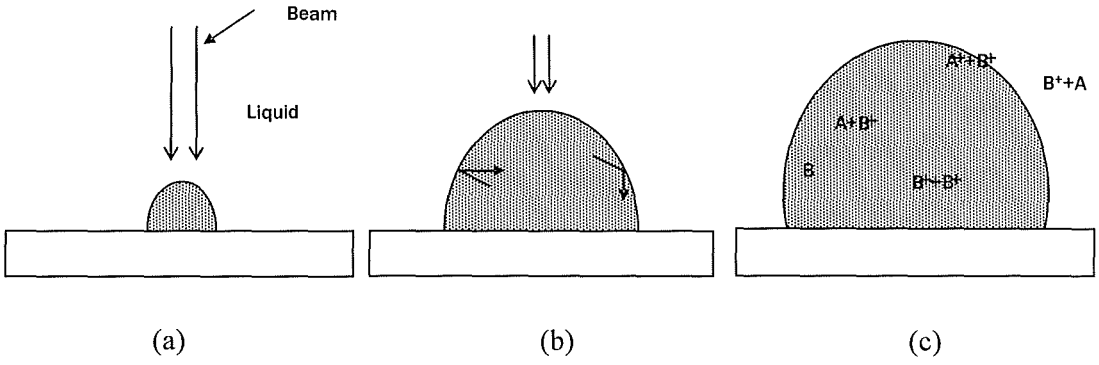

Figure 11-10: Three stages of ablation in a confining fluid: (a) initial period of pulse instigates plasma plume; (b) end of pulse energizes plume and plasma induced shockwave both cause plume expansion, confining liquid limits expansion; and (c) Four different reactions occurring in the plasma, the liquid and at the interface between the two.

Fabbro has been involved in a wide range of research to understand the nature of the plasma induced in a solid-liquid system [54, 102, 103].from this an analytical model has been developed to predict the maximum pressure, p_{max}, measured in GPa, by the laser induced plasma in water as described in Equations (8) and (9). These values are identical to those commonly quoted as acoustic impedance values measured in Rayles [265]. The acoustic impedances for the media and material used in this target have been collected [34]: air has an impedance of 413.2 Rayles; water 1480 Rayles and Polycarbonate is larger still with 2770 Rayles. Calculation using the values given above and Equations (8) and (9), allows the estimation of the plume pressure during the laser pulse. The pressure generated in ambient air is predicted to be an increase of 7.9 GPa, a large increase over atmospheric pressure; however, the use of filtered water immersion posed a significantly larger increase in plume pressure of 12.1 GPa, a result that is a multiple of 1.6 greater than the pressure generated in a similar plume in ambient air.

The change in plume pressure and the resultant increase in plume temperature, coupled with greater plume density, which had the effect of increasing plume shielding through the plume when machining using closed thick film flowing filtered water immersion of the sample may impact the machining mechanism in several significant manners. The result of this is evident in the darkened surface of the all the samples machined. Cleaning of these samples did not result in removal of this blackened surface as the two features given in Figure 11-11 show: Figure 11-11(a) gives a sample after machining without any post-process cleaning, clearly displaying the characteristic darkened surface attribute of closed thick film filtered water immersed laser ablation; Figure 11-11(b) shows the sample feature following 10 minutes ultrasonic cleaning in DI water.

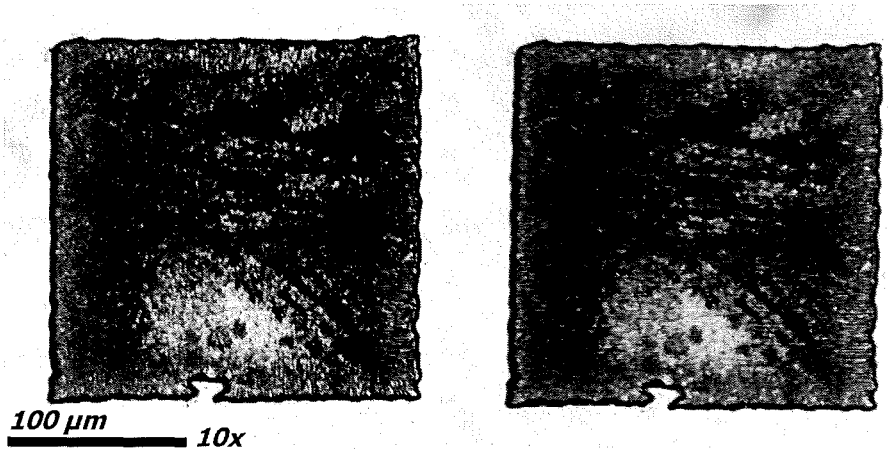

(a) (b)

Figure 11-11: Optical micrographs displaying the dark floor of sample machined under closed thick film flowing filtered water immersion directly after machining (a) and (b) the same feature given in Figure 11-11(a) after ultrasonic cleaning for 10 minutes.

This darkening could be the result of a number of scenarios. Previous research has identified the existence of laser ablation-generated and controllable surface plasmon features on the surfaces of nanoparticles manufactured using laser ablation [266, 267]. A plasmon can be described as a quaziparticle; a method of describing phenomena that have many random forms possible at any specific point in time but can be described as a single entity, much in the same way as a photon is used to describe a unit of light energy. The quaziparticle offers a method of specifying a magnitude of the cumulative plasma oscillation existent in the free electron gas of any substance [266]. A surface plasmon is a more specific item, that occurs only on the outer electron shells of exposed atoms of surfaces. These interact strongly with light, causing significant polarization of planar light, it is these that produce the anomalies recorded in diffraction of light from metal surfaces [268]. Surface plasmons can have critical modification of the reflected electromagnetic radiation; they have been used to modify the apparent colour of surfaces and can afford the ability for low optical diffraction levels below the traditional optical diffraction limit [269]. Both of these effects can go some way to explain the observed darkening of the features machined under closed thick film flowing filtered water immersion. Typically increased surface absorption of photons by the action of plasmon phenomena have been reported as a feature of metallic materials [253-255], but the work of work others [256] has shown that surface plasmons also exist on the surface of silica; thus, it is not inconceivable for a similar effect to exist on polymer surfaces. Some previous contributions have proposed that Plasmon production and size is proportional to laser ablation plume pressure [266], thus the pressure increase calculated above for the techniques described in this contribution could result in significant modification to the interaction between light and the surface of machined features.

Alternately, the apparent change in colour could be a result of charring of the feature surface. This charring could have been promoted by increased plume temperature which was thermodynamically coupled with the calculated increased plume pressure. However, the lack of impact caused by ultrasonic bath immersion of 10 minutes in ultrapure water on the feature shown

in Figure 11-11 suggests that this is not a significant contributor in this case, as such a rigorous cleaning technique should have removed oxidized detritus from the feature surface leaving an apparently brighter surface.

The modification of the ablation mechanism, to feature a significant plume etching contribution as alluded in Chapter 10 of this thesis and supported by the findings of this Chapter, where the drag of immersion fluid flowing past the ablation plume distorted the plume geometry. Varying the flow velocity resulted in modified ablation threshold as demonstrated in Section 10.1, ablation rate (see Section 10.2) and surface topography as has already been demonstrated by the work presented in this Chapter. The recorded modification of surface topography demonstrated that the surface roughness was proportional to flow velocity and laser fluence. It also demonstrated a significant increase in surface roughness of the features. This increase in surface roughness would have the effect of high diffusivity of light supplied from the microscope objective, reducing the intensity of light reflected to the camera as described schematically in Figure 11-12. Such a characteristic could doubtlessly have a significant use in the displays or lighting industry, where even light distribution over a broad area is a desirable feature.

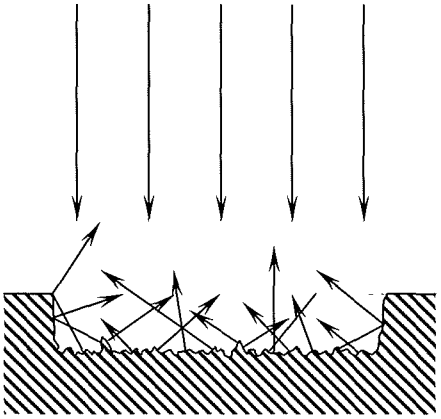

Figure 11-12: Schematic diagram describing the high diffusion of reflected light from a feature surface with high roughness.

Part IV

Verification of Closed Thick Film Flowing Liquid Immersion Ablation of Bisphenol A Polycarbonate by Modification of Liquid Chemistry

CHAPTER 12

INFLUENCE OF IMMERSION MEDIUM TYPE ON ABLATION THRESHOLD

The use of a medium with a different chemistry to that used previously would provide further understanding of the phenomena described earlier. In this Chapter DI water, a fluid that is chemically and mechanically similar, but deviates from filtered water significantly in its electrostatic conduction properties, was used. DI water should offer similar ablation etching efficiency to filtered water when used in the context of closed thick film flowing liquid immersed KrF excimer laser ablation.

The efficiency of the interpretation between a laser beam and a material can be measured to ascertain the magnitude of the ablation threshold. High etch efficiency maybe indicated by a low threshold fluence, where minimal laser energy would be required to remove material from a substrate. In Figure 12-1 the ablation threshold of 248 nm KrF excimer laser radiation machining bisphenol A polycarbonate, measured at multiple flow velocities (0.03, 0.1, 1.85 and 3.70 m/s) in two mediums. Trend lines have been fitted to all plots, black trend lines for DI water immersed samples and grey for filtered water. Only the lowest flow velocity used displays poor linear plot correlation for both liquids: an outlier exists at 522 mJ/cm^2 for filtered water and 561 mJ/cm^2 for DI water. Inspection and comparison of remaining points for the two results machined at 0.03 m/s under differing media show great similarity; this is especially true for the features machined at increased fluence, where the filtered water repeatedly provided lower etch efficiency than ablation under DI water. Lower fluence points are also similar. The fact that both trends appear similar barring outliers indicates that use of very low flow velocity closed thick film immersed laser ablation machining is highly fluence dependent.

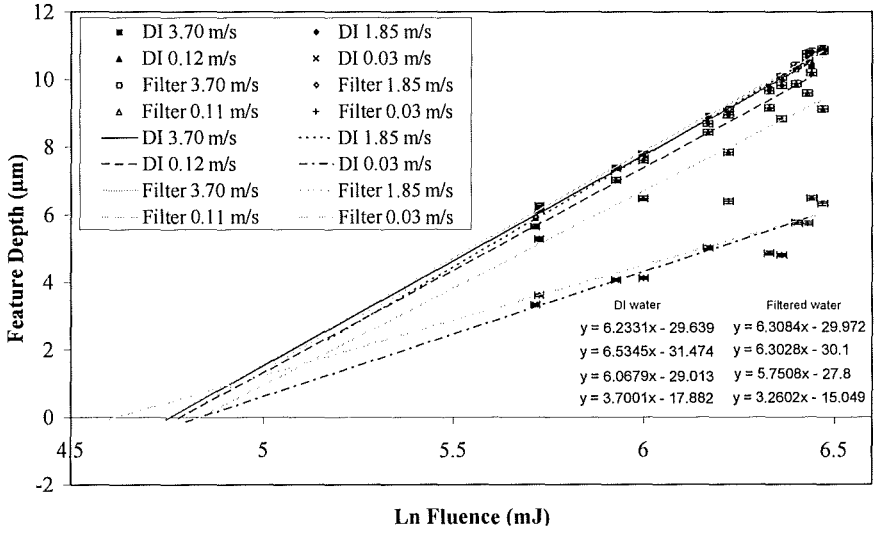

Figure 12-1: Ablation depth against number of pulses to determine etching threshold fluence for closed think film flowing filtered and DI water.

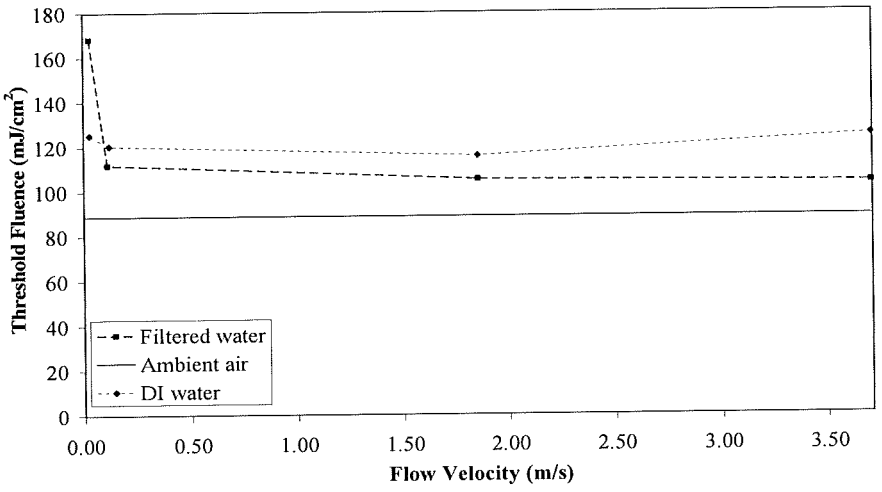

(a)

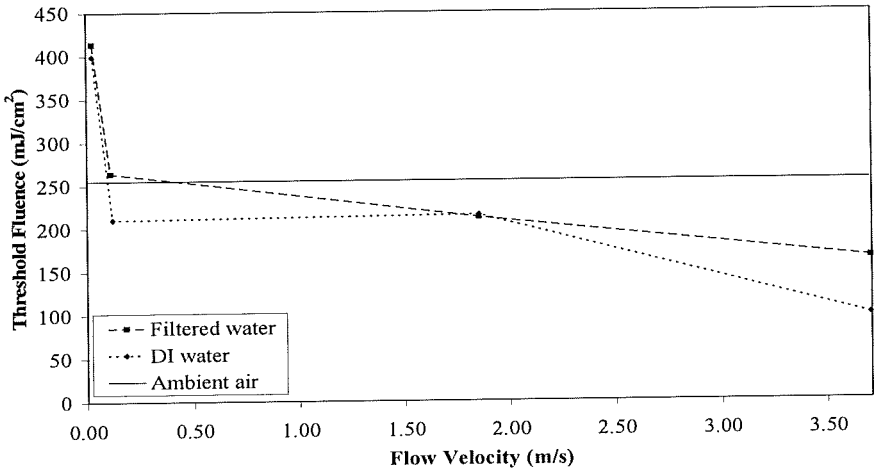

(b)

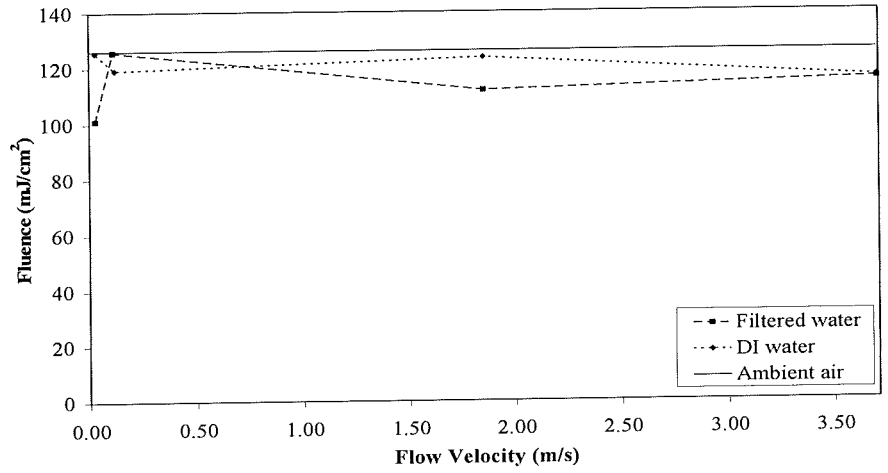

(c)

Figure 12-2: Fluence against flow velocity to give etching threshold fluence under closed thick film flowing filter and DI water for (a) low etch threshold fluence regime ablating, (b) average etch threshold fluence regime ablating and (c) high etch threshold fluence regime ablating.

This assertion is borne out somewhat by the plots shown in Figure 12-2(a) and Figure 12-2(b), where the etching threshold is plotted with respect to closed thick film immersed ablation flow velocity. Comparison of the low flow velocity ablation rate results between Figure 12-2(a) and Figure 12-2(b) highlights the large variance in performance between low and high fluence respectively. The collaboration of DI and filtered water results is stronger for high fluence regime results plotted in Figure 12-2(b) than those of low fluence results in Figure 12-2(a); however, both indicate use of DI and filtered water along with very low flow velocity (0.03 m/s) resulted in a loss of etch efficacy (signified by the increased etch threshold fluence). This is a result that is in agreement with the assertions made in Chapter 10 that pulsed beams are obstructed by insufficient removal of debris produced by an earlier pulse in the low velocity flow. This reduced the contribution of laser etching and therefore limited the volume of plume generated, reducing or removing the contribution of plume etching [54]. This phenomenon is explained as a result of low liquid volume refresh rate when compared to the laser pulse frequency, which for 0.03 m/s flow velocity was just 0.7. All other flow velocities test had ratios larger than 11; thus, debris was not removed from the volume above the feature to be machined between laser pulses, leaving suspended debris ejected by a pulse to obstruct the following pulse. Increased debris size magnified this problem as large debris absorbed larger volume of laser energy in the following pulse before being ablated. Larger debris is encouraged by a non conducting medium such as DI water *via* the action of colloidal adhesion [19].

Further inspection of Figure 12-1, with attention paid to average etch depths plotted against the natural log of laser fluence used at the flow velocities of 0.12, 1.85 and 3.70 m/s in both filtered and DI water, shows that the etching efficacy and therefore thresholds returned are similar. Only the trend of DI water flowing at 1.85 m/s generates an abnormally high etching threshold at 144 mJ/cm^2, this is caused by an outlying depth value measured for the natural log of beam fluence measured at 375.67 mJ/cm^2, indicated in Figure 12-1; barring this, all points closely follow linear trends, so this point can be discarded, resulting in a more acceptable projected threshold fluence of 123.6 mJ/cm^2. The flow velocities all produced an etch threshold range of 9.99 mJ/cm^2, about a central value of 120.75 mJ/cm^2. Further analysis is possible by inspecting the plot giving in Figure 12-2(c), where the average ablation rate taken by projecting the trend of all beam fluences tested is plotted with respect to the flow velocities used for machining. Figure 12-2(c) makes it clear that both immersion media produced similar etching efficacy, but the use of filtered water in closed thick film flowing immersion laser ablation generally produced higher efficacy than both KrF excimer laser ablation of bisphenol A polycarbonate in ambient air and when using DI water as an immersion medium by 4.3% and 8.6% respectively. Fluence dependency is also important at increased flow velocity, as shown in Figure 12-2(a) and Figure 12-2(b), by inspection of the threshold fluence magnitude used. Low fluence regime machining in both media required a typical threshold fluence value of 115 mJ/cm^2, a value greater than that produced by low fluence machining in ambient air (88.7 mJ/cm^2). High fluence regime machining shows the opposite response, where efficacy is gained using both immersion media (producing a typical threshold of approximately 200 mJ/cm^2) over machining in ambient air, that required more than 250 mJ/cm^2.

CHAPTER 13

INFLUENCE OF IMMERSION MEDIUM TYPE ON ABLATION RATE

The poor electrostatic conduction of DI water will promote electrostatic colloidal debris aggregation. This interaction could result in increased volumes of larger debris than produced when using filtered water in the technique of closed thick film flowing liquid immersion of KrF excimer laser ablation as proposed for the first time in this thesis. These larger debris items will cause greater localized attenuation of the laser beam and so could generate reduced etching efficiency, which is a measurable manifestation of such an interaction.

The ablation rate achieved using 3, 6, 12, 60, 120 and 480 when machining using differing closed thick film flowing immersion media during KrF excimer laser ablation shows a reliably repeated trend. Figure 13-1 is a 3D chart describing the depth machined with respect to the number of pulses used and also the flow velocity used. Figure 13-1 shows that 0.03 m/s flow velocity resulted in equivalent machined depth or slightly lower machined depth when using filter water than that achieved when using DI water. Use of 0.11 m/s flow velocity follows this trend for 3, 6 and 12 pulses, but changes to an opposite trend.

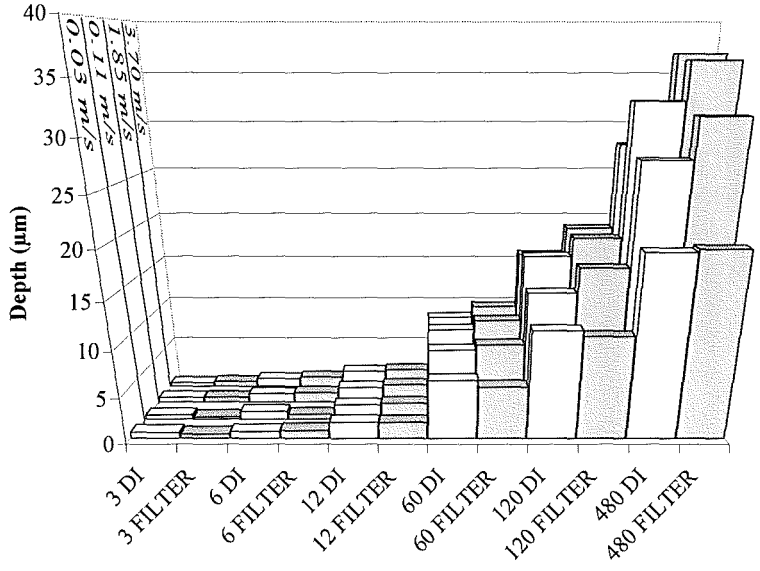

Figure 13-1: Comparative 3D bar chart describing etch depth achieved in either medium by 'n' pulses using 0.03, 0.11, 1.85 and 3.70 m/s, with flow velocity increasing into the page.

Use of more than 60 pulses resulted in closed thick film flowing filtered water immersion producing greater machined depth than DI water immersion. Use of turbulent flow velocities produced increased etched depth for all pulse numbers. This suggests that filtered water provides increased etching efficacy once above the ablation threshold when using turbulent flow velocities.

Detailed analysis of the ablation rates produced at the four flow velocities tested in this thesis using both media (0.03, 0.11, 1.85 and 3.70 m/s) is afforded from Figure 13-2, where the machined depth is plotted with respect to the number of pulses used to give a number of linear relationships. The fluences used to produce the samples machined with KrF excimer laser pulses immersed in filtered water were all within 3% of 578 mJ/cm^2. The measured fluences used to machined the samples using an immersing fluid of DI water were all within 2% of 561 mJ/cm^2. This 3% discrepancy in average lasing fluence goes some way to explain some of the differences witnessed in the feature depths discussed previously. The ablation rates given in the form of trend line gradients in Figure 13-2 show that the use of filtered water produced a mean increase in ablation rate of 14.25 nm/pulse. This is a margin of 11.7% over the samples machined using DI water as a medium for closed thick film flowing liquid immersed ablation. Clearly, this 11.7% gain cannot be attributed to the 3% advantage in fluence held by the filtered water samples. Furthermore, comparison of the calculated ablation rates at each machining flow velocity shows that only at the lowest flow velocity, 0.03 m/s, did DI water produced a higher ablation rate of 5.8 nm/pulse than filtered water. Filtered water produced an ablation rate in excess of 15.7 nm/pulse greater than DI water at all other flow velocities.

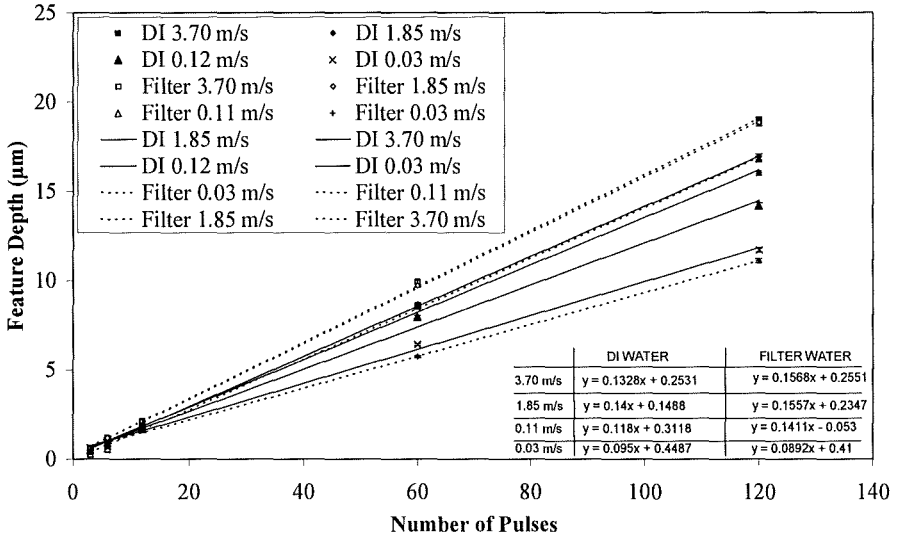

Figure 13-2: Ablation depth against number of pulses to determine ablation rate for four flow velocities: 0.06, 0.11, 1.85 and 3.70 m/s, under closed thick film flowing filtered and DI water.

Figure 13-3 plots the calculated ablation rates, shown graphically as linear trend line gradients in Figure 13-2, with respect to the flow velocities used to produce them for immersion ablation using DI and filtered water. Also included is a benchmark ablation rate achieved using a similar laser fluence of 581 mJ/cm^2 in ambient air for comparison. There is good agreement between trends produced by both immersion media: ablation rate generally increases with flow velocity. KrF excimer laser ablation of bisphenol A polycarbonate under closed thick film flowing DI water did not result in an ablation rate greater than that achieved by excimer laser ablation in ambient air, whereas use of filtered water did result in an ablation rate greater than that achieved in ambient air for both turbulent velocities tested for this thesis. The ablation rate produced by KrF excimer laser ablation in DI water flowing at 3.70 m/s was 7.2 nm/pulse less effective than ablation in DI water flowing a 1.85 m/s. This supports the findings presented in Chapter 10 of this thesis that indicated an optimum flow velocity

existed where the interaction of the flow with the ablation plume generated in the immersing fluid by the action of laser etching resulted in distortion of the plume to minimize the traverse distance through the compressed plume for the beam, minimizing plume shielding, whilst supporting the action of plume etching [33] by the intact but distorted ablation plume. As the velocity increased, the plume was destroyed, resulting in the removal of the plume etching action but simultaneous increased access for the laser beam to the material surface. The minimal reduction in ablation rate suggests the total ablation rate is dominated by the action of laser etching.

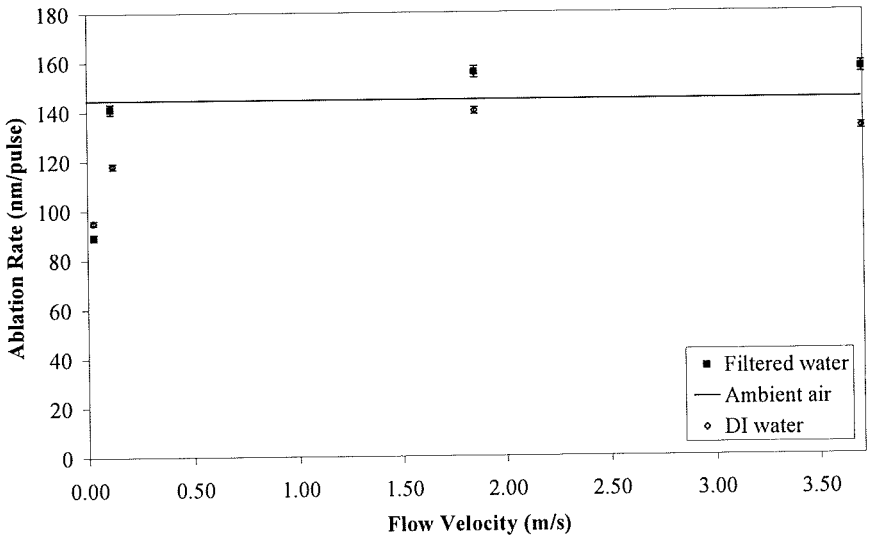

Figure 13-3: Measured ablation rate against the flow velocity for KrF excimer laser ablation in ambient air, under closed thick film flowing filtered water immersion and closed thick film flowing DI water immersion.

CHAPTER 14

FLOW – PLUME INTERACTION STATES

In Part III it was proposed that the laser ablation plume could be modified by the drag of a flowing liquid surrounding it during closed thick film flowing liquid immersion of KrF excimer laser ablation. This is a concept that is novel and at the vanguard of laser - material interaction research. Following on from the findings presented in Part III the use of DI water allows the verification of this proposal, given the trends observed in Chapters 12 and 13 of this thesis.

The close agreement of the samples machined under differing media is useful in the support of the work presented in Chapter 10 of this thesis that is demonstrated. Again, a flow-plume interaction states have been identified as the motivation for modification to the ablation mechanism. The data described in Figure 12-2(a), Figure 12-2(b) and Figure 13-3 shows strong support for suspended debris that remains unmoved between pulses due to insufficient flow velocity intercepting the following pulse as described in Figure 14-1(a), where the time taken for the volume of liquid covering the laser machined feature is greater than the period between two laser pulses.

The results given in Part III, which have been supported by the findings of Part IV of this thesis indicate that increased laminar flow became sufficient to remove debris from above the feature between pulses, yet insufficient to distort the ablation plume during a pulse as shown in Figure 14-1(b). The immersion of the ablation plume with liquid restricted the expansion of the plume. This resulted in a plume of increased optical and physical density compared to that produced by ablation in ambient air. This compressed plume attenuates the laser beam producing the plume, reducing the beam energy that arrives at the material and as a result, reducing the laser etching efficacy. Simultaneously, the compressed plume reduced the loss in etch efficacy by the action of plume etching [54]. This scenario is indicated in actuality for the 0.11 m/s results in Figure 12-2(a), Figure 12-2(b) and Figure 13-3, where the etch threshold dropped sharply and the ablation rate increased markedly respectively.

The experiments conducted for this thesis show that a flow velocity of 1.85 m/s resulted in the production of an optimum measured ablation rate in Figure 13-3, where the plume was distorted by the flowing filtered water, reducing the path length that the beam had to endure through the plume to reach the material surface, and as a result the losses to the beam due to plume shielding are lower as described schematically in Figure 14-1(c). In concert, the distorted, but still intact ablation plume was providing a plume etching contribution using the mechanism described above. This occurrence can also be identified by the dip in threshold fluence in Figure 12-2(a).

Further increase to flow velocity has indicated that the ablation plume became disrupted by it's interaction with the flow molecules; thus, allowing maximum access to the material surface for the beam and removing the plume etching contribution as shown in Figure 14-1(d). This reduced the total ablation rate, as indicated by the DI water plots in Figure 13-3, and the increase in threshold

fluence in Figure 12-2(a) caused by the action of fast flowing closed thick film DI water immersion of the ablation plume. The close agreement of DI water and filtered water in all of these analysis techniques shows that the scenario described above is plausible.

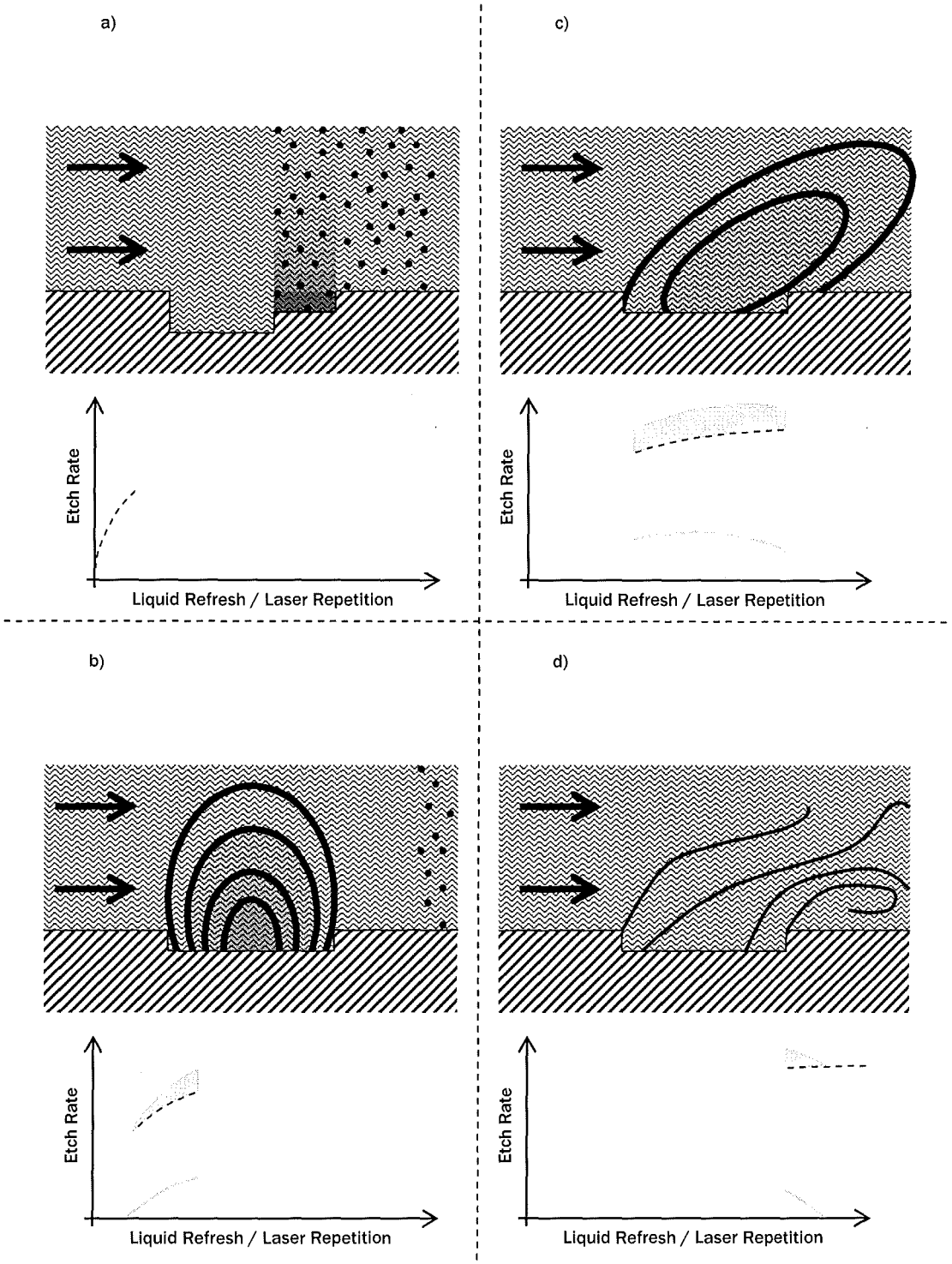

Figure 14-1: Diagram describing the etch rate with respect to closed thick film flowing liquid volume refresh rate over the machined feature by means of a schematic plot and a schematic describing the actual interaction between the flow and plume when: liquid volume refresh rate is less than the laser repetition rate (a); liquid volume refresh rate is similar to the laser repetition rate (b); liquid volume refresh rate is greater than 10x the laser repetition rate (c); and liquid volume refresh rate is greater than 100x the laser repetition rate (d).

CHAPTER 15

INFLUENCE OF IMMERSION MEDIUM TYPE ON IMMERSION CONTROLLED DEBRIS DEPOSITION

As already stated, DI water has significantly greater electrostatic insulation properties than the filtered water employed in Part III of this thesis. This poses the possibility of markedly reduced Yukawa repulsion interactions occurring between debris groups and debris particles and the bisphenol A polycarbonate surface ablated using closed thick film flowing liquid immersed KrF excimer laser radiation. Therefore, the size of debris deposited and the numbers of deposited items should be measured to increase. This Chapter investigates this postulation.

The use of closed flowing thick film filtered water as an immersing medium has been shown to be effective in the control of laser ablation generated particulate debris in Chapter 5 of this thesis. Filtered water is an electrically conducting liquid due to the impurities contained within it [270]. This is important in terms of its impact on the adhesion properties of the particles suspended within it. Electrostatic interactions are significant in long range attraction and contact interaction of particles [38, 41].

Figure 15-1 is given to allow simple comparison between samples machined under closed film flowing liquid immersion: 4 samples using filtered water and 4 others using DI water. The samples are paired by flow velocity. The results in Figure 15-1 show the number of particles of three specific size ranges (0 to 0.3375, 1.913 to 3.713 and 28.91 to 57.71 μm^2) discretely by use of contour plot for four flow velocities: 0.03, 0.11, 1.85 and 3.70 m/s. Each group of result plots have been generated by taking a mean average of the deposition frequency of three separate machined samples to guard against experimental inaccuracy. The full results are split into 10 debris particle size classes, but here the smallest, middling and second largest particle size frequency plots are given as they provide representative findings of this thesis and allows for simple interpretation of the general trend of deposition across the entire surface. Frequency gradient legends are given for each set of results, calibrated to the maximum debris population registered for an average sample machined under each condition across all size classes. The legend is useful in assessing the magnitude of population of debris produced by each fluid machining medium.

Figure 15-1(a) and Figure 15-1(b) demonstrate similarity in the deposition trend of the debris deposited at turbulent flow velocities in both mediums. In both filtered water and DI water samples the vast majority of debris is deposited downstream of the feature. Also the characteristic localized high population density areas of the debris are visible in the turbulent flow DI water immersion results, supporting the findings of previous work, that explains that the high density deposition areas are the result of flow turbulence as explained in Chapter 5 of this thesis.

Laminar flow machined samples displayed for comparison in Figure 15-1(c) and Figure 15-1(d) also show clear similarity in deposition trend. Two samples machined using laminar flows of

DI water both demonstrate an even distribution of debris that was also evident on all of the filter water machined samples. However, differences do exist: when machining using filtered water, only the lowest flow velocity, 0.03 m/s, showed evidence of significant deposition upstream of the feature; whereas the samples machined under DI water at both 0.03 and 0.12 m/s show significant debris deposition upstream of the feature. This result supports the adhesion theory alluded to above and in the literature [16]. DI water does not conduct the larger electrostatic charge of the substrate to the machined particles as effectively as filtered water. This meant that that the debris suspended by DI water experienced greater long range attraction forces towards the substrate surface, resulting in both increased total debris population and increased frequency of upstream deposition, as more debris is attracted to the sample surface when using the insulating DI water as opposed to the conducting filtered water.

Inspection of the frequency legends presented in Figure 15-1 further supports the adhesion theory described above. Closed thick film flowing DI water immersion KrF excimer laser machined samples display markedly larger magnitude of deposition frequency than the samples machined under filtered water immersion. Conduction of the electrostatic charge of a large particle to a smaller neighbouring particle would set up a Yukawa repulsion between the two. Therefore the use of a non-conducting fluid should result in an increase in particle deposition when compared to the results demonstrated by filtered water, which has a typical conductivity of 0.005 to 0.05 S/m. DI water is a significantly better insulator, with a minimum conductivity of 1 x 10-7 S/m, because DI water has significantly fewer charge carriers available in the form of mineral ions from impurities [270].

The frequency gradient legends in Figure 15-1 reveal that the real volume of small debris produced was larger when machining under DI water than when machining under filtered water. The contour plots given in Figure 15-1 across all flow velocities show the proportion of medium size debris was much lower than the proportion of small size debris produced by KrF excimer laser ablation under closed thick film flowing DI water than the same comparison taken from the features machined under closed thick film flowing filtered water. Large debris was less common when machining using DI water. A more detailed inspection of this can be given by using plot of debris frequency against debris size for multiple flow velocities, as is presented in Figure 9.

Figure 15-2 describes filtered water results as greyscale filled area plots behind line plots that demonstrate the frequencies of debris produced by ablation under DI water. This graph shows that the typical size of debris produced during immersed KrF excimer laser ablation is flow velocity and medium dependent. The images displayed in Figure 15-1 are distorted for interpretation by the greatly increased volume of small debris produced by closed thick film flowing DI water immersion. The large deposition of small debris in DI water can be directly credited to the dominating action of the electrostatic insulation provided by the DI water compared to that of filtered water causing the smaller debris particles be attracted to the sample substrate.

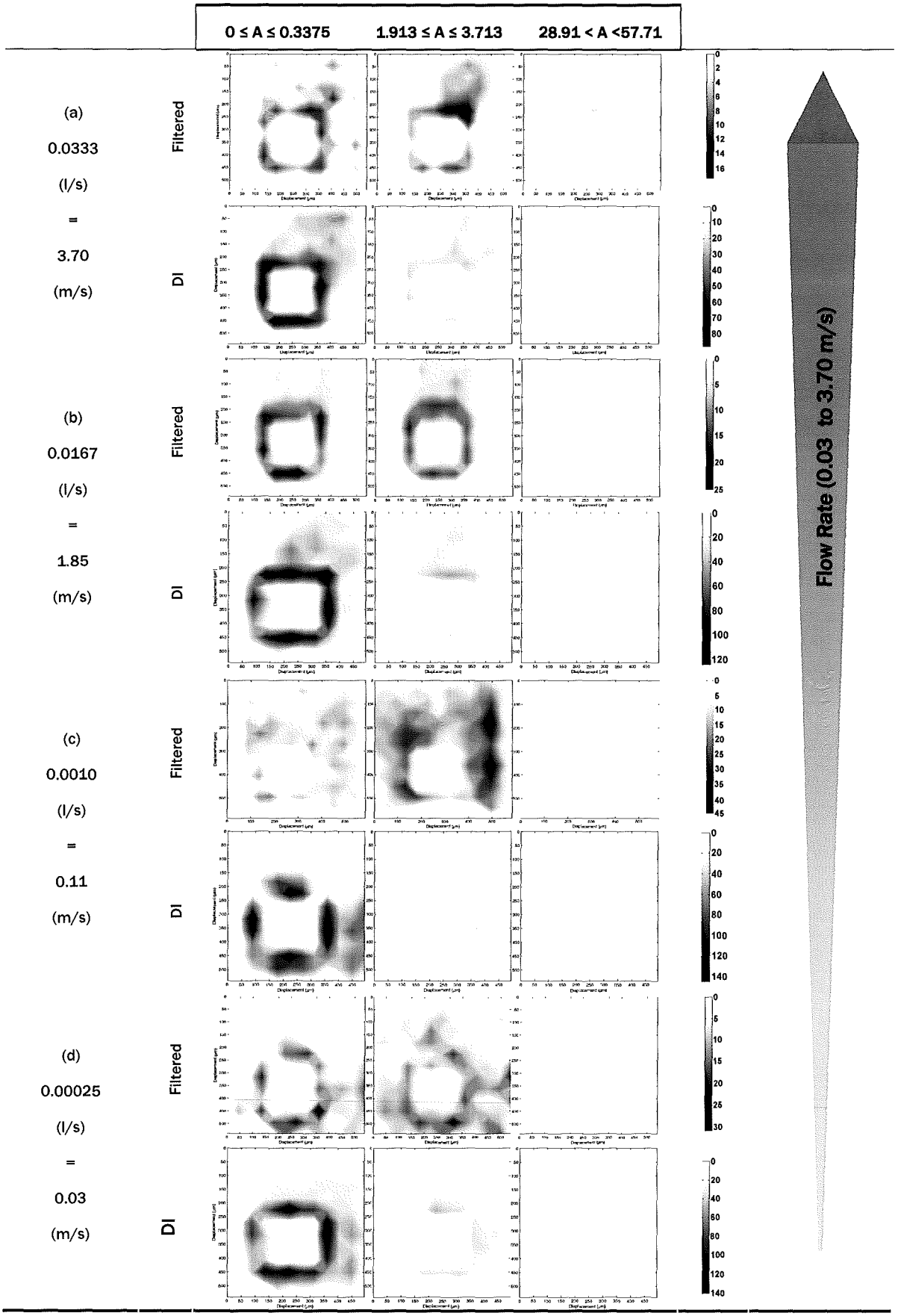

Figure 15-1: Discrete contour plots of particle density with respect to size class and flow velocity for closed thick film flowing filtered and DI water.

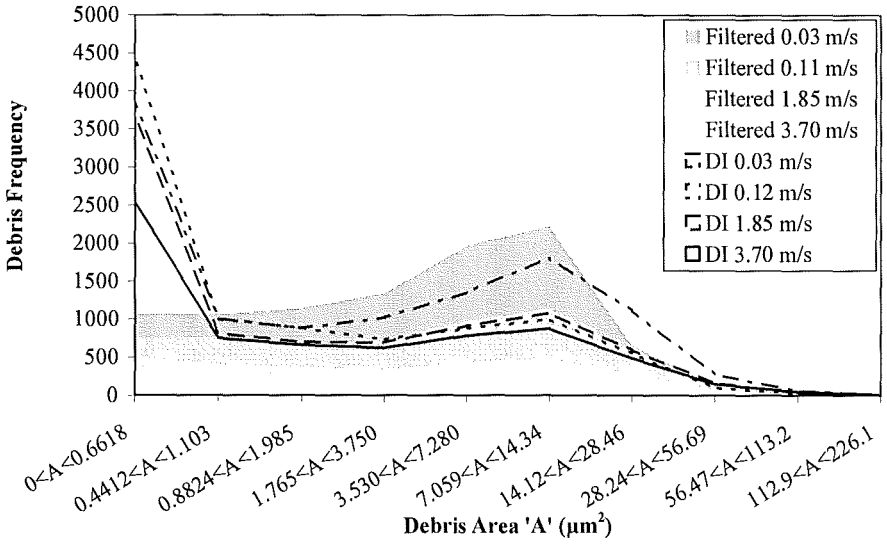

Figure 15-2: Frequency of debris particles against particle size to describe the total particle population of samples produced under closed thick film flowing filtered water immersion ablation at various flow velocities for filtered and DI water.

Furthermore, the second lowest flow velocity returned the largest debris population of small debris in the same manner as filtered water. In Section 10.1.4 it is proposed that this occurrence is caused by interactions between the slow moving suspended debris and the laser beam of the following pulse resulting in decreased laser fluence at the feature and therefore a lower ablation rate and smaller volume of debris being generated at the lowest flow velocity than those above it. The volume of debris produced changes back to a more flow proportional relationship for all debris larger than 1.103 μm^2, the lowest flow velocity produced the largest volume of debris and the highest flow velocity the smallest volume of debris. This is a result in contradiction to that produced by filtered water; the increased electrostatic attraction between debris and a surface is size dependant, the force generated by electrostatic interaction dominated small debris but this changed to a flow drag dependency for large debris. Capillary forces can be considered nil: the immersing liquid removes any meniscus between particles and the sample substrate. F_{vdW} is halved by the presence of water. This implies the occurrence of colloidal interactions, where multiple small debris particles combine to produce medium size particles. These are inversely proportional to drag [38] and therefore flow velocity. This is a situation that can be explained by stress induced on the particles by eddies in turbulent flow acting to break up medium and large colloids, whereas smaller colloids are less susceptible because of their smaller surface area for drag to be applied and the higher relative action of the adhesion forces on their constituent particles. particles of medium size were proportionally markedly less common on DI water immersed samples than for samples machined in filtered water. Once again this can be explained by the action of the electrostatic insulation provided by the DI water, the particles are more attracted to the sample surface that has a comparatively large, typically opposite [38], electrostatic charge compared to the other surrounding suspended particles that typically have the same charge [41], causing particles to repel each other. The total debris volume generated by flow velocities of 0.12, 1.85 and 3.70 m/s were separated in frequency by only 30% of the lowest population, compared to

the 3300% range of flow velocity; this could be the result a combination electrostatic and F_{vdW} on the remaining minority of particles, forming large, strong colloids that are effected little by increasing turbulence.

Distribution skew, a numerical value that denotes the shape of a distribution about its mean, can be used as a technique to measure the displacement of a typical particle of a specific debris size. A positive skew value is the result of a distribution where a greater proportion of the population lies between the mean and infinity, as shown in Figure 15-3(a); a negative skew value is the result of a distribution where a greater proportion of the population lies between the origin and the mean, as shown in Figure 15-3(b). A large skew value denotes a strong population 'lean', where the mean is further from the origin.

In Figure 15-3(b) a plot of the magnitude of skew for samples immersed by filtered water are plotted as the filled areas behind the line plots for DI water immersed samples to allow the simple comparison of the two. All of the skew values measured are positive, indicating that majority of debris lies between the mean position and infinity. The magnitude of skew is lower when using DI water as an immersion medium for KrF excimer laser ablation, denoting lower displacement of the debris from the machined feature in flowing DI water than is achieved in filtered water. The plots indicated medium sized debris had the lowest typical displacement from the feature. Small debris had a larger typical displacement and the largest debris had the largest typical displacement. This result is in line with that of the filtered water, providing good support for previous findings in filtered water discussed in detail in Chapter 9 of this thesis. The fact that typical debris displacements are lower than gives more support for the proposal that the electrostatic insulation provided by DI water increases the electrostatic attraction between the debris and the sample surface, resulting in earlier debris deposition in the fluid stream.

Inspection of Figure 15-3(c) allows quantifiable analysis of the same trends. Indeed, the smallest debris, of 0.66 μm^2, were consistently deposited approximately 230 μm downstream. Debris of sizes ranging from 1.10 to 3.75 μm^2, had smaller displacement of less than 180 μm. This supports the adhesion theory cited above, where the attraction forces acting on the smallest debris were dominated more by flow drag than the medium sized debris. The displacement of debris over 3.75 μm increases steadily for the debris generated in turbulent flow velocity DI water in the same way as was the case for 1.85 m/s filtered water immersion. The laminar flow DI water samples return unstable results much like the laminar flow velocity filtered water samples. This result is in line with the idea that drag imparted on large debris particles increasingly dominates the adhesion forces that are proportional to size. The multiple vectors generated by eddies on the particles are small when compared to the general vector of the overall flow. The slow liquid volume refresh rate generated at laminar flow velocities means the interruption and distortion to the flow by the laser generated plume is significant; thus the flow vectors generated become unstable, resulting in the high variance of debris deposition recorded.

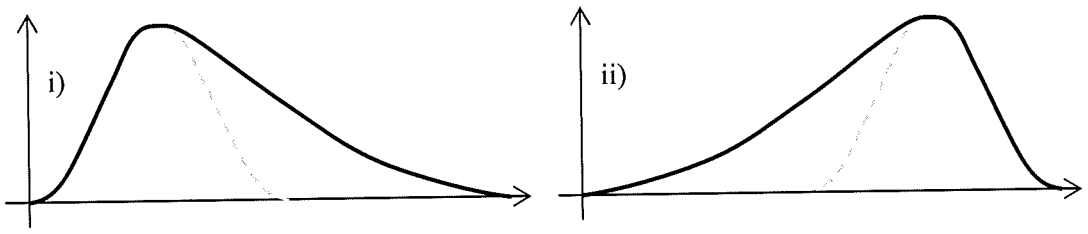

(a)

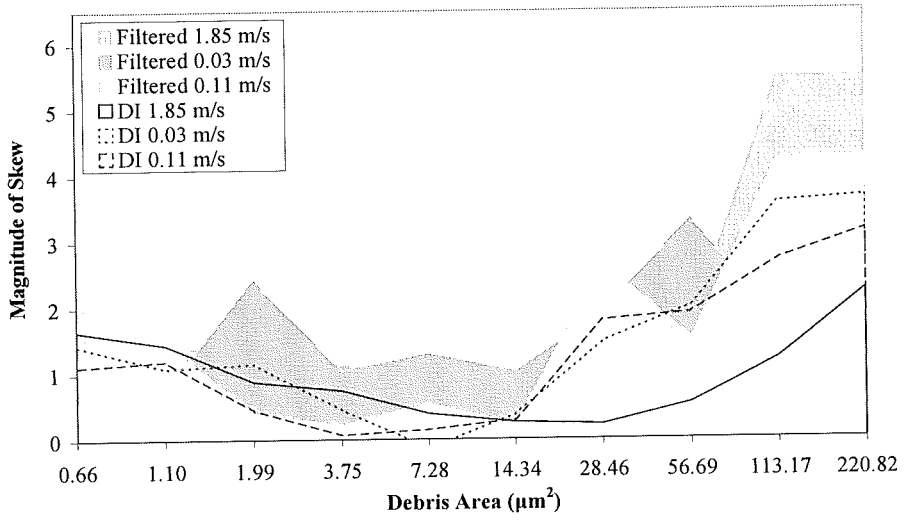

(b)

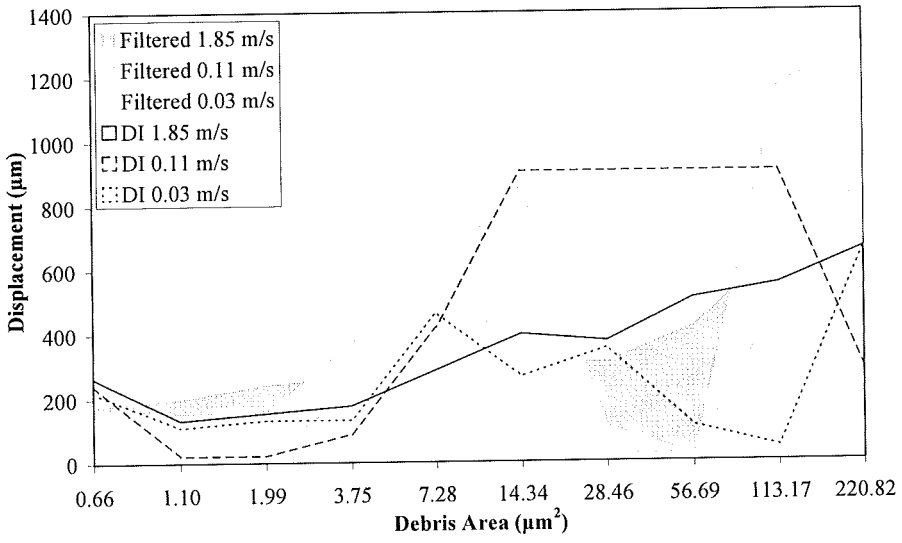

(c)

Figure 15-3: Schematic description of the typical distribution of (a(i)) positive skew, (a(ii)) negative skew, (b) the magnitude of skew with respect to debris size and (c) modal displacement from the machined feature with respect to size.

CONCLUSIONS

1. Modal trends in debris deposition resultant from KrF excimer laser ablation of bisphenol A polycarbonate in ambient air.

The positional debris deposition of samples machined in ambient air showed a modal tendency reliant on the feature shape machined. It is likely this is the result of the interaction of multiple shockwaves at the extent of ablation plumes generated at geometry specific locations in the feature. Circular features typically leave a horn shaped smear extending from the perimeter of the machined sample; square features leave large mushroom-shaped smears lying at a normal to the edges of the feature machined. The results reveal that a four-leaf-clover-shaped ablation plume is the cause of the square feature smearing pattern since this plume shape produces a separate shockwave emanating from each corner of the feature; debris is deposited where the shockwaves collide, to consequently produce the mushroom smear pattern.

KrF excimer laser ablation machining in ambient air has been shown to deposit debris with respect to species size. Large debris, measured to be between 3.43 μm^2 and 13.94 μm^2, has small range, not travelling much further than the boundary of the machined feature; intermediate debris, classified as items returning a signal of between 0.86 μm^2 and 3.65 μm^2, travels significantly further, being found in radial streaks at a normal to the circular features perimeter. This finding suggests shockwave-driven transport.

2. Use of open thin film flowing de-ionized water above ablation area for control of ejected debris produced during KrF excimer laser ablation

Sample immersion by flows of liquid has shown potential to modify the end position of the debris produced: the use of immersion has reduced typical range by 17% from 180 μm from the feature boundary in ambient air to a concentrated area between 75 and 150 μm from the feature edge under open thin film flowing de-ionized (DI) water immersion. The homogeneity of debris density was found to be increased by use of the open immersion ablation, with deposition within the boundary of the ablation plume having a comparatively even population density with respect to the sample machined in ambient air. This was particularly evident when comparing the square features machined in ambient air and under open thin film flowing DI water immersion. The ability to restrict the range of debris offers possibilities for dynamic optic protection to those implementing laser micromachining where optics must be positioned close to the sample.

Outside the evident ablation plume extents the evidence of positional control of deposited debris species by open thin film flowing DI water immersion were more pronounced. Both circular and square features displayed debris deposited in rippled flow line patterns, indicating the action of transport by fluid flow. This was achieved by the use of very low flow rates caused by a standing head pressure of just 0.1 bar. This result demonstrates that increased flow rates coupled with

the eradication of defocusing surface ripples should offer better geometric feature accuracy with greater debris control. Further, liquids with greater conducting properties would aid in preventing deposition on the ablated workpiece.

The ability of open thin film flowing DI water immersion ablation to restrict the expansion of the ablation plume was demonstrated by the 17% reduction in range of the debris produced and the clear outline of fine debris boundaries left on the samples produced by open thin film flowing DI water immersion ablation when compared to traditional ablation in gaseous media.

Open thin film flowing DI water immersion ablation has demonstrated the ability to increase significantly the size of the debris species produced by laser machining. Inspection of the mean debris size produced in ambient air revealed a value of 0.86 μm^2 and 0.64 μm^2 for circular and square features respectively. The same two features ablated under open thin film flowing DI water immersion returned signals of 7.08 μm^2 and 15.23 μm^2. This result was confirmed by inspection of population spread of debris according to size. Whereas the samples ablated in ambient air produced vast numbers of small debris and very few intermediate or large species, the samples ablated under open thin film flowing DI water immersion produced a quarter of the number of small debris, but the same amount of intermediate debris with very few large debris. This result was in-line with a colloidal interaction response. The ability to produce larger, colloidal type debris that has a homogenous deposition trend, rather than small particles that tend to be deposited in small areas may present benefits to sputter coating techniques. Also, the production of large debris items poses the potential for more efficient post-process cleaning: more removal force can be applied to larger debris items than to small species.

3. Impact of open thin film flowing de-ionized water immersion on the liquid immersed ablation threshold and ablation rate of features machined by KrF excimer laser ablation of bisphenol A polycarbonate.

Measurements of ablation threshold and ablation rate when KrF excimer laser machining bisphenol A polycarbonate samples in ambient air and under open thin film flowing DI water immersion showed differences in the machining mechanisms. Attenuation of the KrF excimer laser beam in the DI water was negligible. This decrease resulted from confinement of the vapour plume by the liquid medium which caused plume shielding and splashing events - critical mechanisms that modified the primary ablation characteristics. Indeed, whereas in ambient air the threshold fluence was measured as 37 mJ/cm^2, in the open thin film regime threshold fluences of 83.9 and 58.6 mJ/cm^2 were observed with and without splashing respectively. This also contributed to the loss of total etching efficiency. The observed change in ablation rate and ablation threshold cannot be directly explained by the attenuation coefficient of the DI water medium. It is believed that the change in ablation rate was generated by the increased confinement of the vapour plume by the liquid medium during immersion ablation. This in turn generated higher plume shielding of the beam and subsequently produced the observed 20% reduction in the laser etching rate from 0.459 μm/pulse to 0.367 μm/pulse. This is reasonable because in contrast to closed thick film flowing liquid immersion where the confinement and resultant increased pressure of the plume etches the sample to a greater extent than the laser, the ablation plume can only be constricted to a limited extent by the open thin film of flowing DI water before the ablation plume causes rupture

and splashing of the DI water. This means that the KrF excimer laser beam still experiences some extra plume shielding before liquid rupture occurs, but the action of plume etching is nonexistent for thin films.

The observed splashing of the open thin film flowing DI water during KrF excimer laser machining was recorded in the data spread. This suggests that two independent interaction types are active: (i) an intermediate threshold fluence level where splashing occurs after every pulse in a mode that interrupts the flow entirely. This leaves an ambient air interaction for the following pulse; and (ii) a high threshold fluence level where splashing occurs for every pulse in a mode which allows the flow to recommence over the image before the next pulse. This results in every pulse experiencing high plume shielding. These two scenarios show a relationship between pulse fluence and fluid rupture timing, where medium fluence causes maximum flow disruption by splashing and high fluence results in instantaneous but short term interruption of the flow.

Further verification was obtained from measurement of the attenuation of the immersing liquid, which was found to be negligible. This establishes that the immersing liquid is not in itself responsible for the loss of fluence at the image and therefore lasing efficiency, but instead is the consequence of the action of the ablation plume when constrained within a thin flowing immersing liquid and the resultant plume shielding and splashing events that occur. Clearly it is the interaction of the confined plume with the beam, combined with the inability of the plume to etch the surface of the sample that is of importance.

4. Impact of open thin film flowing de-ionized water immersion on the topography and geometry of features machined by KrF excimer laser ablation of bisphenol A polycarbonate.

All data collated using white light interferometry (WLI) techniques and interpretation using filters of 8, 16 and 32 μm was shown to possess similar trends which would suggest that KrF excimer laser ablating of bisphenol A polycarbonate in both mediums of air and under DI water generated features with undulation wavelength less than 8 μm and that the data collated was reliable for analysis.

The surface waviness, defined as macroscopic surface topography, was found to differ depending upon the medium surrounding the ablation interaction area. KrF excimer laser ablation of bisphenol-A polycarbonate in ambient air typically exhibits 26% less deviation from a planar normal over long undulations than surfaces machined by KrF excimer laser ablation of bisphenol A polycarbonate under open thin film flowing DI water immersion.

The use of open thin film flowing DI water immersion has been found to reduce markedly the geometric definition of features machined with respect to samples machined in ambient air. KrF excimer laser ablation in ambient air produced features with far steeper wall angles and therefore crisper feature shapes were perceived, suggesting that the photomechanical etching mechanism is not dominant in this case. Ripples in the immersing DI water and the inconsistent ablation plume containment this caused resulted in unpredictable macroscopic surface ablation rate. This ripple and the unpredictable feature geometry it caused provide support for the proposal that photomechanical etching is amplified by immersion of the ablation plume in viscous media.

The results showed a typical increase in surface roughness of 17% at the bottom of the feature when using open thin film flowing DI water immersion. The proposed modification in dominant ablation mechanism described above to a photomechanical case by vapour plume confinement explains the observed increase in surface roughness when KrF excimer laser machining under open thin film flowing DI water immersion. It is believed this was due to plume compression caused by immersion, which generated high vapour turbulence, pressure and temperature inside the plume causing a more aggressive removal of material by action of stress generated by acoustic style shock generated by the high pressure plume than is possible when using a homogenized KrF excimer laser beam profile in ambient air.

Significant splashing of the DI water immersing the sample was observed during these experiments, which could pose danger for delicate laser optics and also gives rise to potentially unstable machining conditions, and therefore inconsistent machining. These results clearly show that modifications in surface topography were caused by the form of the immersion medium rather than variation in fluence level. Indeed, the effects of splashing observed at higher fluences support this as the splashing caused a discernible drop in the surface topography of the features machined using the open thin film flowing immersion technique.

5. Ablation debris control by means of closed thick film flowing filtered water immersion.

The average bisphenol A polycarbonate sample machined using ablation under closed thick film flowing filtered water immersion deposited just 7% of the volume of debris generated when machining in ambient air. What is more, samples produced using closed thick film flowing filtered water immersion techniques outperform open thin film techniques in terms of debris removal. There are three contributing reasons for this. First, the prevention of fluid rupture by the closed geometry of the duct that the liquid flows through ensures a more stable and repeatable ablation mechanism than can be achieved in open thin film immersion. Second, the drag imparted on the flow by a closed duct is symmetrical, unlike the drag on a liquid flowing across a plate; hence rolling turbulence is not generated by the closed technique and the suspended particulates are not guided into the sample surface in the manner that open thin film immersion across a plate are. Thirdly, a small contribution to the lower deposition rate of the closed technique inspected in this thesis could be the action of subtle differences in the chemical composition of the differing fluids used in this thesis compared to the de ionized water used in the open thin film immersion ablation.

The debris deposition trend of bisphenol A polycarbonate samples machined using ablation under closed thick film flowing filtered water immersion display none of the characteristic mushroom deposition patterns that are generated by ablation of bisphenol A polycarbonate in ambient air showing that use of ablation under closed thick film flowing filtered water immersion changes the deposition positional tendency from being a variable of the beam shape to a variable of fluid flow. The use of ablation under closed thick film flowing filtered water immersion even prevented the cumulative deposition of close proximity neighbours lying across the direction of flow, further underlining the control of species generated by ablation using closed thick film flowing filtered water immersion.

The use of frequency scaled intensity distribution contour plots demonstrated that both the total population of debris and the deposition positional tendency are effected by immersion liquid flow velocity. Most obviously, there was significant difference between the particulate distribution generated by high flow velocity, turbulent flow and low flow velocity laminar flow; turbulent flow guides debris downstream effectively, laminar flow merely causes the debris to achieve a more even distribution than that given by ambient air. The population size of debris produced was inversely proportional to the flow velocity. For high flow velocity regimes an increase in flow velocity of 100% from 1.85 to 3.70 m/s results in a 33.8% decrease in total debris population size. Laminar flow closed thick film flowing filtered water immersion ablation results in larger total debris population, with an average total debris population 156% greater than the total population of the lowest turbulent flow velocity. Of significance is the observation that the population of debris is greater for the higher laminar flow velocity. This is proposed to be caused by the interaction of suspended debris in the flow with the ablation plume: at very low flow velocities the suspended debris intercepts the beam en-route to the feature, lowering the laser fluence across the feature area, hence total ablation rate of the material was achieved and therefore reduced the volume of debris produced. At the increased laminar flow velocity, the suspended debris is displaced more rapidly, preventing beam interception by suspended debris, allowing maximum laser etching.

The use of closed thick film flowing filtered water immersion generated a shift in typical debris population by size class. Ablation in ambient air generates a large majority of small sized particulate debris; ablation under closed thick film flowing filtered water immersion negates this majority of small sized debris, as an equal proportion of the total debris population are medium sized particles. Large particles were still found to be uncommon when using closed thick film flowing filtered water immersion ablation. This change in debris size population trend is accredited to the action of colloidal particle interactions, where small debris was collected across the walls of gas micro-bubbles in the immersing liquid volume, generated as the ablation plume is dispersed, as the micro-bubble gas cools and reduces in volume the bubbles contract and the action of capillary and van der Waals, F_{vdW}, forces bind the collection of small particles to form a single medium sized colloidal item. Once formed these colloidal particles tend not to combine to form large debris, as the small adhesion forces are not high enough in magnitude to reliably bind these together.

The interaction between debris with regards to size and any given flow velocity is also interesting. Measures of frequency distribution skewness and inspection of the median of the 95^{th} percentile of the normalized distribution of the debris frequency demonstrates that large debris is displaced further by any given turbulent flow than a small debris particle. This is a confusing result when considering the drag imparted by a flow onto a particle with respect to that particles' mass. It is proposed that the action of turbulence does not affect large debris as easily as small debris: large debris more readily follows the general vector of the flow than small debris and is therefore less commonly smeared onto the sample surface. Also the drag on a particle with respect to the size of the adhesion forces acting upon it will be favourable for easy removal of larger debris. This analysis technique also show that there is an optimum removal flow velocity, where the displacement of any given debris size is at a maximum in the filtered water medium. This flow velocity is shown to be approximately 1.85 m/s.

When using DI water instead of filtered water for closed thick film flowing immersed KrF excimer laser ablation, observation and discrete analysis of the debris deposition on the samples produced showed that the total volume of debris deposited in DI water was significantly greater than that deposited by using filtered water. This can be directly attributed to the larger electrostatic attraction possible in DI water. Also, the proportion of medium sized debris generated using DI water was markedly larger for turbulent flow velocities. This can again be credited to the inability of DI water to support Yukawa repulsion, unlike filtered water which is a better electrostatic conductor. This offers measurable proof for the explanations of beam obstruction by colloidal debris stated above. The high density deposition areas downstream of the feature characteristic of turbulent velocity flow are evident with great similarity in geometry and size between the two media used, showing support for the proposal that these deposition areas are dictated by turbulence. Analysis of debris deposition displacement with respect to debris size using 0.03, 0.11 and 1.85 m/s flows shows that DI water deposits debris after less displacement than similar conditions in filtered water. Again, the action of electrostatic attraction can be cited for this. Moreover, medium sized debris was deposited with the least displacement downstream of the feature, offering further confirmation of the controlling balance of force on debris in the flows between drag and adhesion. This seems to tip from adhesion forces having a controlling stake to fluid drag dominating at 1.10 μm^2

6. Effects of closed immersion filtered water flow velocity on the ablation threshold and ablation rate of bisphenol A polycarbonate during KrF excimer laser ablation.

It was shown, using the inspection of etch depth machined into thick film flowing filtered water immersed bisphenol A polycarbonate with respect to the number of KrF excimer laser pulses used, that etch depth increased rapidly with flow velocity through the laminar flow velocity regime, and became more stable in the turbulent velocity regime. Etch depths achieved using DI water in the same technique at flow velocities of 0.03, 0.11, 1.85 and 3.70 m/s were similar or marginally greater at 0.03 m/s when compared to the features machined in filtered water flowing at the same velocity. However, as flow velocity increased this trend was reversed and filtered water produced markedly greater etch depths over 3, 6, 12, 60, 120 and 480 laser pulses than DI water, indicating medium chemistry is important to the ablation mechanism.

The use of a turbulent flow velocity regime has shown (using six flow velocities: 1.39; 1.85; 2.31; 2.78; 3.24 and 3.70 m/s) the closed thick film flowing filtered water immersion ablation demonstrated a very similar ablation threshold to a similar beam in ambient air, which marks a significant improvement in etching efficiency over the open flowing thin film immersion technique also experimented with earlier in this thesis. Detailed analysis of the ablation rates produced using a beam fluence of 578 ± 5.78 mJ/cm^2 demonstrated that the mean ablation rate measured was 8.5% greater than that achieved by ablating with a similar KrF excimer laser beam in ambient air using a fluence of 581 mJ/cm^2. This is the result of the combined action of laser etching and ablation plume etching, which is a symptom of the plume pressure being increased as the expansion of the plume is restricted by viscous surrounding liquid medium. Conversely, laminar flow velocity regime closed thick film flowing filtered water immersion ablation results in a decrease in ablation threshold of just

0.3% compared to ablation using a similar beam in ambient air; thus, it can be likened to a negligible gain. Analysis of the ablation rate generated by flow velocities of 0.03 and 0.11 m/s, both being laminar regime velocities, during closed thick film flowing filtered water immersed KrF excimer laser ablation of bisphenol A polycarbonate showed that modification of flow velocity in the laminar flow velocity regime causes large variance of the ablation rate. Moreover, inspection of the flow velocity with respect to traverse distance of the flow over the feature required to provide a refreshed volume of water over the feature between laser pulses is important.

The effect of closed thick film flowing filtered water immersion on ablation threshold has been shown to vary with respect to beam fluence. For high fluence beams, the ablation threshold was significantly reduced when compared to ablation in ambient air at turbulent flow velocities. Conversely, for low fluence beams all but the lowest flow velocity tested showed significant increase in ablation threshold over a similar beam in ambient air. This is attributed to the action of plume etching being flow velocity dependant. For high fluence beams, the removal of the plume allows maximum laser etching, but when using low fluence beams, the significant relative attenuation posed by the closed flowing thick film filtered water immersion equipment became a serious disadvantage when compared to ablation in ambient air.

Use of DI water resulted in an ablation threshold that was similar to that of filtered water immersed ablation and 8.6% greater than that of laser ablating in ambient air. In both mediums 0.03 m/s was found to produce the most unstable depth - fluence relationship. Inspection of threshold dependency on pulse fluence magnitude shows a close agreement between the results produced in both media, further demonstrating the accuracy of the finding of this thesis. By measuring the ablation rate achieved, use of DI water was shown to perform 11.7% less efficiently than filtered water in thick film flowing immersed KrF excimer laser ablation. This discrepancy is too large to be explained by the 3% discrepancy in laser fluence used between the two. The ablation rate achieved by immersed KrF excimer laser ablation in DI water did not exceed that produced by ablation in ambient air and was 11.2% lower than the mean ablation rate produced by immersion using filtered water across all flow velocities, that did produce greater ablation rates than ablation in ambient air at 1.85 and 3.70 m/s. Furthermore, the trends of both media were similar in shape, supporting the theory of flow-plume interaction The assertion that the efficiency of low fluence machining is deteriorated by the use of immersion ablation was maintained by the DI water results and further confirms the proposal that low flow velocity coupled with high laser pulse frequency results in high attenuation of the beam, which impacts low fluence machining more than high fluence machining.

7. Topography of features machined into bisphenol A polycarbonate using closed thick film flowing filtered water immersed KrF excimer laser ablation.

KrF excimer laser machining of bisphenol A polycarbonate in mediums of air and under thick film flowing filtered water produced increasingly irregular surface waviness as laser beam fluence increased. This is a result that is expected, as localized beam energy variations across the beam area would become amplified at high fluences.

Feature geometry was shown to vary greatly between medium. In ambient air, machining bisphenol A polycarbonate with a 580.7 mJ/cm^2 KrF excimer laser pulse produced a relatively well defined feature that exhibited high wall draft angles of 82.1°; however, it had a noticeably domed bottom surface, though this was near level with the sample surface. Machining with a 617 mJ/cm^2 KrF excimer laser pulse immersed in closed thick film filtered water flowing at a laminar flow velocity of 0.11 m/s resulted in a poorly defined feature by comparison: having a floor slant angle of 1.6° and low wall draft angles of 66.2°. Increasing the filtered water flow velocity to 1.85 m/s resulted in a reduction of floor slant to 1.2° and increased wall draft angle to 81.6°. Use of further increased flow velocity, at 3.70 m/s, the best features were achieved, displaying near negligible feature floor slant at 0.5° and draft angles greater than those achieved in ambient air at 84.4°. The poor performance of the low flow velocity flow can be explained by the interaction of photomechanical etching then becoming superseded by non-laser plume effected KrF excimer laser machining at turbulent flow velocities.

The surface waviness, defined as macroscopic surface topography, was found to differ dependent upon the medium surrounding the ablation interaction and the flow velocity of the medium in the case of closed thick film filtered water immersed KrF excimer laser ablation of bisphenol A polycarbonate. Machining in a medium of ambient air resulted in the most consistent waviness data and using the laminar regime flow velocity of 0.11 m/s during closed thick film flowing filtered water immersion resulted in the least consistent data other six fluence values for each medium, ranging between 334.8 to 769 mJ/cm^2 and 306.8 to 644.8 mJ/cm^2 respectively. The mean waviness of samples machined using a flow velocity of 0.11 m/s across all fluences tested was 8.3% lower than that machined in ambient air. Furthermore, flow velocity was found to be important to the surface waviness measured. A peak mean waviness amplitude was measured for the flow velocity of 1.85 m/s, 23 nm greater than that measured for the samples machined using a flow velocity of 3.70 m/s.

A significant variation in trend from that produced by KrF excimer laser ablation in ambient air was achieved when using closed thick film flowing filtered water immersed ablation. The roughness generated in ambient air appeared unconnected to beam fluence. The plume generated at the start of a laser pulse went on to slightly shield the sample from the raw beam for the duration of the rest of the pulse, softening its profile and resulting in the low surface roughness values measured. This is in marked contrast to the immersed ablation case, where roughness was clearly dependent upon laser fluence. Moreover, the significance of fluence on the feature roughness was again proportional to immersion medium flow velocity. This relationship appeared to follow a power law, as the difference between the ratio that described roughness amplitude with respect to fluence for 3.70 and 1.85 m/s was significantly smaller than that displayed between 1.85 and 0.11 m/s.

8. Flow – plume interaction

Plotting the threshold fluence values projected from this data against the flow velocity they were produced with resulted in a plot trend of subtle but interesting significance. To achieve minimum threshold fluence an optimum flow velocity existed of 3.00 m/s. Furthermore, similar interpretation of ablation rate yielded a similar trend, where a maximum ablation rate was reached between 2.78 and 3.24 m/s.

Comparison of the ablation rates measured with the flow velocities they were machined in shows a trend that confirms that suggested by the initial analysis of etch depth with respect to flow velocity. The trend also supports a scenario of flow-plume interactions previously proposed. When suspended debris was not removed between pulses due to insufficient flow velocity, the following pulse was intercepted by the suspended debris. Next, the flow velocity was sufficiently high to remove debris from above the feature between pulses, but insufficient to distort the ablation plume during a pulse. The immersion of the ablation plume with filtered water restricted the expansion of the plume, resulting in a plume of increased optical and physical density compared to that produced by ablation in ambient air. This compressed plume attenuates the laser beam producing the plume, reducing the beam energy that arrives at the material and as a result, the ablation rate. At the same time, the compressed plume reduced the loss in ablation rate by the action of plume etching. Increased flow velocity resulted in the production of an optimum ablation rate, that lay between 2.78 and 3.24 m/s, where the plume was distorted by the flowing filtered water, reducing the path length that the beam had to endure through the plume to reach the material surface, and as a result the losses due to plume shielding are lower. Simultaneously, the distorted, but still intact ablation plume was still providing a plume etching contribution. Further increased flow velocity began to destroy the ablation plume, allowing maximum access to the material surface for the beam and removing the plume etching contribution. The small variance of ablation rate achieved by modification of turbulent regime flow velocity indicates that laser etching provided the dominating contribution to the total ablation rate measured.

Analysis of the frequency at which the liquid volume above the feature being machined was refreshed with respect to the period between laser pulses supplied proved to be interesting. At 0.03 m/s the filtered water volume above the feature was refreshed 0.695 times between laser pulses and 11.1 times at 0.11 m/s. This means that the lower velocity flow could not remove suspended debris generated by one laser pulse from above the sample before the arrival of the next; this suspended debris intercepted the oncoming pulse before it arrived at the intended destination, reducing effective laser fluence at the feature. This is in contrast to the high laminar flow velocity, where the debris is completely removed from above the sample and the laser beam has clear access to the feature for machining. This effect is a critical component in the 37% variance between the two laminar flow velocities. Comparison of the mean ablation rate achieved in a laminar regime flow shows a 26.6% reduction in ablation rate to that achieved in a turbulent regime flow and 20% reduction compared to that produced by a similar KrF excimer laser beam with a fluence of 581 mJ/cm^2 ablating bisphenol A polycarbonate in ambient air.

The surface trends observed from the interpretation of the surface waviness and roughness data also suggested that the photomechanical etching mechanism, that was contributed to by viscous fluid compression of the ablation plume, was modified by flow velocity. Plumes in low velocity flows were limited by plume shielding; thus reducing the volume of the plume generated and the etching component provided by the plume resulting in poor macroscopic, uneven feature profile and low surface roughness Flow velocities greater than 2.31 m/s began to destroy the plume, preventing a plume etching contribution; resulting in well defined macroscopic feature geometry and high surface roughness as a result of the high proportional contribution of laser etching to the ablation mechanism.

The topography results again support the theory of an intermediate flow velocity that offered distortion to the plume, causing the high surface roughness produced by two amplified aggressive etching mechanisms: flow drag motivated plume distortion reduced beam attenuation (giving highly accurate macroscopic profile machining); and pressure based mechanical etching that was resultant of the laser ablation plume that had merely been distorted by this intermediate flow velocity (slightly reducing the feature profile definition and adding to surface roughness). The removal of the possibility for immersion film rupture and splashing afforded by the use of a fully enclosed duct system, employed for this thesis, has resulted in the flow-plume interactions proposed above. If splashing had occurred, as it did when using an open immersed KrF excimer laser ablation technique, this would not have been possible, as the plume etching contribution to material etching supported by this thesis would have been seriously limited by immersion film rupture.

9. Analysis of beam modification caused by the closed thick film filtered water immersed KrF excimer laser ablation technique.

Immersion of the ablation plume in filtered water resulted in a modification to the ablation mechanism as has been documented above. The ablation plume is less free to expand once generated by the initial phase of the laser pulse, this restriction in growth being caused by the increased viscosity of the filtered water medium and the vastly larger shock impedance that comes associated. The compression of the ablation plume resulted in a calculated plume pressure of 12.1 GPa, an increase of 53% over the value achieved in ambient air. Increased pressure resulted in associated thermal increase and greater plume density. This increased the effect of shielding through the plume, further raising the plume temperature. Previous contributors have shown a correlation between laser ablation plume pressure and surface Plasmon size and frequency. Plasmons interact strongly with photons to polarize, diffuse and refract light that illuminates the plasmon surface. Since the ablation plume pressure was increased significantly by laser ablation plume confinement when using closed thick film flowing filtered water immersion, this phenomena could be the cause, partially or as contributor thereof, of the darkened feature base surfaces observed to be a result of using this equipment; where the darkening is an optical symptom of the plasmons. Surface oxidation and charring could also have contributed; however, this is unlikely after ultrasonic bath immersion in ultra pure water did not remove significant amounts of charred material as would have been expected. It is believed the largest contribution was given by the effect of dramatically increased surface roughness, where the amplitude of surface asperities with base areas lower than 16 μm^2, act to reflect light unevenly from the surface to diffuse the light and prevent it from being reflected back to the observer through the microscope objective. If this is the case, such a characteristic could doubtlessly have a significant use in the displays or lighting industry, where even light distribution over a broad area is a desirable feature.

The deflection of the laser image by introduction of the closed thick film flowing filtered water immersion was calculated by use of the thin lens theory, Snell's law and the ray tracing technique. This technique predicted an increase to the DoF of the system of 2.958 mm, given the known thicknesses of 1.5 and 5.0 mm and refractive indexes for 248 nm radiation of 1.3787 and 1.5084 of the filtered water and ultra violet (UV) grade fused silica respectively, obstructing the beam when the equipment was installed in the ambient air of the micromachining centre used, which

typically has a refractive index of 1.0008. The actual increase in optical length measured to be in best focus when using the closed thick film flowing filtered water immersion equipment was 2.9 mm, showing that this modelling technique is relatively accurate and can be used as a tool for simple and quick system design.

The modification to the depth of focus (DoF) was measured discretely by comparing the variance in wall angle as samples, machined in ambient air and under closed thick film flowing filtered water immersion moved outside the DoF of the de-magnifying optic installed in the micromachining centre. This findings of this thesis indicated that the use of closed thick film flowing filtered water immersion can match the level of focus achieved by laser machining in ambient air.

When machining bisphenol A polycarbonate in ambient air, the optical length of the system could vary by 0.1 mm around the optimum focus to produce a measured mean wall angle of more than 77°; the same wall angle was only achievable over a range of 0.075 mm when machining under closed thick film flowing filtered water immersion. This indicates a 25% reduction in DoF that cannot be accredited to beam modification by the equipment, as this actually had the effect of increasing the DoF by virtue of reducing the angle of convergence of the characteristic rays in the image. This loss in perceived DoF must be due to the modification and proposed increased contribution of plume etching to the ablation mechanism.

FURTHER WORK RECOMMENDATIONS

This thesis has demonstrated the feasibility and effectiveness of a liquid immersed laser ablation technique for the purpose of in-line debris control. The level of control has been shown to be high and the impact on the laser ablation machining process is small and manageable. There are five key areas that have been identified in the generation of this thesis where further work is required to further enhance the understanding of the concepts involved and improve the functionality of this technique.

Ablation mechanism and shockwave modelling:

Much work has been conducted on the modelling of ablation in ambient air. A prediction technique of the action of these etch mechanisms, either alone or in a combination thereof has been created, named the Monte Carlo model. This model is vigorous and of good quality, but much debate surrounds its adoption as general solution.

Another approach can be taken to consider the result of an interaction between a laser beam with known parameters: pulse energy, duration, temporal shape, cross-sectional area and wavelength; and a material with known properties: component elements, the bond structure and bond energies maintaining the atomic structure and temperature. Given this detail it must be possible to calculate the nature of laser coupling with the surface, allowing the volume of the material ablated to be predicted; from thence, the ejection velocity could be predicted if the characteristics of the surrounding medium such as the shock impedance and mach number are known, the expansion rate of the shock wave can be predicted. With knowledge of the volume removed and the geometry of the material removed, the shockwave geometry and range could be predicted. This work would be complex and time consuming, and could be the subject of a number of further research theses alone. Some exploratory work was conducted as part of the work contributing to this thesis, but it was not directly relevant to the stated aims of the project, although it is of great interest for the sake of greater understanding.

Experimental measurement of ablation plume expansion and shock confinement:

Theoretical work, as outlined above must be verified using the case of a real shockwave by application of experimental analysis. A Schlieren based shadowgraphy technique can be employed, where a CCD based imaging system that is sensitive to the excimer laser wavelength (as can be achieved by removal of the notch filter on a DSLR camera) is used to image the disruption to an illumination beam passing through the ablation plume and onto the CCD. The illumination laser pulse could be timed to run a specific delay to the ablating pulse by use of a prism to split a single original source into the ablating and illumination beam. The illuminating pulse could be heavily attenuated by neutral density filters to allow only the laser energy given at the peak of the pulse temporal profile to excite the CCD, thus a very fast shutter speed would be simulated, allowing crisp imaging. Attempting such a technique would require considerable time and finance to collate the equipment needed, as the equipment used for the work in this thesis is not easily modifiable to suite the

requirements of a Schlieren technique. If conducted this work would be of great interest to the wider laser community and be groundbreaking research alone.

Increased data resolution:

When the novel application a flowing liquid film is applied, as has been done for this thesis, the flow velocity has been identified as a critical parameter that had a direct effect on the symptoms of laser ablation: ablation threshold, ablation rate and feature topography. This is a major finding, and more must be done to understand this interaction, thus allowing mathematical modelling and prediction to be applied. To do so, greater understanding can be gleaned of the flow-plume interaction by use of smaller increments of flow velocity to give a higher resolution plot of ablation rate, ablation velocity and topographical characteristics with respect to flow velocity. This would enable the relationship between these to be identified with greater accuracy. Also, the use of other immersion fluids for the same experimental investigation will allow understanding of the relationship between fluid characteristics and their impact on the ablation plume to be increased. Such work is highly time consuming and requires robust and efficient equipment for success. The equipment used for this thesis was designed for the function of feasibility analysis and initial experiments alone and is not ideal for the large volume of samples ideally desired to achieve the aim outlined above. Further development of equipment would be required to allow greater flow velocity and increased sample size.

Flow-plume interaction modelling and use of CFD for chamber design:

Given the greater understanding of the plume-flow interaction that will be afforded by the further work described above, understanding of the flow occurring inside the liquid immersion ablation chamber must be gained. Debris deposition has been shown to be inversely proportional to closed thick film filtered water flow velocity by this contribution; thus, increased flow velocity would appear to be preferable. However, flow velocity is proportional to ablation plume distortion. Computational Fluid Dynamics (CFD) can be used to model the flow characteristics within a flow chamber; hence, CFD could be used to optimize the chamber design. The impact of flow turbulence on the ablation plume must be better understood, and resulting design modification, with the aid of CFD, must be made to the chamber to further improve the performance of the system depending upon the desired etching characteristics. This thesis used two evolutions, moving from open geometry to simple closed geometry. More time and funding would allow further development and evolution of the closed thick film flowing immersion technique, that has been shown in this thesis to be beneficial and potentially viable for commercial use, to be conducted.

All off this work and insight will allow the greater understanding of the contributions of laser etching and compressed ablation plume etching, dependent upon flow velocity. Understanding this will allow users to intentionally modify the liquid immersed laser ablation characteristics to better suit desired feature function. Also, such control may allow a new level of laser ablation manufacturing innovation that has been strong throughout the history of the technology.

Factors involved in feature floor darkening:

Further investigation is needed of the characteristic feature floor darkening produced when using the closed thick film flowing liquid immersion technique during KrF excimer laser ablation. In the contribution given by this thesis, three plausible causes are proposed: increased surface roughness, surface charring and generation of surface plasmons. The impact of liquid modification in terms of chemistry has not been inspected in the work as yet. Understanding this could offer further interesting insight into the impact of dynamic viscosity on the distortion and removal of the ablation plume during the laser pulse. By proxy, this will allow prediction of surface topography characteristics, as the work presented in this contribution has shown that modification to the ablation plume by variation of flow velocity is a critical factor.

One expects that a large proportion of particulate detritus that is characteristic of charring would be removed by the action of Ultrasonic bathing, which was an eventuality not observe in this thesis. However, conclusive evidence can be obtained by application of X-ray photoelectron spectroscopy (XPS), to ascertain the surface chemistry of the features. This is a step that should be taken for features machined using a number of flowing liquid media for the closed thick film flowing filtered water immersed KrF excimer laser ablation technique; however time constrains (for sample production and careful preparation (for XPS), has made this unachievable for this thesis.

Another plausible, but little documented phenomena that could produce the modification to the feature surface that has been witnessed in the samples produced for this are surface plasmons. Some previous work by others has indicated that the surface plasmon population and plasmon dimensions may be related to the laser fluence used for surface machining. This thesis demonstrates that the laser ablation plume can be modified in a controllable manner by application or a closed thick film flowing liquid to immerse the ablation event. Further work is required to enhance the detail of understanding in this area, as it could present manufacturing potential for a number of significant industries including waveguide manufacture and hologram production. The presence and scale of surface plasmons can be interpreted by use of surface plasmon resonance imaging (SPRI) analysis. Work needs to be conducted to clarify the scale of modification to feature surface plasmons that is caused by use of closed thick film flowing liquid immersed laser ablation compared to laser ablation in ambient air. Work of this kind will go to compliment that conducted into the prediction and understanding of contributing factors involved in laser ablation, as discussed above.

Equipment development for greater industrial practicability:

The equipment developed iteratively in this thesis is not practicable for industrial use. The open liquid immersion system, that was initially experimented with in this contribution was designed giving priority to the ease of sample loading. The poor performance of this technique in terms of repeatable feature geometry, surface topography, ablation rate and ablation threshold dictated that this technique was not satisfactory. Since the open immersion technique did indicate promise in terms of ablation generated debris control and the losses in feature quality were identified to be a result of ablation plume motivated rupture and splashing of the thin film flowing immersion fluid, further development of the technique was commenced. A cure to these problems was found by use of the closed thick film flowing immersion equipment and resulted in the marked success that has been documented in this

thesis. As a consequence of achieving a closed geometry, the sample had to be sealed inside a machining chamber that had to be unfastened and dismantled to allow sample reloading. This was a complex and time consuming process that was not conducive to application in a production environment. Moreover, the size of samples that can be machined is limited by the size of the laser window used in the closed thick film liquid immersion equipment. The stiffness of the UV grade fused silica or quartz used as the window is limited and as a result the window thickness must increase proportionally with the area covered to contain the pressure drop across the flow chamber (a value that is dependent on flow velocity through the chamber and chamber size). Another limiting factor on window area used with this fully sealed technique is the prohibitive cost of large windows, which must be regularly changed and cleaned to maintain optimum performance.

To solve this practical issue, a new technique that provides the excellent stability of the closed thick film flowing immersion laser ablation technique with simple loading and maintenance of the optical characteristics of the micromachining centre must be developed. Ideally, a small chamber that can traverse a large open sample must be developed. A small chamber requires only a small chamber window, that has low cost and could easily be removed from the system for cleaning and maintenance by a user with minimal training. If the chamber was mounted rigidly in some manner to the de-magnifying optic and mask cradle at the correct separation, using the calculation shown to successfully predict such dimensions in this thesis, the correct focus of the laser micromachining centre could be maintained if the chamber was able to track the surface local level of an uneven large wafer. This is a simple premise, but requires some complex tooling, such as linear bearings, high torsional rigidity and low mass components (to minimize the inertia of the system). Most importantly, the equipment must remain a non-contact machining technique. This requirement dictates that the chamber must adopt an innovative technique to maintain a constant separation from the wafer surface. This separation must be small, and include a complex technique designed to prevent the immersion liquid inside the chamber from leaking through the separation gap between the sample surface and the chamber.

All of this means equipment that successfully answers all of these technical hurdles will be highly innovative in a number of areas. It will provide an in-line excimer laser ablation machining debris control solution that is novel, capable and a great benefit for those that excimer laser machine large numbers of samples for which debris population during and after manufacture is critical to yield. It will also present new possibilities for the user of the closed thick film flowing liquid immersed laser ablation technique to the characteristics of features machined in terms of increased user control of the process by modification of the flow velocity to impact the ablation rate, threshold, and critically, the feature geometry and surface topography.

REFERENCES

1 Harvey, E. C. and Rhumsby, P. T. "Fabrication techniques and their application to produce novel micromachined structures and devices using excimer laser projection", *Proceedings of SPIE*, 1997, **3223**, Washington. pp.26-33.

2 Rizvi, N. H., Rhumsby, P. T., and Gower, M. C. "New Developments And Applications In The Production Of 3D Microstructures By Laser Micromachining", *Proceedings of SPIE*, 1999, **3898**, pp.240-249.

3 Braun, A., Zimmer, K., Hösselbarth, B., Meinhardt, J., Bigl, F., Mehnert R. "Excimer laser micromachining and replication of 3D optical surfaces", *Applied Surface Science*, 1998, **127-128**, pp. 911-914.

4 Taguchi, G. *Quality engineering through design optimisation.* 1984

5 Gower, M. C. "Industrial Applications of Pulsed Lasers to Materials Microprocessing" *Proceedings of SPIE*, 1998, **3343**, pp.171-182.

6 Aso, K., Sasaki, Y., Yamada, N., Sony Corporation, Exitech Limited, 2006, "Laser processing apparatus, laser processing head and laser", U.S. Pat. **21912171**.

7 Kaiser, R. "Enhanced removal of sub-micron particles from surfaces by high molecular weight fluorocarbon surfactant solutions" *Particles on surfaces: detection, adhesion and removal*, 1989 (2) Ed. Mittal, K. L., Plenum Press, New York, pp.269-282.

8 Steen, W. M. *Laser material processing*, 2003 (3) Springer-Verlag, London.

9 Crafer, R., and Oakley, P. J. *Laser Processing in Manufacturing*, 1993, Chapman & Hall, London.

10 Pearcea, S. R. J., Henleya, S. J., Claeyssensa, F., May, R. W., Hallamb, K. R., Smitha, J. A., and Rosser, K. N. "Production of nanocrystalline diamond by laser ablation at the solid/liquid interface", *Diamond and related materials*, 2004, **13** (4-8), pp.661-665.

11 Dyer, P. E., Farrar, S., and Key, P. H. "Investigation of excimer ablation of ceramic and thin film Y-Ba-Cu-O using nanosecond photoacoustic techniques", *Applied Physics Letters*, 1992, **60** (15) pp.1890-1892.

12 Scaggs, M. J. *Method and apparatus for fine liquid spray assisted laser material processing*, Lambda Physic Application Center, 2003, **WO/2003/028943**, USA.

13 Vezenov, D. V., Noy, A., and Ashby, P. "Chemical force microscopy probing of fundamental chemical interactions", *Handbook of Molecular Force Spectroscopy*, 2005, Ed. Noy, A. Springer, USA. pp.97-122.

14 Chang, S. W., Ayothi, R., Bratton, T., Yang, D., Felix, N., Cao, H. B., Deng, H., and Ober, C. K. "sub-50 nm feature sizes using positive tone molecular glass resists for EUV lithography", *Journal of materials chemistry*, 2006, **16**, pp.1470-1474.

15 Shapiro, A., and Falco, C. M. "Implications of particle contamination for thin film growth", *Particles on surfaces: detection, adhesion and removal*, 1989 (2) Eds. Mittal, K. L., Plenum, New York. pp.245-251.

16 Bowling, R. A. "behaviour and detection of particles in vacuum processes", *Journal of the Electrochemical Society*, 1987, **134** (3), pp.122-133.

17 Alberg, M. "Particle generation and control in tubing and piping connection design", *Particles on surfaces: detection, adhesion and removal*, 1995, Ed. Mittal, K. L. Marcel Decker, New York. pp.189-203.

18 Stutman, M. B. Gore, W. L. "Measurement of detachable submicrometer particles and surface cleanliness of clean room garments", *Particles on surfaces: detection, adhesion and removal*, 1989 (2) Eds. Mittal, K. L., Plenum, New York. pp.67-76.

19 Bardina, J. "Methods for surface particle removal: a comparative study", *Particulate Science and Technology*, 1988, **6** (2) pp.121-131.

20 Lankard J. R., and Wolbold, G., "Excimer Laser Ablation of Polyimide in a Manufacturing Facility", *Applied Physics A*, 1992, **54**, pp.355-359.

21 Lobo, L. M., *Solid Phase By-Products of Laser Material Processing*, Doctoral Thesis, 2002, Loughborough University.

22 Krupp, H., "Particle adhesion: theory and experiment", *Advanced Colloid Interface Science*, 1967, **1** (2) pp.111-239.

23 Menon, V. B., Michaels, L. D., Donovan, R. P. and Ensor, D. S. "Ultrasonic and hydrodynamic techniques for particle removal from silicon wafers". *Particles on surfaces: detection, adhesion and removal*, 1989 (2) Eds. Mittal, K. L., Plenum, New York. pp.297-306.

24 Dyer, P. E., Key, P. H., Sands, D., Snelling, H. V., and Wagner, F. X. "Blast-wave Studies of Excimer Laser Ablation of ZnS", *Applied Surface Science*, 1995, **86** (1-4) pp.18-23.

25 Dyer, P. E., Karnakis, D. M., Key, P. H., and Tait, J. P. "Excimer Laser Ablation of Low and High Absorption Index Polymers", *Applied Surface Science*, 1996, **96-98**, pp.596-600.

26 Dyer, P. E., Karnakis, D. M., Key, P. H., and Sands, D. "Fast Photography of UV Laser Ablated Metal Films", *Applied Surface Science*, 1997 **109-110**, pp.168-173.

27 Clarke, P., Dyer, P. E., Key, P. H., and Snelling, H. V. "Plasma Ignition Thresholds in UV Laser Ablation Plumes", *Applied Physics A*, 1999, **69** (7) pp.S117-S120.

28 Xu, X. F. "Phase explosion and its time lag in nanosecond laser ablation", *Applied Surface Science*, 2000, **197**, pp.61-66.

29 Xu, X. F., and Song, K. H. "Phase change phenomena during high power laser-materials interaction", *Materials Science and Engineering A*, 2000, **292**, pp.162-168.

30 Kelly, R., and Miotello, A. "Comments on explosive mechanisms of laser sputtering", *Applied Surface Science*, 1996, **96**, pp.205-215.

31 Lee, S. K., Chang, W. S., and Na S. J. "Numerical and experimental study on the thermal damage of thin Cr films induced by excimer laser irradiation", *Journal of Applied Physics*, 1999, **86** (8) pp.4282-4289.

32 Pataulf, G., and Dyer, P. "Photomechanical Processes and Effects in Ablation", *Chemical Review*, 2003, **103** (2) pp.487-518.

33 Georgiou, S., and Koubenakis, A. "Laser-Induced Material Ejection from Model Molecular Solids and Liquids: Mechanisms, Implications, and Applications", *Chemical Review*, 2003, **103** (2) pp.349–394.

34 Prasad, M., Conforti, P. F., and Garrison, B. J. "Coupled molecular dynamics-Monte Carlo model to study the role of chemical processes during laser ablation of polymeric materials", *Journal of Chemical Physics*, 2007, **127** (8) pp.127-139.

35 London. F. "The general theory of molecular forces", *Transactions of the Faraday Society*, 1937, **33** (8) pp.8b-37.

36 Lifshitz, E. M. "The theory of molecular attractive forces between solids", *Soviet physics JETP-USSR*, 1956, **2** (1) pp.73-83.

37 Leite, F. L., and Herrmann, P. S. P. "Application of atomic force spectroscopy to studies of adhesion phenomena: a review". *Atomic force microscopy in adhesion studies*, 2005, **19** (3-5) pp.365-405.

38 Visser, J. "The Adhesion of Colloidal Polystyrene Particles to Cellophane as a Function of pH and Ionic Strength", *Journal of Colloid and Interfacial Science*, 1976, **55** (3) pp.664-667.

39 Fuller, K. N. G., and Taber, D. "The Effect of Surface Roughness on the Adhesion of Elastic Solids", *Proceedings of the Royal Society A*, 1975, **345** (3) pp.327-342.

40 Feiler, A. A., Jenkins, P., and Rutland, M. W. "Effect of relative humidity on adhesion and frictional properties of micro and nano-scopic contact", *Journal of adhesion science and technology*, 2005, **19** (3-5) pp.165-179.

41 Yukawa. H. "Quantum theory of non-local fields: Part 1. Free fields", *Physical Review*, 1950, **77** (2), pp.219-226.

42 Mizes, H., Ott, M., Eklund, E., and Hays, D. "Small particle adhesion: measurement and control", *Colloids and Surfaces A*, 2000, **165** (1-3) pp.11-23.

43 Stowers, I. F., and Patton, H. G. "Techniques for removing contaminants from optical surfaces", *Proceedings of the Conference on Contamination*, 1978, Washington, DC, USA, pp.127-141.

44 Hutcheson, G. D. "Recent trends in clean technology", *Microcontamination*, 1988, **8**, pp.33-41.

45 Rizvi, N. H. "Production of Novel 3D Microstructures Using Excimer Laser Mask Projection Techniques", *Proceedings of SPIE*, 1999, **3680**, SPIE, pp.546-552.

46 Pedder, J. E., Holmes, A. S., Booth, H. J. "Pulsed Laser Ablation of Polymers for Display Applications", *Proceedings of SPIE*, 2008, **6879**. SPIE Bellingham, WA, USA.

47 Exitech EUV microstepper tool for resist testing and technology evaluation presentation, 2004, *International SEMATECH Litho Forum*, Los Angeles. SEMATECH Inc.

48 Richerzhagen, B *Material shaping device with a laser beam which is injected into a stream of liquid*, Synova S.A., 1999, **WO/1999/056907**, Switzerland.

49 Wang. J., Niino. H., Yabe. A. "Micromachining of transparent materials with super-heated liquid generated by multiphotonic absorption of organic molecule", *Applied Surface Science*, 2000, **154–155**, pp.571–576.

50 Elaboudi, I., Lazare, S., Belin, C., Talaga, D., and Labrugere C. "From polymer films to organic nanoparticles suspensions by means of excimer laser ablation in water", *Applied Physics A*, 2008, **93** (4) pp.827-831.

51 Elaboudi, I., Lazare, S., Belin, C., Talaga, D., and Labrugere C. "Underwater excimer laser ablation of polymers", *Applied Physics A*, 2008, **92** (4) pp.743-748.

52 Elaboudi, I., Lazare, S., Belin, C., Talaga, D., and Labrugere C. "Organic nanoparticles suspensions preparation by underwater excimer laser ablation of polycarbonate", *Applied Surface Science*, 2007, **253** (13) pp.7835-7839.

53 Sattari, R., Sajti, C. L., Kahn, S., and Barcikowski, S. "Scale-up of nanoparticle production during laser ablation of ceramics in liquid media", *The proceedings of The 27th International Congress on Application of Lasers and Electro-Optics: Laser Materials Processing Section*, 2008, pp.49-54.

54 Berthe, L., Fabbro, R., Peyre, P., and Bartnicki, E. "Wavelength dependent of laser shock-wave generation in the water-confinement regime", *Journal of Applied Physics*, 1999, **85**, (11) pp.7552-7555.

55 Katto, M., Kuroe, Y., Kaku, M., Kubodera, S., Yokotani, A., Katayama, H., and Nakayama, T. "Nano-particles of hydroxyapatite formed by underwater laser ablation method", *The proceedings of The 27th International Congress on Application of Lasers and Electro-Optics: Laser Materials Processing Section*, 2008, pp.65-67.

56 Zhu, S., Lu, Y. F., Hong, M. H., and Chen, X. Y. "Laser ablation of solid substrates in water and ambient air", *Journal of Applied Physics*, 2001, **89** (4) pp.2400-2403.

57 Phipps, C. R. *Laser Ablation and its Applications*, 2007, Springer. NL.

58 Hecht, E. *Optics*, 1998 (3) Addison Wesley Longman, New York.

59 Gray, D. E. *American Institute of Physics Handbook*, 1972 (3) McGraw-Hill, London.

60 Allmen, M. V., and Blatter, A. *Laser-Beam Interaction with Materials – Physical Principles and Applications*, 1995 (2) Springer-Verlag, Berlin.

61 Slater, T. *The underwater propagation of high-power pulsed and continuous-wave visible lasers: non-linear effects and a solid state beam manipulation tool for imaging applications*, 2000, Thesis, Loughborough University.

62 Schwarz, B., Gruttner, M., and Rohle, W. "Beam attenuation measurement of hydrosols by means of a new measuring technique", *Measurement science and technology*, 1990, **1**, pp.1102-1105.

63 Quickenden, T. I., and Irvin, J. A. "The ultraviolet absorption spectrum of liquid water", *Journal of Chemical Physics*, 1980, **72** (8) pp.4416-4428.

64 Buiteveld, H. and Hakvoort, J. M. H. and Donze, M. "The optical properties of pure water", *Proceedings of SPIE*, 1994, **2258**, pp.174-183.

65 Shackelford, J. F., and Alexander, W. *CRC Materials Science and Engineering Handbook*, 2001 (3) CRC Press.

66 Zel'dovich, Y. B., and Raizer, Y. P. *Physics of shock waves and high-temperature hydrodynamic phenomena*, 2002, Dover Publications, Inc, USA, pp604-605.

67 Quickenden, T. I., and Irvin, J. A. "The ultraviolet absorption spectrum of liquid water," *Journal of Chemical Physics*, 1980, **72**, pp.4416-4428.

68 Buiteveld, H., Hakvoort, J. M. H., and Donze, M. "The optical properties of pure water," *Proceedings of SPIE*, 1994, **2258**, pp.174-183.

69 Kopelevich, O. V. "Optical properties of pure water in the 250 - 600 nm range," *Optical Spectroscopy*, 1976, **41**, pp.391- 392.

70 Sogandares, F. M., and Fry, E. S. "Absorption spectrum (340 - 640nm) of pure water. I. Photothermal Measurements", *Applied Optics*, 1997, **36**, pp.8699--8709.

71 Pope, R. M., and Fry, E. S. "Absorption spectrum (380 - 700nm) of pure water. II. Integrating cavity measurements", *Applied Optics*, 1997, **36**, pp.8710-8723.

72 *The concise Oxford dictionary of current English*, 1995, Ed. Thompson, D. Clarendon, Oxford.

73 Sakka, T., Takatani, K., Ogate, Y. H., and Mabuchi, M. "Laser ablation at the solid-liquid interface: transient absorption of continuous spectral emission by ablated aluminium atoms", *Journal of Applied Physics*, 2002, **35** (1) pp.65-73.

74 Song, K. H., and Xu, X. "Explosive phase transformation in excimer laser ablation", *Applied Surface Science*, 1998, **127**, pp.111-116.

75 Lippert, T., Hauer, M., Phipps, C. R., and Workaun, A. "Fundamentals and applications of polymers designed for laser ablation", *Applied Physics A*, 2003, **77** (2) pp.259-264.

76 Yang, G. W. "Laser ablation in liquids: Applications in the synthesis of nanocrystals", *Progress in Materials Science*, 2006, **52** (4) pp.648-698.

77 Yung, K. C., Mei, S. M., and Yue, T. M. "Pulsed UV laser ablation of a liquid crystal polymer", *Advanced Manufacturing Technology*, 2005, **26** (11-12) pp.1231-1236.

78 Dyer, P. E. "Excimer laser polymer ablation: twenty years on", *Applied Physics A*, 2003, **77** (2) pp.167-173.

79 Srinivasan, R., and Braren, B. "Ultraviolet Laser Ablation of Organic Polymers", *Chemical Reviews*, 1989, **89** (6) pp.1303-1316.

80 Weisbuch, F., Tokarev, V. N., Lazare, S., and Débarre, D. "Ablation with a single micropatterned KrF laser pulse: quantitative evidence of transient liquid microflow driven by the plume pressure gradient at the surface of polyesters", *Applied Physics A*, 2003, **76** (4) pp.613-620.

81 Lippert, T. "Interaction of Photons with Polymers: From Surface Modification to Ablation", *Plasma Processes and Polymers*, 2005, **2**, pp.525-546.

82 Arnold, N., and Bityurin, N. "Model for laser-induced thermal degradation and ablation of polymers", *Applied Physics A*, 1999, **68** (6) pp.615-625.

83 Rabek, J. F. *Mechanism of photophysical processes and photochemical reactions in polymers: theory and applications*, 1987, J. Wiley & Sons, New York.

84 Masubuchi, T., Fukumura, H., Masuhara, H., Suzuki, K., and Hayashi, N. "Laser induced decomposition and ablation dynamics studied by nanosecond interferometry 3. A polyurethane film", *Journal of Photochemistry and Photobiology A*, 2001, **145** (3) pp.215-222.
85 Baker, A. K., and Dyer, P. E. "Refractive-index modification of polymethylmethacrylate (PMMA) thin films by KrF-laser irradiation", *Applied Physics A*, 1993, **57** (6) pp.543-544.
86 Lippert, T., David, C., Dickinson, J. T., Hauer, M., Kogelschatz, U., Langford, S. C., Nuyken, O., Phipps, C., Robert, J., and Wokaun, A. "Structure property relations of photoreactive polymers designed for laser ablation", *Journal of Photochemistry and Photobiology A*, 2001, **145** (3) pp.145-157.
87 Hare, D. E., Franken, J. and Dlott, D. D. "Coherent Raman measurements of polymer thin-film pressure and temperature during picosecond laser ablation", *Journal of Applied Physics*, 1995, 77 (11) pp.5950-5960.
88 Tsuboi, Y., Hatanaka, K. Fukumura, H., and Masuhara, H. "The 248-nm Excimer-Laser-Ablation Mechanism of Liquid Benzene Derivatives: Photochemical Formation of Benzyl Radical Leads to Ablation", *Journal of Physical Chemistry*, 1998, **102** (10) pp.1661-1665.
89 Furutani, H., Fukumura, H., Masuhara, H., Lippert, T. and Yabe, A. "Laser-Induced Decomposition and Ablation Dynamics Studied by Nanosecond Interferometry 1. A Triazenopolymer Film ", *Journal of Physical Chemistry A*, 1997, **101** (32) pp.5742–5747.
90 Hauer, M., Funk, D. J., Lippert, T., and Wokaun, A. "Time-resolved techniques as probes for the laser ablation process", *Optics and Lasers in Engineering*, 2005, **43** (3-5) pp.545-556.
91 Yoo, J. H., Jeong, S. H., Greif, R., and Russo, R. E. "Explosive changes in crater properties during high power nanosecond laser ablation of silicon", *Journal of Applied Physics*, 2000, **88** (3) pp.1638-1649.
92 Bauerle, D. "Laser processing and chemistry: recent developments", *Applied Surface Science*, 2002, **186** (1) pp.1-6.
93 Torrisi, L., Gammino, S., Andò, L., Nassisi, V., Doria, D., and Pedone, A. "Comparison of nanosecond ablation at 1064 and 308 nm wavelength", *Applied Surface Science*, 2003, **210** (3-4) pp.262-273.
94 Ullmann, M., Friedlander, S. K., and Schmidt-Ott, A. "Nanoparticle formation by laser ablation", *Journal of Nanoparticle research*, 2002, **4** (6) pp.499-509.
95 Gartner, G., Janiel, P., Lydtin, H., and Rehder, L. *Synthesis and measurement of Ultrafine Particles*, 1993, Eds. Marijnissen, J. C. M. and Pratsinis, S. Delft University Press, Netherlands.
96 Sasaki, T., Teraguchi, S., Koshizaki, N., and Umehara, H. "The preparation of iron complex oxide nanoparticles by pulsed-laser ablation", *Applied Surface Science*, 1998, **127-129**, pp.398-402.
97 Ogawa, K., Vogt, T., Ullmann, M., Johnson, S., and Friedlander, S. K. "Elastic properties of nanoparticle chain aggregates of TiO_2, Al_2O_3, and Fe_2O_3 generated by laser ablation", *Journal of Applied Physics*, 2000, **87** (1) pp.63-73.
98 Bereznai, M., Heszler, P., Tóth, Z., Wilhelmsson, O., and Boman, M. "Measurements of nanoparticle size distribution produced by laser ablation of tungsten and boron-carbide in N_2 ambient", *Applied Surface Science*, 2006, **252** (13) pp.4368-4372.
99 Ashfold, M. N. R., Claeyssens, F., Fuge, J. M., and Henley, S. J. "Pulsed laser ablation and deposition of thin films", *Chemical Society Reviews*, 2004, **33**, pp.23-31.
100 Vogel, A., and Venugopalan, V. "Mechanisms of pulsed laser ablation of biological tissues", *Chemical Review*, 2003, **103**, pp.577-644.
101 Kruusing, A. "Underwater and water-assisted laser processing: Part 2: Etching, cutting and rarely used methods", *Optics and Lasers in Engineering*, 2004, **41** (2) pp.329-352.
102 Fabbro, R., Peyre, P., Berthe, L., and Scherpereel, X. L. "Physics and applications of laser-shock processing", *Journal of Laser Applications*, 1998, **10** (6) pp.265-269.
103 Peyer, P., Berthe, L., Fabbro, R., and Sollier, A. "Experimental determination by PVDF and EMV techniques of shock amplitudes induced by 0.6-3 ns laser pulses in a confined regime with water", *Journal of Physics D*, 2000, **33**, pp.498-503.
104 Kim, D. S., Oh, B., and Lee, H. "Effect of liquid film on near-threshold laser ablation of a solid surface", *Applied Surface Science*, 2004, **222** (1-4) pp.138-147.
105 Nonhof, C. J. *Material processing with Nd-YAG*, 1988, Electro Chemical Publications Ltd, Ayr, Scotland.
106 Saha, M. N. "On a Physical Theory of Stellar Spectra", *Proceedings of the Royal Society of London A*, 1921, **99**, (697) pp.135–153.
107 Lancaster, J. F. *The Physics of Welding*, 1984, Pergamon, Oxford. P.127.
108 Mróz, W. "Physics of deposition of hydroxyapatite layers by the pulsed laser deposition method" *Functional properties of nanostructured materials*, 2006, Ed. Kassing, R., Springer, Netherlands. pp. 185-186.
109 Faenov, A. Y., Magunov, A. L., Pikuz, T. A., Skobelev, I. Y., Pikus, S. A., Bollanti, S., DiLazzaro, P., Lisi, N., Flora, F., Letardi, T., Palladine, L., Reale, A., Scafati, A., Grilli, A., Batani, D., Mauri, A., Osterheld, A., and Goldstein, W. "Characteristics of plasma heating by short wavelength excimer laser radiation", *Kvantovaya Elektronika*, 1996, **23** (8) pp.719-724.

110 Vergunova, G. A., Magunov, A. L., Dyakin, V. M., Faenov, A. Y., Pikuz, T. A., Skobelev, I, Y., Batani, D., Bossi, S., Bernardinello, A., Flora, F., DiLazzaro, P., Bollanti, S., Lisi, N., Letardi T., Reale, A., Palladino, L., Scafati, A., Reale, L., Osterheld, A. L., and Goldstein, W. H. "Features of plasma produced by excimer laser at low intensities" *Physica Scripta*, 1997, **55** (4) pp.483-490.
111 van de Hulst, H. C. *Light scattering by small particles*, 1957, John Wiley & Sons, Inc. USA.
112 van de Hulst, H. C. *Multiple light scattering – tables, formulas and applications*, 1980, **2**, Academic Press, USA.
113 Schittenhelm, H., Callies, G., Straub, A., Berger, P., and Hügel, H. "Measurements of wavelength-dependent transmission in excimer laser-induced plasma plumes and their interpretation", *Journal of applied physics*, 1998, **31**, pp.418-427.
114 Wise, J. L., and Chhabildas, L. C. "Laser interferometer measurements of refractive index in shock-compressed materials", *Proceedings of the American Physical Society Topical Conference on Shock Waves in Condensed Matter*, 1985, Spokane, Washington.
115 Sommersel, O. K., Bjerketvedt, D., Christensen, S. O., Krest, O., and Vaagsaether, K. "Application of background oriented Schlieren for quantitative measurements of shock waves from explosions" *Shock Waves*, 2008, **18**, pp.291-297.
116 Settles, G. A., Grumstrupa, T. P., Dodsona, L. J., Millera, J. D., and Gattob, J. A. "Full-scale high-speed schlieren imaging of explosions and gunshots", *Proceedings of SPIE*, 2005, **5580**, pp.60-68.
117 Kleine, H., Hiraki, K., Maruyama, H., Hayashida, T., Yonai, J., Kitamura, K., Kondo, Y., and Etoh, T. G. "High-speed time-resolved color schlieren visualization of shock wave phenomena" *Shock Waves*, 2005, **14** (5/6) pp.333.341.
118 Hauer, M., Funk, D. J., Lippert, T., and Wokauna, A. "Time resolved study of the laser ablation induced shockwave", *Thin Solid Films*, 2004, **453-454**. pp.584-588.
119 Lee, J., and Beckera, M. F. "Dynamics of laser ablation of microparticles prior to nanoparticle generation", *Journal of Applied Physics*, 2001, **89** (12). pp.8146-8152.
120 Hirata, T., and Miyazaki, Z. "High-Speed Camera Imaging for Laser Ablation Process: For Further Reliable Elemental Analysis Using Inductively Coupled Plasma-Mass Spectrometry", *Analytical Chemistry*, 2007, **79** (1). pp.147-152.
121 Nahen, K., and Vogel, A. "Shielding by the ablation plume during Er:YAG laser ablation", *Proceedings of SPIE*, 2001, **4257**. pp.282-297.
122 Wang, J., NiiNo. H., and Yabe. A. "Micromachining of quartz crystal with excimer lasers by laser-induced backside wet etching" *Applied Physics A*, 1999, **69** (S1) pp.S271-S273.
123 Kopitkovasa. G., Lipperta. T., David. C., Wokauna. A., and Gobrechtb. J. "Fabrication of micro-optical elements in quartz by laser induced backside wet etching", *Microelectronic Engineering*, 2003, **67–68**, pp.438–444.
124 Kopitkovasa. G., Lipperta. T., David. C., Wokauna. A., and Gobrechtb. J. "Surface micromachining of UV transparent materials", *Thin Solid Films*, 2004, **453–454**, pp.31–35.
125 Zimmer. K., and Böhme. R. "Precise etching of fused silica for micro-optical applications", *Applied Surface Science*, 2005, **243** (1-4) pp.415-420.
126 Yasui. Y., NiiNo. H., Kawaguchi. Y., and Yabe. A. "Microetching of fused silica by laser ablation of organic solution with XeCl excimer laser", *Applied Surface Science*, 2002, **186**, (1-4) pp.552-555.
127 Zapka, W., Ziemlich, W., and Tam, A. C. "Efficient pulsed laser removal of 0.2 μm sized particles from a solid surface", *Applied Physics Letters*, 1991, **58** (20) pp.2217-2219.
128 Munson, B. R., Young, D. F., and Okiishi, T. H. *Fundamentals of fluid mechanics*, 2002, **4**, John Wiley & Sons.
129 Wu., B. Q. "Photomask plasma etching: a review". *Journal of Vacuum Science and Technology B*, 2006, **24** (1) pp.1071-1123.
130 Customer correspondence with Compugraphics Ltd, Fife, UK, 2006.
131 Booth, H. J. "Recent applications of pulsed lasers in advanced materials processing", *Thin Solid Films*, 2004, **453**, pp.450-457.
132 Product dimensions and specifications for 'UV copying lens' range, 2007, Optec. S.A., Framerais, Belgium.
133 Wall, S., John, W., and Goren, S. L. "Application of impact adhesion theory to particle kinetic energy loss measurements", *Particles on surfaces: detection, adhesion and removal*, 1989 (2) Eds. Mittal, K. L., Plenum, New York. pp.19-34.
134 Reed, J. "The adhesion of small particles to a surface", *Particles on surfaces: detection, adhesion and removal*, 1989 (2) Eds. Mittal, K. L., Plenum, New York. pp.3-17.
135 Shi, X., and Zhao, Y. P., "Comparison of various adhesion contact theories and the influence of dimensionless load parameter", *Atomic force microscopy in adhesion studies*, 2005, Eds. Drelich, J. and Mittal, K. L., Leiden-Boston. pp.61-74.

136 Rimai, D. S., Demejo, L. P., Bowen, R., and Morris, J. D. "Particles on surfaces: adhesion induced deformations", *Particles on surfaces: detection, adhesion and removal*, 1995, Ed. K. L. Mittal, Marcel Decker; New York. pp.1-31.
137 Grierson, D. S., Flater, E. E., and Carpick, R. W. "Accounting for the JKR-DMT transition in adhesion and friction measurements with atomic force microscopy", *Journal of Adhesion Science and Technology*, 2005, **19** (3-5) pp.291-311.
138 Fowkes, F. W. "additivity of intermolecular forces at interfaces. I. Determination of the contribution to surface and interfacial tensions of dispersion forces in various liquids", *Journal of Physical Chemistry*, 1963, **67** (12) pp.2538-2541.
139 Rabinovich, Y. I., Alder, J. J., Ata, A., Singh, R. K., and Moudgil, B. M. "Adhesion between Nanoscale Rough Surfaces: I. Role of Asperity Geometry", *Journal of Colloidal Interface Science*, 2000, **232** (1) pp.10-16.
140 Rabinovich, Y. I., Alder, J. J., Ata, A., Singh, R. K., and Moudgil, B. M. "Adhesion between Nanoscale Rough Surfaces: II. Measurement and Comparison with Theory", *Journal of Colloidal Interface Science*, 2000, **232** (1) pp.17-32.
141 Maugis, D., "Adhesion of spheres: The JKR-DMT transition using a dugdale model", *Journal of Colloid and Interface Science*, 1991, **150** (1) pp.243-269.
142 Zhang, L., and Zhao, Y. P. "Adhesion between Nanoscale Rough Surfaces: I. Role of Asperity Geometry", *Journal of Colloid and Interface Science*, 2000, **232** (1) pp.10-16.
143 Van der Waals, J. D. *On the continuity of the gas and liquid state*, 1873.
144 Corn, M. *Aerosol Science*, 1966, Ed. Davies, C. N., Academic Press, New York. p.359.
145 Hamaker, C. N., "The London-van der Waals attraction between spherical particles", *Physica*, 1937, **4** (10) pp.1058-1072.
146 Corn, M. "The adhesion of solid particles to solid surfaces. I. A review", *Journal of Air Pollution Control Association*, 1961, **11** (11) pp.523-528.
147 Corn, M. J., and Silverman, L. "Removal of Solid Particles from a Solid Surface by a Turbulent Air Stream", *American Industrial Hygiene Association Journal*, 1961, **22** (5) pp.337-347.
148 Rumpf, H. "The strength of granules and agglomerates", *Agglomeration*, 1962, Wiley, New York. p.97.
149 London, F. Z. "On Centers of van der Waals Attraction.", *Journal of Physical Chemistry*, 1942, **46** (2) pp.305-316.
150 Menon, V. B., Michaels, L. D., Donovan, R. P., and Ensor, D.S. "effects of particulate size, composition, and medium on silicon-wafer cleaning", *Solid State Technology*, 1989, **32** (3) pp.S7-S12.
151 Mahanti, J., and Ninham, B. W. *Dispersion Forces*, 1980, Academic Press, London.
152 Hough, D. B. and White, L. R., "The calculation of Hamaker constants from Lifshitz theory with applications to wetting phenomena", *Advances in Colloid and Interface Science*, 1980, **14** (1) pp.3-41.
153 Israelachvili, J. N., and Tabor, D. "The Measurement of Van Der Waals Dispersion Forces in the Range 1.5 to 130 nm", *Proceedings of the Royal Society A*, 1972, **331** (1) pp.19-38.
154 Kitchener, J. A. "Surface forces in the deposition of small particles", *Journal of the Society of Cosmetic Chemists*, 1973, **24** (11) pp709-725.
155 Morgan, B. B. "The adhesion and cohesion of fine particles", *The British Coal Utilisation Research Association Monthly Bulletin*, 1961, **25** (4) pp.125-127.
156 Ibrahim, T. H., Burk, T. R., Etzler, F. M., and Neuman, R. D. "Direct adhesion measurement of pharmaceutical particles to gelatine capsule surfaces", *Journal of Adhesion Science and Technology*, 2000, **14** (10) pp.1225-1242.
157 Lam, K. K. and Newton, J. M. "Influence of particle size on the adhesion behaviour of powders, after application of an initial press-on force", *Powder Technology*, 1992, **73** (2) pp.117-125.
158 Leenaars, A. F. M., Huethorst, J. A. M., and Van Oekel, J. J. "Marangoni drying: A new extremely clean drying process", *Langmuir*, 1990, **6** (11) pp.1701–1703.
159 Pollock, H. M., Burnham, N. A., and Colton, R. J. "Attractive Forces Between Micron-Sized Particles: A Patch Charge Model", *The Journal of Adhesion*, 1995, **51** (1) pp.71-86.
160 Hao, H. W., Barò, A. M. and Saenz, J. J. "Electrostatic and contact forces in force microscopy", *Journal of Vacuum Science and Technology*, 1991, **9** (2) pp.1323-1328.
161 Deryagin, B. V. and Zimon, A. D. "Adhesion of particles to planar surfaces", *Kolloid Zournal*, 1961, **23** (5) p.454.
162 Hays, D. A. "Electric field detachment of toner", *Photographic Science and Engineering*, 1978, **22** (4) pp.232-235.
163 Cooper, D. W., Wolfe, H. L. Yeh, J. T. C., and Miller, R. J. in "Surface Cleaning by Electrostatic Removal of Particles", *Aerosol Science and Technology*, 1990, **13** (1) pp.116-123.
164 Derjaguin, B. V., and Landau, L.D. "Theory of the stability of strongly charged lyophobic sols and of the adhesion of strongly charged particles of electrolytes" *Acta Physicochim*, 1941, **14**, pp.633-662.

165 Verwey, E. J. W., and Overbeek, J. T. G. "Theory of the stability of Lyophobic Colloids". *The Journal of Physical Chemistry*, 1947, **51** (3) pp.631-636.
166 Esayanur, M. S., Yeruva, S. B., Rabinovich, Y. I., and Moudgil, B. M. "Interaction force measurements using atomic force microscopy for characterisation and control of adhesion, dispersion and lubrication in particle systems", *Journal of Adhesion Science and Technology*, 2005, **19** (8) pp.611-626.
167 Schneider, J., Barger, W., and Lee, G. U. "Nanometer Scale Surface Properties of Supported Lipid Bilayers Measured with Hydrophobic and Hydrophilic Atomic Force Microscope Probes", *Langmuir*, 2003, **19** (5) pp.1899-1907.
168 van der Vegte, E. W., and Hadziioannou, G. "Scanning Force Microscopy with Chemical Specificity: An Extensive Study of Chemically Specific Tip−Surface Interactions and the Chemical Imaging of Surface Functional Groups", *Langmuir*, 1997, **13** (16) pp.4357-4368.
169 Rimai, D. S., Quesnel, D. J., and Busnaina, A. A. "The adhesion of dry particles in the nanometer to micrometer-size range", *Colloids and Surfaces A*, 2000, **165** (1) pp.3-10.
170 Warszyński, P., Papastavrou, G., Wantke, K. D. and Möhwald, H. "Interpretation of adhesion force between self-assembled monolayers measured by chemical force microscopy", *Colloids and Surfaces A*, 2003, **214** (1-3) pp.61-75.
171 Beach, E. R., Tormoen, G. W., Drelich, J. and Han, R. "Pull-off force measurements between rough surfaces by atomic force microscopy", *Journal of Colloid Interface Science*, 2002, **247** (1) pp.84-99.
172 Méndez-Vilas, A., González-Martin, M. L., Labajos-Broncano, L. and Nuevo. M. J. "Experimental analysis of the influence of surface topography on the adhesion force as measured by an AFM", *Journal of Adhesion Science and Technology*, 2002, **16** (13) pp.1737-1747.
173 Tormoen, G. W., Drelich, J., and Nalaskowski, J. "A distribution of AFM pull-off forces for glass microspheres on a symmetrically structured rough surface". *Journal of adhesion science and technology*, 2005, **19** (3-5) pp.215-234.
174 Ott, M. L., and Mizes, H. "atomic force microscopy adhesion measurements of surface-modified toners for xerographic applications", *Colloids and surfaces A*, 1994, **87** (3) pp.245-256.
175 Beach, E. R., Tormoen, G. W., and Drelich, J. "Pull-off forces measured between hexadecanethiol self-assembled monolayers in air using an atomic force microscope: analysis of surface free energy", *Journal of Adhesion Science and Technology*, 2002, 16 (7) pp.845-868.
176 Ata, A., Rabinovich, Y. I. and Singh, R. K. "Role of surface roughness in capillary adhesion", *Journal of Colloid and Interface Science*, 2000, **232** (1) pp.10-16.
177 Segeren, L. H. G. J., Siebum, B., Karssenberg, F. G., van den Berg, J. W. A., and Vansco, G. J. "Microparticle adhesion studies by atomic force microscopy", *Journal of adhesion science and technology*, 2005, **16** (7) pp.793-828.
178 Bradley, R. S. "The cohesive force between solid surfaces and the surface energy of solids", *Philosophical Magazine*, 1932, **13** (86) pp.853-862.
179 Heim, L. O., Ecke, S., Preuss, M., and Butt, H. J. "Adhesion forces between individual gold and polystyrene particles", 2002, *Journal of Adhesion Science and Technology*, **16** (7) pp.829-843.
180 Tormoen, G. W., Drelich, J., and Beach, E. R. "Analysis of atomic force microscope pull-off forces for gold surfaces portraying nanoscale roughness and specific chemical functionality". *Journal of Adhesion Science and Technology*, 2004, **18** (1) pp.1-17.
181 Hertz, J. "On the contact of elastic solids", *Journal für die reine und angewandte Mathematik*, 1881, **92**, pp.156-171.
182 Johnson, K. L. *Contact mechanics*, 1987, Cambridge University Press, Cambridge.
183 Zhao, Y. P., Wang, L. S., and Yu, T. X. "Mechanics of adhesion in MEMS - a review", *Journal of Adhesion Science and Technology*, 2003, **17** (4) pp.519-546.
184 Enachescu, M., van den Oetelaar, R. J. A., Carpick, R. W., Ogletree, D. F., Flise, C. F. J., and Salmeron, M. "Atomic Force Microscopy Study of an Ideally Hard Contact: The Diamond(111)/Tungsten Carbide Interface", *Physical Review Letters*, 1998, **81** (9) pp.1877-1880.
185 Tormoen, G. W. and Drelich, J. "Deformation of soft colloidal probes during AFM pull-off force measurements: elimination of nano-roughness effects", *Journal of adhesion science and technology*, 2005, **19** (3-5) pp.425-442.
186 Maugis, D., and Pollock, H. M. "Surface forces, deformation and adherence at metal microcontacts", *Acta Metallurgica*, 1984, **32** (9) pp.1323-1334.
187 Johnson, K. L., Kendall, K., and Roberts, A. D., "Surface energy and the contact of elastic solids", *Proceedings of the Royal Society A*, 1971, **324**, pp.301-313.
188 Tabor, D. "Surface forces and surface interactions", *Journal of Colloid and Interface Science*, 1977, **58** (1) pp.2-13.

189 DeMejo, L. P., Remai, D. S., Chen, J. H., and Bowen, R. "Surface force tensile interactions between micrometer size particles and polyester-PDMS block copolymer substrate". *Particles on surfaces: detection, adhesion and removal*, 1995, Ed. Mittal, K. L., Marcel Decker, New York. pp.33-45.
190 Leonard-Jones, J. E., and Taylor, P. A. "Some Theoretical Calculations of the Physical Properties of Certain Crystals", *Proceedings of the Royal Society A*, 1925, **109** (751) pp.476-508.
191 Muller, V. M., Yushchenko, V. S., and Derjaguin, B. V. "On the influence of molecular forces on the deformation of an elastic sphere and its sticking to a rigid plane", *Journal of Colloid and Interface Science*, 1980, **77** (1) pp.91-101.
192 Carpick, R. W., Ogletree, D. F., and Salmeron, M. "A general equation for fitting contact area and friction vs load measurements", *Journal of Colloid and Interface Science*, 1999, **211** (2) pp.395-400.
193 Johnson, K. L. and Greenwood, J. A. "An Adhesion Map for the Contact of Elastic Spheres", *Journal of Colloid and Interface Science*, 1997, **192** (2) pp.326-333.
194 Davis, R. M. "The Determination of Static and Dynamic Yield Stresses Using a Steel Ball", *Proceedings of the Royal Society A*, 1949, **197**, pp.417-432.
195 Reed, J. "Energy losses due to elastic wave propagation during an elastic impact", *Journal of Physics D*, 1985, **18** (12) pp.2329-2337.
196 Rogers, L. N. and Reed, J. "Adhesion of particles undergoing an elastic-plastic impact with a surface", *Journal of Physics D*. 1984, **17** (4) pp.677-689.
197 Zimon, A. D. *Adhesion of Dust and Powder*, 1969, **1**, Plenum Press, New York.
198 Leite, F. L., Riul Jr., A., and Herrmann, P. S. P., "Mapping of adhesion forces on soil minerals in air and water by atomic force spectroscopy", *Journal of Adhesion Science and Technology*, 2003, **17** (16) pp.2141-2156.
199 Bickel, W. S., and Wentzel, T. M. "Adhesion due to a meniscus in a crossed-fibre system". *Particles on surfaces: detection, adhesion and removal*, 1989 (2) Eds. Mittal, K. L., Plenum, New York. pp.35-48.
200 Bhattacharya, S., and Mittal, K. L. "Mechanics of removing glass particulates from a solid surface", *Surface Technology*, 1978, **7** (5) pp.413-425.
201 Biggs, S., Cain, R. G., Dagastine, R. R., and Page, N. W. "Direct measurements of the adhesion between a glass particle and a glass surface in a humid atmosphere", *Journal of Adhesion Science and Technology*, 2002, **16** (7) pp.869-885.
202 de Lazzer, A., Dreyer, M., and Rath, H. J. "Particle– Surface Capillary Forces", *Langmuir*, 1999, **15** (13) pp.4551-4559.
203 Adamson, A. W., *Physical Chemistry of Surfaces*, 1967, **2**, Interscience, New York.
204 Marmur, A., "Tip-surface capillary interactions", *Langmuir*, 1993, **9** (7) pp.1922-1926.
205 Fisher, L. R., and Israelachvili, J. N. "Direct measurement of the effect of meniscus forces on adhesion: A study of the applicability of macroscopic thermodynamics to microscopic liquid interfaces", *Colloids and Surfaces*, 1981, **3** (4) pp.303-319.
206 Rabinovich, Y. I., Esayanur, M. S., Johanson, K. D., Alder, J. J., and Moudgil, B. M. "Measurement of oil-mediated particle adhesion to a silica substrate by atomic force microscopy". *Journal of adhesion science and technology*, 2002, **16** (7) pp.887-903.
207 Israelachvili, J. N. *Intermolecular and Surface Forces with Applications to Colloidal and Biological Systems*, 1985, Academic Press, London.
208 Parker, J. L., Claesson, P. M., and Attard, P. "Bubbles, cavities, and the long-ranged attraction between hydrophobic surfaces", *The Journal of Physical Chemistry*, 1994, **98** (34) pp.8468-8480.
209 Attard, P. "Friction, adhesion and deformation: dynamic measurements with the atomic force microscope", *Journal of Adhesion Science and Technology*, 2002, **16** (7) pp.753-791.
210 Meagher, L., and Craig, V. S. J. "Effect of dissolved gas and salt on the hydrophobic force between polypropylene surfaces", 1994, *Langmuir*, **10** (8) pp.2736-2742.
211 J. Wood and R. Sharma, "How Long Is the Long-Range Hydrophobic Attraction?", *Langmuir*, 1995, **11** (12) 4797-4802.
212 Carambassis, A., Jonker, L. C., Attard, P., and Rutland, M. W. "Forces Measured between Hydrophobic Surfaces due to a Submicroscopic Bridging Bubble", *Physical Review Letters*, 1998, **80** (24) pp.5357-5360.
213 Christendat, D., Abraham, T., Xu, Z. and Masliyah, J. "Adhesion forces between functionalized probes and hydrophilic silica surfaces", *Journal of Adhesion Science and Technology*, 2005, **19** (3-5) pp.149-163.
214 Xu, Z., Chi, R., Difeo, T., and Finch, A. "Surface forces between sphalerite and silica particles in aqueous solutions", *Journal of adhesion science and technology*, 2000, **14** (14) pp.1813-1827.
215 Lin, X. Y., Creuzet, F. and Arribart, H. "Atomic force microscopy for local characterization of surface acid-base properties", *The Journal of Physical Chemistry*, 1993, **97** (28) pp.7272-7276.
216 Green, J. D., McDermott, M. T., and Porter, M. D. "Nanometer-Scale Mapping of Chemically Distinct Domains at Well-Defined Organic Interfaces Using Frictional Force Microscopy", *The Journal of Physical Chemistry*, 1993, **99** (27) pp.10960-10965.

217 Lide, D. R., *CRC handbook of chemistry and physics*, 1972 (80) CRC Press, Boca Raton. pp.6-147.
218 Senden, T. J., and Drummond, C. J. "Surface chemistry and tip-sample interactions in atomic force microscopy", *Colloids and Surfaces A*, 1995, **94** (1) pp.29-51.
219 Bain, C. D., Evall, J., and Whitesides, G. M. "Formation of monolayers by the coadsorption of thiols on gold: variation in the head group, tail group, and solvent", *The Journal of the American Chemical Society*, 1989, **111** (18) pp.7155-7164.
220 Jacquot, C., and Takadoum, J. "A study of adhesion forces by atomic force microscopy", *Journal of Adhesion Science and Technology*, 2001, **15** (6) pp.681-687.
221 Plunkett, M. A., and Rutland, M. W. "Dynamic adhesion of grafted polymer surfaces as studied by surface force measurements", *Journal of adhesion science and technology*, 2002, **16** (7) pp.983-996.
222 Méndez-Vilas, A., González-Martín, M. L., Labajos-Broncano, L., and Nuevo, M. J. "Experimental analysis of the influence of surface topography on the adhesion force as measured by an AFM". *Journal of adhesion science and technology*, 2002, **16** (13) pp.1737-1747.
223 Ghosh, A., and Ryszytiwskyj, W. P. "Removal of glass particles from glass surfaces: a review", *Particles on surfaces: detection, adhesion and removal*, 1995, Ed. Mittal, K. L., Marcel Decker, New York. pp.353-362.
224 Nagarajan, R. "Particle removal characteristics of surface cleaning methods involving sonication and/or spray impingement". *Particles on surfaces: detection, adhesion and removal*, 1995, Ed. Mittal, K. L., Marcel Decker, New York. pp.363-378.
225 Ko, M. "Comparison of Freon with water cleaning processes for disk-drive parts". *Particles on surfaces: detection, adhesion and removal*, 1989 (2) Eds. Mittal, K. L., Plenum, New York. pp.283-295.
226 Kaiser, R. "Enhanced particle removal from inertial guidance instrument parts by fluorocarbon surfactant solutions". *Particles on surfaces: detection, adhesion and removal*, 1995, Ed. Mittal, K. L., Marcel Decker, New York. pp.395-404.
227 Skidmore, K. "Cleaning Techniques for Wafer Surfaces", *Semiconductor International*, 1987, **9** (9) pp.80-85.
228 Koppenbrink, J. W., McConnell, C. F., and Walter, A. E. "Particle reduction on silicone wafers as a result of isopropyl alcohol vapour displacement drying after wet processing". *Particles on surfaces: detection, adhesion and removal*, 1989 (2) Eds. Mittal, K. L., Plenum, New York. pp.235-243.
229 Musselman, R. P., and Yarbrough, T. W. "shear-stress cleaning for surface departiculation" *Journal of Environmental Science*, 1987, **51** (1) pp.51-56.
230 Mayer, A., and Schwartzman, S. "Megasonic cleaning: A new cleaning and drying system for use in semiconductor processing", *Journal of Electronic Materials*, 1979, **8** (6) pp.855-864.
231 Weiss, A. D., "Endpoint Monitors", *Semiconductor International*, 1983, **6** (9) pp.98-106.
232 Mullins, M. E., Michaels, L. P., V. Menon, V., Locke B., and Ranade, M. B. "Effect of Geometry on Particle Adhesion", *Aerosol Science and Technology*, 1992, **17** (2) pp.105-118.
233 Schwartzman, S., Mayer, A., and Kern, W. "Megasonic particle removal from solid-state wafers", **RCA Review**, 1985, **46** (81) pp.81-105.
234 Visser, J. "The concept of negative Hamaker coefficients. I. History and present status", *Advances in Colloid and Interface Science*, 1981, **15** (2) pp.157-169.
235 Hotaling, S. P., and Dykeman, D. A. "An advanced surface particle and molecular contamination identification removal and collection system". *Particles on surfaces: detection, adhesion and removal*, 1995, Ed. Mittal, K. L, Marcel Decker, New York. pp.111-140.
236 DeGeest, W. F. *Electrostatic Cleaner and Method*, 1970, Patent **3,536,328**, USA.
237 Zapka, W., Asch, K., Keyser, J., and Meissner, K. *Removal of particles from solid-state surfaces*, 1989, Patent **EP 0 297 506 A2**. DE.
238 Song, W. D., Lu, Y. F., Ye, K. D., Tee, C. K., Hong, M. H., Liu, D. M., and Low, T. S. "Cleaning force in laser cleaning of silicone substrates", *Proceedings of SPIE*, 1997, **3184**, pp.158-165.
239 Feng, Y., Liu, Z., Vilar, R., and Yi, X. S. "Laser surface cleaning of organic contaminants", *Applied Surface Science*, 1999, **150**, pp.131-136.
240 Lu, Y.F., Song, W.D., Ye, K.D., Hong, M.H., Liu, D.M., Chan, D.S.H., and Low, T.S. "Removal of submicron particles from nickel-phosphorus surfaces by pulsed laser irradiation", *Applied Surface Science*, 1997, **120**, pp.317-322.
241 Tam, A. C., Leung, W. P., and Zapka, W. "Laser - cleaning techniques for removal of surface particulates", *Journal of Applied Physics*, 1992, **71** (7) pp.3515-3523.
242 Mosbacher, M., Dobler, V., Boneberg, J., and Leiderer, P. "Universal threshold for the steam laser cleaning of submicron spherical particles from silicon", *Applied Physics A*, 2000, **70**, pp.669-672.
243 Low, D. K. Y., Li, L., and Byrd, P. J. "Spatter prevention during the laser drilling of selected aerospace materials", *Journal of Materials Processing Technology*, 2003, **139**, pp.71-76.

244 Li, L., and Achara, C. "Chemical assisted laser machining for the minimization of recast and heat affected zone", *Annals of the CIRP*, 2004, **53** (1),pp.175-178.
245 She, M., Kim, D., and Grigoropoulosb, C. P. "Liquid-assisted pulsed laser cleaning using near-infrared and ultraviolet radiation", *Journal of Applied Physics*, 1999, **86** (11), pp.6519-6524.
246 Birley, A. W., Haworth, B., Batchelor, J. *Physics of Plastics: processing, properties and materials engineering*, 1992, Hanser Gardner Publications, Cincinatti.
247 Kim, J. Y., Sohn, D., Kim E. R. "Polymer-based multi-layer conductive electrode film for plastic LCD applications", *Applied Physics A*, 2001, **72** (6) pp.699-704.
248 Jang, B. N., and Wilke, C. A. "The thermal degradation of bisphenol A polycarbonate in air", *Thermochimica acta*, 2004, **246** (1-2) pp.73-84.
249 Ball, Z., Feurer, T., Callahan, D. L., Sauerbray, R. "Thermal and mechanical coupling between successive pulses in KrF-excimer-laser ablation of polyimide", *Applied Physics A*, 1996, **62** (3) pp.203-211.
250 Lemoine, P., Magan, J.D., Blau, W.J. "Photoablative etching of materials for optoelectronic integrated devices", *Proceedings of SPIE*, 1991, **1377** (45) pp.45-56.
251 Kelly, R., and Miotello, A. "On the role of thermal processes in sputtering and composition changes due to ions or laser pulses", *Nuclear Instruments & Methods In Physics Research B*, 1998, **141** (1) pp.49-60.
252 Gower, M. C. "Excimer laser microfabrication and micromachining", *Laser Precision Microfabrication, RIKEN Review*, 2001, pp.50-56.
253 Khurgin, J. B., and Sun, G. "Enhancement of light absorption in a quantum well by surface plasmon polariton", *Applied Physics Letters*, 2009, **94** (19).
254 Luque, A., Marti, A., Mendes, M. J., and Tobias, I. "Light absorption in the near field around surface plasmon polaritons", *Journal of Applied Physics*, 2008, **104** (11).
255 Le Perchec, J., Quemerais, P., Barbara, A., and Lopez-Rios, T. "Why metallic surfaces with grooves a few nanometers deep and wide may strongly absorb visible light", *Physical Review Letters*, 2008, **100** (6).
256 Andersson, M., Iline, A., Stietz, F., and Trager, F. "Silicon nanoclusters formed through self-assembly on CaF2 substrates: morphology and optical properties", *Applied Physics A*, 2000, **70** (6). pp.625-632.
257 Glassner, A. S. *An introduction to ray tracing*, 1989 **(1)** Elsevier Science, Amsterdam.
258 Shaw M. J., Hooker, C. J., Wilson, D. C. "Measurement of the nonlinear refractive index of air and other gases at 248 nm", *Optics communications*, 1993, **103** (1-3) pp.153-160.
259 Equipment data sheet supplied with UV grade fused silica windows by Comar Instruments, Ltd
260 Liang, W., Huang, Y., Xu, Y., Lee, R. K., and Yariv, A. "Highly sensitive fiber Bragg grating refractive index sensors", *Applied physics letters*, 2005, **86** (15) pp.86-89.
261 Abbott C., Allott R., Bann B., Boehlen K. L., Gower M. C., Rumsby P. T., Stassen-Beohlen I. and Sykes N. "New techniques for laser micromachining MEMS devices", *Proceedings of SPIE*, 2002, **4760**, pp.281-289.
262 Cooper, J. B., Julian, B., Morrison, H. Song, P. Albin, S. and Zhen, J. L. "Surface characterization of pulsed UV-laser modified polyamide films", *Thin Solid Films*, 1997, **303** (1-2) pp.180-190.
263 Xu, X. F., and Song, K. H. "Interface kinetics during pulsed laser ablation; *Applied Physics A*, 1999, **69** (S1) pp.869-873.
264 Henderson, L. F., Jia-Huanb, M., Akirac, S., and Kazuyoshid, T. "Refraction of a shock wave at an air—water interface", *Fluid Dynamics Research*, 1990, **5** (5-6) pp.337-350.
265 Webb, J. D., and Woods, R. I. *Noise Control in Mechanical Systems*, 1976 **(1)** Sound Attenuators Ltd. & Sound Research Laboratories Ltd. UK
266 Kabashin, A. V., Meunier, M. "Synthesis of colloidal nanoparticles during femtosecond laser ablation of gold in water", *Journal of Applied Physics*, 2003, **94** (12) pp.7941-7943.
267 Dolgaeva, S. I., Simakina, A. V., Voronova, V. V., Shafeeva, G. A., and Bozon-Verdurazpp, F. "Nanoparticles produced by laser ablation of solids in liquid environment", *Applied Surface Science*, 2002, **186** (1-4) pp.546-551.
268 Maier, S. A. *Plasmonics: Fundamentals and Applications*, 2007, **1**, Springer, Oxford.
269 Böer, K. W. *Survey of Semiconductor Physics*, 2002 (1) Wiley, New York
270 Weast, R. C. *CRC Handbook of Chemistry and Physics*, 1978 (59) CRC Press, West Palm Beach, Florida, pp.D265–D314.